PHARMACEUTICAL SCIENCES

HOME SCIENCE

PHYSICS

SERI CULTUR

ENGINEERING

CHEMISTRY

ROBOTICS

Statistics

Electronics & Computer Science

ZOOLOGY

MICROBIOLOGY

BOTANY

Biochemistry

Geology

MATHEMATICS

RASHTRASANT TUKADOJI MAHARAJ NAGPUR UNIVERSITY

SCIENCE JOURNAL – 2018

VOL. XIV

EDITORIAL BOARD

FORM – IV

1. Place of Publication : Rashtrasant Tukadoji Maharaj
   Nagpur University, Nagpur.

2. Periodicity of its Publication : Annual

3. Printer's Name : Shri. Premanand S. Kharad
   Manager (Acting)

   Nationality : Indian

   Address : Rashtrasant Tukadoji Maharaj
   Nagpur Universi ty Press, Nagpur.

4. Publisher's Name : Dr. Puranchandra Meshram, Registrar

   Nationality : Indian

   Address : Rashtrasant Tukadoji Maharaj
   Nagpur University, Nagpur.440 001

5. Editor's Name : Dr. L. J. Paliwal

   Nationality : Indian

   Address : Editor in Chief
   Professor, Department of Chemistry,
   Mahatma Jotiba Phule Educational
   Campus, Rashtrasant Tukadoji Maharaj
   Nagpur University,
   Amravati Road, Nagpur.440 033.

6. Name & Address of : The journal is owned by the
   Individuals who own the Rashtrasant Tukadoji Maharaj
   Journal and Partners of Nagpur University, Nagpur.
   Share-holders, holding more
   Than one percent of the total capitals.

I Dr. Puranchandra Meshram, hereby declare that the particulars given above are true to the best of my knowledge and belief.

The University assumes no responsibility for the statements and expressed by the contributions.

Sd/-
Signature of Publisher
Dr. Puranchandra Meshram
Rashtrasant Tukadoji Maharaj
Nagpur Univ ersity, Nagpur

Date : 14-08-2018

INSTRUCTIONS FOR AUTHORS

1. General Information :

The Science Journal is a State level, peer -reviewed, journal published and financed by the Rashtrasant Tukadoji Maharaj Nagpur University, Nagpur. The Journal features topics in all areas of Science including Life Science, Physics, Chemistry, Mathematics, Statistics, Computer Science, Pharmaceutical Science, Environmental Science etc. The main purpose is to provide a platform to regional researchers to publish the high-quality articles of outstanding scientific significance.

When submitting an article to the Science Journal authors are not changed any publication fee. All publication costs for the journal authors are covred completely by the Rashtrasant Tukadoji Maharaj Nagpur University, Nagpur. To support rapid publication authors re required to submit new manuscripts electronically by email on **publicationrtm@gmail.com.**

A <u>Submission Checklist</u> is available to help authors to provide all relevant data and information. Authors can interrupt the submission process at any time.

Manuscripts which fall within the scope of the journal and are of potential interest to its readership are subject to a peer review process. Based on the referees, recommendation, the editor -in-chief or the associate editors make a decision on the manuscript regarding publication, revision or rejection. On case of acceptance, a;; papers are subject to copyediting and layout to ensure that they conform to the journal style. Once the submitting author returns a corrected proof of the manuscript new articles are published in the journal.

2. Manuscript Preparation :

2.1 Word processing formats

The following word processor file formats are acceptable for the main manuscript document for Science Journal :

a. Microsoft word (DOC,DOCX)

b. Note that figures, schemes and tables, equations should be included in the manuscript after the paragraph where they are first referenced. Chemical structures should preferably be embedded in their original chemical structure drawing file format (e.g. CDX for Chem. Draw)

c. TIFF (for photographs and screen dumps, 300 dpi if possible).

d. Text within figures should usually be either Arial or Times New Roman fonts: Courier may be used if a monospaced font is required. Text should be designed to be legible when illustration is scaled to a width of 600 pixels.

2.2 Style and Language :

a. The Science Journal accepts only manuscripts written in English.

b. Abbreviations should be used consistently throughout the whole manuscript. Non-standard abbreviations must be defined the first time they are used in the text.

c. Even though articles in the Science Journal have no page limit or restrictions on length and in the number of graphics, tables or supporting information they should adhere to scientific conciseness. Authors should provide enough background information to support the aim of study and the main claims of the paper, but unimportant or trivial information should not be included.

d. Authors are advised to write clearly, concise and simpy, and their article should be checked by colleagues before submission. The significance of the research should be objectively discussed. Nomnative speakers of English may choose to make use of a copyediting service since a manus cript may be rejected if it. Contains too many grammati cal arrors or typing mistakes. Alternatively, authours may seek the advice from expert in English language.

2.3 Typography and Formatting :

a. Please format the manuscript as single-column text using double line spacing.

b. Common font (Arial) should be used to reduce prob lems during conversion of the manuscript to a PDF file.

c. Type the text without manual hyphenating words at line breaks.

d. Use line breaks only to end headings and paragraphs, and not to rearrange lines.

e. All pages should be numbered.

f. Footnotes must not be used in any section of the paper.

g. Greek and other special characters should preferably be included using the font type "sympol". If you are unable to reproduce a particular special character, please type out the name of the symbol in full.

2.4 Article Types :

Every manu script submitted to the Science Journal has to be assigned by the authors to one of the following types of article:

a. Full Research Paper
b. Letter
c. Review

2.5   Organization of full Research Papers : 2500 words :

Manuscripts for full Research   Paper articles submitted to the Science Journal should be divided into the following sections :

a. Title Font : Arial, Font Size: 12 pts, Bold

b. Authors' Names and affiliations: Font: Arial, Font Size: 11pts.
    Where possible, supply given names, middle initi als, and family names for complete identification. Use superscript lowercase letters to indicate different addresses. The corresponding author should be indicate with an asterisk, and contact details Ifax, e- mail) should be placed in a footnote. Information relating to other authors (e.g., present addresses) should be placed in footnotes indicated by the appropriate symbols.

c. Abstract : 250 words Font : Arial (Italic), Font Size : 11pts

d. Keywords : 6 words separated by semicolon, Font : Arial, Font Size : 10pts

e. Introduction : Font : Arial Font Size : 11pts

f. Results and Discussion : Arial Font Size :11pts

g. Materials and Methods : Arial Font Size : 11pts

h. Conclusion : Arial Font Size : 12 pts

i. Supporting Information (if any) : Arial Font Size :11pts

j.   Acknowledgements (Optional) : Arial Font Size :11pts

k. References : Arial Font Size :11pts

   a. <u>Scientific articles</u> :

1. Mishra, S.; Karmodiya, K,; Suroliab, N.; Suroliaa, A. Bioorg. Med. Chem. 2008, 16, 2894.
    b. <u>Books </u>:

2.   Doe, J. S.; Smith, J. In Medicinal Chemis try ; Roe, P., Ed,; Pergamon : Oxford, 1990; Vol. 1, pp 301-383.
    c. <u>Patent/Chem. abstract </u>:

3. Lyle, F. R. U.S. Patent 6,973,257, 1995;

    d. <u>Chem, Abstr. 1995, 123, 2870.</u>

    e.   Conference Proceedings/Meeting abstract :

1. Prasad, A; Jackson, P. Abstracts of Papers, Part 2, 212th National Meeting of the American Chemical Society, Orlando, FL, Aug 25 -29, 1996; American Chemical Society: Washington, DC, 1996; PMSE 189.

    f.   Citing and listing of Web references :

As a Minimum, the full URL should be given. Any further information, if known (author names, dates, reference to a source publication, etc.) should also be given. Web references can be   listed separately (e.g. after the reference list) under a different heading if desired, or can be included in the references list.

The digital object identifier (DOI) may be used to cite and link to electronic documents.

Figures, Schemes and Tables:

The Figures, Schemes and Tables should be illustrated in the manuscript as a Figures, Schemes and Table respectively. The de signation scheme should be used primarily for reaction schemes.

1. Figures and schemes are consecutively numbered with Arabic numerals in the order they are first cited in the manuscript text (i.e. Figure 1, Figure2, etc.)

2. The legends of figures and schemes should be positioned directly below the corresponding graphic in the main manuscript rather than as part of the graphic file. They should comprise the bold typed figure.

3. Figures and schemes should be cropped as closely as possible to minimize whire space surrounding the graphic.

    All tables must be inserted in the manuscript text after the paragraph where they are first mentioned. The following guidelines must be considered when preparing tables:

4. Tables are consecutively numbered with Arabic numera ls in the order they are first cited in the manuscript text (i.e. Table 1, Table 2,etc.)

___

Contents

ARTICLE

Synthesis and anticancer activity of Imidazole and Triazole Derivatives of Flavonoids

Prafulla M. Sable[1*], Lata C. Potey[2]

[1] Department of Pharmaceutical Sciences, Rashtrasant Tukadoji Maharaj Nagpur University, Nagpur
Corresponding Author
Dr. Prafulla M. Sabale, Professor in Pharmaceutical Chemistry
E-mail:prafullasable@yahoo.com

Abstract: Flavonoids are a group of polyphenolic compounds that occurs naturally in foods of plant origin. It shows a wide variety of biological activities, such as Antioxidant, Antimicrobial, Anti-inflammatory and more specific is Anticancer activity. It is observed that the Flavonoids moiety possess characteristic pharmacophore pattern which is essential for binding to aromatase enzyme and their by its inhibition. Currently non-steroidal aromatase inhibitors posses heterocyclic ring such as imidazole and or triazole act as ligands, substituted aromatic ring at nucleus at suitable position acts as H bond acceptor which bound with Serine-478 present in active site of aromatase enzyme. Basic nucleus plays role as hydrophobic spacer moiety which maintained distance between heme coordinating group and hydrogen bond acceptor moiety. This work has been emphasized on the safe treatment of breast cancer by the synthesis of flavonoids derivatives with imidazole and triazole nucleus as a fundamental hetero-aromatic system with modification as non-steroidal aromatase inhibitors. Flavonoids have been synthesized by Baker Venkatraman reaction. Synthesis of substituted flavonoids scaffold was started by reacting 2, 4-dihydroxy acetophenone and substituted benzoyl chloride in acetone in presence potassium carbonate which was stirred for 30 minutes at room temperature, intermediate (2, 4 Bis-(substituted benzyloxy) acetophenone was obtained which on refluxed for 24 hrs, three flavonoids derivatives were obtained by modified Baker-Venkatraman method which has been reported recently. These derivatives by two pot synthesis were further reacted with imidazole in tetrahydrofuran by stirring for 24 hrs. Imidazole derivatives of flavonoids were obtained and also reacted with 1,2,4-Triazole in thionyl chloride and acetonitrile by stirring for 1 hr. at $0-5^0c$, triazole derivatives of flavonoids were obtained by a modified scheme of synthesis. Novel synthesized flavonoids have been confirmed by physical and spectral studies like IR, NMR and Mass and evaluated for in-vitro Anti-breast cancer activity against MCF-7 cell line through SRB assay. The triazole derivative with nitro substitution (H-bond accepting group) was found to be more active when compared with standard drug letrozole

Introduction

Flavonoids are a group of polyphenolic compounds that occur naturally in foods of plant origin. It shows a wide variety of biological activities such as anti-cancer, anti-inflammatory, anti-microbial, Alzheimer's Disease, anti-malarial, antioxidant, gastro-protection and α1-adrenoceptor (α1-AR) antagonists. Due to their structural and functional similarities with endogenous estrogen, Flavonoids have a potential role in ER-dependent breast cancer. [1]

Aromatase enzyme is highest in or near breast tumor sites. Several studies have been shown that serum level of estrogen is very low in postmenopausal women but the concentration of estrogen in breast tissues are 5-6 fold higher than serum level

estrogen, concentration in the tumor is even higher as compared to normal breast tissues. [2] Therefore, there are more chances

for an expansion of tumors in breasts of post-menopausal women.

Flavonoids interact with the heme moiety of the CYP prosthetic group of the of the aromatase molecule. These inhibitors contain suitably positioned hetero atoms usually in the imidazole and triazole ring that are capable of binding to CYP enzymes such that their hetero atoms coordinate the heme iron. Non-steroidal aromatase inhibitors are reversible and the resultant estrogen blockade is dependent on continuous presence of the drug. [3]

From the literature and structure-activity relationship, [4] it has been felt worthwhile to synthesize novel Flavonoids as possible antineoplastic agents with pharmacophoric pattern required for aromatase inhibition.

Pharmacophore Pattern of Aromatase Inhibitors with suitably positioned hetero atom, which strongly interact with heme iron, hydrophobic spacer moiety between heme coordinating group and hydrogen bond acceptor moiety which can abstract hydrogen from Serine 478 present in active site of enzyme and hydrophobic group is required to interact with aliphatic amino acid residue in active site. [5]

With this objective, we report the synthesis of non-steroidal aromatase inhibitors having flavones moiety with imidazole and triazole nucleus as a fundamental hetero-aromatic system with modification and accepted pharmacophoric pattern.

Figure 1: Flavonoids with required Pharmacophore pattern for aromatase inhibition flavones nucleus with imidazole and triazole ring as a fundamental hetero-aromatic system with modification.

All synthesized compound have been evaluated for *in-vitro* anticancer activity against MCF-7 cell line through SRB assay and assessed for percent Cell growth inhibition on MCF-7 cell line and potency (IC_{50}) value discussed for each compound after comparing with a standard drug. [4]

Result and Discussion

Chemistry

Synthesis of substituted flavonoids scaffold was started by reacting 2, 4-dihydroxy acetophenone and substituted benzoyl chloride in acetone in presence potassium carbonate which was stirred for 30 minutes at room temperature, intermediate (2,4 Bis-(substituted benzyloxy) acetophenone was obtained which on refluxed for 24 hrs, three flavonoids derivatives (1a, 1b, 1c) were obtained by modified Baker-Venkataraman method which has been reported recently.[6] These derivatives by two pot synthesis were further reacted with imidazole in tetrahydrofuran by stirring for 24 hrs. imidazole derivatives of flavonoids (2a, 2b, 2c) were obtained and also reacted with 1,2,4-Triazole in thionyl chloride and acetonitrile by stirring for 1 hr. at 0-5⁰c, triazole derivatives of flavonoids (3a,3b,) were obtained by a scheme of synthesis. [7] (Fig.2)
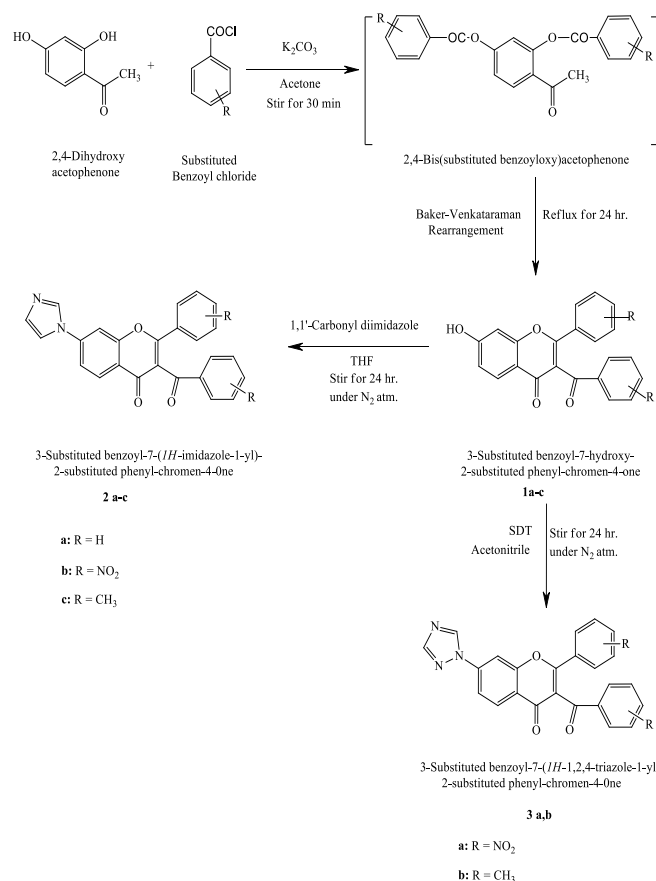
Figure 2: Scheme for synthesis of Imidazole and Triazole Derivatives of Flavonoids Reagents and conditions 1. Potassium carbonate, acetone, stirred for 30 min 2. Baker-Venkataraman rearrangement, refluxed for 24 hrs 3. Imidazole, tetrahydrofuran, stirred for 24 hrs under pressure of nitrogen, 4. 1, 2, 4 Triazole, acetonitrile, stirred for 24 hrs. [8]

Synthesized Compounds were analyzed by Melting point, IR, ¹HNMR, Mass Spectrophotometry and completion of reaction was monitored by TLC. Analytical Data of 2a, 2b, 2c and 3a, 3b, has been given in detail. (Table 1)

3-Benzoyl-7-(1H-imidazol-1-yl)-2-phenyl-4H-chromen-4-one (2a)

It shows characteristic peak at 1637, 1661 cm⁻¹ (C=O str. of flavones), 1584 cm⁻¹ (C=N str.), 1073 cm⁻¹ (C-O-C bend) in IR spectrum and M+18 peak at 411 in mass spectrum. The ¹H NMR of compound give signal at 6.9-7.14 (m, 2H, 6,7-CH), 7.15-7.68 (m, 9H, Ar-H), 7.72-7.8 (m, 4H, Ar-H), 8.2 (S, 1H, imidazole H-2"); m.p. 212-214 ºC

3-(4'-Nitrobenzoyl)-7-(1H-imidazol-1-yl)-2-(4'-nitrophenyl)-4H-chromen-4-one (2b)

It shows characteristic peak at 1619, 1669 cm⁻¹ (C=O str. of flavones), 1580 cm⁻¹ (C=N str.), 1034 cm⁻¹ (C-O-C bend), 1520, 1348 cm⁻¹ (NO₂) in IR spectrum and M+1 peak at 483.34 in mass spectrum. m.p.: 256-258 ºC

Table 1: Physiochemical data of all synthesized compounds

S.N.	Compound No	Mol. Formula	Mol. Wt. gm	Yield %	R_f	Solvent System
1	1a	$C_{22}H_{16}O_4$	342.09	74.00	0.89	A
2	1b	$C_{22}H_{12}O_7N_2$	432.06	62.90	0.94	A
3	1c	$C_{24}H_{18}O_4$	370.12	71.22	0.83	A
4	2a	$C_{25}H_{16}N_2O_3$	392.12	43.15	0.54	B
5	2b	$C_{25}H_{14}N_4O_7$	482.09	51.34	0.45	B
6	2c	$C_{27}H_{20}N_2O_3$	420.15	69.20	0.50	A
7	3a	$C_{24}H_{13}N_5O_7$	483.08	43.00	0.71	A
8	3b	$C_{26}H_{13}N_5O_7$	421.14	38.40	0.64	A

3-(4'-Methylbenzoyl)-7-(1H-imidazol-1-yl)-2-(4'-methylphenyl)-4H-chromen-4-one (2c)

It shows characteristic peak at 2864, 2726 cm^{-1} (C-H str.), 1683, 1640 cm^{-1} (C=O str. of flavones), 1071 cm^{-1} (C-O-C) in IR spectrum and M+1 peak at 483.34 in mass spectrum. The ^{1}H NMR of compound give signal at 2.55 (s, 3H, CH$_3$), 3.11 (s, 3H, CH$_3$), 6.90 (s, 1H), 7.37-7.6 (m, 4H, Ar-H), 7.63-7.8 (m, 2H, Ar-H), 8.22 (m, 2H, Ar-H) m.p.: 232-234ºC.

3-(4'-Nitrobenzoyl)-7-(1H-1, 2, 4-triazol-1-yl)-2-(4'-nitrophenyl)-4H-chromen-4-one (3a)

It shows characteristic peak at 1674, 1620 cm^{-1} (C=O str.), 1524, 1346 cm^{-1} (-NO$_2$), 1051 (C-O-C) in IR spectrum and M+2 at 485.7 in mass spectrum. ^{1}H-NMR Shows signals at 6.8-7.0 (d, 2H, 6, 7-CH), 7.3-7.8 (m, 7H, Ar-H), 8.0-8.2 (m, 3H, Ar-H), 8.3 (s, 1H, triazole 2-H"). m.p.: 228-23 ºC

3-(4'-Methylbenzoyl)-7-(1H-1,2,4-triazol-1-yl)-2-(4'-methylphenyl)-4H-chromen-4-one (3b)

It shows characteristic peaks at 1667 cm^{-1} (C=O str.), 2923, 2840 (C-H str.), 1060 (C-O-C str.) and M$^+$ at 420.3. The ^{1}H NMR shows 2.34 (s, 3H, CH$_3$), 2.63 (s, 3H, CH$_3$), 6.89 (s, 1H, 8-CH), 7.0-7.21 (m, 4H, Ar-H), 7.28-7.8 (m, 7H, Ar-H), 8.25 (s, 1H, imidazole H-2''); m.p. 206-208 ºC

Biology

All synthesized compounds were evaluated for *in-vitro* anticancer activity against MCF-7 cell line through SRB assay. This activity has been carried out in collaboration with Dr. Arti S. Juvekar, Head, Screening department at Advanced Centre for Treatment Research and Education in Cancer (ACTREC), Khargarh, and Mumbai.

MCF-7 is a breast cancer cell line is the acronym of Michigan Cancer Foundation-7. MCF-7, it is not possible for cancer researchers to obtain a mammary cell line that was capable of living longer than a few months. The cell lines were grown in RPMI (Roswell Park Memorial Institute) 1640 medium containing 10% fetal bovine serum and 2 ml L-glutamine.

SRB Assay

Sulforhodamine B (SRB) assay was carried out as per method given by Skehan et al [4] Experimental drugs were solubilized in 0.1% DMSO at 400-fold the desired final maximum test concentration and stored frozen prior to use. Then 10-fold serial dilutions were made to provide a total of four drug concentrations plus control. Aliquots of 10 µl of these different drug dilutions were added to the appropriate microtiter plate with 90 wells which previously air dried. [9]

The optical density of wells was determined at wavelength 540 nm by a colorimetric plate reader. Percent growth was calculated on a plate-by-plate basis for test wells relative to control wells. Percent Growth was expressed as the ratio of average absorbance of the test well to the average absorbance of the control wells * 100.

Using the six absorbance measurements [time zero (Tz), control growth (C), and test growth in the presence of drug at the four concentration levels (Ti)], the percentage growth was calculated at each of the drug concentration levels. Percentage growth inhibition was calculated as:

[(Ti-Tz)/(C-Tz)] x 100 for concentrations for which Ti>/=Tz (Ti-Tz) positive or zero

[(Ti-Tz)/Tz] x 100 for concentrations for which Ti<Tz. (Ti-Tz) negative

The IC$_{50}$ value was determined by Graph pad prism software. [10] (Table 2, 3)

Table 2: % Cell growth inhibition data on MCF-7 cell line by assay

	Log Conc.	% Inhibition of Cell Growth					
		Std Letrozole	**2a**	**2b**	**2c**	**3a**	**3b**
0.05	-1.29	-27.26	-32.61	-29.06	-30.06	-28.39	-29.71
0.15	-0.82	-22.69	-28.02	-26.89	-28.32	-26.02	-27.45
0.46	-0.34	-16.88	-22.08	-23.33	-24.0	-21.36	-24.15
1.37	0.14	-10.80	-15.88	-18.18	-17.08	-13.19	-18.02
4.12	0.61	-4.89	-07.1	-11.24	-14.82	-9.08	-10.56
12.35	1.09	3.34	9.91	3.59	1.59	8.87	6.06
37.04	1.57	10.61	15.07	5.66	3.14	19.21	13.88
111.11	2.05	17.84	22.62	11.06	7.63	24.81	22.06
333.33	2.52	24.29	32.81	15.08	10.21	34.02	30.87
1000.00	3.00	32.02	46.29	21.22	17.87	49.88	41.96

Table 3: Potency (IC$_{50}$) of all synthesized compound and compared with standard drug

Compounds	IC$_{50}$ (µM)
Letrozole	10.62
2a	15.88
2b	28.48
2c	42.02
3a	11.23
3b	21.48

Experimental

Material and Method

All the chemicals of analytical grade were purchased from LOBA chemicals, SDFCL and Spectrochem. Chemicals and solvents were purified by general laboratory techniques before use. All moisture free operations were performed in oven-dried glassware and under the nitrogen atmosphere. Synthesized compounds were characterized by melting point, IR, HNMR, MASS Spectrophotometry and progression of the reaction was monitored by TLC. Melting points were determined by VEEGO to make microprocessor based melting point apparatus having silicone oil bath and are uncorrected. IR spectra (wave numbers in cm⁻¹) were recorded on a BRUKER ALPHA FT-IR spectrophotometer using Potassium bromide discs. NMR spectra were recorded on BRUKER AVANCE II 400 MHz instrument in CDCl₃ with TMS as an internal standard for ¹H NMR. Chemical shift values were mentioned in δ, ppm. Mass spectra were recorded on Advion Expression, CMS, the USA at Syntel Research Solutions, Gandhinagar. Chromatographic separations were performed on columns using silica gel 100–200 mesh. The progress of all reactions was monitored by TLC on 2 cm X 5 cm pre-coated silica gel 60 F254 (Merck) plates of a thickness of 0.25 mm. The chromatograms were visualized under UV 254 nm and/or exposure to iodine vapors.

3-Benzoyl-7-hydroxy-2-phenyl-4H-chromen-4-one [1a]

Anhydrous potassium carbonate (6.150 g, 0.0472 mmol) was added to a stirred solution of 2′,4′- Dihydroxyacetophenone (1.0 g, 0.0065 mmol) in dry acetone (60 ml). The mixture was stirred at room temperature for 10 min and then benzoyl chloride (1.67 ml, 0.01314 mmol) was added dropwise through the pressure equalizing dropping funnel (PEDF) and the mixture was stirred at room temperature for an additional 30 min. After refluxing for 24 h, the solvent was removed under reduced pressure. The residue was cooled to room temperature and acidified in a beaker with dilute hydrochloric acid to weak acidity. The precipitate formed was filtered off, dried and then recrystallized from acetic acid. [10]

3-(4′-Nitrobenzoyl)-7-hydroxy-2-(4′-nitrophenyl)-4H-chromen-4-one [1b]

Anhydrous potassium carbonate (6.150 g, 0.0472 mmol) was added to a stirred solution of 2′,4′- Dihydroxyacetophenone (1.0 g, 0.00657 mmol) in dry acetone (60 ml). The mixture was stirred at room temperature for 10 min and then 4-Nitrobenzoyl chloride (2.438 g, 0.01314 mmol) was added dropwise through PEDF and the mixture was stirred at room temperature for an additional 30 min. After refluxing for 18 h, the solvent was recovered under reduced pressure. The residue was cooled to room temperature and acidified in a beaker with dilute

hydrochloric acid to weak acidity. The precipitate so formed was filtered off, dried and then recrystallized with acetic acid.

3-(4′-Methylbenzoyl)-7-hydroxy-2-(4′-methylphenyl)-4H-chromen-4-one [1c]

Anhydrous potassium carbonate (6.150 g, 0.0472 mmol) was added to a stirred solution of 2′,4′- Dihydroxyacetophenone (1.0 g, 0.00657 mmol) in dry acetone (60 ml). The mixture was stirred at room temperature for 10 min and then 4-Methylbenzoyl chloride (2.01 ml, 0.01314 mmol) was added dropwise through PEDF and the mixture was stirred at room temperature for an additional 30 min. After refluxing for 20 h, the solvent was evaporated under reduced pressure. The residue was cooled to room temperature and acidified in a beaker with dilute hydrochloric acid to weak acidity. The precipitate formed was filtered off, washed with acidified water dried and then recrystallized with acetic acid.

3-Benzoyl-7-(1H-imidazol-1-yl)-2-phenyl-4H-chromen-4-one [2a]

To a solution of 3-benzoyl-7-hydroxy-2-phenyl-4H-Chromen-4-one (0.5 g, 0.00146 mmol) in anhydrous THF (20 ml) was added 1, 1′-Carbonyldiimidazole (0.95 g, 0.00584 mol). The mixture was stirred under nitrogen atmosphere at room temperature for 24 hrs. Subsequently, the semi-solid mass was quenched with chloroform. Impurities were removed by filtration and the organic layer was collected and the solvent was recovered under reduced pressure. The resulting crude product was purified by passing through column chromatography using silica gel (100-200 mesh) and eluted with hexane: ethyl acetate (7:3)

3-(4′-Nitrobenzoyl)-7-(1H-imidazol-1-yl)-2-(4′-nitrophenyl)-4H-chromen-4-one [2b]

To a solution of 3-(4'-Nitrobenzoyl)-7-(1H-imidazole-1-yl)-2-(4'-nitrophenyl)-4H-1-Chromen-4-one (0.5 g, 0.00115 mmol) was stirred with,1'-Carbonyldiimidazole (0.750 g, 0.00462 mmol) in anhydrous THF (25 ml). The mixture was stirred under nitrogen atmosphere at room temperature for 20 hrs. Subsequently, the semi-solid mass was quenched with chloroform. Impurities were removed by filtration and the organic layer was collected and the solvent was recovered under reduced pressure. The resulting crude product was purified by passing through column chromatography using silica gel (100-200 mesh) and eluted with hexane: ethyl acetate (5:5).

3-(4′-Methylbenzoyl)-7-(1H-imidazol-1-yl)-2-(4′-methylphenyl)-4H-chromen-4-one [2c]

To a solution of 3-(4'-Methylbenzoyl)-7-(1H-imidazole-1-yl)-2-(4'-Methylphenyl)-4H-Chromen-4-one (0.4 g, 0.00108 mmol) in anhydrous THF (20 ml) was added 1,1'-Carbonyldiimidazole

(0.70 g, 0.00432 mol). The mixture was stirred under nitrogen atmosphere at room temperature for 30 hrs with the addition of 1,1'-Carbonyldiimidazole. Subsequently, the semi-solid mass was quenched with chloroform. Impurities were removed by filtration and the organic layer was collected and the solvent was recovered under reduced pressure. The resulting crude product was purified by passing through column chromatography using silica gel (100-200 mesh) and eluted with hexane: ethyl acetate (5:5).

3-(4'-Nitrobenzoyl)-7-(1H-1,2,4-triazol-1-yl)-2-(4'-nitrophenyl)-4H-chromen-4-one[3a]

To a chilled solution (0-5°C) of thionyl chloride (0.25 ml, 0.00173 mmol) in dry acetonitrile (3 ml) 1,2,4-triazole (0.317 g, 0.0046 mmol) in dry acetonitrile (10 ml) was added slowly maintaining the temperature at 0-5°C. The reaction mixture was stirred for 1 hr. at 0-5°C. Previously dissolved 3-(4'-Nitrobenzoyl)-7-hydroxy-2-(4'-Nitrophenyl)-*4H*-Chromen-4-one(0.5 g, 0.00115 mmol) in dry acetonitrile (10 ml) was added dropwise to the above reaction mixture. The reaction mixture was further stirred for 24 hr. under the nitrogen atmosphere. Subsequently, the semi-solid mass was quenched with chloroform. Impurities were removed by filtration and the organic layer was collected and the solvent was recovered under reduced pressure. The resulting crude product was purified by passing through column chromatography using silica gel (100-200 mesh) and eluted with hexane: ethyl acetate (8:2).

3-(4'-Methylbenzoyl)-7-(1H-1,2,4-triazol-1-yl)-2-(4'-methylphenyl)-4H-chromen-4-one [3b]

To a cooled solution (0-5°C) of thionyl chloride (0.3 ml, 0.00202 mmol) in dry acetonitrile (3 ml) was added 1, 2 ,4-triazole (0.37 g, 0.0054 mmol) in dry acetonitrile (10 ml). The reaction mixture was stirred for 1 hr. at 0-5°C. 3-(4'-Methylbenzoyl)-7-hydroxy-2-(4'-Methylphenyl)-*4H*-Chromen-4-one(0.5 g, 0.00135 mmol) in dry acetonitrile (10 ml) was added dropwise to the above reaction mixture. The reaction mixture was stirred for 24 hr. under the nitrogen atmosphere. Subsequently, the semi-solid mass was quenched with chloroform. The organic layer was separated by filtration and solvent was recovered under reduced pressure. The resulting crude product was purified by passing through column chromatography using silica gel (100-200 mesh) and eluted with hexane: ethyl acetate (8:2).[10]

Conclusion

Imidazole and Triazole derivatives of Flavones were synthesized, characterized by IR, ^{1}HNMR, and Mass Spectrometry and evaluated for anticancer activity, after the result, it was found that compounds 2a,b,c and 3a,b possess anticancer activity. Compound with triazole ring possesses good activity. The triazole derivative with nitro substitution (3a) has shown highest activity. The imidazole ring with methyl substitution (2a) has shown lesser activity.

Copyright Statement

This work has not been published in any journal, and "Author is solely responsible for the plagiarism.

Acknowledgement

We take this privilege and pleasure to acknowledge the contributions of many individuals who have been inspirational and supportive throughout this work undertaken and endowed us with the most precious knowledge to see success in our endeavor.

References and notes

1. Brueggeemeier RW; Hachett JC; Diaz-Cruz ES, *Endocr. Rev.* 2005, **26,** 331-345.
2. Hackett JC; Brueggemeier RW; Hadad CM, J. Am. *Chem. Soc.* 2005, 127, 5224-37.
3. Brodie A, Oncol. 2003, **30,** 12-22.
4. Skehan P; Storeng R; Scudiero D; Monks A; McMahon J; Vistica D; Warren JT; J *Natl Cancer Inst.* 1990**; 82**(13):1107–1112.
5. Silvia G; Christina Z; Federica B; Angela R; Hartmann RW; Maurizio R; Alessandra B,*J. Med. Chem.* 2010, **53**, 5347-5351.
6. Costantino L; Rastelli G; Gamberini MC; Vinson JA; Bose P; Iannone A; Staffieri M; Antolini L; Corso AD; Mura U; Albasini A, J. Med. Chem. 1999, **42**, 1881-1893.
7. Kulkarni VG; Jadhav G, J. *Indian. Chem. Soc.* 1954, 31, 746-754.
8. Lijun T; Shufen Z; Jinzong Y; Wentao G; Jian C; Tianyu Z; *Molecules.* 2004, **9**, 842-848.
9. Rauckman BS; Tidwell MY; Johnson J; V Roth B.J *Med. Chem.* 1989, **32**, 1927-1936.
10. Richard LB; Min T; Diana FC; Tien TD; Scott MT; Taghreed A; Roshantha AS, *Bio org. Med. Chem. L.* 1997, **7**, 2373-2378.

ARTICLE

VOLUMETRIC PROPERTIES OF PROCAINE HYDROCHLORIDE, BETAINE HYDROCHLORIDE AND MYOINOSITOL IN DIFFERENT ELECTROLYTES AT 293.15 and 303.15 K

Vijay M. Tangde, Nikhat Sheikh, Latha Malladi
Post Graduate Teaching Departmet of Chemistry, Rashtrasant Tukadoji Maharaj Nagpur University, Nagpur – 440033, (MS) India (Corrresponding Author; vijaytn6@gmail.com)

Abstract: The experimental values of density of Procaine hydrochloride in aqueous and aqueous Glycine solutions,Betaine hydrochloride in aqueous and aqueous NaCl solutions, and Myo-inositol in aqueous and aqueous NaCl solutions at 293.15 K and 303.15 K are reported.The apparent molar volume $\left(V_\phi\right)$, limiting apparent molar volume of solute $\left(V_\phi^{\,0}\right)$ and limiting apparent molar expansivity$\left(E_\phi^0\right)$ have been calculated and the corresponding discussion has been reported.

Keyword: Density, Apparent Molar VolumeExpansivity

l. Introduction

Procaine hydrochloride is the local anesthetic of the ester types that has a slow onset and a short duration of action.It is mainly used for infiltration anesthesia, peripherial nerve block and spinal block.It is the hydrochloride salt form of procaine,benzoic acid derivative with local anesthetic and antiarrhythmic properties **[**Frelin et al**(**1982**)**,Mathews et al**(**1983**)].**Procaine binds to and inhibits the voltage gated sodium channels,thereby inhibiting ionic flux required for the initiation and conduction of impulses.Moreover,this agent increases electrical excitation threshold,reduces the rate of rise of action potential and slows nerve impulse propagation thereby causing loss of sensation**[**Fishmann et al**(**1981**)**,Bolger et al**(**1987**)].** It is used as an anti-aging antioxidant supplement designed as a nutritional tonic for elderly persons.It is an anti-cortisal oxygenator.Glycine is an important amino acid that has a single hydrogen atom as its side chain.It is the simplest possible unique proteinogenic achiral amino acid.It is a colorless,sweet-tasting crystalline solid.It can fit into hydrophilic or hydrophobic environments since it exists as Zwitter ion at natural pH or due to its minimal side chain of only one hydrogen atom and the acyl radical is glycol [Kharakoz et al(2000)]. Therefore, in the present study it has been used as a co-solute with Procaine hydrochloride to study the ternary system. The another drug compound used in the present study is Betaine Hydrochloride which increases the

level of hydrochloric acid (HCl) in the stomach necessary for proper digestion and assimilation of nutrients from food. In the absence of adequate HCl, poor digestion can arise leading to a range of digestive symptoms, such as bloating, belching, indigestion, diarrhoea, or constipation. Betaine hydrochloride helps restore the proper acid levels in the stomach and maintain healthy gastrointestinal function [Chennuri et al(2014)].The co-solute used with Betaine hydrochloride is Sodium chloride being the major electrolyte in most natural waters and geothermal fluids. Its accurate description of the properties in aqueous solutions is very well known and reported in the literature. The volumetric properties of NaCl solutions are of interest for many industrial and engineering applications. This is so because they give the dependence of free energy, enthalpy and heat capacity with temperature and pressure. The derived values of NaCl are reasonable and vary smoothly with temperature and molality. The basic temperature-concentration properties of NaCl aqueous solutions are of prime importance for various thermodynamic calculations in solution chemistry, geochemistry, oceanography, also in engineering calculations such as the process of converting salty water to potable water, etc[Jengathe et al(2015)]. Myo-inositol is the third drug compound chosen for density measurements and further derived parameters with NaCl as a co-solute being a universal electrolyte. Inositol or cyclohexane-1,2,3,4,5,6- hexanol is a chemical compound with formula $C_6H_{12}O_6$,a six fold alcohol of cyclohexane.It exist in nine possible

stereoisomers of which the most prominent form,widely occurring in nature is cis-1,2,3,5-trans -4,6 cyclohexanehexol or Myo-inositol.Inositol is sugar alcohol.Its taste has been assayed at half the sweetness of table sugar.Myo-inositol plays an important role as structural basis for a number of secondary messengers in eukaryotic cells [Kell et al (1967)].

In the present work, densities of aqueous solutions of binary systems of Procaine hydrochloride,glycine,Betaine hydrochloride and myo-inositol at temperatures T= (293.15 and 303.15) K have been measured by using modified Lypkin's bi-capillary pycnometer.The temperatures of the experimental water bath were maintained constant upto ± 0.002 K by circulating the thermostatted liquid from Julabo cryostat which maintains the temperature constant to ± 0.01K in the cryostat.The density of pure water at different temperatures was taken from literature and was used to obtain radius of the capillary and the volume of the pycnometers.

2. Experimental

2.1 Chemicals

Procaine.HCl procured from Sigma Aldrich,U.S.A. were of high purity (0.97 mass fraction), Glycine (S.D.Fine Chemicals,India) used for calibration purpose was of Analytical Reagent Grade,Betaine Hydrochloride procured from Sigma Aldrich,Sodium Chloride was procured from E-Merck,India. These compounds were dried in a vaccum oven at T= 343.15 K.All the solutions were prepared by using electronic balance (from shimadzu corporation, Type-ATX224,capacity =220 mg,readability = 0.1mg,Model No.D307031855) with a precision of ± 0.1 mg was employed for the preparation of binary and ternary solution of drugs.

Density measurements of all aqueous binary and ternary systems of Procaine hydrochloride, Betaine hydrochloride and Myo-inositol at T=293.15 and 303.15 K were performed by means of modified Lypkin's bi-capillary pycnometer.The temperature of experimental bath was maintained constant upto ± 0.01K by circulating the thermostatted liquid from Julabo cryostat (Model: F32 ME/Germany)which maintains the temperature constant to ± 0.01K in the cryostat.The volumes of the pycnometer used in the present work were found to be 26 cm³,39 cm³ and 32 cm³.Pycnometer were calibrated by measuring the densities of aqueous solutions of sodium chloride at T= 293.15 and 303.15 K.The density of pure water was taken from Literature[Millero et al (1970)].

3. Results and Discussion

3.1 Volumetric Properties

3.1.1 Density
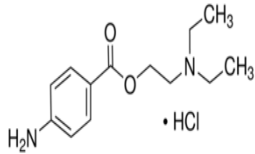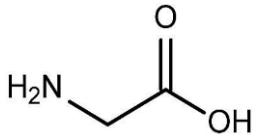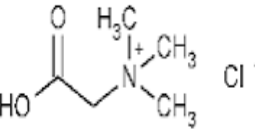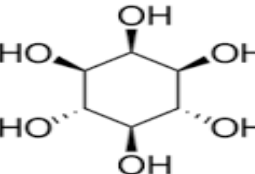
The experimental density (ρ) of first system comprising of solution for Procaine·HCl in aqueous solution and in aqueous solution of 0.06 mol.kg⁻¹Glycine in the concentration range (0.05-0.1) mol.kg⁻¹; the second system of aqueous solution of Betaine hydrochloride and Betaine hydrochloride in 0.06 mol.kg⁻

¹NaCl, and the third system of aqueous Myo-inositol and in 0.06 mol.kg⁻¹NaCl were calculated using the following equation,

$$\rho = \frac{w}{V_p - \pi r^2 dh} \dots\dots\dots\dots\dots 1$$

Where, w is the weight of the solution, V_p is the volume of pycnometer, r is the radius of capillary of pycnometer and *dh* is the difference in the meniscus of the pycnometer.The experimental data of density of 0.06 mol.kg⁻¹ aqueous NaCl solutions are in well agreement with the literature values[Redlich (1963)].The values for density are reported in Table1 for all systems.Figure 1 and figure 2 represents the variation of density as a function of molality for aqueous binary and ternary systems at studied temperatures (T=293.15).It can be seen from the figure that the density of solution increases linearly with the increase in concentration of the solute in the solution and decreases slightly with increase in temperature at a particular concentration.

Table 1 : Provenance and mass fraction purity of compounds

Sr.No.	Compound	Structure	Mass fraction purity
1.	Procaine Hydrochloride		≥ 0.97
2.	Glycine		≥ 0.97
3.	Betaine Hydrochloride		≥ 0.97
4.	Myo-inositol		≥ 0.99
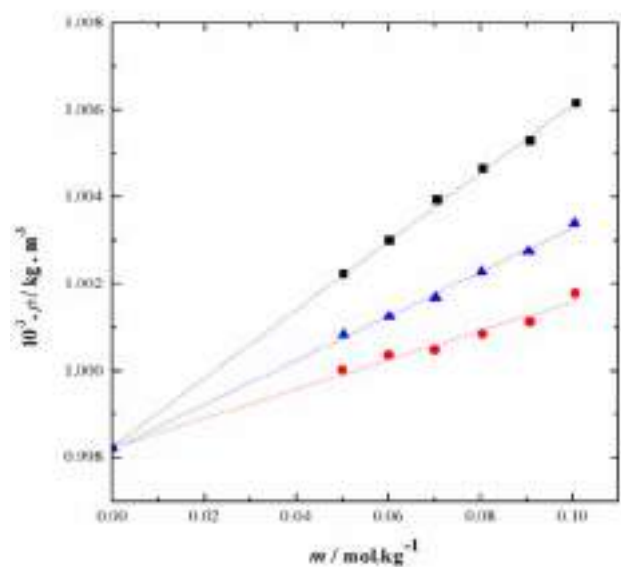
FIGURE 1. Plot of variation in density (ρ) of solution against molality (*m*) of aqueous solutions of some drugs (procaine.HCl ▲-▲, myo-inositol ■-■ and betaine hydrochloride ●-●)
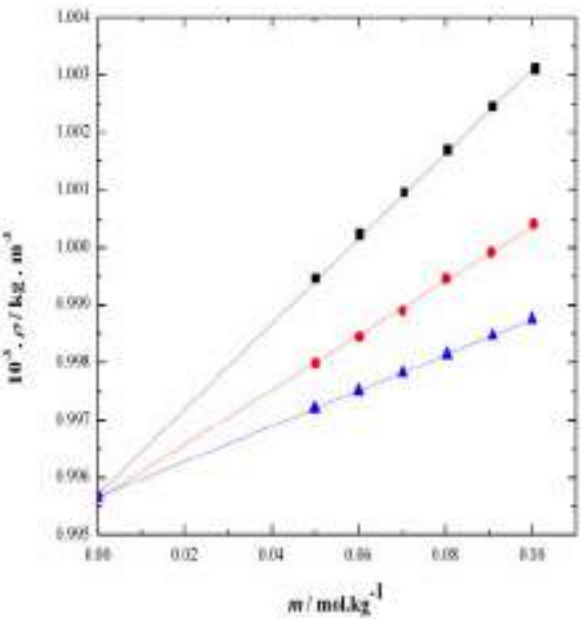
at *T* = 293.15 K.

FIGURE 2. Plot of variation in density (ρ) of solution against molality (*m*) of ternary solutions of some drugs (procaine.HCl ▲-▲ , myo-insitol ■-■ and betaine hydrochloride ●-●) at *T* = 293.15 K.

3.1.2 Apparent molar volume

The experimentally determined values of densities of solution (ρ) and solvent (ρ_0) for Procaine·HCl in Glycine (0.06 mol.kg^{-1}), Betaine hydrochloride in 0.06 mol.kg^{-1}NaCl and Myo-inositol in 0.06 mol.kg^{-1}NaCl system at different temperatures *T* =

(293.15 and 303.15) *K* were used to calculate apparent molar volume (V_ϕ) of solute using following equation,

$$V_\phi = \frac{1000(\rho_0 - \rho)}{m\rho\rho_0} + \frac{M}{\rho} \dots\dots\dots\dots\dots\dots 2$$

Where, ρ_0 and ρ are densities of solvent and solution respectively, m and M are the molality of solution and molar mass of solute, respectively. The values of apparent molar volume are reported in Table 2 for all the studied systems. These values are important because they form the basis for understanding the molecular interactions.

Table 2: Molality (*m*), Apparent molal volume of solute ($V_\emptyset$) for aqueous solution of Procaine-HCl in aqueous glycine, betaine hydrochloride in aqueous NaCl and myo-inositol in aqueous NaCl at T= 293.15 and 303.15 K.

| PC + Water					
T=293.15K			*T*=303.15K		
Molality *m*/mol.kg^{-1}	10^{-3}.ρ / kg.m^{-3}	10^6. ($V_\emptyset$) m^3.mol^{-1}	Molality *m*/mol.kg^{-1}	10^{-3}.ρ / kg.m^{-3}	10^6.($V_\emptyset$) / m^3.mol^{-1}
0.0000	0.99820	221.53	0.0000	0.99565	228.81
0.0503	1.00095	217.75	0.0503	0.99797	226.80
0.0603	1.00151	217.56	0.0603	0.99844	226.66
0.0706	1.00205	217.44	0.0706	0.99889	226.62
0.0806	1.00264	216.87	0.0806	0.99945	225.28
0.0908	1.00321	216.65	0.0908	0.99991	225.48
0.1009	1.00364	215.77	0.1009	1.00040	225.15
PC in glycine					
0.0000	0.99988	226.84	0.0000	0.99700	232.90
0.0511	1.00228	224.31	0.0511	0.99916	229.76
0.0606	1.00276	224.24	0.0606	0.99960	229.56
0.0701	1.00318	224.21	0.0701	1.00000	229.34
0.0802	1.00373	223.75	0.0802	1.00055	228.17
0.0899	1.00430	222.73	0.0899	1.00106	227.36
0.1000	1.00482	222.27	0.1000	1.00151	227.26
B10.HCl in water					
0.0000	**0.99820**	112.90	0.0000	**0.99565**	120.00
0.0500	1.00005	116.70	0.0500	0.99723	122.20
0.0601	1.00039	117.21	0.0601	0.99751	122.81
0.0700	1.00070	117.91	0.0702	0.99780	123.16
0.0804	1.00099	118.82	0.0804	0.99805	123.87
0.0907	1.00127	119.62	0.0907	0.99833	124.09

0.1005	1.00153	120.28	0.1004	0.99858	124.46

B10 in aqueous NaCl					
0.0000	**1.00073**	116.00	0.0000	**0.99787**	122.90
0.0503	1.00245	119.22	0.0506	0.99927	124.63
0.0610	1.00278	119.67	0.0607	0.99953	125.01
0.0705	1.00306	120.27	0.0709	0.99978	125.64
0.0811	1.00337	120.70	0.0811	1.00004	125.95
0.0904	1.00359	121.55	0.0914	1.00031	126.08
0.0999	1.00382	122.22	0.1015	1.00054	126.49

Myo-inositol +water					
0.0000	**0.99821**	90.9	0.0000	**0.99565**	102.4
0.0503	1.00253	93.9	0.0503	0.99944	104.5
0.0610	1.00338	93.9	0.0603	1.00016	105.0
0.0706	1.00425	94.0	0.0706	1.00085	106.1
0.0806	1.00501	95.1	0.0806	1.00156	106.3
0.0908	1.00579	95.9	0.0908	1.00230	106.4
0.1009	1.00660	96.1	0.1009	1.00298	106.9

Myo-inositol in aqueous NaCl					
0.0000	1.00078	98.1	0.0000	0.99791	105.1
0.0511	1.00479	101.3	0.0511	1.00162	107.2
0.0606	1.00553	101.2	0.0606	1.00229	107.5
0.0701	1.00624	101.6	0.0701	1.00295	107.8
0.0802	1.00698	102.2	0.0802	1.00364	108.1
0.0899	1.00761	103.5	0.0899	1.00429	108.6
0.1000	1.00836	103.5	0.1000	1.00494	109.2

The limiting apparent molar volumes $\left(V_\phi^0\right)$, are normally obtained by smooth extrapolation of $V_\phi - m$ curves to zero concentration using relation

$$V_\phi = V_\phi^0 + S_V m \quad \ldots\ldots\ldots\ldots\ldots 3$$

However, the current study concerned with all the solutes are treated as 1:1 electrolyte. The limiting apparent molar volumes or partial molar volumes at infinite dilution $\left(V_\phi^0\right)$ were obtained using a least-square treatment of plots of $\left(V_\phi - A_V m^{1/2}\right)$ versus m for aqueous binary and ternary mixtures of Procaine·HCl using Redlich-Meyer equation [Dunn (1968)].

$$V_\phi = V_\phi^0 + A_V \sqrt{m} + S_V m \quad \ldots\ldots\ldots\ldots\ldots 4$$

Where, A_V is the Debye–Hückel limiting slope for electrolytic solutions, which changes with the temperature. The values of A_V for 1:1 electrolyte at T = (293.15 and 303.15) K have been taken as 1.781 cm³.mol⁻³/².dm³/² and 1.955 cm³.mol⁻³/².dm³/² respectively [Iqbal et al (2009)]. S_V is the experimental slope or semi-empirical solute-solute interaction parameter. Similar types of graphs are obtained for all other binary and ternary systems. Figure 3 and Figure 4 represent the variation in apparent molar volume of solute (V_ϕ) against molality (m) of aqueous solutions of Procaine.HCl, Betaine hydrochloride and Myo-inositol at T = 293.15K temperature.

The limiting apparent molar expansivity arises due to two major components in case of electrolytes [13], namely,

$$E_\phi^0 = E_\phi^0\left(Elect\right) + E_\phi^0\left(Str\right) \ldots\ldots\ldots\ldots\ldots\ldots 5$$

Where, $E_\phi^0\left(Elect\right)$ is the expansivity due to electrostriction changes (contribution of hydration around the solute) and $E_\phi^0\left(Str\right)$ is the expansivity based on the changes in the structure of solvent. At low temperature, the structural component $E_\phi^0\left(Str\right)$ is the predominant factor whereas the electrostriction component $E_\phi^0\left(Elect\right)$ is predominant at higher temperatures.

The apparent molar expansivity E_ϕ^0 values for all the studied systems are reported in Table 3. It is observed that the values of apparent molar expansivity decreases from binary to ternary solutions for all the studied systems. The E_ϕ^0 values are employed in interpreting the structure making or breaking properties of various drugs. The positive values of E_ϕ^0 indicate that the drug is "kosmotrope" in water as well as in co-solute medium.

Table 3: Apparent molar expansivity, experimental slope and limiting apparent molar volume for aqueous solution of Procaine-HCl in aqueous glycine, betaine hydrochloride in aqueous NaCl and myo-inositol in aqueous NaCl at T= 293.15 and 303.15 K.

System	T=293.15K		T=303.15K		
	$10^6 V^0\varphi$	$10^6 S_V$	$10^6 V^0\varphi$	$10^6 S_V$	$10^6 E^0\varphi$
	m³·mol⁻¹	m³·kgmol⁻²	m³·mol⁻¹	m³·kgmol⁻²	(m³·kgmol⁻²)
Betaine hydrochloride + water	112.9	73.28	120.0	45.35	3.55

Betaine hydrochloride + 0.06 mol·kg⁻¹ NaCl	116.0	60.81	122.9	35.94	3.45
Procaine-HCl+water	221.1	-54.06	232.9	-57.83	
Procaine-HCl+Glycine+Water	226.8	-43.49	228.8	-37.34	
Myo-inositol+ water	90.9	52.189	102.4	45.92	5.75
Myo-inositol+ water+ NaCl	98.1	54.845	105.1	39.977	3.5
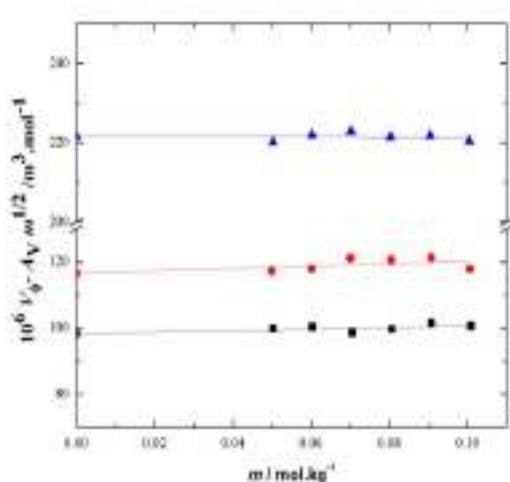
FIGURE 3. Plot of variation in apparent molar volume of solute (V_ϕ) against molality (m) of ternary solutions of some drugs (procaine.HCl ▲-▲ , myo-insitol ■-■ , and betaine hydrochloride ●-●) at T = 293.15 K.
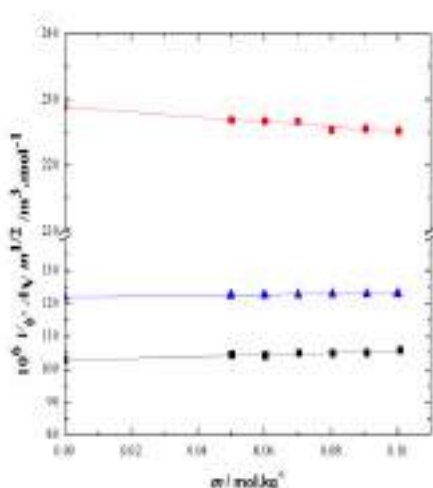
FIGURE 4. Plot of variation in apparent molar volume of solute (V_ϕ) against molality (m) of aqueous solutions of some drugs (procaine.HCl ●-● ,myo-insitol ■-■ , and betaine hydrochloride ▲-▲) at T = 293.15 K.

4. Conclusion

The density of aqueous solutions of binary systems of procaine hydrochloride in Glycine,Betaine hydrochloride in NaCl and Myo-inositol in NaCl at temperatures T= (293.15 and 303.15) K were carried out at T=293.15 K and 303.15 K. From the experimental data various derived parameters were calculated.The results indicate that there exist strong (solute-solvent) (ion+ hydrophilic) interaction.

References:

[1]   C. Frelin, P. Lazdunski, Biochem Biophys. Res. Communication, 1982, 106, 967-973;

[2]   J. Mathews, C. Collins , Biochem. Pharmacol., 1983, 32, 455-460;

[3]   M. Fishmann, C Spectar, Potassium Current Suppression by Quinidine Reveals Additional Calcium Currents in Neuroblastoma Cells. Proc. Natl., Acad. Sci. U.S.A,S 1981, 78, 5245-5249;

[4]   G Bolger, K. A Marcus, J. W. Daly, P. Skolnick, Journal of Pharmacol. Exp. Ther, 1987, 240, 922-930;

[5]   D P Kharakoz, Biophysical Journal, 2000 ,79 , 511-525;

[6]   B K. Chennuri, R. Noothi, S. J. Tangeda, S.Ryshetti, A. Gupta, S .Tangeda, R. Gardas, 2014 , 77, 123-130;

[7]   S.Jengathe, S. Dhondge, L. Paliwal, V. Tangde, S. Mondal, Journal of Chemical Thermodynamics 2015, 87, 78-87;

[8]   G.kell ,Journal of Chemical and EngineeringData, 1967,12, 66-69;

[9]   F. Millero, Journal of Physical Chemistry,1970, 74, 356-362;

[10]   O. Redlich, J. Physical, Chemistry,1963, 67, 496-498;

[11]   L. Dunn, Trans Faraday Soc,1968, 64, 2951-2961;

[12]   M. Iqbal, M. Choudhary,Journal of Chemical and Engineering Data, 2009, 54, 2772-2776.

ARTICLE

Analysis on structural, thermal and optical properties of Sm(TTA)₃dpphen hybrid organic complex for OLEDs and solid state lighting applications

Akhilesh Ugale[1], N. Thejo Kalyani[2*] and S.J. Dhoble[3]

[1]*Department of Applied Physics, G.H. Raisoni Academy of Engineering and Technology, Nagpur- 440028, India.*
[2]*Department of Applied Physics, Laxminarayan Institute of Technology, Nagpur-440033, India*
[3]*Department of Physics, RTM Nagpur University, Nagpur-440033, India.*

Corresponding author: thejokalyani@rediffmail.com

Abstract: We propose the synthesis of orange-red light emitting Sm(TTA)₃dpphen (Sm-Samarium, TTA-ThenyolTrifluoroacetone, dpphen- 4,7-diphenyl1,10-phenanthroline) hybrid organic complex at pH 7 by precipitation method. Structural, thermal and optical properties of the synthesized hybrid complex were characterized by X-ray diffraction (XRD), Fourier Transform Infrared (FT-IR) spectra, Thermo gravimetric analysis/Differential thermal analysis (TGA/DTA), UV-Visible absorption spectra and Photoluminescence spectra (PL), respectively. XRD spectra displayed many strong, sharp diffraction peaks inferring the crystalline nature of complex. The molecular bonding, packing arrangement and structure formation of the complex was explored by the FTIR spectra. TGA curve infers that the complex maintains its properties unchanged till around 250^0C and significant loss in weight was observed thereafter. DTA curve shows good thermal stability with combination of endothermic and exothermic peaks. Two endothermic peaks at 333^0C and 373^0C corresponding to the distortion of water from the complex and evaporation of residual moisture respectively were observed. Exothermic peak at 420.67^0C indicates the decomposition of the residual organic complex. To explore the spectroscopic properties of the synthesized complex, UV-Visible absorption spectra were carried out in different basic and acidic media. When the complex was excited under a wavelength range of 250 to 700 nm, a broad band with a prominent peak with maximum intensity at 379 nm has been observed in the excitation spectra, while emission peak registered at 566 nm, which falls in the orange-red region of visible spectrum of electromagnetic radiation. The emission wavelength corresponds to the chromaticity coordinates (0.387, 0.368) on CIE diagram, proving it's prospective as red light emitting phosphor for fabricating red organic light emitting diodes (OLEDs)

Keywords: Sm(TTA)₃dpphen, β-diketonate, Photoluminescence, OLEDs, Solid State lighting.

1 . Introduction

The most noteworthy advance in the field of electronics and technology is the development of OLEDs and flat panel display on flexible substrates [1]. Passionate research has been carried on the use of organic materials for such electroluminescent devices as well as the next generation solid state lighting devices solely due to their energy saving traits [2]. Pioneer work of C. W. Tang [3] in this field demonstrated that the organic materials have numerous advantages like easy synthesis, elevated quantum efficiency, quick response, elevated contrast and lighter weight. In this regard lanthanide complexes, especially europium and samarium have long been recognized as bright red light emitters under UV radiation because of effective energy transfer from ligands to central ions called antenna effect [4, 5]. These lanthanide trivalent cations exhibit well defined emission properties such as long lifetime, large Stokes shift and sharp band emission. As a result, more and more complexes of this kind have been synthesized and deliberated intensively. In congruence, we synthesized hybrid organic complex Sm(TTA)₃ dpphen by solution technique at constant pH and investigated its structural, thermal and optical properties.

2. Experimental

All the chemicals used in the synthesis procedure are of analytical reagents (AR) grade, procured from Sigma Aldrich.

The reactions were carried out with dry, freshly distilled solvents under anhydrous conditions or in an inert atmosphere.

2.1 Reagents and Solvents

Starting materials used for the synthesis of Sm(TTA)$_3$dpphen complexes are Samarium chloride hexahydrate (SmCl$_3$6H$_2$O) purity > 99%, M.wt. = 364.81 g/mol, 2-thenoyl Tri Fluoroacetone (TTA) purity 99%, M.wt. = 222.19 g/mol, m.p. 40-45^{0}C, 4,7-diphenyl-1,10- phenanthroline (dpphen) purity 99%, M.wt. = 332.396 g/mol,Phen- 1,10 Phenanthroline, (C$_{12}$H$_8$N$_2$.H$_2$O)[Fisher scientific] purity – 99.9%, M.Wt = 198.23 g/mol. Ethanol absolute (C$_2$H$_5$OH), purity – 99.98%, M.Wt = 46.07 g/mol, chloroform(CHCl$_3$) [Qualigens company] purity – 99.7 %, M.wt.= 119.38, Toulene (C$_6$H$_5$CH$_3$), M.wt = 92.14 gm purity - 99.9%, refractive index is 1.493-1.497, b.p (92%) = 110-111 ^{0}C , Tetra hydro Furan(THF)(C$_4$H$_8$O), M.wt = 72.11 gm purity - 99.9%, refractive index at 20 ^{0}C is 1.407-1.409, boiling range 65-67^{0}C, Acetic acid (CH$_3$COOH) [sd fine chemicals] purity – 99.5%, M.wt.=60.05 , Potassium hydroxide (KOH), purity – 99.9% and double distilled water.

Fig. 1 shows the molecular structure of TTA and 4, 7-diphenyl 1, 10-phenanthroline, while Fig.2 (a) and 2(b) gives the chemical structure of Sm(TTA)$_3$dpphen in 2D and 3D, respectively. It infers that TTA and 4, 7-diphenyl 1, 10-phenanthroline are bidendate. Sm^{3+} forms bond with one molecule of dpphen and three molecules of TTA [6].

(a)

(b)
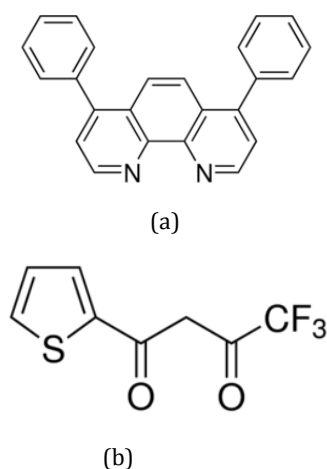
Fig. 1: Chemical structure of (a) 4, 7-diphenyl 1, 10-phenanthroline and (b) 2-Thenoyl Trifluoro Acetone
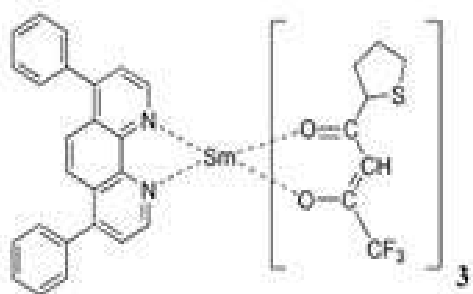
Fig. 2 (a): 2D Chemical structure of Sm(TTA)$_3$dpphen
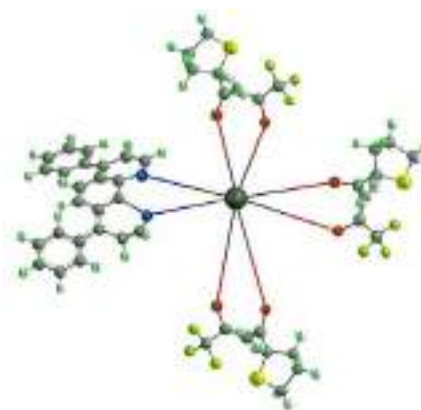
Fig. 2 (b): 3D chemical structure of Sm(TTA)3dpphen

2.2 Synthesis procedure

Sm(TTA)$_3$dpphen (Sm: samarium, TTA: Thenoyl trifluoro acetone, dpphen: bathophenanthroline) hybrid organic complex has been synthesized by simple precipitation method at room temperature. TTA (6.63 mmol= 0.842 gm) and hen (2.21 mmol = 0.438 gm) were dissolved in 20ml ethanol (Sol I). Later, SmCl3.6H2O (2.21 mmol = 0.809 gm) was separately dissolved in 10 ml double distilled water in another beaker (Sol II). Both the solutions were mixed and KOH solution is added drop by drop till pH of the resultant solution reached pH=7. The solution thus obtained was heated at 60^{0}C on a hot plate with continuous stirring with a magnetic stirrer for 1 hour. The precipitate so obtained was filtered and washed with double distilled water twice or thrice. The complex was dried at room temperature and then eventually in the hot air oven at 80^{0}C for two hours [7]. Synthesis scheme of Sm(TTA)$_3$dpphen complex. The synthesis procedure of the complex is depicted in Fig.3.
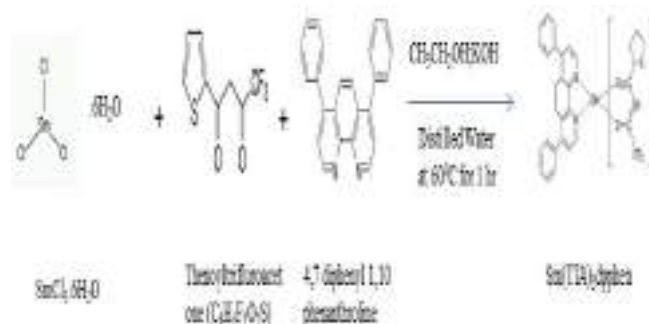
Fig. 3: Synthesis scheme of Sm(TTA)$_3$dpphen complex

3. Result and discussion

3.1. Structural properties of Sm(TTA)$_3$ dpphen

Structural properties of Sm(TTA)$_3$dpphen complex at pH 7.0 were probed by diffractograms obtained from X-Ray diffraction (XRD), while structural confirmation was done by Fourier Transform Infra-Red (FTIR) spectroscopy.

3.1.1. X-ray Diffraction (XRD) analysis

Crystalline nature of Sm(TTA)$_3$dpphen is evaluated by wide angle X-ray diffraction experiments, recorded on Philips Analytical X' Pert Pro Powder Diffractometer. The diffractogram of Eu(TTA)$_3$dpphen display strong and sharp diffraction peaks

inferring the crystalline nature of the synthesized complex as shown in the Fig.4. 100% relative intensity corresponds to d-value of 4.0057 A^0 at 2θ value of 22.1742^0 with full width half maxima (FWHM) at 0.3264^0. Scherrer equation was employed to determine the size of particles in the synthesized complex. This equation relates the size of sub-micrometer particles or crystallites, in a solid to the broadening of a peak in a diffraction pattern , given by $\tau = \dfrac{k\lambda}{\beta\cos\theta}$ where , τ is the mean size of the ordered (crystalline) domains, which may be smaller or equal to the grain size; k is a dimensionless shape factor, with a value close to unity (0.9) ; λ is wavelength of X-ray ; β is the line broadening at half the maximum intensity (FWHM) in radians ; θ is the Bragg angle (in degrees).

$$\tau = \frac{0.9 \times 1.54}{0.3624 \times \cos(0.1934)} = 0.4246 nm$$
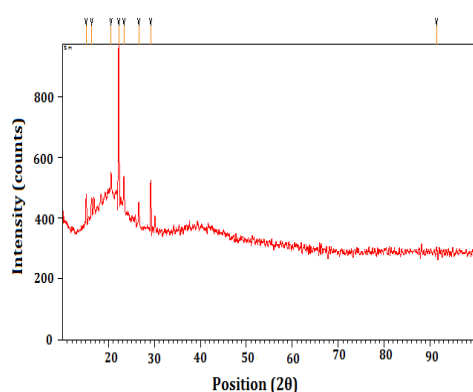
Fig. 4: Diffractogram of Sm(TTA)₃dpphen

3.1.2. Fourier Transform Infrared (FTIR) spectra

FTIR is an analytical technique, which confirms the molecular structures of the synthesized complex and also measures the absorption of various infrared light wavelengths by the material of interest. The molecular structure of Sm(TTA)₃dpphen chromophore are confirmed by FT-IR spectra over the range 4000–700 cm⁻¹ by averaging 500 scans at a maximum resolution of 20 cm⁻¹as shown in Fig. 5.
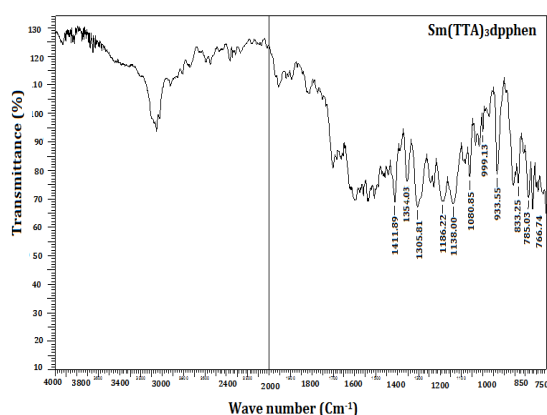
Fig. 5: FTIR Spectrum of Sm(TTA)₃dpphen

Broad background with some asymmetric peaks were observed below 700 cm⁻¹ and hence not recorded. This may be due to scattering of crystalline nature of the phosphor. The peaks in the range of 3900-3500 cm⁻¹ reveal the presence of O-H bonding. The absorption bands in the finger print region (1500-1400 cm⁻¹) are generally due to intra molecular phenomena, and are highly specific for each material. The peak at 1411.89 cm⁻¹ predicts aromatic ring stretching, revealing the presence of C=C group. The spectrum shows a strong absorption at 1354.03 cm⁻¹, reflecting the presence of (C-H) plane bend. Moreover, the peaks in the range of 1100-1200 cm⁻¹confirms the presence of aromatic nitro compounds (C-N) stretch and (C - O). The peaks between 1000 - 1100 cm⁻¹ divulge the presence of (C-F) aliphatic fluoro-compounds. The peaks below 1000 cm⁻¹ shows bending of phenyl group. Prominent peaks in the lower range at 933.55 cm⁻¹ 833.25 cm⁻¹, 785.03 cm⁻¹, and 765.74 cm⁻¹ are due to C-H alkaline bonding. These results confirm the formation of samarium β-diketonate hybrid organic complex.

3.2. Thermal analysis

Thermal properties such as thermal stability, decomposition temperature have been explored by Thermogravimetric analysis and Differential thermal analysis (TGA/DTA).

3.2.1. Thermo gravimetric and differential thermal analysis (TGA/DTA)

Thermo gravimetric analysis (TGA) and differential thermal analysis (DTA) are carried out simultaneously to assess direct correlation of weight and heat changes as function of time and temperature in various gaseous environments. The TGA curve displays a plateau, representing no weight loss in the Sm(TTA)₃dpphen sample up to 250^0C as indicated in Fig. 6. With further increase in temperature, the thermogram takes curved portion, indicating decomposition or weight loss of the sample due to heating. End peak at 350^0C indicates the final temperature at which the cumulative weight change first reaches its maximum value, corresponding to the complete reaction. DTA curve of Sm(TTA)₃dpphen displays a combination of endothermic and exothermic peaks. Endothermic peak, one centred at 99.9°C, corresponds to the distortion of water from the synthesized complex.
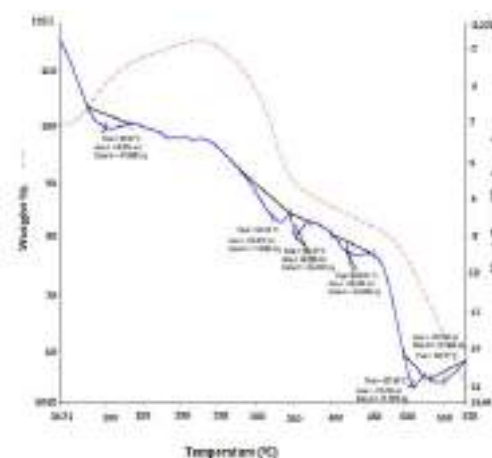
Fig.6: TGA/DTA curve of Sm (TTA)₃ dpphen for pH=7.0

Other peaks at 322.26^{0}C and 352.29^{0}C, corresponds to the evaporation of residual moisture. Around 352.29^{0}C, 420.67°C and 502.86°C, exothermic peaks were observed in the DTA curve, which can be attributed to the decomposition process of the residual organic materials.

3.3. Optical properties of Sm(dmh)$_3$phen

The optical properties of Sm(dmh)$_3$phen complex have been explored by UV-Visible absorption spectra on HR 4C 4568 UV – Vis spectrophotometer and photoluminescence spectra on RF5301 Spectrofluorometer. CIE co-ordinates of Sm(dmh)$_3$phen complex have been calculated using color calculator program radiant imaging.

3.3.1. UV-Visible absorption spectra

In order to study the shift of π→π* and the n→π* optical transitions due to Sm^{3+} ion and β-diketonate moieties, Sm(dmh)$_3$phen complex was solvated in five different solvents (taken separately) viz., chloroform, Toluene, Dichloromethane (basic medium), acetic acid and formic acid (acidic medium), respectively with different molar concentrations. Initially, the apparatus was calibrated by taking that particular solvent in the cuvet to get a baseline and then running a cuvet filled with the respective solutions. Fig. 7 clearly illustrates hypsochromical shift of absorption peaks by few nm with a variation in the solvent from basic to acidic media, which is clearly depicted in the comparative graph of the absorption spectra at 10^{-3}mol/L molar concentration [8]. Among all the solvated complexes, Sm(TTA)$_3$dpphen in formic acid and acetic acid shows poor absorption, which may be due to the protonation of the organic ligand in acidic media.
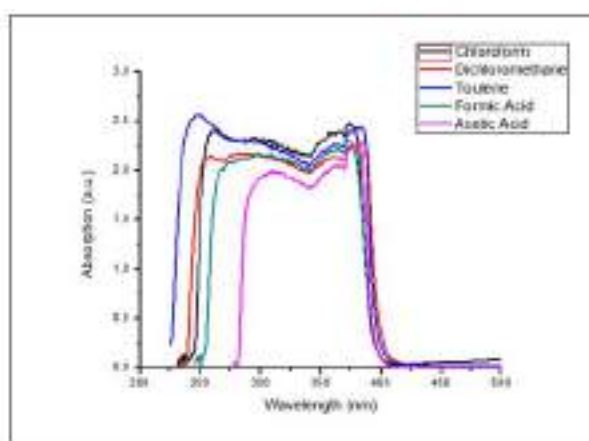
Fig.7: Absorption spectra of Sm(TTA)$_3$dpphen in different solvents, Chloroform, Dichloromethane, Toluene, Acetic acid and Formic acid.

Table 1: UV-Visible optical absorption parameters of solvated Sm(TTA)$_3$dpphen in different solvents

Complex	Solvent	Molar Ratio	Band	λ_{max} (nm)
Sm(TTA)$_3$ dpphen	Acetic Acid	10^{-3}	I	263
			II	374
	Formic Acid	10^{-3}	I	298
			II	371
	Chloroform	10^{-3}	I	288
			II	382
	Toulene	10^{-3}	I	310
			II	381
	Dichloromethane	10^{-3}	I	247
			II	384

3.3.2. Photoluminescence spectra of Sm(dmh)$_3$phen

To reveal the excitation and emission wavelength of the complex, photoluminescence spectra was carried out in the range of 250 to 700 nm.
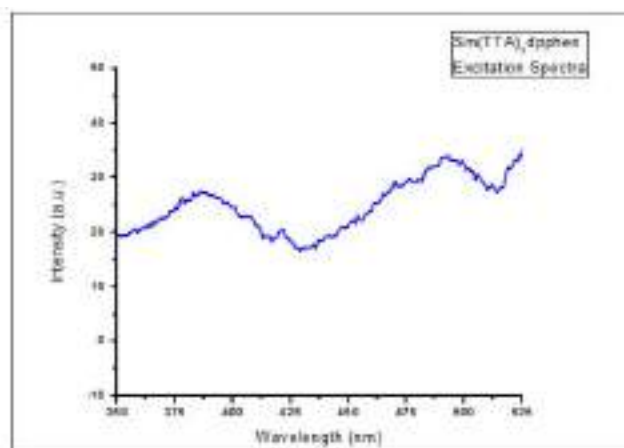
Fig. 8: Excitation spectra of Sm(TTA)$_3$dpphen complex

Under the excitation wavelength of 379 nm, complex showed three prominent peaks registered at 566 nm, 600 nm and 646 nm which falls under the orange-red region of visible spectrum as shown in Fig. 8 and 9, respectively. These emission peaks originates from $^4G_{5/2} \rightarrow {}^7H_{5/2}$, $^4G_{5/2} \rightarrow {}^7H_{7/2}$ and $^4G_{5/2} \rightarrow {}^7H_{9/2}$, respectively. PL in the complex is due to the transfer of energy from the ligand TTA to the Sm^{3+} ion in excited state through synergistic effect [9, 10].
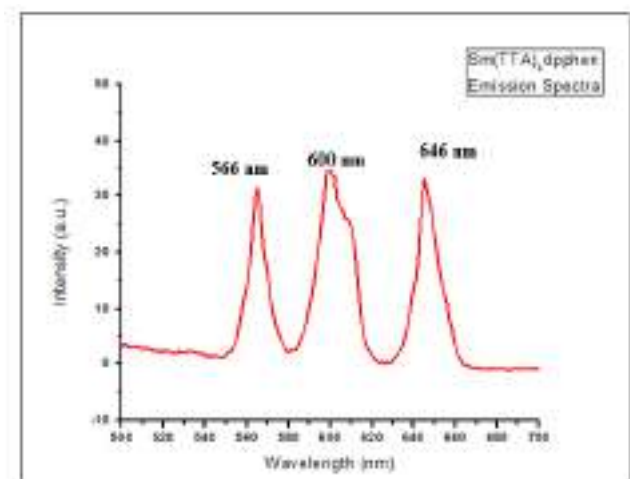
Fig.9: Emission spectra of Sm(TTA)₃dpphen complex

3.3.3. CIE coordinates

The CIE chromaticity coordinates of Sm(TTA)₃dpphen complex reveals that the colour of light emitted by the complex lies in orange-red region with CIE (Commission International d'Eclairage) coordinates (0.387, 0.368) and colour correlated temperature (CCT) at 3747K when excited at 385 nm as shown in Fig.10.
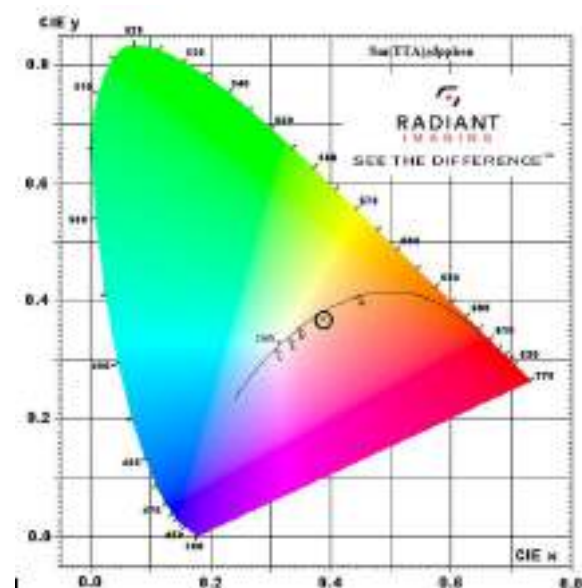
Fig. 10: CIE diagram displaying emission color coordinates of Sm(TTA)₃dpphen.

4. Conclusions

We synthesized an orange-red light emitting Sm(TTA)₃dpphen hybrid organic complex at pH 7 by precipitation method. XRD spectra displayed strong, sharp diffraction peak with 100% relative intensity corresponding to d-value of 4.0057 Å, inferring the crystalline nature of complex, while FTIR spectra confirms the complex formation. TGA/DTA curve represents the thermal stability of the complex up to 250⁰C and around 352.29⁰C, 420.67°C and 502.86°C, exothermic

peaks were observed in the DTA curve, which can be attributed to the decomposition process of the residual organic materials. UV-Visible absorption spectra, carried out in different basic and acidic media at 10⁻³mol/L molar concentration reveals hypsochromic shift of absorption peaks by few nm with a variation in the solvent from basic to acidic media. Under the excitation wavelength of 379 nm, complex showed three prominent peaks registered at 566 nm, 600 nm and 646 nm which fall under the orange-red region of visible spectrum. The emission wavelength corresponds to the chromaticity coordinates (0.387, 0.368) on CIE diagram. These observations and outcomes suggest the application of synthesized complex as an emissive layer of OLEDs.

Copyright statement

Author is solely responsible for the Plagiarism

References

1. Dipti Chitnis, N. Thejo Kalyani, H.C. Swart, S.J. Dhoble , Renewable and Sustainable Energy Reviews, 64 , 2016, 727–748.

2. Pei-Pei Sun, Jiun-Pey Duan, Huai-Ting Shih, and Chien-Hong Cheng Applied Physics Letters,81(5),2002,792-794.

3. C.W.Tang, S.A.Vanslyke, Appl.Phys. Lett.51, 1987, 913-918.

4. Dipti Chitnis, N. Thejo Kalyani, S.J. Dhoble, Journal of Luminescence 185 (2017) 61–71.

5. G.Baldacchini, T.Baldacchini, A.Pace, R.B.Pode, Electrochem. Solid State Lett, 8, 2005, 24-29.

6. S.Watanabe, A. Furube, R.Katoh, J.Phys. Chem. A, 110, 2006, 10173-10179

7. Dipti Chitnis, N. Thejo Kalyani, S.J. Dhoble, Optik 130 (2017) 237–244.

8. Rafie H. Abu-Eittah, Sayed A. Marie, Mabrouka B. Salemsdf, Canadian Journal of Analytical Sciences and Spectroscopy,2004,49(4)248-257.

9. E.G.Mik, T.Johannes, C.J.Zuurbier, A.Heinen, J.H.Houben-Weerts, G.M.Balestra, J.Stap, J.F.Beek, C.Ince, Biophys .J, 95,2008,3977-3402.

10. N.Thejo Kalyani, S.J. Dhoble and R.B. Pode, Luminescence: The Journal of Biological and Chemical Luminescence, 28(2), 2013,183-187.

ARTICLE

Design of Low Cost Instrumentation for Measurement of Frequency Response of Piezoelectric Transducers

R. V. Vyaghra[a*], V. M. Pendsey[b], S. J. Sharma[c] and S. Rajagopalan[d]

Abstract: Characterization of piezoelectric transducer is very important to study the behaviour of transducers. Frequency response is considered as one of the most important parameters to verify the response of piezoelectric transducers with frequencies and determine the resonant frequency of transducer under study. Once the resonant frequency is determined, precision and performance of the system improves significantly and maximum power transfer can also be achievable. There are several traditional methods (manual and automatic) to determine the characteristic resonant frequency of the transducer. Also, the instruments available for such characterization are expensive. In the present work, an attempt has been made to design a microcontroller based low cost in-house system with high repeatability to find the characteristic resonant frequency of piezoelectric transducers, under test. DDS is interfaced with the microcontroller that operates through commands resulting in generation of sinusoidal waveform at the output. Graphical LCD and switches are interfaced to carry out the operation. The readings are taken using a Digital Storage Oscilloscope. This indigenous system is programmable and designed to work up to 10MHz. The sweeping frequency, in the present work, is maintained at a resolution of 10 kHz. The resolution of sweeping frequency of 1Hz is also achievable using this system. The objective of this system is to provide rapid and uniform test procedure and pattern for characterization of piezoelectric transducers, besides it is low cost and portable

Introduction

Piezoelectric transducers occur naturally in certain single crystals having polar axes, such as quartz, tourmaline, Rochelle salt, lithium sulphate, cadmium sulphide and zinc oxide. But the artificial crystals such as barium titanate, lead titanate, lead zirconium titanate (PZT), lead niobate, PVDF etc. are widely used for generation and detection of ultrasonics due to several advantages over the natural piezoelectric crystals. The possible frequency range extends from 20 KHz to 10 GHz. Thus, these transducers are widely used as sensors and actuators, including medical instruments, flow measurement and NDT equipments. Based upon the application, resonant frequency needs to be precisely known and monitored as the conclusion of measurement depends on it[1][2][3][4][5]. For this purpose, an input to the system and the characteristics of the transducer used must be known. Errors, if any, are either compensated or mentioned in the AC/DC characteristics of the designed instruments.

In the present work, an attempt has been made to design a compact set up with high repeatability for characterization of

PZT piezoelectric transducers [6][7][8]. The system is based on a microcontroller which acts as a central unit and a DDS which generates analog output frequency through digital data [9]. The output is further amplified and then fed to the transducer. The objective of this system is to provide rapid and uniform test procedure and pattern for characterization of piezoelectric transducer and overcome limitations of manual measurement[10].

Experimental Setup

The design setup of the measurement of resonant frequency of the piezoelectric transducer under test consists of a microcontroller ATmega32 interfaced with direct digital synthesizer (DDS) AD9835 over I2C bus[11][12]. Four buttons are also interfaced with this microcontroller to navigate the menu to be displayed on Graphic LCD (GLCD). The output of the DDS is fed to an amplifier which in turn drives the transducer under test. A dedicated display module is designed by interfacing 128x64 graphic LCD with another ATmega32 microcontroller. The four buttons are placed below the GLCD to navigate the

menu. Out of the four buttons, two buttons are used for incrementing and decrementing frequency values, one button ("OK") to confirm and fourth button ("CANCEL") to cancel the action taken. The two microcontrollers communicates with each other over serial/COM port. The microcontrollers, GLCD, buttons and the DDS operate on +5V supply whereas amplifier operates on ±12V.

Working Principle

Fig.1 shows the block diagram of the designed system for characterization of piezoelectric transducers. Transducer under test is connected as load at the output of the designed system. Transducer under test is connected at the output of the amplifier. With the help of this instrument, an attempt has been made to find accurate resonant frequency of the piezoelectric transducer under test[13][14]. The given frequency (in MHz) is entered through keys labelled as "UP" and "DOWN" and the corresponding value is displayed on the LCD. The entered value is communicated to the oscillator to generate frequency of that value by pressing "START" key. The generated frequency, after amplification is fed to the piezoelectric transducer under test. The output is viewed on a Digital Storage oscilloscope (DSO). The amplitude of the frequency is measured. Again by pressing "UP" key, the frequency value is incremented by 10 kHz followed by "START" button. The process is repeated till resonant curve is obtained. The value at which maximum amplitude is obtained is the resonant frequency of the piezoelectric transducer under test. An XY graph is plotted in which X-axis is the frequency and Y-axis is ratio of V_{out}/V_{in}.

Circuit Description

In the present work, Atmel's AVR series ATMega32 microcontroller is used. It is an 8-bit, 40 pin chip operated at 16 MHz derived from a Piezo crystal oscillator of 16MHz.
AD9835 is an analog programmable oscillator (DDS) used in the present designed system. Its operating speed is 50MHz. It receives command from microcontroller through I2C protocol. The chip has 10-bit internal D/A converter which is responsible for producing the resultant analog output waveform. DDS is interfaced with ATmega32 through I2C bus as shown in the Fig 2. LM7171 used to boost the output power of the DDS and the designed amplifier has a wide bandwidth of 200MHz and very high slew rate of 4100 V/μS. In the present work, the operating voltage used for amplifier is ±12V. The output of this amplifier drives the piezo transducer. Fig. 3 shows the amplifier circuit connected at the output of the DDS.
An 128x64 graphic LCD is interfaced to the ATmega32 along with four push to ON buttons as shown in the Fig 4. The two microcontrollers are connected via serial port. The program is written in C language using AVR Studio 6 IDE.

Results and Discussion

The designed system in the laboratory is tested successfully using PZT transducers of 1MHz, 2MHz, 5MHz and 10 MHz,. Fig. 5 to Fig 8 show the resonance curves obtained for each transducer, respectively. It is observed that for piezoelectric crystal specified at 1MHz the resonance is observed at 1.27MHz, for 2MHz at 2.28MHz, for 5MHz at 5.28MHz and for 10MHz at 10.28MHz.

Conclusion

It can be seen that the curve is shifting as per the resonance of the respective transducer. The experimental measurements of the resonant frequencies of the piezoelectric transducers have been utilised to design pulser or receiver units in ultrasonic measurement systems. The designed lab prototype of piezoelectric transducer characterisation system is capable of taking readings in steps of 1 kHz and 100 Hz also.

Diagrams
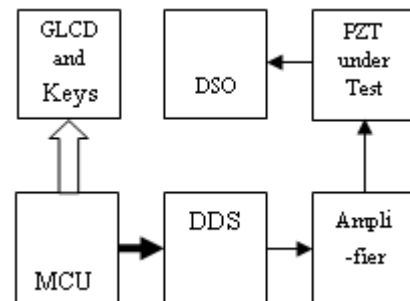
Fig 1: Block Diagram of DDS based System
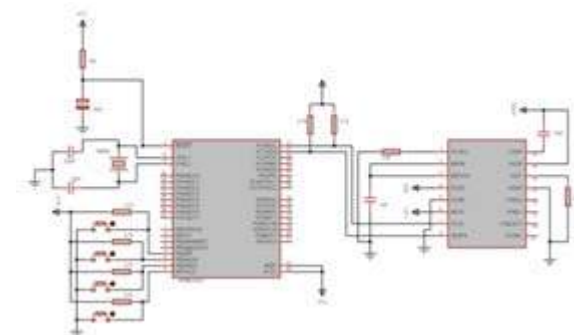
Fig. 2: DDS interfacing with ATmega32
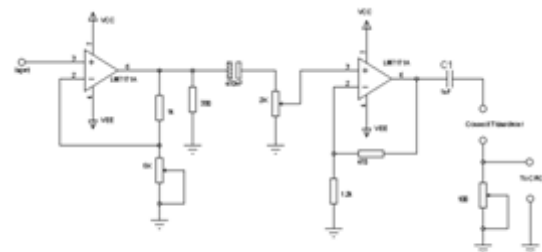
Fig. 3 Amplifier driving PZT transducer
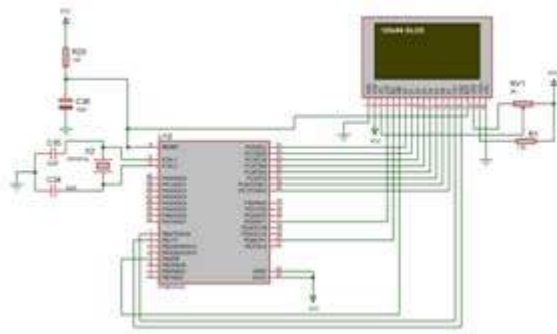
Fig. 4: LCD 128x64 interfacing with ATmega32
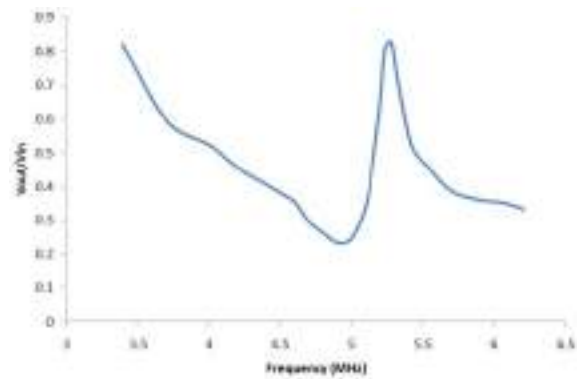
Fig 7: Resonance Curve of 5MHz PZT Transducer

Graphs
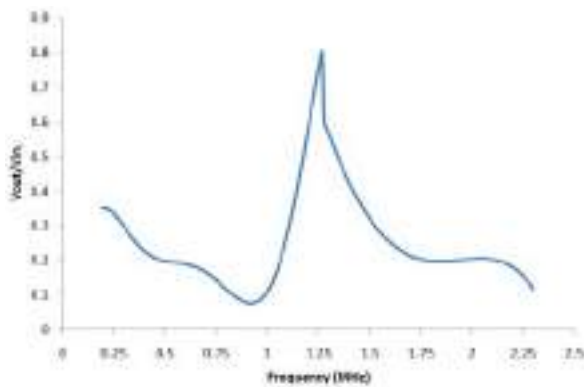
Fig 5: Resonance Curve of 1MHz PZT Transducer
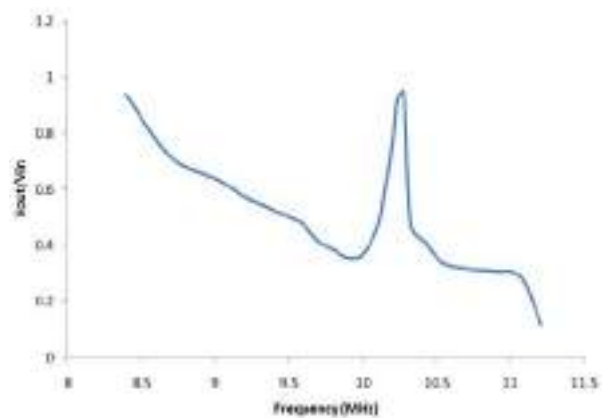
Fig 8: Resonance Curve of 10MHz PZT transducer
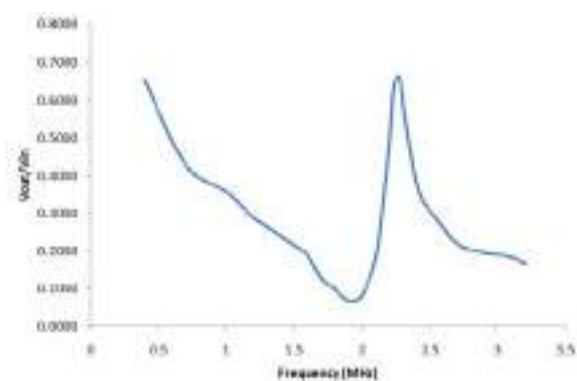
Fig 6: Resonance Curve of 2MHz PZT transducer

Copyright statement

We, the authors -

1. Reserve all proprietary rights such as patent rights and the right to use all or part of the article in future works of their own such as lectures, press releases, and reviews of textbooks.

2. Hereby declare that the material being presented by me/us in this paper is my/our original work, and does not contain or include material taken from other copyrighted sources.

3. The manuscript has not been published and is not being submitted or considered for publication elsewhere.

4. Hereby assign all the copyright relating to the said Article/Research Paper to RTMNU.

5. Are solely responsible for the plagiarism.

References

1. Dubey P. K., Ashok Kumar, Yudhisther Kumar, Reeta Gupta, and Joshi D., *Review of Scientific Instruments*, 2010, **81**, 104904;

2. Jeong J. J. and Choi H., *Measurement*, 2010, **97**, 138-144;

3. Ishiguro Y., Zhu J., Tagawa N., Okubo T., and Okubo K., *Japanese Journal of Applied Physics*, 2017, **56**, 07JD11;

4. Yokozawa H., Twiefel J., Weinstein M. and Morita T., *Japanese Journal of Applied Physics,* 2017, **56**, 07JE08;

5. Arnold F. J., Ximenes R. L., Arthur R., and Mühlen S. S., *Physics Procedia*, 2015, **63**, 114-119;

6. Ermolov I. N, *Russian Journal of Non Destructive Testing*, 2003, **39(4)**, 257-265;

7. Man C. and Cérez, *Journal of Physics. E: Scientific Instruments*, 1980, **13**, 157-159;

8. Arnold F. J., Bravo-Roger L. L., Gonçalves M. S. and Grilo M., *Latin American Journal of Physics Education*, 2011, **5(4)**, 680-685;

9. Patrick O. Olabisi P. O. and Olufeagba B. J., *Journal of Electrical and Electronics Engineering*, 2014, **9(2)(VI)**, 85-89;

10. Silva R. E., Marcos A R Franco M. A. R., Bartelt H. and Pohl A. A. P., *Measurement Science and Technology*, 2013, **24**, 094020;

11. Padmagirwar S, Jadhao Y., Chokhandre T., Deshpande S., Kale Y. and Jumle P. M., *International Journal of Computer and Electronic Research*, 2013, **2(6)**, 677-679;

12. Gaikwad S. and Dekate K., *Journal of VLSI and Signal Processing,* 2013, **2(4)**, 53-56*;*

13. Chivers R. C., *Journal of Physics. E: Scientific Instruments*, 1986, **19**, 834-843;

14. Ferrari V., Marioli D. and Taroni A., *Sensors and Actuators A*, 2001, **92**, 182-190;

ARTICLE

Ultrasonic Velocity Measurements in Critical Mixture of Cyclohexane and Methanol

Rupali J. Thete[1], Satish Sharma[2] and S. Rajagopalan[2]
[1]Department of Physics
Rashtrasant Tukadoji Maharaj Nagpur University, Nagpur-440 033

[2]Department of Electronics and Computer Science,
Rashtrasant Tukadoji Maharaj Nagpur University, Nagpur-440 033

Abstract: Recently, study of physical properties of the critical mixtures, their nature and behavior with change in frequency, temperature or concentration has gained more interest. Liquid mixtures behave critically for a particular concentration and a particular temperature. In this regard, ultrasonic technique is widely used as a nono-destructive tool to study the nature of molecular interactions in liquids, liquid mixtures and liquid metals, since a low amplitude ultrasonic propogation does not change the molecular struccture of the liquid; instead, it elaborates the molecular interaction between two liquids at critical temperature and concentration. This technique is mostly preferred as; a very short duration ultrasonic pulse is passed through the mixture which avoids local heating of the liquid under investigation. In the present work, we have carried out ultrasonic velocity measurements in binary mixture of cycfixed concentration lohexane and methanol, using a pulse echo technique operated at 5 MHz, developed in our laboratory. The measurements are carried out in the temperature range of 400C to 500C for a fixed concentration and temperature is varied with a difference og 0.10C, using themostat Julabo ME32. The results shows that this mixture behave critically at aparticular temperature for a specific concentration

Keywords: Ultrasonic pulse echo technique, critical mixture, cyclohexane-methanol, molecular interacti

Introduction

Ultrasonic propogation in liquid critical mixture has been widely used as powerful and reliable tool to study the inter-molecular and intra-molecular interactions[1-4]. The study of molecular interactions in solutions provide valuable information regarding internal structure, internal pressure, molecular association, complex formation, phase separation, degree of salvation, compatibility or miscibility etc. Various techniques are used to study the physical properties such as thermal (which includes measurement of heat capacity and transition temperatures, differential thermal analysis (DTA), thermal effects of dilution), mechanical (which includes measurements of limiting, deformational and relaxational properties), electric (which includes electric permeability, dielectric losses, electric conductance), spectroscopic (which includes infrared (IR), optical, ultraviolet(UV), X-rays, photo-acoustic microwave and electron; Nuclear Magnetic Resonance(NMR), absorption and scattering.

As compared to the other physical properties of a mixture, acoustic properties can be easily studied, as not much stringent experimental conditions are required. Moreover, ultrasonic

waves are much easily absorbed by the mixture at a critical concentration and temperature. Binary mixtures may not possess homogeneous properties. At critical composition and critical temperature they behave critically and shows homogeneous phase. Fixmann's theory proved to be successful in explaining the critical behaviour of the mixture cyclohexane and methanol mixture and is being previously studied by researchers[5-13].

Among the pulse methods, pulse echo technique is more reliable for the measurement of ultrasonic attenuation and velocity[14]. In pulse echo technique, a high frequency burst is introduced into the sample using a piezoelectric transducer. An ultrasonic pulse travels through the sample and an echo is registered each time it returns to the transducer. The amplitude of the successive echoes decreases exponentially due to attenuation in the sample. The received echoes are then fed to the wide band amplifier. Both the transmitted and received signals are seen on the oscilloscope and the time of flight between the transmitted pulse and first received echo or the time of flight between the two successive echoes is measured with the help of oscilloscope. Ultrasonic velocity of propagation in a medium under study is estimated as:

$$u = 2d/t$$

where   u= ultrasonic velocity

d = path length of the sample

t = time of flight

In the present work, we have carried out ultrasonic velocity measurements in the binary mixture of cyclohexane and methanol, using a pulse-echo technique, operated at 5MHz, designed in our laboratory[16].

.

Experimental Details

Pulse echo system has been calibrated using distilled water as the standard[15] for a path length of 55.1325 mm[16]. For critical mixture Cyclohexane (AR Grade of Merck) and Methanol (AR Grade of Merck) are taken in the two different proportions. The readings are taken in the temperature range of 40^0C to 50^0C at 5 MHz frequency with the variation of temperature in the step of 0.1^0C. Thermostat of Julabo ME32 is used for maintaining constant temperature. Readings for ultrasonic velocity is observed on DSO (Tektronix TDS 2014).

It is observed that for two different concentration values (26+74) and (29+71) values of critical temperature are 44.9^0C and 49.1^0C respectively. Methanol and cyclohexane mixture has been already studied by many reaearchers[11, 13]. The critical values obtained for the combination of (29+71) concentration is fairly in good agreement with   values obtained by other researchers[11].
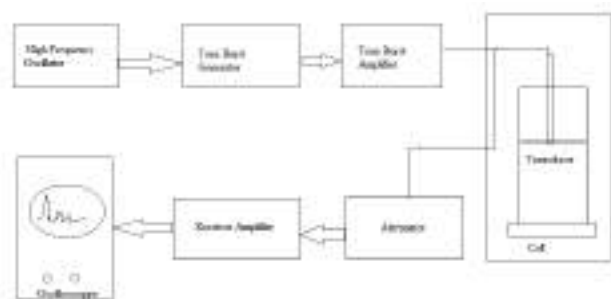
Fig.1 : Block Diagram of Pulse-Echo System

Table: Ultrasonic Velocity Measurements in Cyclohexane and Methanol

Sr. No.	Mixture Composition		Tc (°C) Present work	Tc (°C) Literature
	Cyclohexane (%)	Methanol (%)		
1	71	29	49.2	49.1
2	73.86	26.14	–	45.1
3	74	26	44.9	–

Results and Discussion

It is observed that if there is a change in the concentration of the components in critical mixture, the critical temperature value is observed to change. Velocity measurements at different frequencies and different temperatures reveal the dispersion which sometimes reaches to a maximum of 3% to 6% at the critical temperature. As the concentration of methanol decreases, critical temperature point is observed to shift from 49.1^0C to 44.9^0C. The ultrasonic velocity of a liquid depends upon the structural arrangement in the liquid as well as intermolecular interaction.
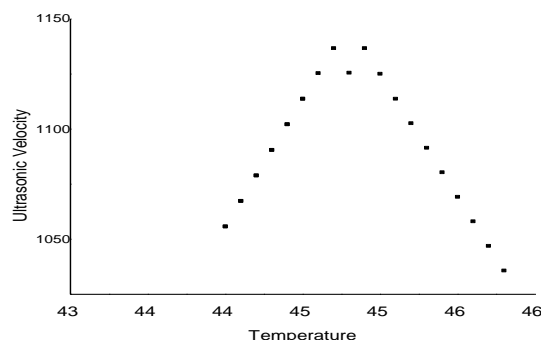
Fig 2 : Variation of ultrasonic Velocity in Binary Mixture of Cyclohexane (74%) and Methanol(26%) with respect   to temperature
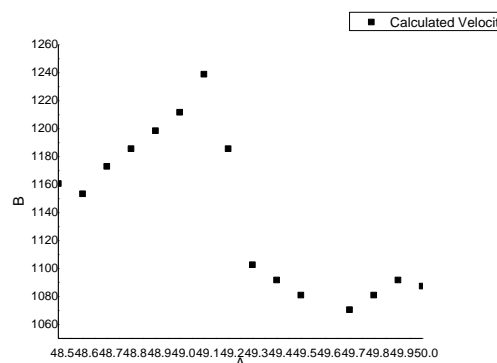
Fig 3 : Variation of ultrasonic Velocity in Binary Mixture of Cyclohexane(71%) and Methanol(29%) with respect   to temperature

The value of velocities decreases with increase of temperature due to breaking of hetero and homo-molecular clusters at high temperature. Variation in the ultrasonic velocity point out on the structural changes associated with the liquid mixtures of weakly or strongly interacting components. Moreover, ultrasonic velocity measurements are sensitive to molecular interaction which could give the quantitative information about physical nature and strength of molecular interaction in liquid mixtures.

Copyright statement

Acknowledgements

References

1. *Fundamentals of Ultrasonics,* J. Blitz, Butterworth Publishers, London, 1963

2. *Absorption and Dispersion of Ultrasonic Waves,* Academic Press, K. F. Herzfeld and T.A. Litovitz, New York and London, Pubs., 1959

3. *Ultrasonic Absorption: An Introduction to the Theory of Sound Absorption and Dispersion in Gases, liquids, and Solids,* A. B. Bhatia, Dover Pubs, 1985

4. S. Rajagopalan, Ultrasonic Absorption in Mixtures of Dioxane and Benzene, *J. Phys. Soc. Japan, 27(4), 1020-1021 (1969)*

5. S. P Dange, O. P. Chimankar, S. T. Hiwarkar, P. D. Borkar, Study of interaction of Ascorbic Acid with NaOH using ultrasonic Technique, *Int. Jr. of Sci & Res. 28, (2015)*

6. Sunita Dandawate, Study of Velocity of Ultrasonic Waves in Binary Mixtures of Liquid at Room Temperature, *Ind. J. Pure and Appl. Phys, 6(4), 489-494, (2010)*

7. G. Sanchez and C. W. Garland, Critical Ultrasonic Attenuation in the Binary Liquid Cyclohexane + Nitroethane, *J. Chem. Phys 79, 3100-3103 (1983)*

8. M. Fixman, Absorption and Dispersion of Sound in Critical Mixtures, *Chem. Phys. 36(8), 1961 (1962)*

9. M. Fixman, Ultrasonic Attenuation in the Critical Region, *J. Chem. Phys, 33(5), 1363-1370 (1961)*

10. G. S. Darbari, R. P. Singh, and *G. S.* Verma, Acoustical Behavior of Critical Mixtures, *Phys. Rev. Letts. 16(25), 1150 -1151 (1966)*

11. R. P. Singh, *G. S.* Verma, Acoustic Behaviour of a Critical Mixture of Methyl Alcohol and Cyclohexane , *J. Phys. SER. 2(1), 1476 -1480 (1968)*

12. R. A. Ferrell and J. K. Bhattacharjee, Universality in the Critical Dynamics of Fluids: Ultrasonic Attenuation , *Physica A250, 83-90 (1998)*

13. V. *C.* Aggarwal and A. K. Gupta, Acoustic Attenuation and Velocity Measurements in Methanol - Cyclohexane Critical Mixture**,** *J. Phys. D: Appl. Phys, 8, 2232-2236, (1975)*

14. S. Rajagopalan, Use of Ultrasonic Flaw Detector in Research, *J. Inst. Elect. & Tele. Engg. 21(4), 223-227 (1975)*

15. V. A. Del Gross and C. W. Mader, Speed of Sound in Pure Water, *J. Acoust. Soc. Am. 52 (7) (part 2), 1442-1446 (1972)*

16. *Design of Virtual Instrumentation For Ultrasonic Characterization,* Anup Balharpure, Ph. D. Thesis submitted to Rashtrasant Tukadoji Maharaj Nagpur University, Nagpur, 2016

ARTICLE

Grey Water Treatment by Constructed Wetland- An Economical Way of Water Reclamation.

D. B. Rana[1][*], M. K. N. Yenkie[1], N. T. Khaty[1], A. G. M. Haldar[2] and P. J. Puri[1]

[1]*Laxminarayan Institute of Technology, Rashtrasant Tukadoji Maharaj Nagpur University, Nagpur-440033*

[2]*Priyadarshini Bhagwati College of Engineering, Nagpur - 440027*

[*] Corresponding author: dbrana81@gmail.com

Abstract: In present investigation portable low cost constructed wetland is designed for treatment of synthetic grey water. Various materials in low cost constructed wetland were studied like soil, fibre waste, adsorbing materials. Percentage COD reduction (>90%), BOD_5 reduction (>80 %), PO_4^{3-} reduction (>60%) and biodegradability index which was shown to be raised (>0.80) were obtained. Optimum results were obtained by taking the combination of red soil, coarse low grade coal, carpentering waste as its gives maximum reduction of COD(95%), BOD_5(92%), PO_4^{3-} (66%) and increase in biodegradability index(0.96). Present study can help to design constructed wetland by using easily available material to treat real grey water generated at a very small scale like office, individual house etc.

Introduction:

According to World Health Organization, shortage of water is adversely affecting more than 40% of the world population and whereas more than 25 % of the world population suffers from health and hygiene problems which are mainly related to water borne diseases (1). United Nation Organization in recent time has taken various proactive actions for providing safe potable water to masses but more than 1000 million people still have no access to improved water supply and sanitation, especially in high population density continents like Asia, Latin America and Africa (2). The demand for stringent control and protection of water resources from pollution has therefore mounted in recent years and stricter anti-pollution measures are imposed by the environmental protection agencies in developed and developing countries. Restrictions on the disposal of wastes, treatment process standards and liability provisions are making it increasingly mandatory for industries to reduce generation of hazardous wastes and are forced to reuse or recycle the wastes after proper treatment (3). In the same context, domestic waste water is found to be one of the major working problems of public, private and family utilities not only in major cities but

also in larger towns. It is attributed to massive activities which produce considerable quantity of waste water from residences, commercial and industrial facilities (4).

Domestic waste water can be broadly categories in two classes i.e. black water and grey water i.e. waste water generated by cloth washing, dish washing, bathing etc except latrine water (5).
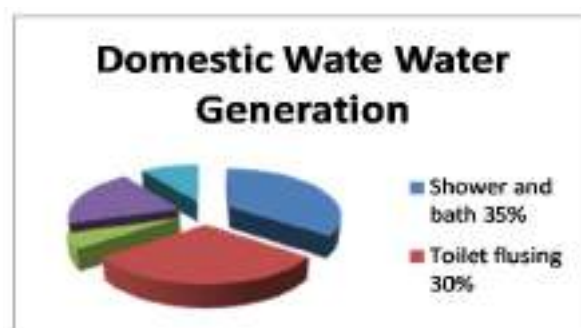
Figure 1: Grey water sources
(Source: WHO/CSIRO Report 2000)

Eriksson et al (2002, 2003), Li et al. (2003), Jefferson et al (2004) proposed applications of gray water reuse in garden,

crop irrigation, toiletry, urinal flushing, washing vehicles, fire protection, development and preservation of wetland, ground water recharge, industrial use such as boiler feed water, cooling system make up water and concrete production (5) (6) (7) (8) (9) (10).

In early grey water treatment various difficulties like maintenance, cost of treatment, operational procedure were observed which effectively addressed by Constructed Wetland (CW) (10) (11). CW can be defined as artificially created ecosystems with partially or completely saturated soils planted with submerging, emergent or floating macro-phytes or a combination of the three (Kadlec and Scott, 2009) (11) (12). CW have been shown to be capable of achieving excellent removal efficiencies for waste water pollutants and contaminants (Kadlec and Scott,2009) (11) (13). Researchers like Brown and Palmer (BSRIA) (2002), Diaper (CSIRO) (2007), Jefferson et al.(2003), Oschmann et al. (2005) proposed use of Synthetic Grey Water (SGW) for study of grey water treatment. In present study SGW was used for study as it gives more close to real characteristic of real grey water as proposed by above researchers.

Present investigation aims, to design a low cost and portable constructed wetland for treatment of grey water generated at very small scale like office, individual house etc. Optimisation of CW is done by studying various combinations of soil, filtering media containing fibre, adsorbing material in CW and its treatment of SGW).

2.0 Materials and methods:

2.1 Preparation of Synthetic Grey Water (SGW):

In the present investigation, stock synthetic grey water (SSGW) was prepared by using available materials (soap, tooth paste, hair oil, shampoo, cooking oil) in 50 liters of tap water. Characterisation of SSGW is given in Table 5. SGW was prepared by diluting SSGW (1:4) with tap water to obtain SGW (COD around 400-500 ppm) and it is used for optimisation.

2.2 Construction of Low Cost Constructed Wetland:

In present experimental work, a portable constructed wetland was prepared - a new of its kind and prepared by using easily available and low cost materials. The construction is discussed as figure 2 Soil sampling as well as its primary study was done as per and methods suggested in Textbook on Soil Analysis by Willey & Co workers, Soil Analysis suggested by Indian Institute of Agricultural Studies (14).

The sequence of various material and dimensions of beds used in CW were as follows,
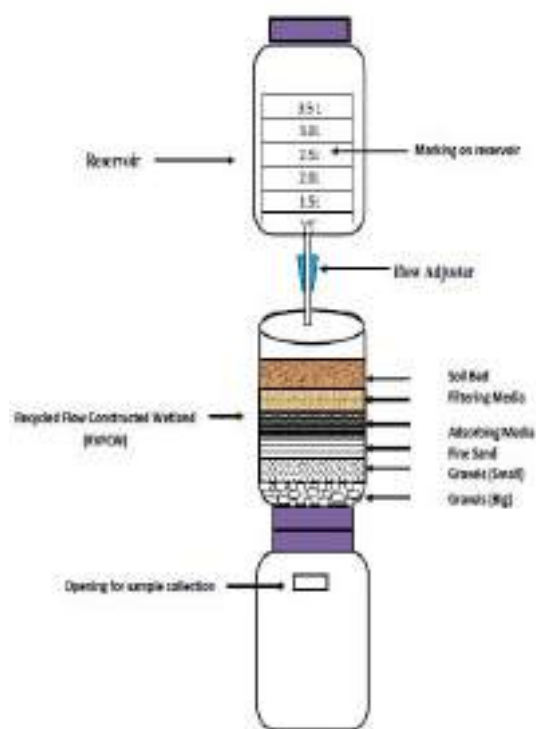
Figure 2 : Low cost Constructed Wetland

Table 1 : Dimensions of different layer in CW.

Constituent	Height (cm)	Radius (cm)
Soil Bed	5	9
Filtering Bed	5	9
Adsorbing Bed	5	9
Fine Sand	5	9
Gravel(Small)	5	9
Gravel(Big)	5	9

Soil surface was seeded with easily available grass (Botanomical Name: Genus-Dactyloctenium, Species – Aegyptium and Family – Poaceae).

2.3 Preparation of different combinations beds for optimization of CW:

By trial and error basis 9 (3 X 3) different combinations were obtained which can be used for preparation of CW. The materials chosen for beds were as follows,

Table 2: Combinations of various materials as bed in CW.

Soil Type	Filtering Media	Adsorbing Media	Fine Sand	Coarse Sand	Gravels
Red Soil	Carpentering waste	Coal (Coarse)	Same	Same	Same
Black Soil	Straw (Crop waste)	Coal (Fine)	Same	Same	Same
Sandy Soil	Khas Khas (natural herb)	Fly ash	Same	Same	Same

Soil from various locations of Nagpur region, Maharashtra, India were collected soil and analyzed with various parameter like texture, water holding capacity, bulk density, particle density (14). Three materials were selected as filtering medium on the basis of avaibality, fragility and cost i.e. carpentering waste, crop waste (rice straw) and natural herb – khas khas (Scientific name is Vetiveria zizanioides , Synonyms- Anatherum Family – Poaceae) (15). Three adsorbing materials were used as adsorbing medium i.e. low grade coal (powder form), low grade coal (coarse form) and fly ash.

The treatment parameters were determined according to USAPE, APHA 1998 norms for examination. Parameter studied were pH, total dissolve solid (TDS), conductance, Chemical Oxygen demand (COD), biochemical oxygen demand (five day), Phosphate and biodegradability index.

3.0 Result and discussion:

SSGW was analyzed which gave following analysis,

Table 3: Characterization of SSGW used in present experimental work.

Sr. No.	Parameter	Quantity
01	COD	2200-2500 mgL^{-1}
02	BOD$_5$	800-1000 mgL^{-1}
03	TDS	1500 mgL^{-1}
04	Conductance	800 µS/cm^{-1}
05	Phosphate	230 mgL^{-1}
06	Biodegradability Index	0.4 – 0.5

SSGW was diluted to get Synthetic Grey Water (SGW) by diluting it with tap water. Most appropriate composition of SGW obtained by diluting SSGW with tap water in the ratio of 1:2, 1:4 so that SGW should have COD of 300 – 400 mgL^{-1}, as COD was taken as main parameter to be studied.

Compositions of SGWs used as initial samples before treatment were as follows,

Table 4: Characterization of SGW's used in present experimental work.

Sr. No.	Parameter	Quantity
01	COD	300-400 mgL^{-1}
02	BOD$_5$	160-200 mgL^{-1}
03	TDS	600-650 mgL^{-1}
04	Conductance	450-600 µS/cm^{-1}
05	Phosphate	80-60 mgL^{-1}
06	Biodegradability Index	0.4 – 0.5

SGW was recycled through CW for 6-7 cycles and sample was collected after each cycle. As number of cycle's increases, time required to drain complete sample through CW takes lesser time as compared to time taken by sample to drain in first cycle.

It was observed that after 6 to 7 cycles, maximum reduction of parameters found to be constant and considerable reduction was not found. At this stage, treatment capacity of bed exhausted. When this CW was used after a given period of time(1 day) for SGW with same initial composition, reduction capacity of parameters found to be reduced (about 50- 60%). This is attributed to the lower dimension of CW. CW (prepared in 5 litres of plastic container) was prepared for treatment of 5 litres of SGW. More quantity of SGW can be treated with by preparing CW with more dimension of CW (scaling up of CW) and treatment capacity of CW will enhanced in the relative way as suggested by researchers in given field. Since objective of present investigation was to optimise the beds used in CW, scaling up of CW was taken as its extension of work, as future aspect, hence it was not carried out in this study.

3.1 optimization of soil bed:

Soil plays an important role in constructed wetland (16). Different types of soils were studies for optimization

When red soil was used filtration rate was found to be moderate rate in first cycle. After first cycle, reduction of COD (70%), BOD$_5$ (60%), phosphate (18%) and increased in biodegradability Index (0.6) of SGW was observed.

When black soil was used as bed, filtration rate found to be faster as compared to red soil. Filtrate obtained was clear, transparent, alkaline pH (pH-9.23) but COD removal after first cycle was found to be lesser than that of COD reduction of red soil (60%). If we compare treatment of SGW with red soil and black cotton soil, later soil shows inferior results in terms of filtration rate (fast filtration) , pH-9.23 and COD reduction i.e. 65 % after first cycle. This was attributed to lack of water holding capacity. Due to lack of suitable microbial flora in black soil do not treat GW and same was supported in the results (12).

When sandy soil was used, filtration rate found to be very slow. It reduced 62 % COD in first cycle. Maximum COD reduction of SGW was lowest i.e. around 85 %. Sandy soil also did not show promising results in reduction of parameters like (BOD$_5$-70%, PO$_4^{3-}$- 50%) and fails to boost biodegradability index (0.80). This is attributed to the contaminates available on the surface of sandy soil which are carried by river, which are separated a river bank.

In consideration with filtration rate, pH, removal of parameter and trend in biodegradable index, red soil gave promising results as compared to black and sandy soil.

3.2 Filtering media:

Role of filtering medium in CW is to remove suspended solids, provide a fixed surface for microbial flora, a base for vegetation (17). Filtering medium along with soil, provide

habitat, maintain permeability in between two medium for microorganism, nutrients, organic materials which are adsorbed and degraded by dense microbial population.

Carpentering waste, shows better results. Maximum percentage reduction of parameters in first cycle found to COD (80 %), BOD_5 (70 %), phosphate (12%) and Biodegradability index found to be 0.75. These results are attributed to better residential time for treatment of GW. It also showed maximum reduction of COD (90 %), BOD_5 (80%), PO_4^{3-} (70%) and increase in biodegradability index from 0.50 to 0.90.

Crop waste as filtering medium showed some contradictory results in terms of removal of parameters and trend in biodegradability index. During farming various chemicals are sprayed as fertilizers, insecticides, pesticides etc to increase crop yield and safety of crop (18) (19). These chemicals on the surface of crop waste, dissolved in GW (18)(19)(21). It results in the increase of all parameters, and decreases biodegradability index.

Khus-khus roots are used for medicinal purposes (15)(22). Speed of filtration was slow. This attributed to dense root hair. It also showed maximum reduction of COD, 75 % in first cycle, BOD_5 (67%), PO_4^{3-} (12%) and biodegradable index (0.50) due to more retention of GW.

In filtering media, carpentering waste gave promising results in comparison with crop waste and khus khus for effective removal of parameters and trend in biodegradable index of SGW.

3.3 Adsorbing material:

Adsorption is surface phenomenon commonly practiced in treatment of waste water as well as drinking water (20) (21) (22)(20) (23).

When low grade coal in coarse size was, maximum COD reduction was observed in the first cycle. The filtrate obtained was clear and transparent. Maximum COD removal was obtained to be around 90 %. Along with reduction of COD, remaining parameters such as BOD_5, Phosphate and biodegradability index also shows better results which was due to effective adsorption of contaminants.

In case of low grade coal in fine powder, first filtration takes more time. This was due formation of compact bed But it gives maximum COD removal in first cycle itself. COD reduction in first cycle is found to be 88 %. After first cycle, removals of COD as well as other parameters were removed with constant rate.

Investigation of fly ash as bed showed that, filtration rate of first cycle was fast but COD reduction was only 60 %. This was lowest in all categories in terms of COD removal (soil, filtering medium and adsorbing material taking together). Percentage reduction of COD obtained to be constant for next few cycles and increases in last two cycles. Overall COD reduction was found to be less (75%) as compared to other adsorption medium. This was attributed to various factor associated with fly ash such as chemicals adhered to surfaces.

Above investigation concludes that low grade coal (coarse) found to be better adsorbing media as compared to low grade (fine) and fly ash.

Summary of bed study can be given as follows,

Table 5: Percentage reduction of various parameters by various beds.

Materials as bed	% COD Reduction	% BOD Reduction	% Phosphate Reduction
Red Soil	91	89	65
Black Cotton Soil	90	82	62
Sandy Soil	85	79	49
Carpentering Waste	90	85	68
Crop Waste	23	40	60
Khas Khas	85	69	75
Coal (Coarse)	91	85	65
Coal (Fine)	90	80	60
Fly Ash	88	79	-20
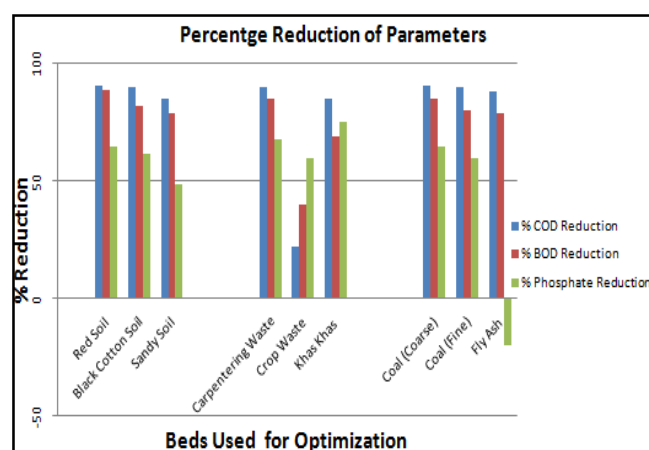
Figure 3 – Percentage reduction of various parameters by various beds.

Conclusion:

Various materials were used as bed such as soil (red, black & sandy), filtering media (carpentering waste, crop waste & khus khus), adsorbing media (low grade coal, fly ash), sand and gravel. Study of different materials as bed, concludes that red soil, carpentering waste, low grade coal in coarse size, treat synthetic grey water effectively. Reduction of parameters to a greater extent was observed like COD (60-90%), BOD_5 (60-80%), PO_4^{3-}(40-60%) and increase in biodegradable index (from 0.4 to 0.9). This investigation concludes that, constructed wetland can effectively treat real grey water and contribute to a greater extent in reclamation of fresh water as treated grey water can be used for many other purposes.

Acknowledgments:

Reference:

[1] Global Water Supply and Sanitation assessment 2000 Report. World Helath Organization and United Nations Child Section. s.l.: WHO/UNICEF Joint Monitoring Programe for water supply and sanitation., 2000, Vol-1, pp 1543-1560.

[2] Koch, E, Haucler, L. and Fischer, Taschenbunchverlag, Global Trend 93/94. 1993,Vol 1, pp.305.

[3] Gilbert, M. Introduction to Environmental Engineering and Science. s.l.: Prentice-Hall of India Pvt.Ltd, 1991. pp.181-190,224-264.

[4] Metcalf and Eddy. Waste water engineering. s.l.: Mc Graw Hill Inc, 1991.Vol-1,pp 1021-1030.

[5] Eva Eriksson, Karina Auffarth, Mogens Henze, Urban Water, 2002, Vol. 4, pp. Pages 85-104.

[6] Eriksson, E., et al., Water SA, 2003, Vol. 29, pp.135-146.

[7] Friedler, E., Environmental Technology, 2004, Vol. 25, pp. pp.997-1008.

[8] EPAV. Victroria, Australia: EPA Publication,464.2, Environment Protection Authority,2003, Vol-2, pp 1367-1384.

[9] Li, Z., et al., Water Science and Technology, 2003, Vol. 48, pp. 101-106.

[10] B. Jefferson, A. Palmer, P. Jeffrey and R. Stuetz, IWA, 2004, Vol. 50, pp.157-164.

[11] Kadlec, Robert H and Wallace, Scott.,Constructed wetlands . Boca Raton, Florida: CRC Press LL, 2009, Vol-1, pp 1268-1279.

[12] A.O.Babatunde, Y.Q.Zhao. M.O'Neill and B.O'Sullivan, Environmental International, 2008, Vol. 34, pp.116-126.

[13] Controll., 4th International Conference on Wetland Systems for Water Pollution, Water Science and Technology. 1995, Vol. 32, pp. 21-29.

[14] Soil Analysis, Willey & Co workers, 1998, pp 879-910.

[15] Mishra, Snigdha and Sharma, Satish Kumar, Reserach Journal of Pharmaceutical, Biological and Chemical Science,2013, Vol. 4, pp. 777-783. ISSN: 0975-8585.

[16] Amit Gross, Drora Kaplan, Katherine Baker, Ecological Engineering, 2007, Vol. 31, pp. 107-114.

[17] Verma, P. S. and Agrawal, V. K. Textbook of Ecology. New Delhi: S. Chand & Company Ltd.,, 2004. pp.226-236.

[18] H. Al-Hamaiedeh., M. Bino,Desalination,2010, Vol. 256, pp. 115-119.

[19] Akhtar, Wasm Md., Sengupta, Dwaipayan and Chowdhury, Ashim, Interdisciplinry toxicology, 2009, Vol. 2, pp. 1-12.

[20] Mark M. Benjamin, Kim F. Hayes and James O. Leckie, Water Pollution Control Federation, 1982,Vol. 54,pp 1472-1481.

[21] Modell, M. R., defilppi, P. and Krukonis, V. Ann Arbour, 1980. Vols. Vol-I.pp 1253-1267.

[22] Wood, P., et al. Ann Arbour Science, 1980,Vol-1,pp 657-680.

[23] Huang, J, Reneau Jr, R. B. and Hadedom, C., Water Research ,2000, Vol. 34, pp. 2582-2588.

ARTICLE

Structural, Thermal and Photo physical investigation of novel pbi-Cl blue light emitting phosphor for OLEDs

Neha B. Khotele[a], N. Thejokalyani*[b], S. J. Dhoble[c]
[a]Department of Physics, Shivaji Science College, Congress Nagar, Nagpur-440012, India
[b]Department of Applied Physics, Laxminarayan Institute of Technology, Nagpur-440033, India
[c]Department of Physics, Rashtrasant Tukadoji Maharaj Nagpur University, Nagpur-440033, India
Corresponding author: thejokalyani@rediffmail.com

Abstract: We have designed and synthesized a new blue light emitting organic phosphor 2-(4-Chlorophenyl)-1-phenyl-1H-benzimidazole (pbi-Cl) by Suzuki Coupling reaction at 135^0C. The structural properties of given organic phosphor has been studied by X-ray diffraction, Fourier transform infrared spectroscopy and scanning electron microscopy. XRD graph demonstrates sharp peaks with maximum relative intensity observed at $2\theta = 23.501^0$ having inter planar distance d= 3.7824 A^0. FTIR spectrum confirms the structural formation of the synthesized organic phosphor. TGA curve reveals its thermal stability to about 262^0C proving its potential even at elevated temperatures, while DTA curve depicts its melting temperature at about 135^0 C and glass transition temperature is at 319^0C. The photo physical properties were studied by using UV-Vis optical absorption spectra and photoluminescence spectra. The solvated pbi-Cl organic phosphor shows absorption peaks at 265 nm, 316 and 361 nm in acetic acid, 263 nm, 319 and 366 nm in chloroform . These results were used in calculating the energy band gap and the same were found to be 2.30 and 2.35 eV in acetic acid and chloroform, respectively. Stokes shift of about 7315 cm^{-1} and 7017 cm^{-1} was observed when the complex is solvated in acetic acid and chloroform, respectively. Under excitation wavelength of 342 nm, pbi-Cl emits light in blue region, peaking at 390 nm in solid state with CIE co-ordinates (Cx=0.172, Cy=0.008).These results reflects the potential of pbi-Cl as blue emissive material for organic light emitting diodes (OLED) devices, displays and solid state lighting**Keywords: Sm(TTA)₃dpphen, β-diketonate, Photoluminescence, OLEDs, Solid State lighting.**
Keywords: 2-(4-Chlorophenyl)-1-phenyl-1H-benzimidazole , Suzuki Coupling reaction, OLEDs

Introduction

Due to the phenomenal excellence such as low power consumption, wide viewing angle and high luminescence efficiency, the OLEDs have received major interest in flat-panel displays and solid state lightning (SSL) sources [1-6]. More and more interest in the field of optoelectronics is attracted towards synthesis of materials based on heavy metals (Ir(III), Pt(II), Os(II), Re(I)), which are used as phosphorescent dopants in OLEDs[7-15]. Among them, Iridium (III) [Ir (III)] complexes have been extensively studied owing to their relatively short phosphorescent lifetime, elevated phosphorescent efficiency, easy-tuning emission, thermal stability, and environmental inertness [16]. Photo physical properties of Ir(III) complexes are strongly governed by the nature of cyclometallated ligand [17-19]. Benzimidazole-type cyclometallated ligand is also very

important component to prepare highly efficient Ir(III) complexes in OLEDs due to their good electron mobility, excellent thermal stability and flexible modification ability. The present work deals with the synthesis of novel blue light emitting 2-(4-Chlorophenyl)-1-phenyl-1H-benzimidazole (pbi-Cl) organic phosphor followed by the study of its structural, thermal and optical properties.

2. Experimental

2.1 Materials

The reagents used in the present study includes: N-Phenyl-o-phenylenediamine[$C_6H_5NHC_6H_4NH_2$],4-Chlorobenzaldehyde [ClC_6H_4CHO], 2-methoxyethanol[$C_3H_8O_2$] and dichloro-methane[CH_2Cl_2], purchased from Aldrich chemicals.

2.2 Synthesis of 2(4Chlorophenyl)-1-phenyl-1H benzimidazole (pbi-Cl)

The organic phosphor 2-(4-Chlorophenyl)-1-phenyl-1H benzimidazole(pbi-Cl) was synthesized from the condensation of N-Phenyl-o-phenylenediamine with 4-Chlorobenzaldehyde dissolved in 2-methoxyethanol using Suzuki coupling reaction as shown in Fig.1. N-Phenyl-o-phenylenediamine (1equiv.) and 4 Chlorobenzaldehyde (1 equiv.) was dissolved in 50 ml of 2-methoxyethanol. The mixture was refluxed for 48 h .The volatiles were removed under vacuum and the residue (brownish colour) was extracted by dichloromethane. The yield [$C_{19}H_{13}ClN_2$] obtained was about 60%.
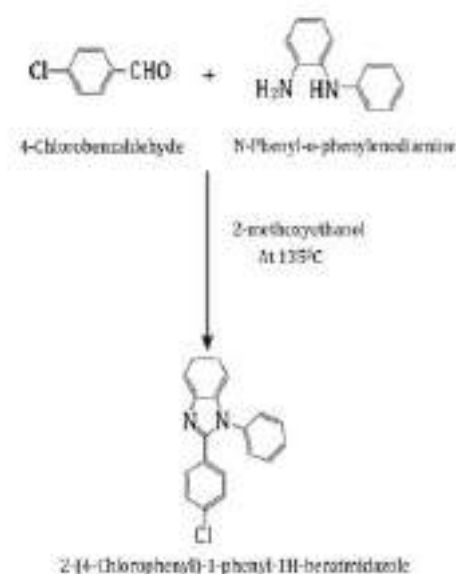
Fig.1: Synthesis route of 2-(4-Chlorophenyl)-1-phenyl-1H benzimidazole (pbi-Cl)

3. Result and Discussion

X-ray diffraction was carried out on X-ray Diffractometer System XPERT-PRO (PAN analytical), while Fourier transform infra-red (FTIR) spectroscopy was carried out on Bruker-Alpha at room temperature over the range 4000–600/cm by averaging 64 scans at a maximum resolution of 04/cmand. Differential thermal analysis (DTA) and Thermo gravimetric analysis (TGA) was carried out on Perkin Elmer diamond, optical absorption spectrum of (pbi-Cl) in acetic acid and chloroform was obtained on PerkinElmer Lambda 35 spectrophotometer and the photoluminescence (PL) spectra was carried out by a Shimadzu RF 5301 Spectrofluorometer. CIE coordinates were calculated using the chromaticity coordinate calculation method based on the CIE 1931 (Commission International d'Eclairage) system.

3.1 Structural analysis

The structural properties and morphology of 2-(4-Chlorophenyl)-1-phenyl-1H-benzimidazole (pbi-Cl) was studied from X-ray diffraction (XRD), Scanning electron microscopy (SEM) and Fourier transform infrared spectroscopy (FTIR) respectively.

3.1.1. XRD analysis

One among the most promising techniques to study the structural analysis is X-ray diffraction (XRD). The XRD spectra of synthesized phosphor (pbi-Cl) is as shown in Fig.2.
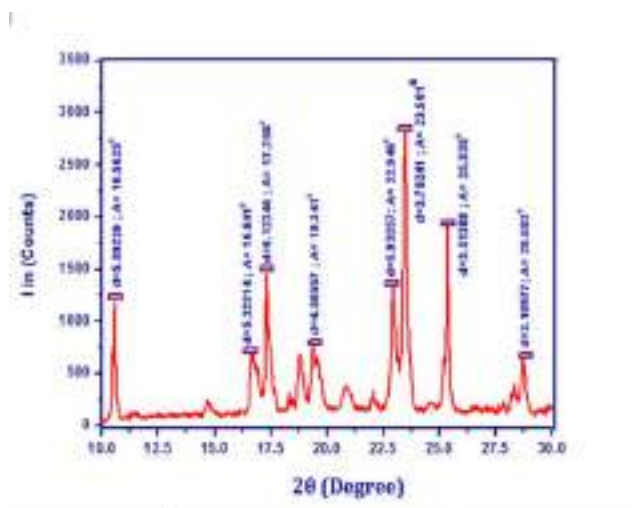
Fig. 2: XRD spectra of (pbi-Cl) in solid state

Many sharp, strong and well defined diffraction peaks confirms the crystalline nature of synthesized phosphor (pbi-Cl).The peak with maximum relative intensity was observed at $2\theta = 23.501^0$ having inter planar distance d=3.7824.

3.1.2. Scanning electron microscopy (SEM)

The morphology of the micro structured 2-(4-Chlorophenyl)-1-phenyl-1H-benzimidazole (pbi-Cl) recorded by SEM with 20μm and 10μm resolutions displays the formation of agglomerated particles with irregular and polygonal shape morphology as shown in Fig. 3.
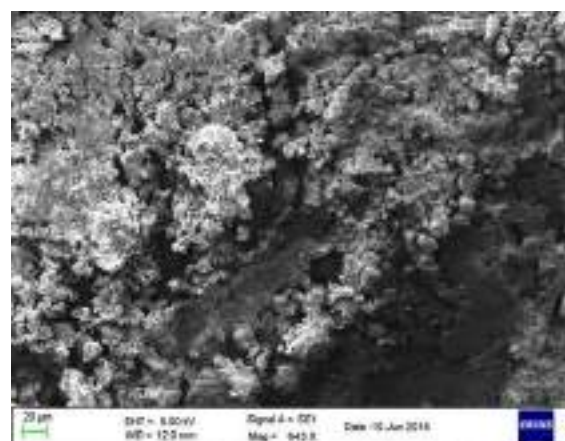
(a)
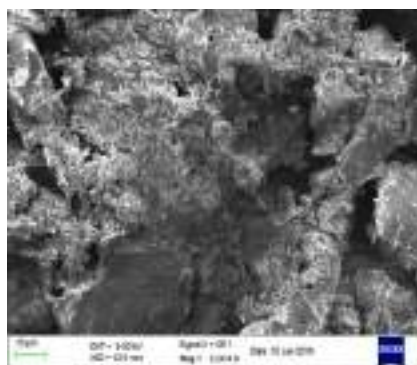
(b)

Fig.3: SEM images of pbi-Cl at different magnifications

3.1.3. Fourier Transform Infrared Spectroscopy (FTIR)

FTIR spectra of 2-(4-Chlorophenyl)-1-phenyl-1H-benzimidazole (pbi-Cl) was carried out over the range of 4000 – 500 cm^{-1} by averaging 64 scans at a maximum resolution of 4 cm^{-1} as shown in Fig. 4(a). The variations in the range of 3294-3950 cm^{-1} can be assigned to double bond N-H stretching vibrations, while the variations in the range 2850-3000 cm^{-1} may be attributed to the double/triple bonded –CH3 stretching, here peaking at 2916.52 cm^{-1}. Sharp peaks in the range of 1579.40 cm^{-1} may be attributed to C=C stretching and the peaks in the range of 1500 -1450 cm^{-1} can be assigned to the aromatic ring stretch.
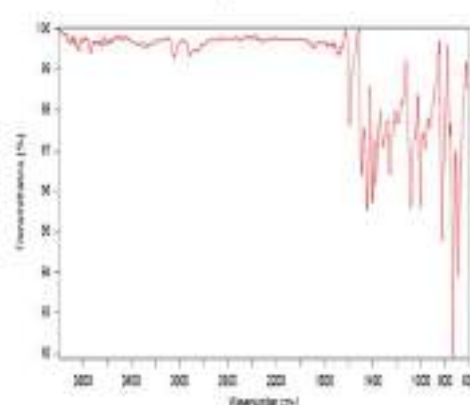
Fig. 4(a): FTIR spectra of (pbi-Cl)

In a finger print region, intense absorbance peaks dictate the presence of C-H bending (690-900 cm^{-1}) showing characteristic peak of benzene ring at 824.32cm^{-1} and C-O stretching (970-1250 cm^{-1}).This confirms the formation of synthesized 2-(4-Chlorophenyl)-1-phenyl-1H-benzimidazole (pbi-Cl) organic phosphor.

3.2.Thermal Analysis

Thermo gravimetric analysis (TGA) and Differential thermal analysis (DTA) were carried out simultaneously for investigation of reactivity, stability andphase transition properties.

3.2.1. Thermo gravimetric analysis (TGA) and Differential thermal analysis (DTA)

Thermal stability of pbi-Cl was evaluated by TGA curve in the temperature range of 35 – 500^{0}C. The organic phosphor (pbi-Cl)

exhibited high thermal stability with no weight loss till 262 °C as indicated in Fig.4(b). With further increases in temperature, thermogram takes curved portion, indicating decomposition on weight loss of sample due to heating.
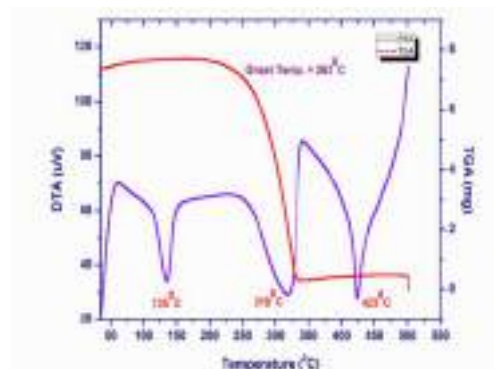
Fig.4(b): TGA and DTA analysis of pbi-Cl

The end point at 334.72^{0}C indicates final decomposition temperature [FDT], corresponding to the given reaction. The DTA curve, accompanied by a change in weight allows the detection of every physical or chemical change in the synthesized material. DTA curve depicts the melting temperature at 135^{0}C, glass transition temperature at 319^{0}C. These sharp endothermic peaks give idea regarding changes in crystallinity or fusion processes.

3.3. Optical Analysis

In order to evaluate the functioning of organic materials in device applications, its photo-physical properties such as absorption maxima, excitation maxima, emission maxima, optical band gap(Eg), Stokes shift (υ_{abs}– υ_{emi}) and CIE Co-ordinates of 2-(4-Chlorophenyl)-1-phenyl-1H-benzimidazole (pbi-Cl) were determined by UV–Vis absorption, photoluminescence (PL) spectroscopy and CIE 1931 (Commission International d'Eclairage) system.

3.3.1.UV-Vis Absorption spectra

The electric transitions of solvated pbi-Cl were explored by UV-visible spectroscopy in acetic acid and chloroform at 10^{-3} M concentration, recorded at room temperature.
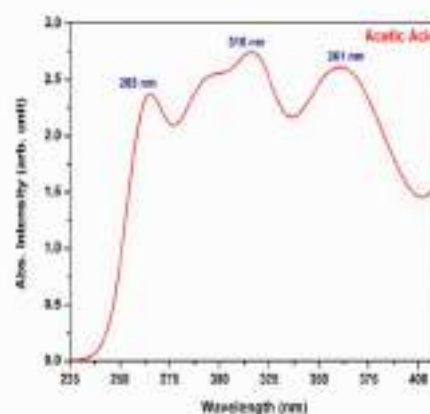
Fig.5: UV-Vis spectra of (pbi-Cl) in acetic acid solution
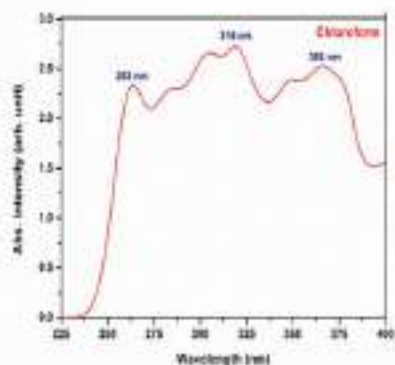
Fig. 6: UV-Vis spectra of (pbi-Cl) in chloroform solution

pbi-Cl shows broad absorption band in acetic acid ranging from 225 to 400 nm with a λ_{max} at around 316 nm and shoulders at 265 nm and 361 nm as shown in Fig.5 and the same was found to be around 316 nm and shoulder at 265 nm and 366 nm with almost same optical density in chloroform as shown in Fig.6 .

3.3.2 Energy band gap (Eg)

Morita et al. theory [21]was used to determine the energy band gap of pbi-Cl from UV-Visible spectra. The intercept of the tangent to the plots of $[\alpha\ h\nu]^2$ versus photon energy gives the calculated energy band gap. The same was found to be 2.30 and 2.35 eV in acetic acid and chloroform as shown in Fig.7.
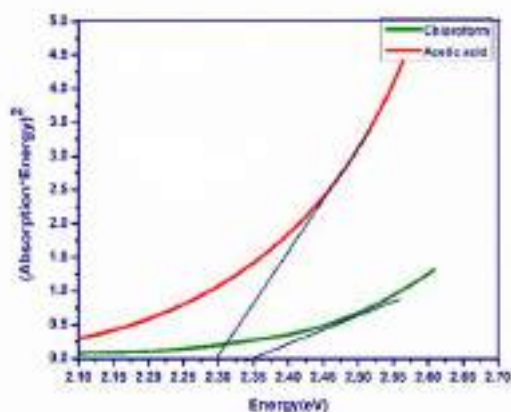
Fig.7: Energy band gap spectra of (pbi-Cl) in Acetic acid and Chloroform solution.

3.3.3. Stokes Shift

Stokes shift (υ_{abs}– υ_{emi}) [20] indicates the difference in absorption and emission wavelengths. The Stokes shift (cm^{-1}) can be determined by the formula,

$$\text{Stokes shift} = \frac{1}{\lambda_{abs}} - \frac{1}{\lambda_{emi}} \times 10^7\ cm^{-1}$$

Substituting the values of absorption wavelength and emission wavelength, it can be concluded that pbi-Cl exhibits Stokes shift of 7315 cm^{-1} and 7017 cm^{-1}, in acetic acid and chloroform respectively.

3.3.4 Photoluminescence Spectra

The Photoluminescence spectra of pbi-Cl in solid state exhibits blue phosphorescence, peaking at 390 nm with a small shoulder at 411 nm under excitation wavelength of 342 nm as shown in Fig.8.
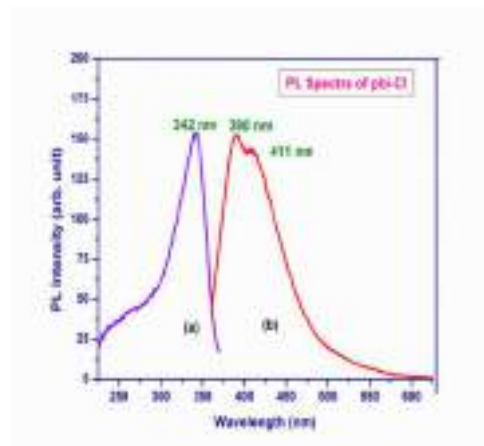
Fig.8: Photoluminescence spectra of (pbi-Cl)in solid state

3.3.5. CIE Coordinates

The chromaticity co-ordinate calculation method, based on CIE 1931 (Commission International d'Eclairage) system can be used to find out the color of phosphorescence, generally represented by color co-ordinates from the results obtained from the emission spectrum. The chromaticity diagram (Fig.9) shows the chromaticity co-ordinates of pbi-Cl in solid state as (Cx=0.172, Cy=0.008) indicating its potential as blue light emitter.
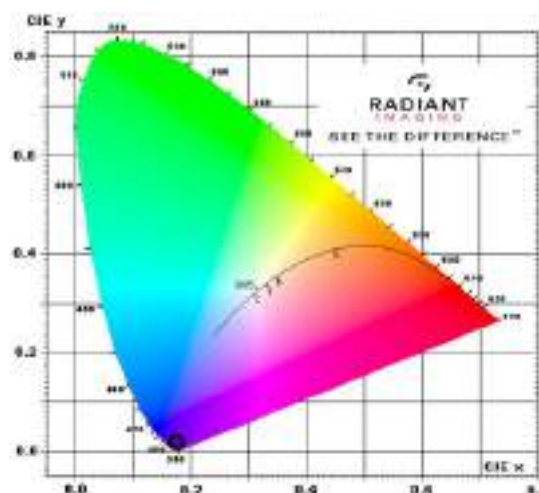
Fig.9: CIE 1931 diagram of (pbi-Cl) in solid state

4. Conclusions

We have designed and synthesized a new blue light emitting organic phosphor pbi-Cl successfully by Suzuki coupling reaction. X-ray analysis of pbi-Cl reveals its crystalline nature. FTIR spectrum result confirms the formation of pbi-Cl phosphor by indicating the characteristic peaks of Chlorophenyl and benzimidazole. SEM micrographs illustrates the formation of

agglomerated particles with irregular and polygonal shapes morphology. DTA/TGA curves infers that the complex has thermal stability till 262^0C and melting point was found to be at 135^0C. UV-Vis spectra shows broad absorption band ranging from 225-400 nm with λ_{abs} = 316 nm in both acetic acid and chloroform. The optical band gap values of solvated organic phosphor in acetic acid and chloroform were found to be 2.30 and 2.35 eV respectively. Stokes shift was found to be 7315 cm^{-1} and 7017 cm^{-1} in acetic acid and chloroform. When excited at 342 nm, the organic phosphor emits light in blue region peaking at 390 nm and 411 nm in solid state with CIE coordinates (Cx=0.172, Cy=0.008). Hence this phosphor can be used as promising blue light emitting material for light-emitting electrochemical cells and solid state lightning due to its thermal stability and broad emission wavelength.

Copyright statement

Author is solely responsible for the Plagiarism

References

1. J. H. Zhao, Y. X.Hu, H. Y. Lu, Y. L. Lü, X. Li, Organic Electronics, 2017,41, 56-72.

2. C. W. Tang, S. A. VanSlyke, Appl. Phys. Lett. , 1987, 51, 913-915.

3. C. Fan, C. Yang, Chem. Soc. Rev. , 2014, 43, 6439-6469.

4. L. Xiao, Z. Chen, B. Qu, J. Luo, S. Kong, Qi. Gong, J. Kido, Adv. Mater., 2011, 23, 926-952.

5. N Thejo Kalyani, S J Dhoble, R B Pode Luminescence., 2013, 28(2),183-189.

6. W.-Y. Wong, C.-L. Ho, Coordin. Chem. Rev., 2009, 253, 1709-1758.

7. I. R. Laskar, S. F. Hsu, T.-M. Chen, Polyhedron, 2005, 24, 189–200.

8. J.K. Lee, D. Yoo, M.F. Rubner, Chem. Mater, 1997, 9, 1710.

9. F.G. Gao, A. Bard, J. Am., Chem. Soc. , 2000, 122, 7426.

10. Y. Li, Y. Liu, J. Guo, F. Wu, W. Tian, B. Li, Y. Wang,, Synth. Met., 2001, 118 175.

11. K. Wang, L. Huang, L. Gao, L. Jin, C. Huang, Inorg. Chem., 2002, 41, 3353.

12. F.G. Gao, A.J. Bard, Chem. Mater., 2002, 14, 3465.

13. C.-L. Lee, K.B. Lee, J.-J. Kim, Appl. Phys. Lett., 2000,77, 2280.

14. R.R. Das, C.-L. Lee, J.-J. Kim, Mat. Res. Soc. Symp. Proc., 2002, 708 BB3.39.1.

15. J.P.J.Markham, S.-C. Lo, S.W. Magennis, P.L. Burn, I.D.W.Samuel, Appl. Phys. Lett., 2002, 80, 2645.

16. Dipti Chitnis, N. Thejo Kalyani, H.C. Swart, S.J. Dhoble Renewable and Sustainable Energy Reviews., 2016, 64,727-748.

17. T. Tsuzuki, N. Shirasawa, T. Suzuki, S. Tokito, Adv. Mater. , 2003, 15, 1455-1458.

18. G.-J. Zhou, Q. Wang, C.-L. Ho, W.-Y. Wong, D. Ma, L. Wang, Z. Lin, Chem. Asian J. , 2008, 03, 1830-1841.

19. D. Liu, L. Deng, W.Li, R. Yao, D. Li, M. Wang, S. Zhang, Adv. Optical Mater. , 2016, 04, 864-870.

20. F. El-Kabbany, S. Taha, M. Hafez. Spectrochimica Acta Part A: Molecular and Biomolecular Spectroscopy , 2014, 128, 481–488.

21. S. Morita, T. Akashi, A. Fujji, M. Yoshida, Y. Ohmori, K. Yoshimato, T. Kawai, A. A. Zakhidov, S. B. Lee and K. Yoshino, Synth. Met, 1995, 69, 433.

Molecular Analysis of *folA* and *folP* genes of Uropathogenic Multi Drug Resistant *E. faecalis*

Archana Moon*, Monali Jariya, Pranjali Gajbhiye, Deeba Khan, Amit Taksande

University Department of Biochemistry, RTM Nagpur University, L.I.T Premises, Amravati Road, Nagpur- 440033 Maharashtra, India.

Abstract : Urinary Tract Infection is a frequent problem worldwide which is caused by microbial invasion into the different tissues of the urinary tract. Although antibiotics are the first treatment choice for urinary tract infections, antibiotic-resistant strains of *E. faecalis* and *E. coli*, the most common cause of UTIs, is increasing worldwide. In this study, wehave isolated *E. faecalis* from uropathogenic UTI patients. Antibacterial activity of Chlorogenic acid (CGA) and Hippuric acid (HA) was checked against *E. faecalis* uropathogenic isolates. Genomic DNA was isolated from *E. faecalis*. The genomic DNA was then used to PCR amplify 535bp and 998bp DNA fragments of *E. faecalis folA* and *folP* respectively. The DHFR activity assay was also performed in presence and absence of inhibitors i.e. CGA and HA *Insilico* docking of CGA and HA on *E. faecalis* DHFR and DHPS proteins has been performed by Autodock

Keywords: Antibacterial activity, Chlorogenic acid, DHFR, DHPS, Hippuric acid, Molecular Docking, MDR, Sulfamethoxazole and Trimethoprim

Introduction

Urinary tract infection is a common contagion among men and women but the incidence is quite high among women due to their physiology (1). Inhibitors of dihydrofolate reductase (DHFR) (EC 1.5.1.3.), an enzyme that catalyses 5,6,7,8 tetrahydrofolic acid, has been used as an antibacterial as well as antimetabolite drugs for a long time. It catalyses NADPH-dependent reduction of 7,8-dihydrofolate to 5,6,7,8-tetrahydrofolate (2,3), thus producing an important cofactor for a number of one carbon transfer reactions and is essential for the biosynthesis of purines, pyrimidine's and amino acids (4). Inhibition of DHFR activity leads to deficiency of thymidylate (dTMP), thus causing inhibition of cell growth (5-7). DHFR is an enzyme of a great importance in metabolic pathways of the majority of both prokaryotic and eukaryotic organisms. In contrast to microbial DHFRs, mammalian DHFRs are highly conserved (8). Although human and bacterial DHFR share only 26 % sequence identity, overall 3D-structure of the proteins is rather similar (9).

Dihydropteroate synthase (DHPS) (EC 2.5.1.15) catalyses the condensation of 6-hydroxymethyl-7, 8- dihydropteridine pyrophosphate to para-aminobenzoic acid to form 7, 8-dihydropteroate. This is the second step in the three-step pathway leading from 6- hydroxymethyl-7, 8-dihydropterin to 7, 8- dihydrofolate. DHPS is the target of sulphonamides, which are substratum analogues that compete with para-aminobenzoic acid. Bacterial DHPS (gene sul or *folP*) is a protein of about 275 to 315 amino acid residues that is either chromosomally encoded or found on various antibiotic resistance plasmids.

Several research studies have proposed natural compounds in combination with antibiotics as a new strategy for developing therapies for infections caused by bacterial species and can potentiate the activity of antibiotics in combination (10).

Molecular docking is an important tool to study the interaction of ligands with active site residues of the receptor (11, 12). The docking involves the use of sampling algorithm and a scoring function to evaluate the proper orientation and pose of ligand molecule in relation to the binding energy. The correct identification of this binding pose of one or more related ligands is important in establishing a structure-activity relationship in lead optimization. The second use of scoring functions is to rank different ligands to predict their relative experimental activity (12-14).

Chlorogenic acid (CGA) has been reported to possess antibacterial activity (5). The antibacterial activity of Hippuric acid (HA) has also been investigated in this study. These two ligands were selected for docking studies using molecular docking tool Autodock. The Dihydrofolate Reductase (DHFR) and Dihydropteroate synthase (DHPS) of *E. faecalis* have been selected as proteins targets for molecular docking simulation.

Materials and Methods

Isolation, identification and antibiotic susceptibility testing of bacterial isolates: The bacterial colonies were isolated by streaking diluted urine sample on a differential medium UTI agar plates (Himedia, SM1353) and then further on Enterrococcus confirmatory Broth (Himedia, M394). The antibacterial activity of chlorogenic acid and hippuric acid was checked against isolated MDR *E. faecalis.* The antibiotic sensitivity was checked for Amplicillin (10μg), Cefazolin (30μg), Nalidixic Acid (30μg), Norfloxacin (10μg), Ciprofloxacin (5μg), Co-Trimoxazole (25μg), Levofloxacin (5μg), Nitrofurantoin (300μg), Augmentin (30μg), Cefuroxime (30μg), Gentamicin (10μg), Cefixime (5μg), Amikacin (30μg), Colistin (10μg), Netillin (30μg), Ceftriaxone (10μg), Cephotaxime (30μg), Furazolidone (50μg), Amoxycillin (10μg) and Vancomycin (30μg) by Kirby-Bauer's Method (16).

Antibacterial Activity of Chlorogenic Acid and Hippuric Acid: Antibacterial activity of chlorogenic acid and hipuric acid against isolated bacteria was tested by well diffusion method (Kirby–Bauer, 1950) (16). Chlorogenic acid of different concentrations (viz; 1mg, 2mg, 5mg, 10mg, 12mg, 14mg, 16mg, 18mg, 20mg and 40mg) and Hippuric Acid (via; 2mg, 5mg, 10mg, 12mg, 14mg, 16mg, 18mg, 20mg and 40mg) was utilized.

DHFR Activity Assay: A modified DHFR activity assay was performed (Osborn and Huennekens, 1958) (19). Briefly, the enzyme activity was measured by monitoring the absorbance at 340 nm of the reaction mixture containing 100μM Cell extract, 50μM TES (pH 6.8), 75μM Beta-mercaptoethanol, 100μM Dihydrofolate, 100μM NADPH and inhibitors i.e. CGA (conc. 2mg, 5mg, 10mg and 12mg), Hippuric acid (conc. 5mg, 10mg, 12mg and 15mg) Trimethoprim (conc. 2mg, 5mg, 10mg and 12mg), Sulfamethoxazole (conc. 2mg, 5mg, 10mg and 12mg) and Cotrimoxazole (conc. 2mg, 5mg, 10mg and 12mg). Incubate at 37ºC for 3 minutes (19).

Statistical analysis: Statistical analysis for activity assay was done using Students't' test. Students't' test for one tailed probability assuming unequal variance was used for significant differentiation. The criterion for significant difference was 0.05.

Genomic DNA Isolation: The genomic DNA was isolated by the method explained by *Wen-ping Chen* and *Tsong-the Kuo* (1993) (9). The bacterial culture was grown overnight for the DNA isolation, 1.5 ml of culture was used to pellet down cells by centrifugation for 10 min at 12000 rpm. Pellet was suspended into 200μl of lysis buffer, 30mM Tris-acetate pH 7.8, 20mM

sodium-acetate, 1 mM EDTA, 1% SDS). Then 66μl of 5M NaCl was added and mixed well and centrifuged at 12000 rpm for 10 min at 30°C to pellet down proteins and cell debris. Supernatant was taken into a new vial and equal volume of chloroform was added and mixed by inverting. Then centrifuged again at 12000 rpm for 3 min. Supernatant was discarded and DNA was precipitated with salt precipitation overnight. DNA was washed twice by 70 % ethanol. DNA was dried in air till smell of ethanol vanished and re-dissolved in 100μl 1X TE (Tris-EDTA) buffer.

PCR amplification: The primers for *folA* and *folP* of *E. faecalis* were designed using NCBI primer blast tool. These primers were custom made from IDT (Integrate DNA technology, India) and PCR reagents were procured from Bioline, USA. The primer pairs used for amplification of *folP E. faecalis* are shown in the table-1 and 2

Table 1: Primers designed for Amplification of *folA E. faecalis*

	Sequence (5'->3')	Tm	Amplicon size
Forward primer	ACGATTAAAGCGCCGATTGC	59.97°C	533 bp
Reverse primer	CGCTCTCGTTGTTCATGCAG	55.00°C	

Table 2: Primers designed for Amplification of *folP E. faecalis*

	Sequence (5'->3')	Tm	Amplicon size
Forward primer	AAATCGCGCACCGTTTACTG	59.83	998bp
Reverse primer	TTAGCGGAGTTGTCCACGAG	59.76	

Conclusions

The conclusions section should come in this section at the end of the article, before the acknowledgements.

folA and *folP* gene amplification of ten MDR *E. faecalis* isolates was done by RT-PCR. A single reaction mixture contained 500ng of genomic DNA extract for *E. faecalis*, 10 μl SYBR Green master mix, 0.5 μl Forward primer, 0.5 μl reverse primer, and reaction volume of 25μL by double distilled water. Amplification was done under following conditions: Hot start at 110° C, 5 min denaturation at 94°C, followed by 30 cycles of 1 min at 94°C, 1 min of annealing at 60.07° C and 2 min final extension at 72°C. The resulting PCR products were run on 1.2% agarose gel.

Molecular docking: Molecular docking studies were performed using Autodock 4 suite (version 1.5 6rC2). The ligands viz., Chlorogenic acid and Hippuric acid were docked with DHFR & DHPS enzymes of *E. faecalis*. The

DHFR (PDB Id 4M7U) protein structure of *E. faecalis* was downloaded from PDB (*X ray diffraction* of 2.10) fig. 1 The crystal structure of DHPS *E. faecalis* is unavailable in PDB hence, to obtain structural information of DHPS; the homology model was generated using Swiss model and PdbSum. DHPS *E. faecalis* protein was found to have 40.86% sequence identities with PDB ID: W767 fig. 2. This structure was used for the preparation of the model of DHPS of *E. faecalis*. The prepared model was further validated by Ramachandran plot with the help of PROCHECK fig. 3. This plot verified the DHPS protein (W767) and hence was used for docking studies. These models were further used to analyse and compare the effect of binding efficiency of DHPS towards inhibitors. The structure of ligands were downloaded from Pubchem (chemical structure data base) online portal and drawn in Marvin Sketch version 5.8.1. After docking, the results were analyzed on the basis of their binding energy and their interactions.

Figure 1: PDB structure of DHFR *E. faecalis*. (PDB ID 4M7U)

Figure 2: Homology model generated structure of DHPS *E. faecalis*.
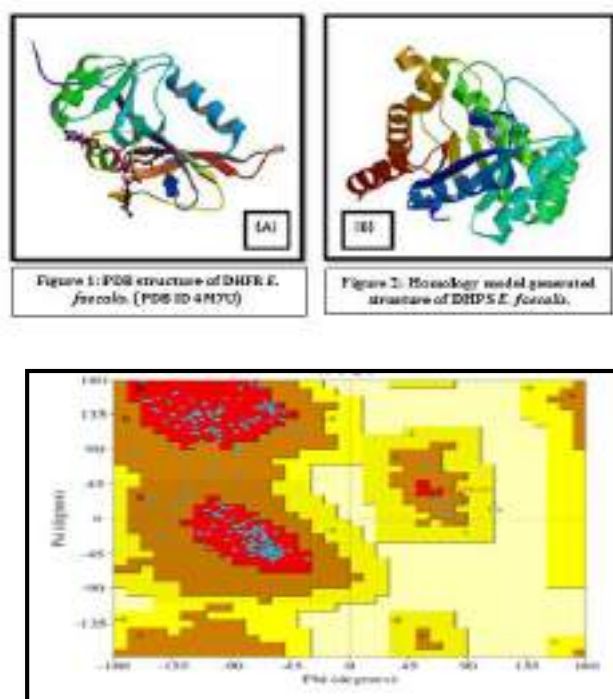
Figure 3: Ramachandran Plot of DHPS *E. faecalis*.

RESULTS AND DISCUSSION

Bacterial identification and drug resistance profile of *E. faecalis*: It was found that 37% of the patients were infected with MDR *E. coli.* The other predominant bacteria isolated were *Pseudomonas aeruginosa* (12%) and *Enterococcus faecalis* (32%). Among them, *E. faecalis* isolates were selected for current analysis. Ten *E. faecalis* isolates were found resistant to Amplicillin (10µg), Cefazolin (30µg), Nalidixic Acid (30µg), Norfloxacin (10µg), Ciprofloxacin (5µg), Co-Trimoxazole (25µg), Levofloxacin (5µg), Nitrofurantoin (300µg), Augmentin (30µg),

Cefuroxime (30µg), Gentamicin (10µg), Cefixime (5µg), Amikacin (30µg), Colistin (10µg), Netillin (30µg), Ceftriaxone (10µg), Cephotaxime (30µg), Furazolidone (50µg), Amoxycillin (10µg) and Vancomycin (30µg). The antibacterial activity of chlorogenic acid and hippuric acid was found out to be between 10-40 mg/ml and 5-40mg/ml of chlorogenic acid and hippuric acid respectively against the ten *E. faecalis* uropathogenic isolates.
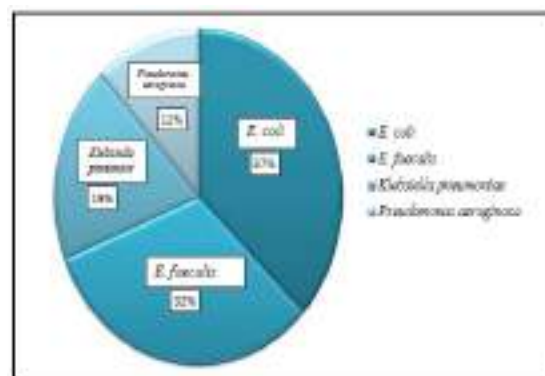
Figure 4: Bacterial isolates found in urine samples

The DHFR Activity in *E. faecalis* Strains: The DHFR activity in *E. faecalis* was checked in presence of inhibitor (chlorogenic acid, hippuric acid, trimethoprim, Sulfamethoxazole and cotrimoxazole) and in absence of inhibitor (chlorogenic acid, hippuric acid, trimethoprim, Sulfamethoxazole and cotrimoxazole). It was found that *E. faecalis* isolates have significant p values (p value <0.05) in samples containing 20mg of Hippuric Acid, 2mg (p value 0.01), 5mg (p value 0.01), 10mg (p value 0.01), and 12mg (p value 0.01) of Sulfamethoxazole. But in hippuric acid significant p values was found to be 0.01 when 15mg of HA is compared with 20mg of HA, 0.01 when 20mg of HA is compared with 5mg of HA and 0.007 in 20mg of HA. In Cotrimoxazole significant p values was found to be 0.02 when 2mg of COT is compared with 5mg of COT and 0.006 when 10mg of COT is compared with 12mg of COT. There are no significant p values found in any concentration of Chlorogenic acid.
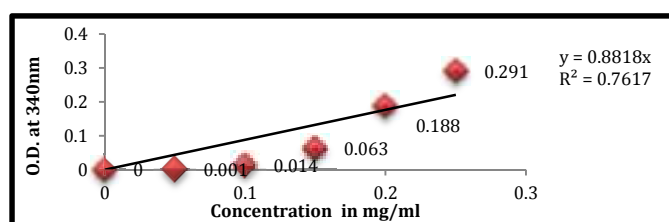
Figure 5: Standard Graph of DHFR activity assay
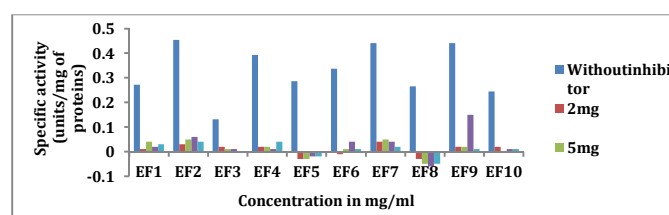
Figure 6: DHFR assay of Chlorogenic acid
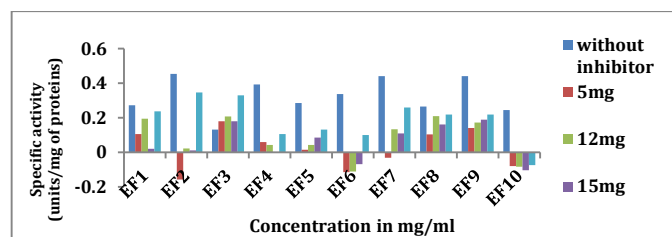
Figure 7: DHFR assay of Hippuric Acid
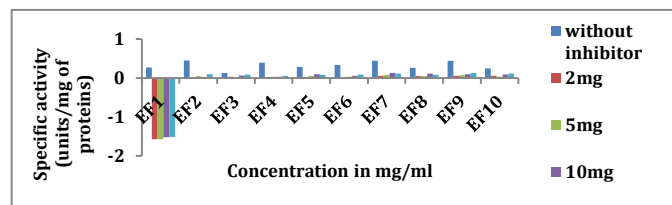
Figure 8: DHFR assay of Sulfamethoxazole
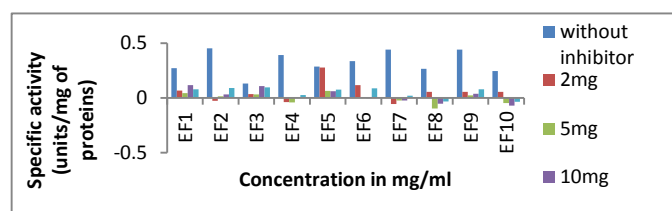
Figure 9: DHFR assay of Trimethoprim
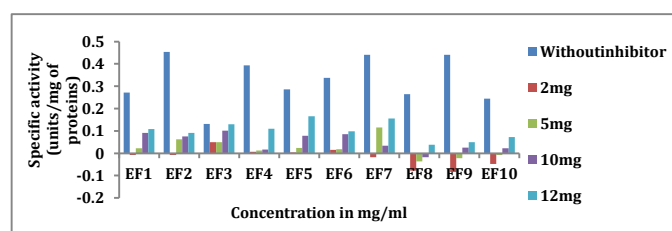
Figure 10: DHFR assay of Cotrimoxazole

Genomic DNA isolation: The genomic DNA was isolated by Wen-ping Chen and Tsong-the Kuo (1993) Method. Total 10 samples of uropathogenic MDR *E. faecalis* were utilized sample no. 1 and 4 were Cotrimoxazole sensitive while sample no. 2, 3, 5 and 6 were Cotrimoxazole resistant samples. The genomic DNA was measured in UV spectrophotometer at 260 and 280 nm respectively and the values of 260/280 ratios was found to be approximately 1.8 in all the samples of *E. faecalis.* Genomic DNA was loaded on 1.2% Agarose gel stained with Ethidium bromide. (Figure 11)
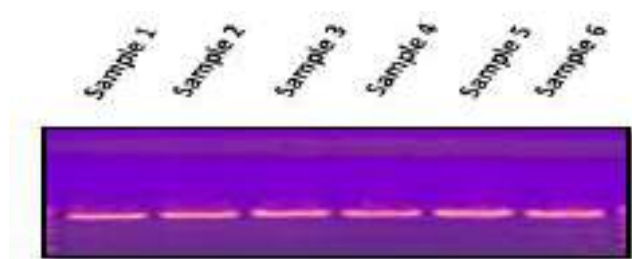
Figure 11: Genomic DNA of *E. faecalis*

PCR Amplification of *folA* and *folP* gene of *E. faecalis* isolates: The PCR products were electrophoresed on 1.2% agarose gel and bands of the amplicons sized at ~553bp and ~990bp corresponded to *folA* and *folP* of *E. faecalis* respectively were obtained.
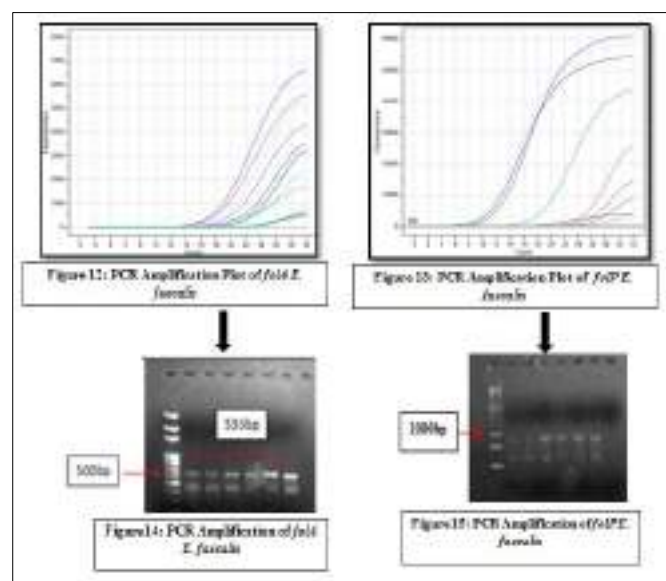
Molecular Docking: Docking Studies revealed the interaction of the proteins (DHFR and DHPS) with the ligands (Chlorogenic Acid, Hippuric Acid, Sulfamethoxazole and Trimethoprim), binding energy, type of interaction and amino acids involved in interactions. Binding energy should be negative. More negative the binding energy, better the binding affinity of ligand and protein (15).

Table 3: Interaction of ligands with DHFR and DHPS protein i.e. Hydrogen bond length, name and amino acid involved in interaction.

Ligand	DHFR *E. faecalis*			DHPS *E. faecalis*		
	Hydrogen Bond Length In A°	Hydrogen Bond Name	Interacting Sites	Hydrogen Bond Length In A°	Hydrogen Bond Name	Interacting Sites
Chlorogenic Acid	2.181 2.034 2.146 1.988	- Gly18 Arg44 Gly99	Thr46 Ser100	1.954 2.205 1.797 2.019	- - Asn15 Arg242	Ser54 Asp171 Asn15
Hippuric acid	1.997 1.967 1.824	Ala45 Thr46 Gly99	Thr46 Ser100	1.736 1.849	Phe21 Thr55	Phe21 Thr55 Asn15 Ser20
Sulfamethoxazole	2.133 2.024 2.071	Gly99 Ser100 Val102	Thr64 Gly99	2.204 1.861 2.034 2.249	- - Thr55 Lys207	Lys207 Thr55
Trimethoprim	2.063 2.062 2.014	- - Val101	Glu105 Arg44	2.152 2.177 2.17 1.926	- Thr55 Arg242 Arg242	Arg242 Thr55

In our study Chlorogenic Acid (Thr46, Ser100), Hippuric acid (Thr46, Ser100), Sulfamethoxazole (Thr64, Gly99) and Trimethoprim (Glu105, Arg44) shows direct interaction with active site residue of DHFR and their docking energy is -6.68 (chlorogenic acid), -6.03 (Hippuric acid), -7.67 (Sulfamethoxazole) and -6.38 (Trimethoprim) which indicates that the chlorogenic acid, hippuric acid, Sulfamethoxazole and Trimethoprim was docked with DHFR *E. faecalis*. Also, Chlorogenic Acid (Ser54, Asp171, Asn15), Hippuric acid (Phe21, Thr55, Asn15, Ser20), Sulfamethoxazole (Lys207, Thr55) and Trimethoprim (Arg242, Thr55) shows direct interaction with active site residue of DHPS and their docking energy is -7.93 (chlorogenic acid), -6.66 (Hippuric acid), -7.77 (Sulfamethoxazole) and -7.58 (Trimethoprim) which indicates that the chlorogenic acid, hippuric acid, Sulfamethoxazole and Trimethoprim was docked with DHPS *E. faecalis* (15).

Figure 16: Interacting Sites of DHFR with Chlorogenic Acid

Figure 17: Interacting Sites of DHFR with Hippuric Acid

Figure 18: Interacting Sites of DHFR with Sulfamethoxazole

Figure 19: Interacting Sites of DHFR with Trimethoprim

Figure 20: Interacting Sites of DHPS with Chlorogenic Acid

Figure 21: Interacting Sites of DHPS with Hippuric Acid

Figure 22: Interacting Sites of DHPS with Sulfamethoxazole

Figure 23: Interacting Sites of DHPS with Trimethoprim

Conclusion

Infections caused by *Enterococcus faecalis* are a major health problem. Moreover, among UTI causing *enterococci*, multi-drug resistant *E. faecalis* such as vancomycin-resistant strains (VRE) have been reported increasingly in many countries. UTI bacteria show MDR towards antibiotics. Hence, it is important to study the antibiotic resistance pattern and possible mechanisms that bacteria uses to resist its action. In the current study, we have isolated uropathogenic MDR *E. faecalis*. The antibacterial activity of Chlorogenic Acid and Hippuric acid was found to be between 10-40mg/ml and 5-40mg/ml of chlorogenic acid and hippuric acid respectively against *E. faecalis* uropathogenic isolates.

The DHFR activity has been investigated and it was found that in presence of inhibitors (HA, SMX, TMP & COT) *E. faecalis* isolates have significantly less DHFR activity (p value <0.05), which indicates that HA, SMX, TMP & COT can inhibit the folate pathway of *E. faecalis* bacteria. But there is no significant p value was found in any concentration of CGA.

Genomic DNA was isolated from *E. faecalis* isolates and PCR amplification was performed for *folA* and *folP* gene. The amplicon size of ~553 and ~990bp corresponded to *folA* and *folP* of *E. faecalis* was successfully amplified.

The second part of this study dealt with molecular docking of CGA, HA, TMP and SMX to DHFR and DHPS this will aid to establish new ligands/inhibitors for the selected target receptor proteins from the different available databases, based on their efficiency to bind the active sites on the receptor. Our studies show that Chlorogenic acid, Hippuric acid, Sulfamethoxazole and Trimethoprim gives best interaction with both DHFR and DHPS *E. faecalis* (15). *Insilico* studies with DHFR & DHPS showed a high binding affinity towards the ligands viz., Chlorogenic acid, Hippuric acid, Sulfamethoxazole and Trimethoprim. The interactions between ligands and proteins were observed for different poses. Binding energy was reported to be negative for both DHFR and DHPS protein which is indicative of better binding affinity of CGA, Hippuric acid, Sulfamethoxazole (SMX) and Trimethoprim (TMP) (15).

Coffee is a complex mixture of chemicals that provides significant amounts of chlorogenic acid and Caffeine (17). Chlorogenic acids are a family of esters formed between quinic and *trans*-cinnamic acids. Coffee represents the richest dietary source of chlorogenic acids and cinnamic acids (caffeic acid) (17). The quinic acid moiety in chlorogenic acid is the major precursor of hippuric acid (18). Hippuric acid itself, deriving from both caffeic and quinic acids moieties accounted for 36.5% of the chlorogenic acid intake (18). These *in silico* studies supported with *invivo*, *invitro* and ADMET testing will certainly help towards developing new treatment of MDR-UTI in the future.

Copyright statement

Acknowledgements

References

1. Parveen K, Momen A, Begum AA, Begum M (2011) Prevalence of urinary tract infection during pregnancy. J Dhaka National Med Coll Hos 17(2): 8-12.

2. Gangjee, W. Li, J. Yang, R.L. Kisliuk, Design, synthesis, and biological evaluation of classical and nonclassical 2-amino-4-oxo-5-substituted-6-methylpyrrolo [*3,2-d*] pyrimidines as dual thymidylate synthase and dihydro*folA*te reductase inhibitors, *J. Med. Chem. 51* (2008) 68-76.

3. J. Feng, S. Goswami, E.E. Howell, R67, the other dihydro*folA*te reductase: Rational design of an alternate active site configuration, *Biochemistry, 47* (2008) 555-565.

4. B.I. Schweitzer, A.P. Dicker, J.R. Bertino, Dihydro*folA*te reductase as a therapeutic target, *FASEB J. 4* (1990) 2441-2452.

5. A. Gangjee, H.D. Jain, S. Kurup, Recent advances in classical and non-classical anti*folA*tes as antitumor and antiopportunistic infection agents: Part I, *Anticancer Agents Med. Chem. 7* (2007) 524-542.

6. A. Gangjee, H.D. Jain, S. Kurup, Recent advances in classical and non-classical anti*folA*tes as antitumor and antiopportunistic infection agents: Part II, *Anticancer Agents Med. Chem. 8* (2008) 205-231. *6.*

7. A. Gangjee, S. Kurup, O. Namjoshi, Dihydro*folA*te reductase as a target for chemotherapy in parasites, *Curr. Pharm. Des. 13* (2007) 609-639.

8. I.M. Kompis, K. Islam, R.L. Then, DNA and RNA synthesis: Anti*folA*tes, *Chem. Rev. 105* (2005) 593-620.

9. J.J. Burchall, G.H. Hitchings, Inhibitor binding analysis of dihydro*folA*te reductases from various species, *Mol. Pharmacol. 1* (1965) 126-136.

10. Premkumar Jayaraman,[1,2] Meena K Sakharkar,[1,3,✉] Chu Sing Lim,[1,2] Thean Hock Tang,[4] and Kishore R. Sakharkar[1,4], Activity and interactions of antibiotic and phytochemical combinations against *Pseudomonas aeruginosa in vitro.* Int J Biol Sci. 2010; 6(6): 556–568.

11.   Brooijmans N, Kuntz I. Molecular recognition and docking algorithms. Annu Rev Biophys Biomol Structure 2003;32:335-73.

12.   Kitchen D, Decornez H, Furr J, Bajorath J. Docking and scoring in virtual screening for drug discovery: methods and applications. Nat Rev Drug Discovery 2004;3:935-49.

13.   Hartshorn M, Murray C, Cleasby A, Frederickson M, Tickle I, Jhoti H. Fragment-based lead discovery using X-ray crystallography. J Med Chem 2005; 48: 403-13.

14.   David E, Stephen N. Virtual screening of DNA minor groove binders. J Med Chem 2006; 49: 4232-8.

15.   ARCHANA MOON[1*], DEEBA KHAN[2*], PRANJALI GAJBHIYE[3*] & MONALI JARIYA[4*], Insilico docking of various ihibitors of E. faecalis *folA*te pathway, International Journal of Scientific and Research Publications, Volume 7, Issue 3, March 2017 430 ISSN 2250-3153.

16.   Bauer A W, Kirby W M, C Sherris and M Turck. Antibiotic susceptibility testing by a standardized single disc method. Am. Clin. Pathol. 36, 1966, 493-496.

17.   Jane V. Higdon and Balz Frei, Coffee and Health: A Review of Recent Human Research, *Critical Reviews in Food Science and Nutrition*, 46:101–123 (2006).

18.   Marie-Paule Gonthier[2], Marie-Anne Verny, Catherine Besson, Christian Re´me´ sy and Augustin Scalbert[1], Chlorogenic Acid Bioavailability Largely Depends on Its Metabolism by the Gut Microflora in Rats, The journal of nutrition, 0022-3166/03, 2003

19.   Rachida Tahar[a, 1], Philippe Eldin de Prcoulas[a, 2], Leonard k. Basco[a, b], Mohammed Chiadmi[c], Andre Mazabraud[a,*] Kinetic properties of dihydrofolate reductase from wild- type and mutant *Plasmodium vivax* expressed in *Escherichia coli*, Molecular and Biochemical Parasitology, 113 (2004), 241-249.

ARTICLE

Understanding the correlation of thermodynamic parameter with topological instability and thermal stability in Zr-Cu-Ag Bulk Metallic Glasses

A. A. Deshmukh[1*], U. A. Palikundwar[1], G. R. Navnage[2]
[1]*X-Ray Research Laboratory, Department of Physics, Rashtrasant Tukadoji Maharaj Nagpur University, Nagpur-440033, M.S. India.*
[2]*Department of Mechanical Engineering, Visvesvaraya National Institute of Technology, Nagpur-440010, M.S., India.*
corresponding author : akdeshmukh9@gmail.com

AbstractA correlation between thermodynamic parameter (P_{HSS}) with topological instability parameter (λ) and thermal stability (ΔT_X) in Zr-Cu-Ag bulk metallic glasses (BMGs) is investigated. It is observed that supercooled liquid region (SLR) increases as the P_{HSS} become more negative. Further, relation between ΔT_X and λ is investigated. It is observed that initially with increase in λ, ΔT_X decreases and attends the minimum value of 51K. Further, increase in ΔT_X is observed with the increase in λ and attend the maximum value of 80K. Moreover, the correlation of P_{HSS} with λ is also evaluated. It is observed that λ also attend the maximum value for more negative value of P_{HSS}. The effect of Cu and Ag on ΔT_X is also evaluated. It is observed that with decrease in Zr and Cu, ΔT_X increases whereas with increase in Ag, ΔT_X increases. The dependence of ΔT_X on P_{HSS} indicates that P_{HSS} is one of the important parameter over λ in designing BMGs compositions and it can be further promoted being one of the GFA parameter

1. Introduction

Bulk metallic glasses (BMGs) have contributed to the new class of materials in the field of materials science community. The presence of short range order at atomic scale in the metallic alloy Au-Si obtained by rapid quenching has fascinated the scientific community. Further, absence of impurities, grain boundaries, dislocations has enabled the BMGs to exhibit excellent physical, mechanical and magnetic properties for different structural and functional applications [1-3]. Glass stability and glass forming ability (GFA) are the two important aspects which must be considered while designing BMGs compositions for applications. Although, glass stability and GFA are related, these are independent properties. Glass stability is defined as the resistance of glasses towards devitrification upon reheating near or above the glass transition temperature. On the other hand, GFA is defined as the ease by which melts can be cooled to form glasses by avoiding the crystallization kinetics [4]. Being thermodynamically metastable, BMGs have the tendency to relax continuously to more stable state upon heating and crystallizes finally. This will results in the loss of unique properties that BMGs exhibits. Therefore, it is importance to understand the GFA and to exploit a method for the evaluation of the thermal stability among BMGs [5].

Since, the discovery of Zr-based BMGs with high glass forming ability (GFA) by Zhang et.al.[6], many attempts have been carried out to find the metallic alloy with high GFA [6,7]. Further, Zr-BMGs have been extensively investigated due to their enhanced properties such as good thermal stability, high glass forming ability (GFA), large compositional region for glass formation and high strength [6,8]. Different parameters [9] has been derived from the characteristic temperatures such as glass transition temperature (T_g), crystallization temperature (T_x), liquidus temperature (T_l). These parameters are partially successful in providing complete idea about thermal stability and GFA of different families of BMGs, but still finding their way to be universal. As these are post-experimental parameters, present research has been moved to identify the pre-experimental parameters such as enthalpy of mixing (ΔH_{chem}) [9], configurational entropy (S_c/R) [9], mismatch entropy (S_σ/k_B) [9], bond parameters such as electronegativity (δ) [10] to design BMGs compositions. In the present paper, compositional dependence on thermal stability and thermodynamic parameter P_{HSS}, being one of the GFA parameter has been evaluated.

2. Calculation of Thermodynamic Parameter:

In the present discourse, thermodynamic parameter, namely P_{HSS} , has been investigated being one of the GFA parameter against topological instability parameter (λ) and thermal stability (ΔT_x). Parameter P_{HSS} is the multiplication of enthalpy of mixing (ΔH_{chem}) [18-20], configurational entropy normalized by Universal gas constant (S_c/R) [18-20], mismatch entropy (S_σ/k_B) [18-20]. These parameters are discussed in the following subsections.

2.1 Enthalpy of Mixing (ΔH_{chem}):

Based on the extended regular solution model of Gallego [21] for the ternary systems, enthalpy of mixing has been calculated for the different compositions in the ternary Zr-Cu-Ag amorphous alloy as shown in Table 1. According to this model ΔH_{chem} can be calculated by using the following equation (1).

$$\Delta H_{chem} = \sum_{\substack{i=1 \\ i \neq j}}^{n} \Delta H_{ij}^C \ldots\ldots\ldots\ldots\ldots\ldots(1)$$

Where,

$$\Delta H_{AB}^C = X_A X_B \left(X_B \Delta H_{A-B}^{interface} + X_A \Delta H_{B-A}^{interface} \right)..(2)$$

Here, X_A and X_B are fraction of element A and B, respectively. The term ΔH_{AB}^C represents the enthalpy of mixing for binary alloy at an infinite dilution of A in B, which is calculated according to the Miedema's semi-empirical model [22].

2.2. Mismatch Entropy (S_σ):

The following empirical relation as stated by equation (3) given by Mansoori et.al. [23] has been used to calculate S_σ for present investigation.

$$S_\sigma = k_B \left[\frac{3}{2}(\zeta^2 - 1)y_1 + \frac{3}{2}(\zeta - 1)^2 y_2 - \left\{ \frac{1}{2}(\zeta - 1)(\zeta - 3) + \ln \zeta \right\}(1 - y_3) \right]\ldots\ldots(3)$$

Where, k_B is the Boltzmann's constant and parameter ζ is defined as $\zeta = \frac{1}{(1-\xi)}$. The parameter ξ stands for random packing density of particles of the system. It is taken as 0.64 [19].

The summation of the dimensionless parameters y_1, y_2 and y_3 is always unity and can be calculated according to following equations.

$$y_1 = \frac{1}{\sigma^3} \sum_{j \geq i=1}^{n} (d_i + d_j)(d_i - d_j)^2 X_i X_j \ldots(4)$$

$$y_2 = \frac{\sigma^2}{(\sigma^3)^2} \sum_{j \geq i=1}^{n} (d_i d_j (d_i - d_j)^2 X_i X_j \ldots\ldots(5)$$

$$y_3 = \frac{(\sigma^2)^3}{(\sigma^3)^2}\ldots\ldots\ldots\ldots\ldots\ldots\ldots\ldots\ldots\ldots\ldots\ldots\ldots(6)$$

$$\sigma^k = \sum_{i=1}^{n} C_i d_i^k \text{ (k=2, 3)}\ldots\ldots\ldots\ldots\ldots(7)$$

In the above equations d_i and d_j are the atomic diameters of ith and j^{th} elements. The atomic diameter used in the above calculations is taken from [24].

2.3. Configurational Entropy (S_c):

Configurational entropy (S_C) depends only on atomic fraction of individual constituting element and independent of the alloy system. It can be calculated by the following equation (8) [18-20].

$$S_c = -R \sum_{i=1}^{n} x_i \ln x_i \ldots\ldots\ldots\ldots\ldots\ldots\ldots(8)$$

Here, R represents universal gas constant and x_i is the atomic fraction of ith element.

2.4. The Parameter (P_{HSS}):

The parameter P_{HSS} is obtained by the following relation [18-20].

$$P_{HSS} = \Delta H_{chem} * \frac{S_\sigma}{k_B} * \frac{S_c}{R} \quad \frac{kJ}{mol}\ldots\ldots\ldots\ldots(9)$$

The successful prediction and experimental validation has motivated the present authors to evaluate the applicability of this parameter for Zr-Cu-Ag amorphous alloy [14-17].

1. Topological Instability Parameter (λ):

Topological instability criterion (λ) was proposed by Kiminami et. al. [25] for the selection of good glass forming compositions. The introduction of the strain either by increasing the atomic radius mismatch or by increasing the solute concentration causes the change in the topology and breaks its long range order [26]. According to this criterion, amorphous alloys with $\lambda > 0.1$ crystallize after T_g, thus exhibiting a supercooled liquid region. Alloys with such behavior are termed as glassy alloys. On the other hand, amorphous alloys with < 0.1 , classified as nanocrystalline alloys, are characterized by primary crystallization prior to the T_g. An intermediate behavior is observed during crystallization of amorphous alloys with $\lambda \approx 0.1$ when nanocrystallization can be preceded by T_g [25]. The parameter can be obtained by the following relation [25].

$$\lambda = \sum_{i=B}^{Z} c_i \left| \binom{r_i}{r_{Ca}}^3 - 1 \right| \ldots\ldots\ldots\ldots\ldots\ldots(10)$$

Here, in Eq. (2), B through Z represents different TM and/or RE solute elements, with corresponding c_i atomic concentrations and r_i metallic radii calculated from [24].

Results and Discussion:

The investigations reported here explore the idea about the correlation among two pre-experimental parameters such as P_{HSS} and λ with one post experimental parameter namely ΔT_X. It is observed that a significant correlation has been noticed between P_{HSS} and ΔT_X as well as P_{HSS} and λ. For the present investigation, thermodynamic parameter (P_{HSS}) and topological instability parameter (λ) are calculated using the data available in the literature [14-17]. The parameter P_{HSS} is the product of enthalpy of mixing (ΔH_{chem}), configurational entropy normalized by Universal gas constant ($\frac{S_C}{R}$) and mismatch entropy normalized by Boltzmann constant ($\frac{S_\sigma}{k_B}$). Further, it also

TABLE 1
(Compositions and ΔT_X values are taken from reference [14-17], and P_{HSS}, λ are calculated in the present work

| Compositions (at.%)			ΔT_X	ΔH_{chem}	$\dfrac{S_\sigma}{k_B}$	$\dfrac{S_c}{R}$	P_{HSS}	λ	Ref.
Zr	Cu	Ag	K	kJ/mol			kJ/mol		
0.50	0.48	0.02	51	-25.98	0.25	0.98	-6.05	0.134	14
0.50	0.45	0.05	59	-25.91	0.24	1.00	-4.63	0.131	14
0.50	0.43	0.07	58	-25.77	0.23	1.05	-4.85	0.128	14
0.50	0.40	0.10	66	-25.59	0.22	1.11	-4.91	0.123	14
0.50	0.38	0.12	71	-27.03	0.21	1.12	-4.91	0.121	14
0.45	0.45	0.10	73	-25.75	0.246	0.95	-6.01	0.137	15
0.48	0.48	0.04	62	-23.93	0.262	0.83	-5.22	0.137	16
0.46	0.46	0.08	68	-25.17	0.251	0.92	-5.79	0.137	16
0.44	0.44	0.12	80	-26.30	0.241	0.98	-6.19	0.138	16
0.42	0.42	0.16	72	-27.34	0.23	1.02	-6.42	0.138	16
0.36	0.57	0.07	43	-20.92	0.261	0.87	-4.77	0.166	17
0.36	0.54	0.10	40	-20.56	0.253	0.93	-4.84	0.162	17
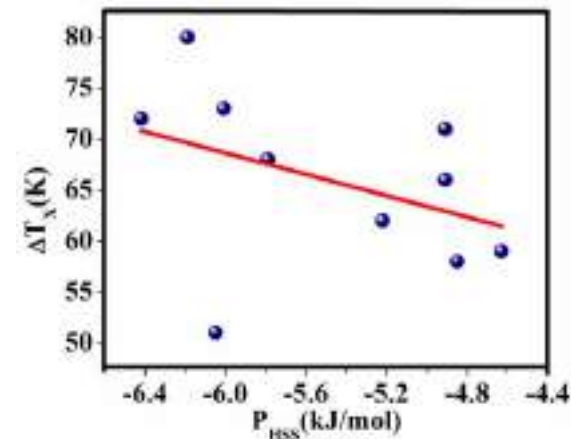
Figure 1: Variation in ΔTx with P_HSS
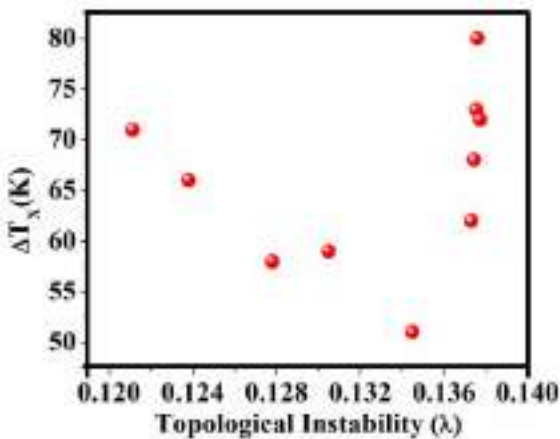
Figure 2: Variation in ΔTx with λ
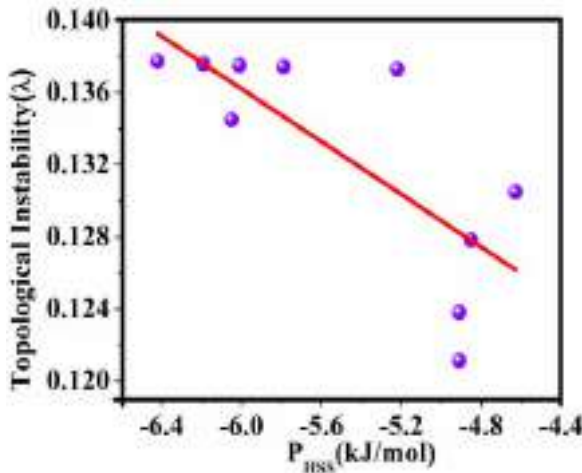
Figure 3: Variation in λ with P_HSS
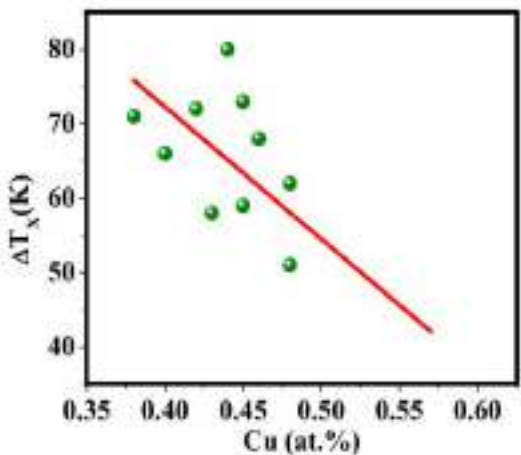
Figure 4: Variation in ΔTx with Cu (at.%)
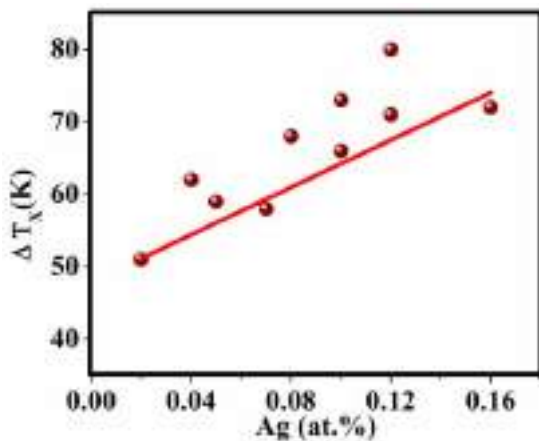
Figure 5: Variation in ΔTx with Ag (at.%)
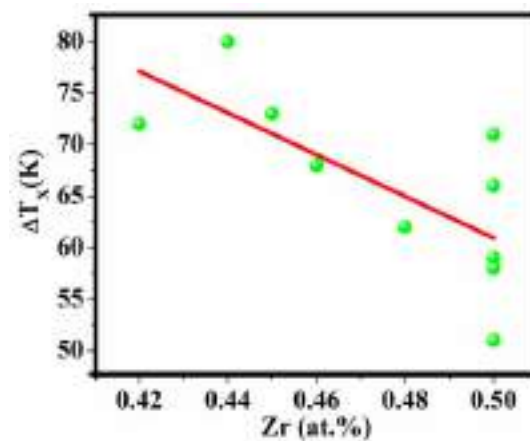
Figure 6: Variation in ΔTx with Zr (at.%)

negative of mixing of the constituent elements in the alloy and atomic radius mismatch as given by the Inoue [12]. Moreover, ΔT_X represents supercooled liquid region (SLR) of the alloy. Therefore, understanding the relationship of P_{HSS} with ΔT_X becomes more important as far as the stability of the alloy is concerned. The relation between ΔT_X and P_{HSS} has been evaluated in the Fig.1. A significant linear relationship has been observed between these two parameters. It is observed that ΔT_X will increases as the P_{HSS} of the alloy becomes more negative. A large SLR of 80K is observed at $P_{HSS} = -6.19 kJ/mol$ whereas small SLR of 51K is observed at $P_{HSS} = -6.05\ kJ/mol$ as shown in Table1. In Fig.2 correlation between ΔT_X and topological instability parameter (λ) has been evaluated. It is observed that ΔT_X has maximum value of 71K at λ = 0.121. Further, with increase in λ width of SLR i.e. ΔT_X decreases and attends the minimum value of ΔT_X = 51K when λ =0.134. Finally, ΔT_X increases to 80K at λ = 0.138. In Fig.3, a plot between P_{HSS} and λ has been drawn. Although, a linear relation is not observed but a significant trend is observed indicating that with increase in P_{HSS}, λ also increases. From the literatures [25-26], it is observed that λ > 0.1crystallizes after T_g and exhibits a large SLR. This can be evident from the plot as shown in Fig. 3. For the present alloy, values of λ are listed in the Table 1. It is observed that from Table1 for the composition Zr44Cu44Ag12 with $P_{HSS} = -6.19 kJ/mol$, λ is maximum i.e. 0.138. Similarly, for the Zr50Cu48Ag2 with $P_{HSS} = -6.05\ kJ/mol$, λ is minimum i.e. 0.134. This observation clearly states that more negative value of P_{HSS} is favorable to obtain the large SLR in the alloy. On the other hand, to investigate the compositional effect on ΔT_X, its correlation with Zr, Cu, and Ag has been evaluated as shown in Fig. 4, Fig. 5, Fig.6 respectively. From Fig. 4 it is clear that there SLR increases with increase in Cu concentration. Similarly, in Fig. 5 it is observed that SLR decreases with increases in Ag concentration. In Fig.6, it is observed that there is a inverse relationship between Zr and ΔT_X. The width of SLR increases as Zr decreases monotonically. This results show that in order to make BMGs in Zr-based amorphous alloy, the composition under consideration should have more negative value of PHSS. This study will certainly provide the insight to

design new BMGs with a proper combination of PHSS and compositions of the constituent elements in Zr based BMGs. Further, it is expected that this study will be extended to the other amorphous systems in order to make BMGs with significant thermal stability.

Conclusions

A linear correlation between P_{HSS} and ΔT_X reflects that more negative value of P_{HSS} leads to the large supercooled liquid region. Further, it is observed that with increase in λ, ΔT_X decreases linearly and then increases with increase in λ. Moreover, it is observed that λ increases as P_{HSS} becomes more negative. This relation strength the fact that λ > 0.1 will exhibit large SLR for the alloy. On the other hand, variation in Cu and Ag concentration with ΔT_X also investigated. It is observed that with increase in Zr and Cu, ΔT_X decreases whereas with increase in Ag, ΔT_X increases linearly. In short, it can be said that ternary amorphous Zr-Cu-Ag alloy will show more thermal stability if the alloy has more negative value of P_{HSS}.

Copyright statement

Acknowledgements

References

1. W. Klement, R. H. Willens, P. Duwez Nature 187 (1960) 869.

2. S. S. Dalgic, M.Celtek, EPJ Web of Conferences 15 (2011) 03009.

3. B. J. Kim, W. T. Kim, Appl Microsc. 45 (2015) 52.

4. M. C. Weinberg, J. Non-Cryst. Solids 167 (1994) 81.

5. M. Xia, S. Zhang, J. Li, C. Ma, APL 88 (2006) 261913.

6. A. Cai, D. Ding, Y. Liu, H. Wu, W. An, G. Zhou, Y. Luo, Y.Peng, Materials 9 (2016) 408.

7. T. Zhang, A. Inoue, T. Masumoto, Mater. Trans., JIM 32 (1991)1005.

8. Y. W. Yang, N. B. Hua, R. Li, S. J. Pang, T. Zhang, Sci. China G 56 (2013) 540.

9. C. Chattopadhyay, K. S. N. Satish Idury, J. Bhatt, K. Mondal, B. S. Murty, Mater. Sci. Technol.,32 (2016) 380.

10. S. Fang. X. Xiao, L. Xia, W. Li, Y. Dong, J. Non. Cryst. Solids 321 (2003) 120.

11. B. R. Rao, A. S. Gandhi, S. Vincent, J. Bhatt, B. S. Murty, Trans. IIM 65 (2012) 559.

12. A. Inoue, Y. Shinohara, J. S. Gook, Mater. Trans. Jpn. Inst. Met. 36 (1995) 1427.

13. S. R. Prajapati, S. Kashyap, A. Pratap, Bull. Mater. Sci. 38 (2015) 1693

14. G. Duan, K. D. Blauwe, M.L. Lind, J.P. Schramm, W.L. Johnson, Scripta Mater. 58 (2008) 159.

15. W. Zhang, Q. S. Zhang, C.L. Qin, A. Inoue, Mater. Sci. Eng. B, 148 (2008) 92.

16. W. Zhang, F. Jia, Q. S. Zhang, A. Inoue, Mater. Sci. Eng. A , 459 (2007) 330.

17. G. Duan, K.D. Blauwe, M. L. Lind, J. P. Schramm, W. L. Johnson, Scripta Mater. 58 (2008) 159.

18. C. Chattopadhyay, K. S. N. Satish Idury, J. Bhatt, K. Mondal, B. S. Murty, Mater. Sci. Technol., 32 (2016) 380.

19. A. A. Deshmukh, A. A. Khond, U. A. Palikundwar, J. Non-Cyst. Solids 477 (2017) 50.

20. B. R. Rao, A. K. Shah, M. Shrinivas, J. Bhatt, A. S. Gandhi, B. S. Murty, Metall. Mater. Trans A 42 (2011) 3913.

21. L. J. Gallego, J. A. Somoza,J. A. Alonso, J. Phys. Condens. Matter.2 (1990) 6245.

22. A. K. Niessen, F.R. de Boer, R Boom, P.F. de Chatel, W. C. M. Mattens, A. R. Miedema, Calphad 7 (1983) 51.

23. G. A. Mansoori, N. F. Carnahan, K. E. Starling, T. W. Leland, J. Chem. Phys. 54 (1971) 1523.

24. Guo Sheng, C. T. Liu, Progress in Natural Science: Materials International 21 (2011) 433.

25. C. S. Kiminami, R. D. Sá Lisboa, M.F. de Oliveira, C. Bolfarini, W.J. Botta, Mater. Trans. 48 (2007) 1739.

26. M. F. de Oliveira, F.S. Pereira, B.T. Ramasco, C.S. Kiminami, W.J. Botta, C. Bolfarini, J. Alloys Compd. 495 (2010) 316

ARTICLE

Pyrolytic degradation of Industrial Waste lignin to Produce Valuable Chemicals

R. A. Nandanwara[1], A. R. Chaudharib[1], J. D. Ekhec[2]

[1]Department of Applied Chemistry, Priyadarshini Bhagwati College of Engineering, Nagpur.
[2]Department of Applied Chemistry, Visvesvaraya National Institute of Technology, Nagpur

Abstract: In pulp and paper industries, a large amount of lignin is generated in wood pulping, a bulk amount of this lignin is generally burned to recover energy or is otherwise considered as waste. The discharge of this industrial waste lignin is of major concern for the environment. The waste lignin is a biomass component with a complex polymeric structure of phenyl propane units. By considering its structural aspects, on its degradation it has a potential to produce valuable chemicals. In this study, the lignin was charactrized with its elemental analysis, structural studies using FTIR and thermal studies using TGA and DTA. Then lignin was subjected to pyrolytic degradation which was carried out without catalyst and in presence of catalysts like Al2O3 and SiO2. The influence of catalyst on the formation of low molecular weight compounds was studied. On degradation, pure lignin yielded aqueous distillate containing various phenolic compounds. The GC-MS studies of the distillate showed the presence of low molecular weight compounds. Thus this study indicates that Industrial waste lignin has a great potential to produce valuable chemicals when subjected to pyrolytic degradation.
Keywords: lignin, pyrolysis, FTIR, TGA, DTA, GC-MS

l. Introduction

Lignin is the major waste product obtained from the paper industry. The spent pulping liquor from wood pulping processes contains lignin compounds. For pulping or delignification, kraft /alkaline and sulphite pulping processes are used in India. The current global production of lignin is approximately 50 million tonnes per annum which causes a disposable problem. In most of cases it is simply burnt or destroyed. The significant environmental burden posed by this waste product can be minimized to a large extent if the lignin could be converted chemically to produce value added fine chemicals and other products.

Lignin is one of the principal component which accounts about 18-40% weight of the dry wood, depending on wood species. As compared to the main components of wood like cellulose and hemi-cellulose, lignin is a complex, three dimensional, polyphenolic, amorphous and natural organic polymeric material. It is less reactive polymeric structure arising from dehydrogenative polymerisation[1] of trans-coniferyl alcohol, trans-sinapyl alcohol and p-coumaryl alcohol. Lot of work can be cited for the utilization of waste lignin e.g. hydrogenation[2,3], alkali fusion[4], pyrolysis[5,6] etc. to obtain various value added products.

In the present work the alkali lignin (kraft lignin) was isolated from paper mill waste and subjected to various techniques of characterization. The elementary composition of lignin was determined by C, H, N, analysis. The presence of functional groups in alkali lignin was assessed using IR technique. TGA-DTA studies were carried out to select the temperature zone for achieving maximum extent of thermal degradation. Lignin is subjected to thermal degradation using catalysts such as silica and alumina. The distillate obtained after thermal degradation was extracted in methanol and the organic components were analyzed qualitatively using GC-MS.

2. Experimental

2.1 Isolation and purification of lignin from industrial waste black liquor

The black liquor obtained from Simplex Paper Mills, Gondia, Maharashtra, was filtered and then acidified upto pH = 5 using dilute HCl, and then allowed to precipitate for 30 mins. It was then filtered and washed with plenty of distilled water, and then it was dried in oven for overnight at 80^0C and weighed. About 5 g of crude lignin was obtained from 100ml of black liquor. The crude alkali lignin was dissolved in minimum quantity of 1,4-dioxane and the dissolved lignin was re-precipitated from water. The residue obtained was in the form of shiny brown crystals. It was dried and weighed (3.5g) and 1,4- dioxane was removed by vacuum distillation. Now the residue can be referred as pure lignin [7-15].

2.2 Elemental analysis of pure lignin

Pure lignin was subjected to elemental analysis for the determination of C, H, N, S & O.

2.3 FTIR characterization of pure lignin

An infrared spectrum of pure lignin was recorded for the characterization of various functional groups present.

2.4 Thermo gravimetric analysis of pure lignin

TGA was recorded to select most useful range of temperature where maximum thermal cleavage would occur to produce greater yields of low molecular weight compounds. The samples were scanned using simultaneous TGA-DTA. It was set to have heating rate 15^0C/ min.

2.5 Thermal degradation of lignin

20 g of purified lignin was taken in a two necked round bottom flask fitted with distilling head, condenser, collector for distillate and a thermometer. It was heated to about 350-400^{0}C for 3 hours. The distillate and solid coke formed was collected and distillate was extracted in methanol. It was further analyzed using GC-MS.

The similar thermal degradation of pure lignin was carried out by using catalysts such as silica and alumina separately.

2.6 Analysis of degraded products by Gas Chromatogram Mass Spectrometer

Gas Chromatogram Mass Spectrometer was used to analyze the organic compounds formed during the thermal degradation of pure lignin and degradation of lignin in presence of silica and alumina.

3. Results and Discussion

Crude lignin on purification gives about 95% solid lignin.
The elemental analysis of lignin gave the following composition mentioned in **Table -1**

Table 1

Elements	C	H	O	N	S
% Composition	62.32	5.91	31.0	0.1	0.1

The FTIR spectrum of pure lignin as depicted in Figure 1 indicates some characteristics features which are helpful for structural investigations. The spectrum clearly indicated the presence of peaks due to hydrogen bonded O-H, C-H stretching in methoxyl group, methyl and methylene group, aromatic skeletal vibrations due to guiacyl group, carbonyl stretching in unconjugated ketone and carboxyl group, aromatic C-H in plane deformation and aromatic C-H out of plane etc. All these bands along with their assignments are tabulated in **Table-2**.
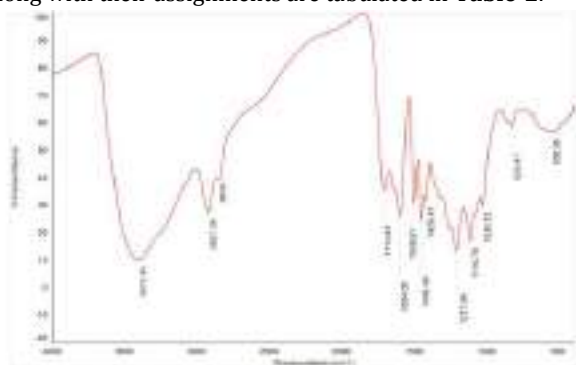
FIGURE 1. FTIR of pure lignin.

TGA of the purified lignin showed (Figure 2) that maximum thermal cleavage occurs around 350^{0}C. It was also noticed as seen from the DTA, that the degradation at this temperature was found to be exothermic process [16] along with evolution of gaseous products [17-19] during the thermal degradation. Mostly CO, CO_2, methane, ethane and other such gases are expected to escape.

Table 2

S.N.	Peaks obtained	Nature of Band Intensity	Assignments
1.	3413cm^{-1}	s	-OH Hydrogen bonded
2.	2927cm^{-1}	s	-CH stretching in methyl and methylene groups
3.	2840cm^{-1}	s	Symmetric stretch for -CH3 of methoxyl group
4.	1713cm^{-1}	m	Carbonyl stretching – unconjugated ketone and carboxyl groups
5.	1604cm^{-1}	s	Aromatic skeletal vibrations
5.	1508cm^{-1}	s	Aromatic skeletal vibrations
7.	1458cm^{-1}	s	Aliphatic CH bending, aromatic skeletal vibrations
8.	1426cm^{-1}	m	Aromatic skeletal vibrations
9.	1325cm^{-1}	w	Syringyl ring breathing with CO stretching
10.	1217cm^{-1}	s	Guaiacyl ring breathing with CO stretching
11.	1119cm^{-1}	s	C-O stretching for secondary alcohols and aliphatic ether, aromatic CH in plane deformation, syringyl type
12.	1035cm^{-1}	m	Aromatic CH in plane deformation, guaiacyl type and C-O stretching for primary alcohol
13.	835cm^{-1}	m	Aromatic C-H out of plane bending

Where s = strong, m = medium, w = weak
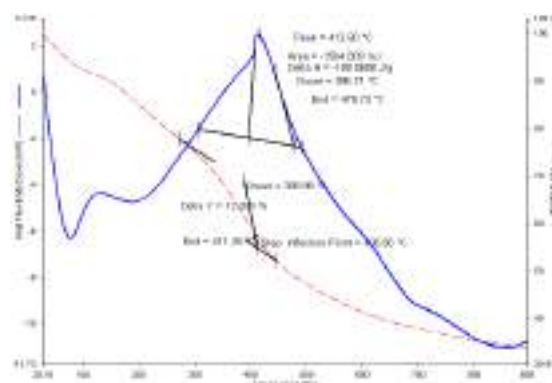
FIGURE 2. TGA and DTA of pure lignin

The thermogram of pure lignin in air has clearly indicated about 7.48% loss upto 101.23⁰C. It seems mainly due to the loss of moisture and some minor other gases due to rearrangements within the lignin molecule. The thermogram showed further gradual loss upto 40.6% at 400.94⁰C, 50.67% at 475.13⁰C. In this temperature range the elimination of phenolic aldehydes are likely to take place. The maximum weight loss occurred at 750.63⁰C .

During thermal degradation of pure lignin and lignin in presence of silica and alumina, few gases were evolved. There was an observed increase in rate of the reaction when the degradation was carried out in presence of silica and alumina. It has been attributed for the greater surface area and uniform heating due to presence of catalyst. The distillate and solid coke obtained was collected. The comparative yield of coke and distillate obtained by thermal degradation of lignin is given in **Table-3.**

Table 3

Sr. NO.	Condition	% Distillate	% Coke
1.	Pure lignin	25	60
2.	Lignin + Silica	30	55
3.	Lignin + Alumina	35	50

The organic components in the distillate were extracted in methanol and analyzed through GC-MS.

Figure 3(A) shows the pyrogram of degradation of pure lignin, the major peaks are identified as phenol, benzofuran, 2-methyl phenol (o-cresol), 3-methyl phenol(m-cresol), p-hydroxy phenyl, benzyl alcohol, phenol-4-methyl (p-cresol), phenol-2,4,6, trimethyl, phenol-2-ethyl, phenol-4-ethyl.

Main Pyrolysis Product

- Naphthalene
- Benzofuran
- Phenol
- 2-methylPhenol(o-cresol)
- 3-methyl phenol (m-cresol)
- p-hydroxy phenyl
- Benzyl alocohol
- 4 Methyl Phenol (p-cresol)
- 2,4,6 trimethyl Phenol
- 2-ethyl Phenol
- 4-ethyl Phenol

FIGURE 3. (A) Pyrogram of pure lignin

Figure 3(B) shows the pyrogram of degradation of pure lignin in presence of silica, the major peaks are identified as phenol, 1,1,biphenyl, p-hydroxy phenyl, 2-methyl phenol(o-cresol), 3-methyl phenol (m-cresol), 4-methyl phenol(p-cresol), Naphthalene etc.

Figure 3(C) shows the pyrogram of degradation of pure lignin in presence of alumina, the major peaks are identified as phenol, benzene, p-hydroxy phenyl, 2-methoxy-4-methyl phenol, Benzene-1,4,dimethoxy, 2-ethyl phenol, 3-ethyl phenol, 4-ethyl phenol, 1,2,4-trimethoxy benzene, Benzoic acid- 4-hydroxy-3-methoxy etc.

It has been observed that pure lignin and lignin with silica both gave similar type of products on pyrolysis. Few additional compounds like 1, 1-biphenyl and Naphthalene were observed in case of degradation of lignin in presence of silica.

Similar type of pyrolysis products were observed in case of degradation of lignin in presence of alumina, but it has been observed that the methoxy group is retained when the degradation is carried out in presence of alumina.
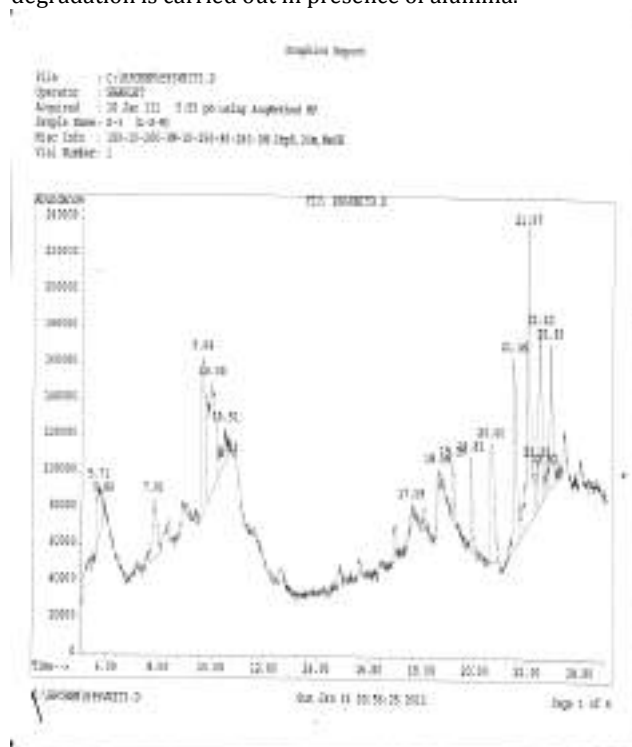
Main Pyrolysis Product

- 1, 1 Biphenyl
- Phenol
- P-Hydroxy Phenyl
- 2,methylphenol (o-cresol)
- 3, methyl phenol(m-cresol)
- 4 Methyl phenol(p-cresol)
- Naphthalene

FIGURE 3. (B) Pyrogram of lignin + silica

Graphics Report

File   : C:\HPCHEM\E95VNIT6.D
Operator   : SHARLET
Acquired   : 16 Jan 111 10:21 pm using AcqMethod MP
Sample Name: S-5 (L-A-M)
Misc Info : 100-10-200-3M-10-250-30-280-3M-3hp5,30m,MeOH
Vial Number: 1

C:\HPCHEM\E95VNIT6.D   Sun Jan 16 22:54:10 2011   Page 1 of 5
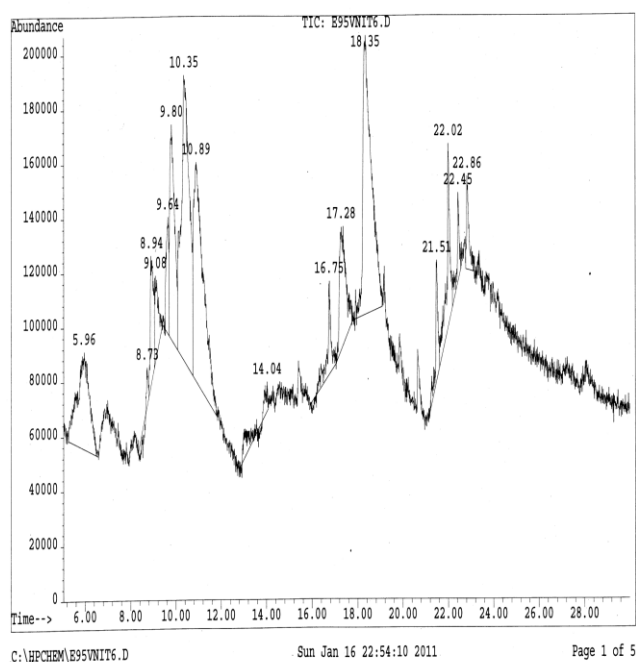
Main Pyroolysis Products
- Benzene
- P-hydroxy phenyl
- Phenol-2, methoxy, 4 methyl
- Benzene-1,4 dimethoxy
- 2,ethyl phenol
- 3, ethyl phenol
- 4, ethyl phenol
- 1,2,4 – trimethoxy benzene

FIGURE 3. (C) Pyrogram of lignin + Alumina

4. Conclusion

The above studies indicated that the industrial waste kraft lignin have a potential as a raw material for chemical industry. Various organic compounds obtained after pyrolysis have a great significance. Phenols obtained can be used in the production of Bakelite (Phenol formaldehyde resin) and alkyl benzene compounds can be used as high octane additives in gasoline. Thus pyrolysis-GC-MS are powerful tools to rapidly chemically characterize various types of lignin degradation products.

The solid coke obtained has a porous structure and can be used as an adsorbent for removal of organic species and heavy metal ions. It can also be used as a fuel.

References:

[1]   Browning, B.L.; The chemistry of wood; Interscience Publishers, Division of John Wiley & Sons; New York London, 1963.

[2]   Brewer, C.P., Cooke, L.M., Hibbert, H., *J. Am. Chem. Soc.*, 1948, 70, 57.

[3]   Shabtai, J., Zmierczak, W., Kadangode, S., Chornet, E., Johnson, D.K., *Proceedings, Fourth Biomass Conference of the Americans*, Oxford, U.K.,1999, 811

[4]   Phillips, M., Goss, M.J., *Ibid*, 1938, 125, 241.

[5]   Whittington, L.E., Naae, D., Davis, C., Templeton, E., presented at *symposium on emerging materials and chemicals from biomass and wastes, Am. Ch. Soc. National Meeting, Denver,* Co, April 1993.

[6]   Naae, D., Whittington, L., Davis, C. presented at the *symposium on Alteration and utilization of lignin, San Francisco*, CA, April 1992.

[7[Shall, Hassan, E., *App. Res. Corp.*, USA, Aug., 1993, 5 .

[8]   Argyropoulos, D.S., Sun, Y., Palns, E., *J. of Pulp and Paper Sc.,* 2002, 28, 50..

[9]   Kosankar, P.T., Ingle, V.N., *IPPTA,* 1999, 11, 4, 1.

[10] Ohman, F., Theliander, H., *International Chemical Recovery Conf.* 19 (2001).

[11] Goheen, D.W., Hoyt, C.H., *"Lignin" Kirk-Othmer encyclopedia of chemical technology,* 1979, .14, 294.

[12] Lin, S.Y., Lebo, S.E., Jr., *"Lignin" Kirk – Othmer encyclopedia of chemical technology,* 4thedition, 1995, 15, 268.

[13] Lin, S., *Ulmann's encyclopedia of Industrial Chemistry,* 1990 A-15, 305.

[14] Rydholm, S.A., Pulping processes, *Wiley Interscience, N.Y.* 1965, 192

[15] Sarkanen, K.V., Ludwig, C.H., Lignin, occurrence, formation, structure, *Wiley interscience, N.Y.* 1971, 698

[16] Sahoo, N., Rohella, R.S., Choudhary, S., Paul.s., Chakravorty, V. *Indian Pulp and Paper Technical Association*, 1996, 8,3, 45..

[17] Pictet A. and Gaulis M, Helv. *Chim,Acta.*,1923, 6,627.

[18] Nagpurkar, L., Chaudhari A., Ekhe J., *Asian J. Of Chemistry* , 2002, 14, 3- 4. 1387 .

[19] Gillet A. and Urlings. *J. Chim. And Ind.* (Paris), 1952, 68, 55.

ARTICLE

Photoluminescence properties of NaYPO$_4$Cl: Cu$^+$ blue phosphor synthesized via wet chemical route

Akhilesh Ugale[1], N. Thejo Kalyani[2*] and S.J. Dhoble[3]

Vrushali Yerpude[a], Archana Deshpande [a], K. B. Ghormare[b] and S. J. Dhoble[a*]

[a] *Department of Physics, R.T.M. Nagpur University, Nagpur-440033, India*
[b] *Department of Physics, V.M.V Commerce, J.M.T Arts and J.J.P. Science College, Nagpur- 440008, India*
Corresponding author : sjdhoble@rediffmail.com

Abstract: This paper presents the photoluminescence (PL) behavior of copper doped sodium yttrium halophosphate (NaYPO$_4$Cl) phosphor. The phosphor successfully synthesized by wet chemical technique for 0.02, 0.05, 0.1, 0.5 mol % of copper concentrations was characterized by Fourier transform infra-red spectroscopy (FTIR) and PL techniques. FTIR spectrum obtained in the frequency range of 400-4000 cm^{-1} illustrates strong characteristics bands of phosphate group. The excitation and emission spectra were studied to explore the luminescence attributes. The phosphor when excited at 357 nm gives PL emission peak at 420 nm for all copper concentrations which could be attributed to 3d^{9}4s^1 $\leftrightarrow$ 3d^{10} transitions of Cu$^+$ ion. The maximum PL intensity was obtained for a 0.02 mol% concentration of Cu$^+$ in NaYPO$_4$Cl host lattice. The CIE chromaticity coordinates (0.1716, 0.1554) calculated from emission spectrum of the phosphor are located in the blue region. The present study reveals that NaYPO$_4$Cl:Cu$^+$ is a potential novel blue emitting phosphor

Introduction

Halophosphate phosphors have great impact in the fields of illumination and display owing to their intense luminescence intensities, high emission efficiencies and simple preparation techniques [1]. Phosphate glasses have been the focus of research in materials science for a broad range of applications [2]. The phosphate family symbolizes one of the most striking feature - the ability of the tetrahedral PO$_4^{-3}$ group to bond with other structural units [1].

Aia et al. studied calcium halophosphate phosphors doped with cadmium efficiently to be used as fluorescent lamps and other devices [3]. Palilla et al. synthesized alkaline earth halophosphate activated with divalent europium possessing spodiosite and apatite structures as host matrices presenting pronounced efficiency and spectral properties [4]. Nagpal et al. studied the PL and TL properties of calcium halophosphate Ca$_5$(PO$_4$)$_3$(F,Cl):Mn,Sb fluorescent material for possible applications in radiation and ultraviolet dosimetry [5]. Our group reported the PL and TL in Sr$_5$ (PO$_4$)$_3$ Cl, doped with Eu^{2+} exploring features viz. emission peaking at 456 nm, negligible fading and excellent reusability [6].

Halophosphate phosphors can be easily prepared by wet chemical method and large number of phosphates with well-characterized structure are known, it was decided to study the synthesis of halophosphate NaYPO$_4$Cl:Cu$^+$. The phosphor was characterized by FTIR and photoluminescence study successfully. The phosphor can be applicable as a blue emitting phosphor.

Experimental

Phosphor Synthesis

NaYPO$_4$Cl:Cu$^+$ phosphor was prepared by conventional wet chemical method. NaCl, Y(NO$_3$)$_3$ and NH$_4$H$_2$PO$_4$, all analytical grade raw materials of high purity were taken in stoichiometric ratio and dissolved in double distilled de-ionized water, resulting in a solution of NaYPO$_4$Cl. Water soluble salt of Cu(NO$_3$)$_2$.3H$_2$O was further added to this solution to obtain NaYPO$_4$Cl:Cu$^+$. It was confirmed that all salts have totally dissolved and no undissolved constituents were left behind. The transparent solution of NaYPO$_4$Cl:Cu$^+$ was slowly evaporated at 80°C for 8 hours in an oven and its dehydrated powder was obtained. The resultant microcrystalline powder was again crushed to fine particles using mortar pestle and was used for further characterization. The series of phosphor was prepared for 0.02, 0.05, 0.1, and 0.5 mole % of copper concentrations. The synthesis reaction is as follows:

NaCl + Y(NO$_3$)$_3$ + NH$_4$H$_2$PO$_4$ → NaYPO$_4$Cl + 2NH$_3$ ↑ + 2NO$_2$↑ + 3O$_2$↑

Phosphor Characterization

FTIR spectrum of the prepared material was analzed on a IR Affinity-1, Shimadzu spectrophotometer at room temperature having resolution of 1 cm^{-1}. PL characteristics of the synthesized NaYPO$_4$Cl:Cu$^+$ phosphor were studied using Shimadzu RF–5301 PC Spectrofluorophotometer. Excitation and emission spectra were recorded using a spectral slit width of 1.5 nm using the same quantity of sample in each case.
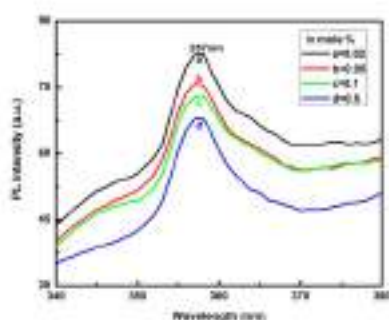
Results and Discussion

FTIR measurements

FTIR spectra analyzed for NaYPO$_4$Cl:Cu$^+$ in the mid infrared range of 400-4000 cm^{-1} helped to obtain indispensable information pertaining to the arrangement of fundamental structural units. The FTIR spectra of the synthesized phosphor NaYPO$_4$Cl:Cu$^+$ as seen in **Figure 1** illustrates a number of strong characteristics bands of phosphate group in the frequency range 500-1400 cm^{-1}. The strong absorption band at 3228.84 cm^{-1} can be assigned to hydroxy stretching due to presence of water molecules. Band position at 1635.64 cm^{-1} is ascribed to O-H stretching mode while the band position at 1350.17cm^{-1} is attributed to P-O-H deformation caused by absorbed water. The band positions at 987.55 cm^{-1} is due to M=O stretching. The absorption band peaks at 831.32 cm^{-1} and 642.30 cm^{-1} are observed owing to M-H (M=metal) bending mode while band at 518.85 cm^{-1} and 433.98 cm^{-1}are expected owing to metal halide stretching [7].
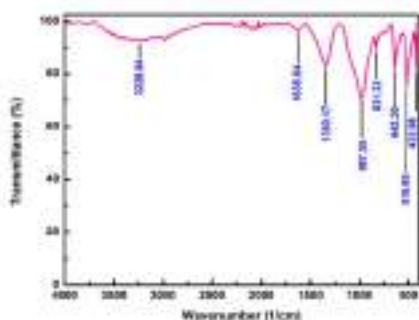
Figure 1. FTIR spectrum of NaYPO$_4$Cl : Cu$^+$ phosphor

Photoluminescence characterizations in NaYPO$_4$Cl:Cu$^+$ phosphor

PL of NaYPO$_4$Cl:Cu phosphor was recorded to confirm the incorporation of copper into the host lattice. The excitation spectra were monitored at 420 nm emission wavelength for all copper concentrations. The nature of the excitation spectra as seen in **Figure 2** remains the same for all copper concentration; however change is witnessed in intensity.
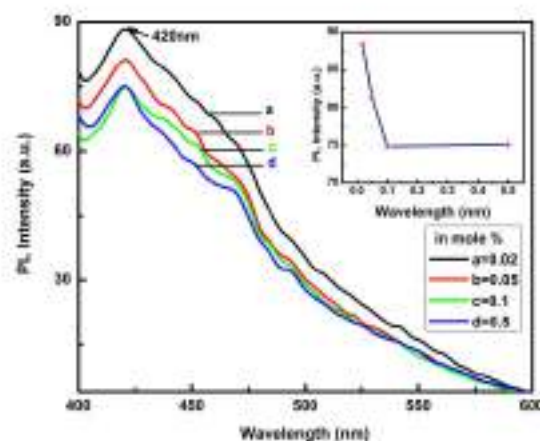
Figure 3. :PL emission spectra of NaYPO$_4$Cl:Cu$^+$ monitored at 357 nm excitation

The sample with 0.02 mole % of activator concentration produces most intense excitation band with peak at 357 nm and hence the emission spectra of the sample was recorded at this wavelength. On excitation of phosphor at 357 nm excitation wavelength, broad PL emission band is achieved with peak at 420 nm in the blue region due to 3d^{9}4s^1 ↔ 3d^{10} transitions [8-10]. The presence of intense emission peak at 420 nm indicate the incorporation of Cu$^+$ ions in the host lattice that functions as emission centers in the phosphor. Emission bands peaking in the blue region of the spectrum originated due to Cu$^+$ ions is clearly presented in the **Figure 3**. However, the PL intensity decreases with increase in the Cu$^+$ concentration. The maximum PL intensity is observed for 0.02 mol% concentration of copper. This indicates that the NaYPO$_4$Cl lattice is more suitable for PL at lower concentrations of Cu$^+$ ions.

Chromatic properties of NaYPO$_4$Cl:Cu$^+$ phosphor :

The chromatic properties of the phosphor are determined by Commission Internationale de l'Eclairage (CIE) coordinates based on the PL emission spectra. PL emission spectrum with highest intensity is used to calculate the CIE chromaticity coordinates that are presented on 1931 CIE chromaticity diagram as shown in **Figure 4**. The figure exhibits that the coordinates of NaYPO$_4$Cl:Cu$^+$ phosphor are in the blue region near the edge of color space. The chromatic coordinates of 0.1716, 0.1554 supports that the phosphor has potential to be applied as blue lamp phosphor.
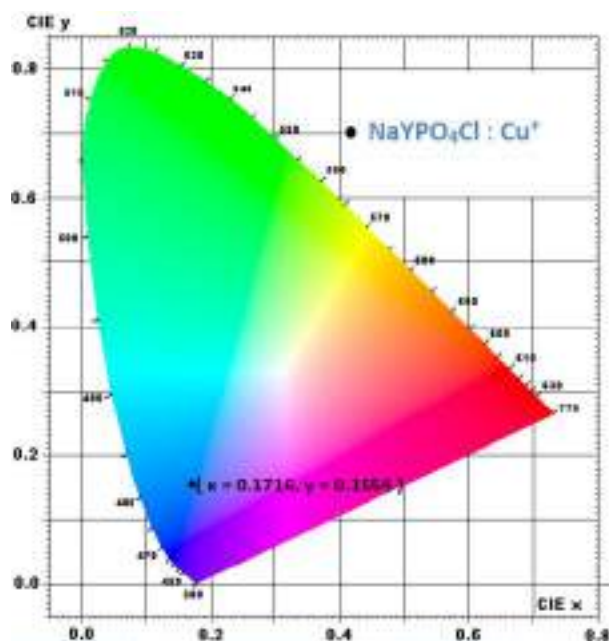
Figure 4. Chromaticity diagram of the NaYPO$_4$Cl:Cu$^+$ phosphor

Conclusions

The sodium yittrium halophosphate NaYPO$_4$Cl:Cu$^+$ was synthesized successfully via wet chemical route. The FTIR absorption spectra of copper doped halophosphate phosphor revealed information about the characteristics frequencies of phosphate bonds present in the phosphor. Photoluminescence of the synthesized material confirms the incorporation of copper into the host lattice matrix. The emission peak at 420 nm upon excitation at 357 nm could be attributed to $3d^9 4s^1 \leftrightarrow 3d^{10}$ transitions. The CIE chromaticity coordinates (0.1716 and 0.1554) are located in the blue region. The present study reveals that NaYPO$_4$Cl:Cu$^+$ compound can be a promising aspirant for application as blue emitting phosphor.

Copyright statement

References

1. K. N. Shinde, S. J. Dhoble and K. Park, *Nano-Micro Lett.*, 2012, **4(2)**, 78-82

2. J. A. Jiménez, *Physica B,* 2016, **498**, 92–97

3. Patent: Stanley M. Poss, Michael A. Aia, "Calcium halophosphate phosphors", 2965786A, Dec. 20, 1960

4. F. C. Palilla, B. E. O'Reilly, *J. Electrochem. Soc.*,1968, 115(**10**), 1076-1081

5. J. S. Nagpal, S. V. Godbole, G. Varadharajan, A. G. Page, *Radiation Protection Dosimetry*, 1998, **80(4)**, 417–422

6. S. J. Dhoble, *J. Phys. D: Appl. Phys.*, 2000, **33** ,158

7. Infrared Spectroscopy: Fundamentals and Applications B. Stuart, 2004, John Wiley & Sons, Ltd., ISBNs: 0-470-85427-8 (HB); 0-470-85428-6 (PB)

8. S. J. Dhoble, S. C. Gedam, I. M.Nagpure, S. V.Godbole, M. K.Bhide, S. V.Moharil, *J.Mater.Sci.*, 2008, **43**, 3189–3196

9. S. P. Puppalwar, S. J. Dhoble, N. S. Dhoble, Animesh Kumar, *Nuclear Instruments and Methods in Physics Research B*, 2012, **274**,167–171

10. R. A. Barve, R. R. Patil, S. V. Moharil, B. C. Bhatt, M. S. Kulkarni, *Physica B,* 2015, **458**, 117–123

ARTICLE

Renal insufficiency in sickle cell anemia patients and in vitro effect of Azocompounds on the patient's blood sample.

Pallavi Mehere a*, Virendra G. Meshram b, and B.A. Mehere.c

a.* Research student, Department of Biochemistry, RTM Nagpur University, Nagpur 440033.
b. Professor, Department of Biochemistry, RTM Nagpur University, Nagpur 440033.
c. Asso. Professor, Department of Biochemistry Dr. Ambedkar college, Nagpur 440010

Abstract: Abstract - Sickle cell disease (SCD) is a hereditary blood disorder caused by a single amino acid substitution [Glu→Val] at the sixth position of the β-chain of haemoglobin S (Hb S). This single amino acid substitution causes a significant reduction in the solubility of the deoxy-form of Hb S, causing polymer formation inside the red blood cells. Blood biochemistry has significant effect on pathophysiology of human body. Recently few studies found the association of biochemical abnormalities in sickle cell patients. Sickle cell disease showed clinical variability where African ancestors have severe phenotype than Indian sicklers. Our aim was to evaluate the biochemicals like (KFT) in sickle cell patients and their effect on severity. Some Azocompounds with antibacterial, anti-inflammatory disorders were synthesized and effect on sickle cell anemia were studied invtro. Here we present the comparative biochemical levels of kidney in sickle cell patients

Keywords- Sickle cell anemia, Azocompounds

Introduction:

Sickle cell disease is one of the most common hematologic disorders in the world and is a serious public health problem in many countries, including India. Sickle cell anemia (SCA) represents the homozygous condition of the beta S (βS) globin allele, is the more severe genotype of sickle cell disease (SCD). SCA is characterized by hemolysis, chronic and acute inflammation, multiple organ damage, and reduced patient survival [1]. The pathophysiology of SCA is complex and influenced by hypoxia, acidosis and cell dehydration, which contribute to the HbS polymerization that leads to erythrocyte deformation [2]. The kidney of the homozygous sickle cell anemia (Hb SS) patient is affected by the hemodynamic changes of chronic anemia and by the consequences of vaso-occlusion, especially in the renal medulla (3,4). The changes in the blood flow may contribute to increase oxidative stress, leading to vaso-occlusive episodes (VOE) complications, such as acute chest syndrome (ACS), stroke, priapism, gallstone, and retinopathy [5,6]. Serum creatinine may be associated with renal insufficiency in sickle cell patients. When serum creatinine is elevated the disease has reached an advanced stage and lead to renal failure [7]. The balance of electrolytes (Na, K) in the body is essential for the normal functioning of the cells and organs. In sickle cells, an abnormal activation of potassium chloride (K Cl) co-transport system was proposed to be involved in cell potassium (K) loss

and dehydration [8]. Deoxygenation of sickle cell is known to increase cation permeability of sodium (Na), potassium (K) [9,10]. Urea, an end product of protein metabolism, is excreted by the kidney. Blood urea nitrogen directly related to protein intake and nitrogen metabolism and inversely related to the rate of excretion of urea. Urea concentration in glomerular filtrate is the same as in plasma, but its tubular re-absorption is inversely related to the rate of urine formation. Urea may play a significant role in the precipitation of sickling crisis [11]. Uric acid is an end product of nucleoprotein metabolism and is excreted by the kidney. An increase in serum uric acid concentration occurs with increased nucleoprotein synthesis or catabolism or decreased renal excretion. It poses a special problem for humans because of its limited solubility, particularly in the acidic environment of the distal nephron of the kidney [12].

Azocompounds like Hydroxyurea (HU) [13] administration seems to be the best available treatment option for SCA patients (HU) has been reported to be effective in improving survival and reducing morbidity in some SCA patients. HU has been shown to reduce the frequency of painful crises and acute chest syndrome in adults, and to lessen the need for blood transfusions. HU has been found to be effective in the prevention of brain injury due to cerebrovascular disease [14,15].

Inspired by the effectiveness of this drug, the further study focuses on the in-vitro testing of other newly synthesised derivatives of Azocompounds on the sickle cell anemia patients. [16] The synthesised derivatives were evaluated for the various hematological studies like anticoagulant activity, oxygen carrying capacity and pharmacological activity. Further extension of work can help in treatment of sickle cell anemia.

Materials and methods:

The study was conducted on 52 sickle cell Anemia patients of both genders with the molecular diagnosis of sickle cell anemia. 2ml of blood samples were collected from the patients in Nagpur area with institutional ethical committee norms and kind consent of donors. After the collection of bold samples, it was centrifuged at 3000rpm for separation of serum. Before the blood samples were used we conformed that the patients had not been treated with hydroxyurea. The samples were further tested by performing cellulose-acetate electrophoresis. Two newly synthesized derivatives of Azocompounds (Azo-1 & Azo -2) were taken for the study with respective solvent and the changes in kidney function test parameters were seen before and after addition of these azo derivatives separately. kidney function test parameters like creatinine urea, sodium potassium, uric acid was done by RMS BCA-20 auto- analyser using Standard kits. This study is approved by the Institutional Ethical Committee, Nagpur, Maharashtra, India.

Inclusion Criteria and Exclusion criteria:

Inclusion Criteria: Patients with Sickle cell anemia disease were included for the study.

Exclusion criteria: Patients were excluded from the study if they were smokers consumed alcoholic drinks and patients who were pregnant were also excluded from the study.

Result and discussion:

Renal dysfunction markers in blood samples of 52 Sickle cell anemia patients study showed that the concentration of urea in 29 samples were beyond the normal limit, concentration of creatinine in 24 samples was high and the concentration in 7 samples was below normal range, sodium in 12 samples were below normal range, potassium in 9 samples and uric acid in 8 samples were beyond the normal range and taken for further investigations. Changes in the above samples were observed after adding Azo-1 and Azo-2 derivatives of Azocompounds. Those patients with higher and lower range than normal range were taken for the further study with Azo-1 and Azo-2. The clinical manifestation of sickle cell anemia in India seems to be milder than in Africa and Jamaica [17].

Table 1-Biochemical parameters (KFT) in Sickle cell Anemia patients.

Sr. no	Parameters	Normal Range	Observed value		
			High	Low	Normal
1	Urea	10-45 (mg/dl)	**29** (47.20±0.713)	-	**23**
2	Creatinine	upto 1.5 (mg/dl)	**24** (1.737± 0.149)	**7** **(0.54**±0.16)	**21**
3	Sodium	135-145mEq/L	-	**12** (124.5±3.989)	**40**
4	Potassium	3.5-4.5mEq/L	**9** (6.544±1.242)	-	**43**
5	Uric Acid	3.4-7.0 (mg/dl)	**8** (8.628±0.458)	-	**44**

(Values represent - Mean ± SD)

Urea-The mean urea concentration in sickle cell anemia patients was found to be was found to be (47.20±0.713) which is more than the normal range and after addition of Azo-1 and Azo-2 separately the concentration of Azo-1 decreased (44.206±0.713) nonsignificantly and the concentration of urea is decreased (fig-1) (42.551±6.206) significantly (P value <0.001) in Azo-2.

Creatinine– Endogenous creatinine is excreted by filtration through the glomerulus and by tubular secretion. Clinically creatinine clearance is an acceptable measure of glomerular filtration rate (GFR) but sometimes over estimates GFR. Patients with sickle cell anemia or sickle cell trait may present several types of renal dysfunction [13] it has been observed that Creatinine concentration in 24 SCA patients was significantly high but in 7 patients it was found lowered. (0.54±0.16). The mean concentration of creatinine which was higher was (1.737± 0.149) and After addition of Azo-1 and Azo-2 mean concentration of creatinine in Azo-1was found to be decreased (1.679±0.251) non-significantly and in Azo-2 it showed (1.583±0.207) significant (fir-2) decrease (P value <0.001) in concentration of creatinine.

Sodium-When Sodium level in SCA patients was evaluated it was significantly low (124.5±3.989) in 12 patients and with Azo-1 it showed a significant (144.66±14.343) increase (P value <0.001). While change in concentration of sodium with Azo-2 was nonsignificant (121.91±17.91).
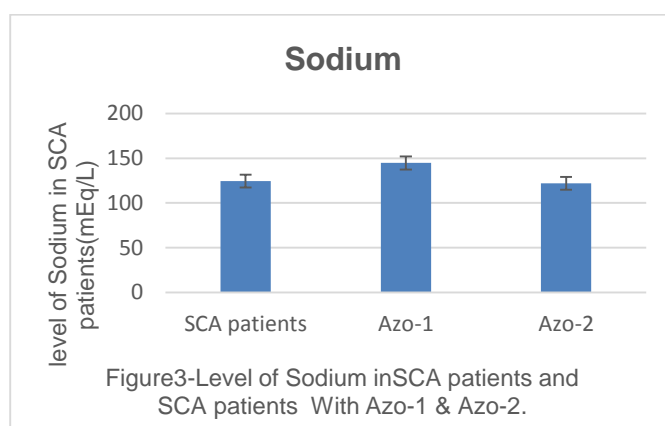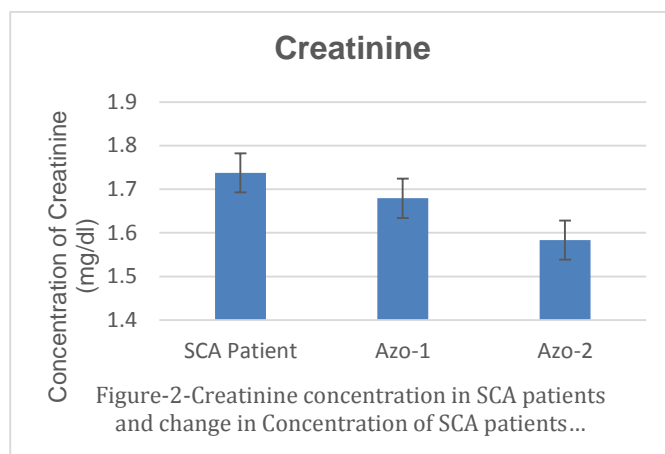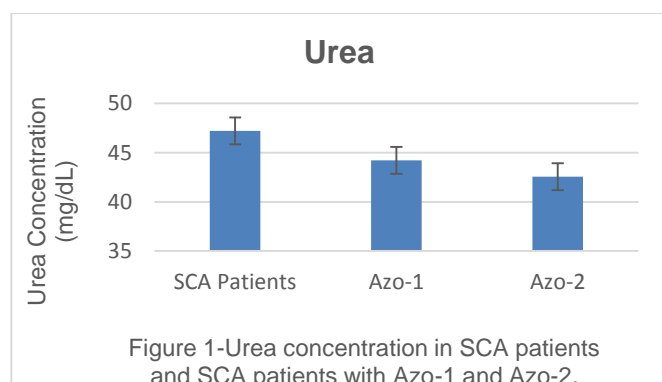
Potassium-Potassium level in SCA patients were found to be elevated (6.544±1.242) significantly. A nonsignificant Change in level of potassium was observed with Azo-1 (5.722±0.90) and Azo-2(5.988±0.95) in SCA patients.

Uric Acid-Uric acid is an end product of nucleoprotein metabolism and is excreted by the kidney. The concentration of uric acid in SCA patients showed a significant (8.628±0.458) increase. SCA patients with Azo-1 and Azo-2 separately showed nonsignificant change in concentration of uric acid.

Table -2 Changes in biochemical parameters (KFT)of SCA patients with Azo-1 and Azo-2.

Parameters	SCA patients above normal range	SCA patients with Azo-1	SCA patients with Azo-2	SCA patients below normal range	SCA patients with Azo-1	SCA patients with Azo-2
Urea	29 (47.20±0.713)	(44.206±0.713)	(42.551±6.206) *	-	-	-
Creatinine	24 (1.737±0.149)	(1.679±0.251)	(1.583±0.207) *	7 (0.54±0.16)	(0.957±0.129)	(0.885±0.299)
Sodium	-	-	-	12 (124.5±3.989)	(144.66±14.343) *	(121.91±17.91)
Potassium	9 (6.544±1.242)	(5.722±0.90)	(5.988±0.95)	-	-	-
Uric Acid	8 (8.628±0.458)	(6.714±0.432)	6.057±0.613	-	-	-

(Values represent the Mean ± SD and *p<0.001)

Figure 1-Urea concentration in SCA patients and SCA patients with Azo-1 and Azo-2.

Figure-2-Creatinine concentration in SCA patients and change in Concentration of SCA patients...

Figure3-Level of Sodium inSCA patients and SCA patients With Azo-1 & Azo-2.

Conclusion-

In the present study, we evaluated the parameters associated with renal dysfunction in SCA patients(tab-1) it has been reported that the biochemical abnormality plays a significant role in sickle cell patients physiopathology and can be used to management of the disease. In this study, we found that urea, creatinine was elevated in most of the patients (tab-2) and treatment with Azo-2 can be positively normal concentration of both the Azocompounds which can prevent the severe renal dysfunction in SCA patients. It was also found that SCA patients have lower sodium concentration and treatment with Azo-1 significantly changes the level to normal. Both Azo-1 and Azo-2 were showed the significance to SCA patients and can be taken as a new promising drug after further investigations.

Copyright statement

"Author is solely responsible for the plagiarism.

Acknowledgement:

References:

1   Platt OS, Brambilla DJ, Rosse WF, Milner PF, Castro O, Steinberg MH, Klug PP. Mortality in sickle cell disease. Life expectancy and risk factors for early death. N Engl J Med. 1994; 330:1639–44.

2   Alexy T, Sangkatumvong S, Connes P, Pais E, Tripette J, Barthelemy JC, Fisher TC, Meiselman HJ, Khoo MC, Coates TD. Sickle cell disease: selected aspects of pathophysiology. Clin Hemorheol Microcirc. 2010; 44:155–66.

3   Serjeant GR (1992). *Sickle Cell Disease*.Oxford University Press, Oxford, 261-281.

4   Mapp E, Karasick S, Pollack H, Wechsler RJ & Karasick D (1987). Uroradiological manifestations of S-hemoglobinopathy.*Seminars in Roentgenology,* 22: 186-194.

5   Adegoke SA, Adeodu OO, Adekile AD. Sickle cell disease clinical phenotypes in children from South-Western, Nigeria. Niger J Clin Pract. 2015; 18:95–101.

6   Iughetti L, Bigi E, Venturelli D. Novel insights in the management of sickle cell disease in childhood. World J Clin Pediatr. 2016; 5:25–34.

7   Guasch A. In: Eckman J, Platt A, editors. Proteinuria and renal insufficiency.

8   Vitoux D, Olivieri O, Garay RP, Cragoe EJ, Jr, Galacterous F, Bevizard Y. Inhibition of K efflux and dehydration of sickle cells by [(dihydroindenyl)oxy] alkanoic acid: an inhibitor of the K -Cl co transport system. Proc Natl Acad Sci USA. 1989;86(11):4273–4276. doi: 10.1073/pnas.86.11.4273.

9   Rhoda MD, Apovo M, Beuzard Y, Giraud F. Ca permeability in de oxygenated sickle cells.Blood. 1990;75(12):2453–2458.

10   Gibson JS, Speake PF, Ellory JC. Differential oxygen sensitive of the K and Cl co transporter in normal and sickle human red blood cells. J Physiol. 1998;511(1):225–233. doi: 10.1111/j.1469-7793.1998.225bi.x.

11   Vener KJ. Urea and sickle cell anemia. J Theor Biol. 1977;66(3):457–460. doi: 10.1016/0022-5193(77)90295-8.

12   Conger JD. Acute uric acid nephropathy. Med Clin N Am. 1990;74(4):859–871.

13   Hassell KL, Eckman JR, Lane PA. Acute multiorgan failure syndrome: a potentially catastrophic complication of severe sickle cell pain episodes. Am J Med 1994; 96: 155-62.

14   Tripathi P, Tripathi M. Biochemical assessment of liver in sickle cell disease patients at a tertiary care hospital of north India. Int J Res Med Sci 2016; 4:57-60.

15   Banerjee S, Owen C, Chopra S. Sickle cell Hepatopathy. Hepathology 2001; 33: 1021-28.

16   Pallavi Mehere and Virendra G. Meshram ˝A Promising ray of hope for a cure: Sickle cell anemia" in the memoir book of national conference on biochemistry: An Essence of life sciences organised by university Department of Biochemistry, RTMNU Nagpur on 23rd sept 2017 pp102-107.

17   Mohanty D, Mukherjee M. Sickle cell disease in India. Haematology. 2002;9(2):117–122.

ARTICLE

Structural and optical properties of Eu³⁺ activated Sr₂SiO₄ phosphors prepared by combustion method

Durga Verma,[a] R. P. Patel,[b] Govind B. Nair *[c] and S. J. Dhoble #[c]

[a]*Department of Applied Physics, Faculty of Engineering and Technology, Shri Shankaracharya Group of Institutions, Shri Shankaracharya Technical Campus Bhilai 490020 India*
[b]*Department of Applied Physics, Professional Institute of Engineering and Technology, Raipur - 492001, India*
[c]*Department of Physics, RTM Nagpur University, Nagpur-440033, India*
*Corresponding author : govind1291@yahoo.com
 #Corresponding author : sjdhoble@rediffmail.com

Abstract: Strontium orthosilicate exists in two crystallographic phases viz. α-Sr_2SiO_4 (orthorhombic) and β-Sr_2SiO_4 (monoclinic). A series of Eu^{3+} (0.1-0.4 mol%) activated Sr_2SiO_4 nanophosphors were prepared by low temperature solution combustion method using urea $[CO(NH_2)_2]$ as a fuel. The as-prepared phosphor was characterized by powder X-ray diffraction, FTIR, scanning electron microscopy and EDX. In XRD analysis obtain Sr_2SiO_4 phosphor is orthorhombic structure with space group Pnma. From scanning electron microscopy (SEM), agglomerations of particles were observed due to the high temperature synthesis process. The Fourier transmission infrared spectroscopy (FTIR) confirms the present elements in Sr_2SiO_4:Eu^{3+} phosphor. The photoluminescence spectra of different doping concentration of Eu^{3+} doped Sr_2SiO_4 phosphor excited at 256 nm, showed intense emission in red region. The photoluminescence emission spectra consist of peaks at 575, 593, 613, 651 and 704 nm which can be assigned transition ($^5D_0{\rightarrow}^7F_0$), ($^5D_0{\rightarrow}^7F_1$), ($^5D_0{\rightarrow}^7F_2$), ($^5D_0{\rightarrow}^7F_3$) and ($^5D_0{\rightarrow}^7F_4$) respectively. The CIE diagram shows the coordinates at x = 0.67 and y = 0.32. These coordinates shows the orange-red luminescence from this phosphor

Keywords: Nanophosphor, Combustion Method, FTIR, Scanning Electron Microscopy, photoluminescence.

Introduction

Rare earth (REs) doped inorganic systems have wide range of applications in the field of display devices, lamp phosphors, white light generation, etc. [1–3]. In particular, white LEDs have excellent properties such as low level of power consumption and long life. Moreover, they have an environment benefit in that they do not use mercury in comparison to fluorescent lamps [4,5]. Therefore, the white LEDs are expected to enable new concepts in lighting field. There are basically two approaches to generate white light using LEDs. One is the combination of light of three primary colors (red, green and blue) emitted from different LED chips. Another is to down-convert the emission from a blue or ultraviolet LED to a longer wavelength light by using down-converting phosphors [6,7].

With the development of various scientific techniques for the chemical synthesis, methods like sol–gel, co-precipitation, spray pyrolysis, combustion synthesis techniques evolved to prepare phosphors. Amongst these, the combustion method has been

proved to be a facile route for the low-temperature preparation (without the use of expensive high-temperature furnaces) of various phosphors, including silicates and aluminates in a short time [8–10]. By this method, it is easy to synthesize compound powders of desirable characteristics, including very fine size, narrow size distribution, high purity and high chemical homogeneity.

Strontium orthosilicate exists in two crystallographic phases viz. α-Sr_2SiO_4 (orthorhombic) and β-Sr_2SiO_4 (monoclinic) [3,11,12]. The transition occurs from low temperature β-phase to high temperature α-phase at 385 K, and involves the rearrangement of tetrahedral SiO_4 without change in bonds. The photoluminescence (PL) observed in these materials are attributed to the f-f and f-d transitions of rare-earth ions. Here the intensity depends on the site symmetry and the nature of the host matrix. In this paper, Sr_2SiO_4:Eu^{3+} phosphors prepared by combustion synthesis were investigated and the effect of Eu^{3+} concentration on micro structural as well as luminescent characteristics of Sr_2SiO_4:Eu^{3+} phosphors were reported. The

powders of Sr_2SiO_4:Eu^{3+} were characterized by X-ray diffraction (XRD), FTIR, scanning electron microscopy (SEM), EDX and photoluminescence (PL).

Experimental

Sr_2SiO_4:Eu^{3+} phosphors were synthesized by combustion method. The raw materials were strontium nitrate [$Sr(NO_3)_2$ (99.99%)], silica gel (99.99%)], and europium oxide [Eu_2O_3 (99.99%)]. All of these analytical grade (A.R.) chemicals were employed in this experiment. A small amount of ammonium chloride (NH_4Cl) was used as the flux while the urea [$CO(NH_2)_2$] was used as fuel [13,14]. Initially, the raw materials were weighed according to the nominal compositions of Sr_2SiO_4: Eu^{3+} phosphor. Eu_2O_3 was used as source for activator, and it was converted into nitrate form by dissolving it in concentrated HNO_3 before pouring them to crucible. Then all constituents in the stated proportions, along with the fuel and oxidizers, were mixed together and a small quantity of double-distilled water was added. After thoroughly grinding, the mixture was transferred to a pre-heated furnace at 600^0C. The mixture ignited with a flame to yield a white product. The entire process is over within a few minutes. The powder so obtained was annealed at 700^0C for 2h under an air atmosphere.

X-ray diffraction (XRD) is a popular and powerful technique for determining crystal structure of crystalline materials. So crystal structure and phase formation of the phosphors were examined using an X-ray diffractometer (Philips PANalytical X'pert Pro) operating at 40 kV and 30 mA with Cu-K$_\alpha$ radiation (λ=1.54056 Å). The scanning electron microscopy (ZEISS EVO 18) was used to observe particle morphology of phosphors. Energy dispersive x-ray spectroscopy (EDX) was used for the elemental (quantitative and qualitative) analysis of the prepared phosphor. FTIR spectra were recorded with the help of IR Prestige-21 by SHIMADZU for investigating the functional group region (4000-1400 cm-1) as well as the finger print region (1400-400cm-1) of sintered phosphor in middle infrared region (4000-4000 cm-1) by mixing the sample with potassium bromide (KBr, IR grade. The PL excitation and emission spectra were recorded by Spectrofluorometer (Perkin Elmer LS 45). All experiments were performed in identical conditions and it was observed that the results are reproducible.

Results and Discussion
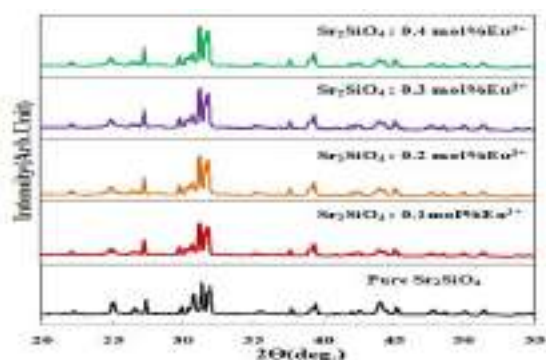
Fig. 1: XRD pattern of different doping concentrations of Eu^{3+} doped Sr_2SiO_4 phosphors.

Fig. 1 shows the XRD spectra of pure Sr_2SiO_4 and different doping concentrations of Eu^{3+} doped Sr_2SiO_4 phosphor. From Fig. 1, it can be seen that all the diffraction peak positions of every sample were same but peak intensities of pure host and doped materials were different. All peak position were indexed to the orthorhombic phase of α-Sr_2SiO_4 (COD card No. 98-003-5667). From the XRD patterns, the structure of this phosphor can be indexed to an orthorhombic system with space group Pnma and their cell parameters a= 7.0800 A^0, b= 5.6720 A^0, and c= 9.7830 A^0.
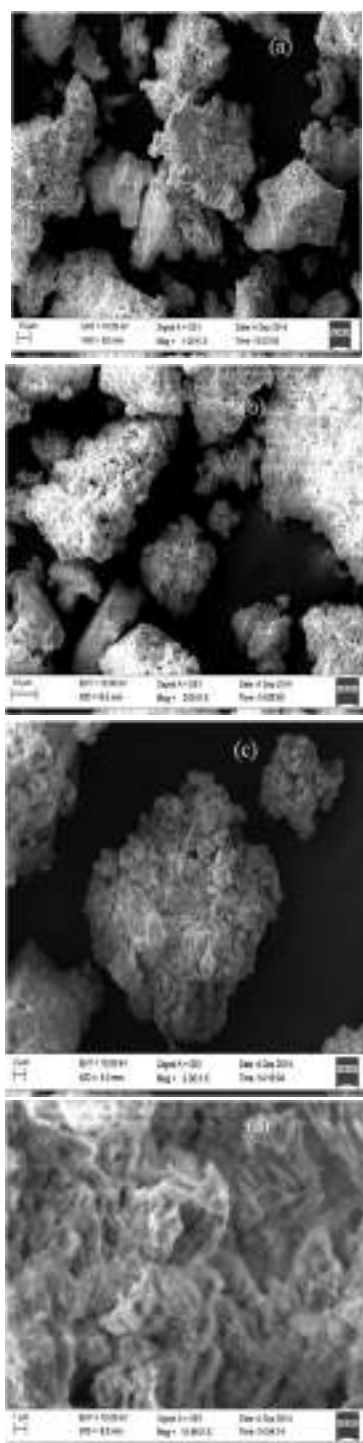
Fig. 2 shows the Fourier transform infrared spectroscopy (FTIR) spectra of Sr_2SiO_4: Eu^{3+} phosphors. FTIR is a technique which is used to identify the presence of certain functional groups in a molecule. The middle infrared region is (4000 to 400 cm^{-1}). In this spectrum observe, Si-O-Si stretching modes for the silicate tetrahedral show infrared absorption bands, located at about 960.62, 912.76, 705.02 and 504.35 cm^{-1}. These Bands correspond to the deformation of the SiO_4 group [15,16]. The wave-number in the region (3572.17 and 3468.01 cm^{-1}) of hydroxyl group shows the stretching vibration of OH group. These bands are due to the double distilled water (H_2O) used for sample preparation.
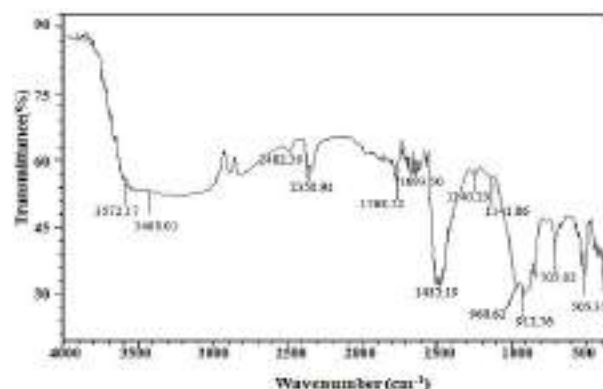
Fig. 2: -FTIR spectra of Sr_2SiO_4:Eu^{3+} phosphor.

The asymmetric stretching vibration of (NO_2^-) nitrites can be observed peaks at 1240.23, 1141.86 cm^{-1}.These bands are due to a slight nitrate of samples preparation [$Sr(NO_3)_2$, HNO_3(raw material)].The band around 1768.72 cm^{-1} was due to C-O stretching vibration and band around 1693.50 cm^{-1} is assigned due to NH_2 deformation vibration. These bands are due to the raw material urea [$CO(NH_2)_2$]. The asymmetric stretching vibration of (N-H) compound can be observed in the range around 2358.94 and 2482.39 cm^{-1}. The bending of a sharp peak in the region of 1485.19 cm^{-1} is assigned due to Sr^{2+} ion. When Eu^{3+} enters the lattice, it will replace the Sr^{2+} in the Sr_2SiO_4 host and occupy Sr^{2+} lattice sites due to distortion in the Sr_2SiO_4 host crystal lattice.

Fig. 3 shows the SEM images of Sr_2SiO_4:Eu^{3+} (0.1mol %) phosphors with different magnifications (x1000, x2000, and x5000, x 10000). The optical properties of phosphor depend on its morphology, such as size, shape, defect etc. It is illustrated in this figure that the particles appear to be non-uniform and they aggregated tightly with each other within several micrometers range. The agglomerated particles, pores and voids were due to gases released during the combustion process [17].

Fig.4:- EDX spectrum of $Sr_2SiO_4:Eu^{3+}$ phosphor.

Table 1: Elemental Composition of $Sr_2SiO_4:Eu^{3+}$ phosphor obtained from EDX.

S.N.	Standard	Element	Atomic (%)	Weight (%)
1	SiO_2	O K	75.84	43.22
2	SiO_2	Si K	9.15	9.16
3	SrF_2	Sr L	14.64	45.69
4	EuF_3	Eu L	0.3	1.92
Total			99.99	99.99

Fig. 5 shows the photoluminescence spectra of different doping concentration (0.1 - 0.4 mol %). The excitation spectra shown in fig 5(a) exhibits spectral range from 200 to 500 nm and shows a broad band at 256 nm which is called charge transfer band (CTB). This broad band is related to Eu-O interactions, which is caused by the electron transfer from filled 2p orbital of O^{2-} ions to vacant 4f orbital of Eu^{3+} ions [18,19]. Other sharp peaks located at 317, 364, 383, 395 and 465 nm, they are assigned electronic transitions of $^7F_0 \rightarrow$ $^5H_6$, $^5D_4$, $^5G_2$, $^7L_6$ and $^5D_2$ respectively, which are attributed to the 4f-4f transition of Eu^{3+} [20,21].

Fig.3: SEM micrograph of Eu^{3+} doped Sr_2SiO_4 phosphor for different magnifications.

From EDX spectra, we measured the chemical composition of the as-prepared phosphor. The energy dispersive X-ray spectrum (EDX) of $Sr_2SiO_4: Eu^{3+}$ phosphor is shown in Fig. 4. There appeared no other emissions apart from strontium (Sr), oxygen (O), silicon (Si) and Europium (Eu) in EDX spectra of $Sr_2SiO_4: Eu^{3+}$ phosphor. Table 1 shows the composition elements of $Sr_2SiO_4: Eu^{3+}$ phosphor, which is compared with the standard element. In the EDX spectrum, the presence of intense peaks corresponding to Sr, O, Si and Eu confirm the presence of these elements in the prepared phosphor.
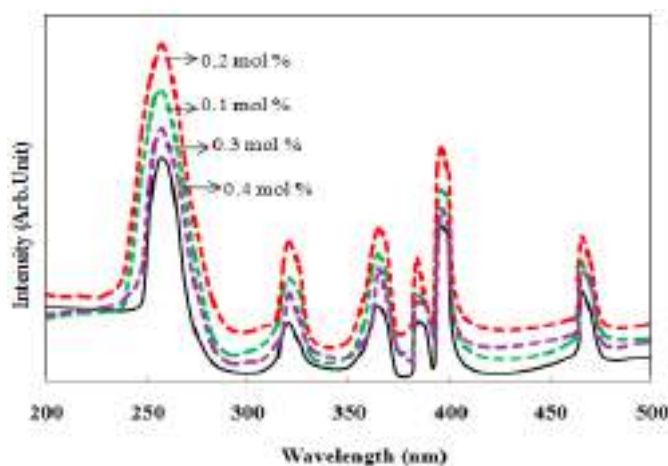

Fig.5 (a) excitation spectra of $Sr_2SiO_4:Eu^{3+}$ phosphors with different Eu^{3+} molar concentrations.

The emission spectra shown in fig.5 (b) would be excited by 256 nm. Here similar nature in both excitation and emission spectra is observed for all the samples; but maximum intensity is found in 0.2 mol % doping concentration. PL peak intensity increases upto 0.2 mol% [fig. 5(b)] and after that, a further increase in doping concentration decreases the PL intensity due to concentration quenching effect. Concentration quenching is due to the energy transfer from one activator to another. The critical transfer distance (R_c) of the activator and quenching site can be estimated with the following equation [22]:

$$R_c = 2\left[\frac{3V}{4\pi x_c N}\right]^{1/3}$$

Where N is the number of host ions in the unit cell, V is the volume of unit cell, and x_c is the critical concentration. The number of host per unit cell in orthorhombic structure Sr_2SiO_4 material is 4 and hence, the value of N is 4. In Sr_2SiO_4, unit cell volume V is 393.71 $(A^o)^3$ and the critical concentration x_c is 0.2mol % . According to the formula, the calculated value of critical transfer distance (R_c) is 45.47 A^o. The value is high and indicating that the nonradiative concentration quenching takes place among two nearest Eu^{3+} via electric multipolar interactions based on the Dexter theory [23,24].
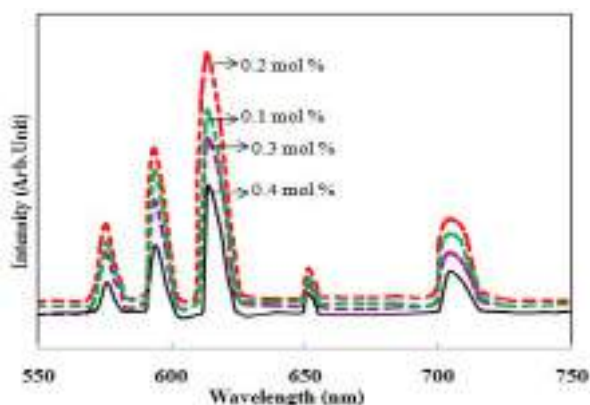

Fig.5 (b) Emission spectrum of Sr_2SiO_4:Eu^{3+} phosphors with different Eu^{3+}.molar concentrations.

The emission spectrum shows five typical peaks in the range of 550-750 nm, which are described by well-known $^5D_0\rightarrow^7F_J$ (J=0, 1,2,3 and 4). Here, the strong emission at 613 nm ($^5D_0\rightarrow^7F_2$) is originated from the electric dipole transition. Other emission bands were observed at 575 nm ($^5D_0\rightarrow^7F_0$), 593 nm ($^5D_0\rightarrow^7F_1$), 651 nm ($^5D_0\rightarrow^7F_3$) and 704 nm ($^5D_0\rightarrow^7F_4$) [20-21] respectively. Taking into account that the 4f electrons of Eu^{3+} ions are the electron in interior electronic shell which is shielded by the outer shell, the wavelength of the emission originating from the $^5D_0\rightarrow^7F_2$ transition can rarely be affected by the crystalline fields. It is well-known that the $^5D_0\rightarrow^7F_1$ transition is magnetic dipole in character and is independent of the crystal fields, unlike the $^5D_0\rightarrow^7F_0$, which is a weak electric dipole transition. The $^5D_0\rightarrow^7F_0$ transition indicates that it is not purely electronic in nature; rather, it may arise due to resonance with phonon.

The CIE chromaticity coordinate calculated using the spectral energy distribution of the Sr_2SiO_4:Eu^{3+} phosphor is shown in fig.6. The coordinated were determined using the emission spectrum of phosphors excited at 256 nm and using the CIE (Commission International de I'Eclairage) 1931 chromaticity diagram. The color coordinates are x = 0.67 and y = 0.32. These coordinates are very near to the orange-red light emission. Hence this phosphor has excellent orange-red light emission.
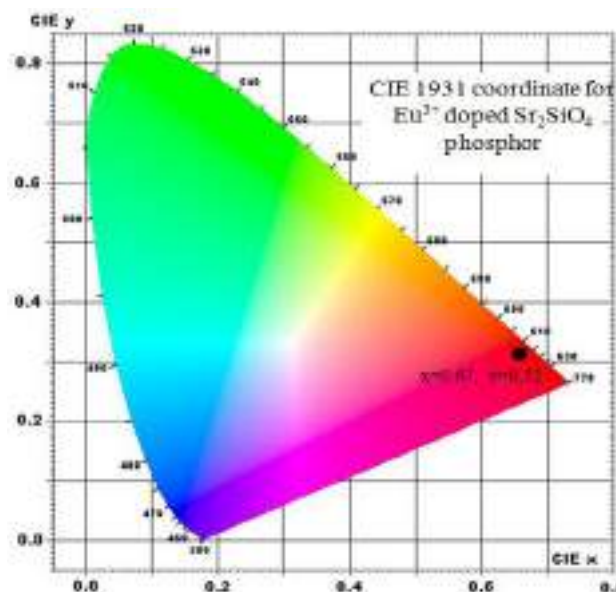
Fig.6 CIE graph of Eu^{3+} doped Sr_2SiO_4 phosphor.

Conclusions

In this work, Sr_2SiO_4:Eu^{3+} phosphors with various concentrations of Eu^{3+} ions were prepared by combustion method. XRD studies confirmed the formation of a single phase compound. SEM studies have been shown the particles appear to be non-uniform and agglomerates composed of circular particles. The EDX and FTIR spectra confirm the presence of Sr, O, Si and Eu elements in Sr_2SiO_4: Eu^{3+} phosphor. In PL spectra, PL intensity increases with Eu^{3+} concentration; it reaches a maximum when the concentration of Eu^{3+} ions is 0.2 mol% and decreases with the further increasing of Eu^{3+} concentration. The phosphor can be excited by 256 nm and consists of the PL peaks at 575, 593, 613, 651 and 704 nm which can be assigned to the transition ($^5D_0\rightarrow^7F_0$), ($^5D_0\rightarrow^7F_1$), ($^5D_0\rightarrow^7F_2$), ($^5D_0\rightarrow^7F_3$) and ($^5D_0\rightarrow^7F_4$) respectively. The CIE coordinates were found to be = 0.67 and y = 0.32. These coordinates show the overall emission color of this to be in orange–red luminescence. Further the excellent properties of this phosphor suggest that it can be used for display applications.

Copyright statement

Author is solely responsible for the plagiarism.

Acknowledgements

References

1. G. B. Nair and S. J. Dhoble, *J. Fluoresc.*, 2017, **27**, 575–585.

2. R. Nayar, S. Tamboli, A. K. Sahu, V. Nayar and S. J. Dhoble, *J. Fluoresc.*, 2017, **27**, 251–261.

3. S. Ray, P. Tadge, G. B. Nair, V. Chopra and S. J. Dhoble, *Ceram. Int.*, 2018, **44**, 5506–5512.

4. Z. Xia and Q. Liu, *Prog. Mater. Sci.*, 2016, **84**, 59–117.

5. S. Pimputkar, J. S. Speck, S. P. DenBaars and S. Nakamura, *Nat. Photonics*, 2009, **3**, 180–182.

6. J. McKittrick and L. E. Shea-Rohwer, *J. Am. Ceram. Soc.*, 2014, **97**, 1327–1352.

7. R. K. Tamrakar, D. P. Bisen, K. Upadhyay and N. Bramhe, *Superlattices Microstruct.*, 2015, **81**, 34–48.

8. V. B. Bhatkar, S. K. Omanwar and S. V. Moharil, *Opt. Mater.*, 2007, **29**, 1066–1070.

9. V. Singh, R. P. S. Chakradhar, I. Ledoux-Rak, L. Badie, F. Pelle and S. Ivanova, *J. Lumin.*, 2009, **129**, 1375–1380.

10. P. J. Yadav, C. P. Joshi and S. V. Moharil, *Int. J. Self-Propagating High-Temperature Synth.*, 2014, **23**, 41–46.

11. H. Feng, Y. Yang, X. Zhang, Y. Xu and J. Guan, *Superlattices Microstruct.*, 2015, **78**, 150–155.

12. C. Guo, Y. Xu, F. Lv and X. Ding, *J. Alloys Compd.*, 2010, **497**, 21–24.

13. G. B. Nair and S. J. Dhoble, *Luminescence*, 2017, **32**, 125–128.

14. P. P. Mokoena, M. Gohain, V. Kumar, B. C. B. Bezuidenhoudt, H. C. Swart and O. M. Ntwaeaborwa, 2014, **595**, 33–38.

15. L. E. Muresan, B. F. Oprea, a. I. Cadis, I. Perhaita and O. Ponta, *J. Alloys Compd.*, 2014, **615**, 795–803.

16. F. J. Caixeta, F. T. Aquino, R. R. Pereira and R. R. Gonçalves, *J. Lumin.*, 2016, **171**, 63–71.

17. G. B. Nair and S. J. Dhoble, *J. Lumin.*, 2017, **192**, 1157–1166.

18. X. Liu, L. Li, H. M. Noh, B. K. Moon, B. C. Choi and J. H. Jeong, *Dalton Trans.*, 2014, **43**, 8814–25.

19. L. Gao, G. Wang, H. Zhu, W. Zhou and G. Ou, *Mater. Res. Bull.*, 2015, **70**, 876–880.

20. M. M. Yawalkar, G. D. Zade, K. V Dabre and S. J. Dhoble, *Luminescence*, 2016, **31**, 1037–1042.

21. Z. Ju, R. Wei, X. Gao, W. Liu and C. Pang, *Opt. Mater.*, 2011, **33**, 909–913.

22. G. Blasse, *J. Solid State Chem.*, 1986, **211**, 207–211.

23. D. L. Dexter and J. H. Schulman, *J. Chem. Phys.*, 1954, **22**, 1063.

24. A. K. Bedyal, V. Kumar, O. M. Ntwaeaborwa and H. C. Swart, *Mater. Res. Express*, 2014, **1**, 1500

ARTICLE

Measure Of Weighted Symmetric Directed Divergence, Weighted Information Improvement, Generalized Measure Of Weighted Information Improvement

Sapna K. Chandbhanani,*a P.A.S. Naidu b

Abstract: In Present Paper We Have Obtained Measure Of Weighted Symmetric Directed Divergence, Weighted Information Improvement, Generalized Measure Of Weighted Information Improvement Corresponding To Kullback Leibler[6], Renyi's[8], And Havrda- Charvat's [4] Measures Of Entropy And Deduce The New Two Parametric Measures Of Measure Of Weighted Symmetric Directed Divergence, Weighted Information Improvement, Generalized Measure Of Weighted Information Improvement

Introduction

The measure of uncertainty introduced by Shannon [9] has tremendous applications in various fields. One of its applications is the problem of efficient coding of messages to be sent over a noiseless channel, that is, our only concern is to maximize the number of messages that can be sent over the channel in a given time. The information measures is of key importance in a number of information theoretical and applied statistical inference and data processing problems. The literature on the development and applications measures has expanded considerably in recent years Om Parkash[7], Taneja [11], Besseville [1], Esteban[2] are good references to review the development of generalized information and divergence measures.

In this paper we have extended the result of measure of weighted symmetric directed divergence, weighted information improvement, generalized measure of weighted information improvement corresponding to Kullback Leibler[6], Renyi's[8], and Havrda- Charvat's [4] measures of entropy and deduce the new two parametric measures of weighted symmetric directed divergence, weighted information improvement, generalized measure of weighted information improvement. This paper is the comparative study of Kapur [5] measure of entropy by introducing new parameters.

In section two we defined some basic properties and definition of measure of weighted symmetric directed divergence, weighted information improvement, generalized measure of weighted information improvement.

In section three we obtained the measure of weighted symmetric directed divergence, weighted information improvement, generalized measure of weighted information improvement corresponding to Kullback Leibler[6], Renyi's[8],

and Havrda- Charvat's [4] measures of entropy and also derive some limiting cases.

In section four we deduce some new two parametric measures of measure of weighted symmetric directed divergence, weighted information improvement and generalized measure of weighted information improvement and also give limiting cases. In section five describe results and some concluding remarks. In section five we give some references of the present paper.

Preliminaries
Properties of Measures of Weighted Directed Divergence and Weighted Symmetric Directed Divergence

Let P= (p₁, p₂,....,pₙ) be non-degenerate probability distribution and W = (w₁,w₂, ..., wₙ) be a set of weights associated with the n outcomes, then corresponding to Shannon's [9] measure of entropy.

$$S(P) = -\sum_{i=1}^{n} p_i \ln p_i \tag{1}$$

Guiasu[3] defined a measure of weighted entropy

$$S(P,W) = -\sum_{i=1}^{n} w_i p_i \ln p_i \tag{2}$$

Naturally $p_i \geq 0, w_i \geq 0$

$$\sum p_i = 1, \sum w_i = 1$$

And characterized it axiomatically. Now Q = $(q_1, q_2, \ldots, q_n)$ is be the another non-degenerate probability distribution then the well know Kullback Leibler [6] gives a measure of directed divergence of P and Q as,

$$D(P,Q) = \sum_{i=1}^{n} p_i \ln \frac{p_i}{q_i} \tag{3}$$

Kapur [5] has defined weighted directed divergence axiomatically measure D(P:Q;W) will be said to be an appropriate measure of weighted directed divergence if
i) It is continuous function of   p₁, p₂, ...,pₙ ; q₁,q₂,....,qₙ; w₁,w₂,...,wₙ.

ii) It is permutationally symmetric i.e. it does not change when the triplets (p_1, q_1, w_1), (p_2, q_2, w_2),......, (p_n, q_n, w_n) are permuted amongst themselves.

iii) It is always greater than zero and vanishes when $p_i = q_i$ $\forall$ i=1,...,n

iv) It is convex function of which has its minimum value zero where $p_i = q_i$ for each I

v) It reduces to positive multiple of an ordinary measure of directed divergence when all the weights are equal.

Taneja and Tuteja [11] gave the following measure of weighted directed divergence corresponding to D (P: Q, W) as

$$D(P:Q,W) = \sum w_i p_i ln \frac{p_i}{q_i} \qquad (4)$$

But very soon Kapur [3] has pointed out that (4) is not a correct weighted directed divergence since it is does not always satisfy (iii).Kapur [5] has suggested following correct measure of weighted directed divergence corresponding to Kullback Leibler [6], Renyi [8] and Havarda charvat's [4]

$$D_1 (P: Q, W) = \sum_{i=1}^{n} w_i \left\{ p_i ln \frac{p_i}{q_i} - p_i + q_i \right\} \qquad (5)$$

$$D_2(P: Q, W) = \frac{\sum w_i q_i}{\alpha(\alpha-1)} ln \left\{ \frac{\sum_{i=1}^{n} w_i (p_i^\alpha q_i^{1-\alpha} - \alpha p_i + \alpha q_i)}{\sum_{i=1}^{n} w_i q_i} \right\}, \alpha \geq 1 \qquad (6)$$

$$D_3 (P: Q.W) = \frac{1}{\alpha(\alpha-1)} \sum_{i=1}^{n} w_i \{ p_i q_i^{1-\alpha} - \alpha p_i + \alpha q_i - \alpha \}, \alpha > 0 \quad (7)$$

It can be easily established that

$$\lim_{\alpha \to 1} D_2(P:Q,W) = D_1(P:Q,W) \qquad (8)$$

$$\lim_{\alpha \to 1} D_3(P:Q,W) = D_1(P:Q,W) \qquad (9)$$

It is well know that

$$D(P:Q) \neq D(Q:P) \qquad (10)$$

a) So naturally, $D(P:Q,W) \neq D(Q:P,W)$ so a weighted symmetric directed divergence has been defined as,

$$J(P:Q,W) = D(P:Q,W) + D(Q:P,W) \qquad (11)$$

$$So \ J(P:Q,W) = J(Q:P,W) \qquad (12)$$

Measure Of Weighted Information Improvement

The measure I (P:Q,R,W) of weighted information improvement in going from Q to R when the true distribution is P and the weight function is W(x) is defined by

$$I(P:Q:R,W) = D(P:Q,W) – D(P:R,W) \qquad (13)$$

This has following properties

(a) when Q = R, I (P: Q:R,W) = 0 $\qquad (14)$

i.e. no improvement intuitionally correct

(b) When Q=P, I (P: Q,R,W) < 0 $\qquad (15)$

i.e. improvement is in negative direction (there cannot be any distribution better than true distribution)

(c)When R=P, I(P:Q:R,W) > 0 $\qquad (16)$

i.e. definitely improvement if we reach to true distribution

Generalized Measure of Weighted Information Improvement

Some times during the course of investigation true distribution P also changes to another distribution S. In this case the generalized measure of weighted information improvement G(P:S/Q/R,W) is defined as

$$G(P:S/Q/R,W) = \frac{1}{2}[I(P:Q:R,W) + I(S:Q:R,W)] \qquad (17)$$

$$Where \ I(P:Q:R,W) = D(P:Q,W) – D(P:R,W) \qquad (18)$$

$$And \ I (S:Q:R,W) = D(S:Q,W) – D(S:R,W) \qquad (19)$$

Where there is no change in true distribution i.e. S=P

$$G(P:P/Q/R,W) = I(P:Q:R,W) \qquad (20)$$

This is again intuitionally correct.

Measure Of Weighted Symmetric Directed Divergence, Weighted Information Improvement, Generalized Measure Of Weighted Information Improvement

Measures Corresponding To Kullback Leibler [6] Measures

$$D_1(P:Q,W) = \sum_{i=1}^{n} w_i \left\{ p_i ln \frac{p}{q_i} - p_i + q_i \right\} \qquad (21)$$

$$D_1 (Q:P,W) = \sum_{i=1}^{n} w_i \left\{ q_i ln \frac{q_i}{p_i} - q_i + p_i \right\} \qquad (22)$$

$$D_1(P:R,W) = \sum_{i=1}^{n} w_i \left\{ p_i ln \frac{p_i}{r_i} - p_i + r_i \right\} \qquad (23)$$

$$D_1 (P:Q,W) \neq D_1(Q:P,W)$$

$$J_1(P:Q,W) = D_1(P:Q,W) + D_1(Q:P,W)$$

$$J_1(P:Q,W) = \sum_{i=1}^{n} w_i \left\{ p_i ln \frac{p_i}{q_i} - p_i + q_i \right\} + \sum_{i=1}^{n} w_i \left\{ q_i ln \frac{q_i}{p_i} - q_i + p_i \right\}$$

$$J_1(P:Q,W) = \sum_{i=1}^{n} w_i \left\{ p_i ln \frac{p_i}{q_i} - p_i + q_i + q_i ln \frac{q_i}{p_i} - q_i + p_i \right\}$$

$$J_1(P:Q,W) = \sum_{i=1}^{n} w_i \left\{ p_i ln \frac{p_i}{q_i} + q_i ln \frac{q_i}{p_i} \right\} \qquad (24)$$

$$J_1(Q:P,W) = D_1(P:Q,W) + D_1(Q:P,W)$$

so $J_1 (P:Q,W) = J_1(Q:P,W)$

∴ (12) is hold

The measure of weighted information improvement corresponding to Kullback Leibler [6], in going from Q to R when the true distribution is P and the weight function is W(x) is defined as

$$I_1(P:Q:R,W) = D_1(P:Q,W) – D_1(P:R,W)$$

$$= \sum_{i=1}^{n} w_i \left\{ p_i ln \frac{p_i}{q_i} + q_i - p_i ln \frac{p_i}{r_i} - r_i \right\} \qquad (25)$$

Similarly we can find

$$I_1(S:Q:R:W) = D_1(S:Q,W) – D_1(S:R,W)$$

$$I_1(S:Q:R:W) = \sum_{i=1}^{n} w_i \left\{ s_i ln \frac{s_i}{q_i} + q_i - s_i ln \frac{s_i}{r_i} - r_i \right\} \qquad (26)$$

$I_1(P:Q:R,W)$ hold the properties (14),(15) and (16)

(I)   if Q=R then $I_1(P:Q:R,W) = 0$

(II)   if Q=P then $I_1(P:Q:R,W) < 0$

(III)   if R=P then $I_1(P:Q:R,W) > 0$

The generalized measure of weighted information improvement $G_1(P:S/Q/R,W)$ is derived as,

$$G_1(P:S/Q/R,W) = \frac{1}{2} [I(P:Q,R,W) + I(S:Q,R,W)]$$

$$G_1(P:S/Q/R,W) = \frac{1}{2} \left\{ \sum_{i=1}^{n} w_i [p_i ln \frac{p_i}{q_i} + 2q_i - p_i ln \frac{p_i}{r_i} - 2r_i + s_i ln \frac{s_i}{q_i} - s_i ln \frac{s_i}{r_i}] \right\} \qquad (27)$$

When   S=P

$$G_1(P:S/Q/R,W) = \sum_{i=1}^{n} w_i \left\{ p_i ln \frac{p_i}{q_i} + q_i - p_i ln \frac{p_i}{r_i} - r_i \right\} \qquad (28)$$

$$G_1(P:/Q/R,W) = I_1(P:Q:R,W) \quad at \ S=P$$

Hence there is no change in true distribution. Hence Kullback Leibler [6] measure of weighted directed divergence verified all

the properties defined in section two therefore it is intuitionally correct.

Measures Corresponding to Renyi's [8] measure

Consider the Kapur [5] suggested following correct weighted directed divergence corresponding to Renyi[8]

$$D_2(P:Q,W) = \frac{\sum_{i=1}^n w_i q_i}{\alpha(1-\alpha)} ln\left\{\frac{\sum_{i=1}^n w_i(p_i^\alpha q_i^{\alpha-1} - \alpha p_i + \alpha q_i)}{\sum_{i=1}^n w_i q_i}\right\}, \alpha \geq 1 \quad (29)$$

$$D_2(Q:P,W) = \sum_{i=1}^n \frac{w_i p_i}{\alpha(1-\alpha)} ln\left\{\frac{\sum_{i=1}^n w_i(q_i^\alpha p_i^{\alpha-1} - \alpha q_i + \alpha p_i)}{\sum_{i=1}^n w_i p_i}\right\} \quad (30)$$

$$D_2(P:R,W) = \sum_{i=1}^n \frac{w_i r_i}{\alpha(1-\alpha)} ln\left\{\sum_{i=1}^n \frac{\sum_{i=1}^n w_i(p_i^\alpha r_i^{\alpha-1} - \alpha p_i + \alpha r_i)}{\sum_{i=1}^n w_i r_i}\right\} \quad (31)$$

$$J_2(P;Q,W) = D_2(P:Q,W) + D_2(Q:P,W)$$

$$J_2(P;Q,W) = \frac{1}{\alpha(\alpha-1)}\left\{\left[\sum_{i=1}^n w_i q_i ln\left(\frac{\sum w_i(p_i^\alpha q_i^{1-\alpha} - \alpha p_i + \alpha q_i)}{\sum w_i q_i}\right)\right] + \left[\sum_{i=1}^n w_i p_i ln(\frac{\sum_{i=1}^n w_i(q_i^\alpha p_i^{1-\alpha} - \alpha q_i + \alpha p_i)}{\sum w_i p_i})\right]\right\} \quad (32)$$

$$J_2(P:Q,W) = J_2(Q:P,W)$$

Now the measure of weighted information improvement I (P:Q:R,W) from Q to R is derived as
$$I_2(P:Q:R,W) = D_2(P:Q,W) - D_2(P:R,W)$$

$$I_2(P:Q:R,W) = \sum_{i=1}^n \frac{w_i q_i}{\alpha(\alpha-1)} ln\left\{\frac{\sum_{i=1}^n w_i(p_i^\alpha q_i^{\alpha-1} - \alpha p_i + \alpha q_i)}{\sum w_i q_i}\right\} - \sum_{i=1}^n \frac{w_i r_i}{\alpha(\alpha-1)} ln\left\{\frac{\sum_{i=1}^n w_i(p_i^\alpha r_i^{\alpha-1} - \alpha p_i + \alpha r_i)}{\sum w_i r_i}\right\} \quad (33)$$

Similarly

$$I_2(S:Q:R,W) = \sum_{i=1}^n \frac{w_i q_i}{\alpha(\alpha-1)} ln\left\{\frac{\sum_{i=1}^n w_i(s_i^\alpha q_i^{\alpha-1} - \alpha s_i + \alpha q_i)}{\sum w_i q_i}\right\} - \sum_{i=1}^n \frac{w_i r_i}{\alpha(\alpha-1)} ln\left\{\frac{\sum w_i(s_i^\alpha r_i^{\alpha-1} - \alpha s_i + \alpha r_i)}{\sum w_i r_i}\right\} \quad (34)$$

$$G_2(P:S/Q/R;W) = \frac{1}{2}\sum_{i=1}^n \frac{w_i q_i}{\alpha(\alpha-1)} ln\left\{\frac{\sum_{i=1}^n w_i[(p_i^\alpha q_i^{\alpha-1} - \alpha p_i + \alpha q_i) - (s_i^\alpha q_i^{\alpha-1} - \alpha s_i + \alpha q_i)]}{\sum w_i q_i}\right\} - \frac{1}{2}\sum_{i=1}^n \frac{w_i r_i}{\alpha(\alpha-1)} ln\left\{\frac{\sum_{i=1}^n w_i[(p_i^\alpha r_i^{\alpha-1} - \alpha p_i + \alpha r_i) + (s_i^\alpha r_i^{\alpha-1} - \alpha s_i + \alpha r_i)]}{\sum w_i r_i}\right\} \quad (35)$$

$$G_2(P:S/Q/R,W) = I_2(P:Q:R,W) \quad \text{at } S=P$$
Hence there is no change in distribution i.e. S=P
As Kullback Leibler [6] measures are limiting case of Renyi[8] measures
when $\alpha \to 1$ and $\alpha \to 0$ in measure (29) approaches to the measure (21)
$\therefore D_2(P:Q,W) = D_1(P:Q,W)$ at $\alpha \to 1$ and $\alpha \to 0$
similarly $J_2(P;Q,W) = J_1(P;Q,W)$ at $\alpha \to 1$ and $\alpha \to 0$,
$I_2(P:Q:R,W) = I_1(P:Q:R,W)$ at $\alpha \to 1$ and $\alpha \to 0$
and $G_2(P:S/Q/R,W) = G_2(P:S/Q/R,W)$ $\alpha \to 1$ and $\alpha \to 0$

The measure of weighted directed divergence corresponding Renyi's[8] verified all the properties of generalized measure of weighted information improvement discussed in section two. Hence it is correct generalized measure of weighted information improvement.

Measures corresponding to Havarda Charvat's [4] Measure

$$D_3(P:Q,W) = \frac{1}{\alpha(\alpha-1)}\sum_{i=1}^n w_i\{(p_i^\alpha q_i^{1-\alpha} - \alpha p_i + \alpha q_i - q_i\}, \alpha > 0 \quad (35)$$

$$D_3(Q:P,W) = \frac{1}{\alpha(\alpha-1)}\sum_{i=1}^n w_i\{q_i^\alpha p_i^{1-\alpha} - \alpha q_i + \alpha p_i - p_i\} \quad (36)$$

$$D_3(P:R,W) = \frac{1}{\alpha(\alpha-1)}\sum_{i=1}^n w_i\{(p_i^\alpha r_i^{1-\alpha} - \alpha p_i + \alpha r_i - r_i\} \quad (37)$$

$$J_3(P:Q,W) = \frac{1}{\alpha(\alpha-1)}\sum_{i=1}^n w_i\{p_i^\alpha q_i^{1-\alpha} + q_i^\alpha p_i^{1-\alpha} - p_i - q_i\} \quad (38)$$

$$I_3(P:Q,R,W) = \frac{1}{\alpha(\alpha-1)}\sum_{i=1}^n w_i\{p_i^\alpha(q_i^{1-\alpha} - r_i^{1-\alpha}) + (\alpha - 1)(q_i - r_i)\} \quad (39)$$

$$G_3(P:S/Q/R,W) = \frac{1}{\alpha(\alpha-1)}\sum_{i=1}^n w_i\left\{\left(\frac{p_i^\alpha + s_i^\alpha}{2}\right)\left(q_i^{1-\alpha} - r_i^{1-\alpha}\right) + (\alpha-1)(q_i - r_i)\right\} \quad (40)$$

As Kullback Leibler [6] measures are limiting case of Havarda Charvat's [4]
when $\alpha \to 1$ and $\alpha \to 0$ in measure (35) approaches to the measure (21)
$\therefore D_3(P:Q,W) = D_1(P:Q,W)$ at $\alpha \to 1$ and $\alpha \to 0$
similarly $J_3(P;Q,W) = J_1(P;Q,W)$ at $\alpha \to 1$ and $\alpha \to 0$,
$I_3(P:Q:R,W) = I_1(P:Q:R,W)$ at $\alpha \to 1$ and $\alpha \to 0$
and $G_3(P:S/Q/R,W) = G_1(P:S/Q/R,W)$ $\alpha \to 1$ and $\alpha \to 0$

The measure of weighted directed divergence corresponding Havarda Charvat's [4] verified all the properties of generalized measure of weighted information improvement discussed in section two. Hence it is correct generalized measure of weighted information improvement.

New Two Parametric Measures

Two Parametric Measures Of Weighted Symmetric Directed Divergence, Measure Of Weighted Symmetric Directed Divergence, Weighted Information Improvement, Generalized Measure Of Weighted Information Improvement

Consider the two parametric measure of weighted of directed divergence which is already deduce in previous paper

$$D_4(P:Q:W) = \sum_{i=1}^n w_i \, p_i \, ln \left(\frac{p_i}{q_i}\right) + \sum_{i=1}^n w_i \, (p_i - q_i) \, ln \left(1+\frac{b}{a}\right) + \frac{a}{b}\left(1+\frac{b}{a}\right) ln \left(1+\frac{b}{a}\right)\sum_{i=1}^n w_i \, q_i - \frac{a}{b}\sum w_i \, (q_i + \frac{b}{a}p_i)ln(1+\frac{b}{a}\frac{p_i}{q_i}), b \geq -1, a>0 \quad (50)$$

above deduced measure of weighted directed divergence (50) is continuous function, it is permutationally symmetric, it is always greater than zero and vanishes when $p_i = q_i$ $\forall i=1,...,n$. It is a twice differentiable convex function of which has its minimum value zero where $p_i = q_i$ for each i

It reduces to positive multiple of an ordinary measure of directed divergence when all the weights are equal

$$D_4(P:R,W) = \sum_{i=1}^n w_i \, p_i \, ln \left(\frac{p_i}{r_i}\right) + \sum_{i=1}^n w_i \, (p_i - r_i) \, ln \left(1+\frac{b}{a}\right) + \frac{a}{b}\left(1+\frac{b}{a}\right) ln \left(1+\frac{b}{a}\right)\sum_{i=1}^n w_i \, r_i - \frac{a}{b}\sum w_i \, (r_i + \frac{b}{a}p_i)ln(1+\frac{b}{a}\frac{p_i}{r_i}), b \geq -1, a>0 \quad (51)$$

$$D_4(Q:P,W) = \sum_{i=1}^n w_i \, q_i \, ln \left(\frac{q_i}{p_i}\right) + \sum_{i=1}^n w_i \, (q_i - p_i) \, ln \left(1+\frac{b}{a}\right) + \frac{a}{b}\left(1+\frac{b}{a}\right) ln \left(1+\frac{b}{a}\right)\sum_{i=1}^n w_i \, p_i - \frac{a}{b}\sum w_i \, (p_i + \frac{b}{a}q_i)ln(1+\frac{b}{a}\frac{q_i}{p_i}), b \geq -1, a>0 \quad (52)$$

$J_4(P:Q,W) = D_4(P:Q,W) + D_4(Q:P,W)$

$J_4(P:Q,W) = \sum_{i=1}^{n} w_i \{p_i[\ln(\frac{p_i}{q_i}) + \ln(\frac{p_i}{r_i})] + \ln(1+\frac{b}{a})[2p_i - q_i - r_i] + \frac{a}{b}(1+\frac{b}{a})\ln(1+\frac{b}{a})(q_i - r_i) - \frac{a}{b}(q_i + \frac{b}{a}p_i)\ln(1+\frac{b}{a}\frac{p_i}{q_i}) - \frac{a}{b}\sum w_i(r_i + \frac{b}{a}p_i)\ln(1+\frac{b}{a}\frac{p_i}{r_i})$
(53)

$I_4(P:Q:R,W) = D_4(P:Q,W) - D_4(P:R,W)$

$I_4(P:Q:R,W) = \sum_{i=1}^{n} w_i \{p_i \ln(\frac{r_i}{q_i}) + (r_i - q_i)\ln(1+\frac{b}{a}) + \frac{a}{b}(1+\frac{b}{a})\ln(1+\frac{b}{a})(q_i - r_i) - \frac{a}{b}(q_i + \frac{b}{a}p_i)\ln(1+\frac{b}{a}\frac{p_i}{q_i}) + \frac{a}{b}(r_i + \frac{b}{a}p_i)\ln(1+\frac{b}{a}\frac{p_i}{r_i})\}$, $b \geq -1$, $a>0$
(54)

$I_4(S:Q:R,W) = \sum_{i=1}^{n} w_i \{s_i \ln(\frac{r_i}{q_i}) + (r_i - q_i)\ln(1+\frac{b}{a}) + \frac{a}{b}(1+\frac{b}{a})\ln(1+\frac{b}{a})(q_i - r_i) - \frac{a}{b}(q_i + \frac{b}{a}s_i)\ln(1+\frac{b}{a}\frac{s_i}{q_i}) + \frac{a}{b}(r_i + \frac{b}{a}s_i)\ln(1+\frac{b}{a}\frac{s_i}{r_i})\}$, $b \geq -1$, $a>0$
(55)

$G_4(P:S/Q/R,W) = \frac{1}{2}\sum_{i=1}^{n} w_i \{(p_i+s_i)\ln(\frac{r_i}{q_i}) + 2(r_i - q_i)\ln(1+\frac{b}{a}) + 2\frac{a}{b}(1+\frac{b}{a})\ln(1+\frac{b}{a})(q_i - r_i) - \frac{a}{b}(q_i + \frac{b}{a}p_i)\ln(1+\frac{b}{a}\frac{p_i}{q_i}) + \frac{a}{b}(r_i + \frac{b}{a}p_i)\ln(1+\frac{b}{a}\frac{p_i}{r_i}) - \frac{a}{b}(q_i + \frac{b}{a}s_i)\ln(1+\frac{b}{a}\frac{s_i}{q_i}) + \frac{a}{b}(r_i + \frac{b}{a}s_i)\ln(1+\frac{b}{a}\frac{s_i}{r_i})\}$
(56)

As Kullback Leibler [6] measures are limiting case of the deduced new two parametric measure of weighted directed divergence**,** measure of weighted symmetric directed divergence, weighted information improvement, generalized measure of weighted information improvement

As b→0 and a = 1 in (50) it approaches (21)
$D_4(P:Q,W) = D_1(P:Q,W)$ at b→0 and a=1
similarly, $J_4(P;Q,W) = J_1(P;Q,W)$ at b→0 and a=1
$I_4(P:Q:R,W) = I_1(P:Q:R,W)$ at b→0 and a=1
and $G_4(P:S/Q/R,W) = G_1(P:S/Q/R,W)$ b→0 and a=1

The deduced new two parametric measure of weighted directed divergence is satisfies all the properties of generalized measure of weighted information improvement discussed in section two. Hence it is correct generalized measure of weighted information improvement.

Conclusion

In the present paper we extend the result of measure of weighted symmetric directed divergence, weighted information improvement, generalized measure of weighted information improvement for two variables the discussion is only for random variables which has finite set of discrete values, it can be easily extend when the number of values taken is infinite or the variate is continues, it can be extended for multivariate distribution.

The weighted directed divergence

$D(P:Q:W) = \sum_{i=1}^{n} w_i p_i \ln(\frac{p_i}{q_i}) + \sum_{i=1}^{n} w_i (p_i - q_i)\ln(1+\frac{b}{a}) + \frac{a}{b}(1+\frac{b}{a})\ln(1+\frac{b}{a})\sum_{i=1}^{n} w_i q_i - \frac{a}{b}\sum w_i(q_i + \frac{b}{a}p_i)\ln(1+\frac{b}{a}\frac{p_i}{q_i})$, $b \geq -1$, $a>0$

are the generalization of Kapur's[5] measure of weighted directed divergence .

Copyright statement

Acknowledgements

References

1 Basseville, M. Divergence Measures for Statistical Data Processing. Publications Internes de l'IRISA, November 2010http://www.mtm.ufsc.br/□taneja/book/book.htm

2 Esteban, M. D., D. M o r a l e s. A Summary on Entropy Statistic. – Kybernetika, Vol. 31, 1995, No 4, 337-346.

3 Guiasu, S. (1971) : "Weighted Entropy", Reports on Math, Physics Vol. 2, pp. 165-179

4 Havarda. J. H. and Charvat F. (1967) : "Quantification Methods of Classification Process : Concept of structural α-Entropy" Kybernetica Vol. 3, pp. 30-55.

5 Kapur J. N. (1994) : "Measure of Information's and their applications"New Age International Ltd., New delhi

6 Kullback S. and Leibler R. A. (1951) : "On Information and Sufficiency" Ann Math Stat. Vol. 22, pp. 79-86

7 Prakash O., Varma S.K. and Trivedi H.R. (2004): On Information Radius on Kapur's Entropy and Its Generalization, Mathematics and Information Theory: Recent topics and applications V.K. Kapoor (Ed), Anamaya Publishers, New Delhi, 160-163.

8 Renyi A. (1961) : "On Measures of entropy and Information" Proc-4th Berkeley Symp. Math Stat. prob. Vol. 1, pp. 547-561

9 Shannon C. E. (1948) : " A Mathematical Theory of Communication" Bell System, Tech. J. Vol. 27, pp. 379-423, 623-659

10 Taneja H. C. and Tuteja R. K. (1984) : "Characterization of Qualitative measure of relative information" Information Sciences, Vol. 33, pp. 1-6

11 Taneja,I.J. Generalized Information Measures and their Applications. – On-Line Book, 2001.

ARTICLE

Thermoluminescence study of cerium activated $Li_6Y(BO_3)_3$ phosphor for C^{6+} ion beam irradiation

Akhilesh Ugale[1], N. Thejo Kalyani[2*] and S.J. Dhoble[3]

Mrunal M. Yawalkar[1*], G.D. Zade[2], S.J. Dhoble [1]

[1] Department of Physics, R.T.M. Nagpur University, Nagpur 440033, India

[2] Department of Physics, J. N. Arts, Commerce & Science College, Wadi, Nagpur- 23, India

*Corresponding author: e-mail: sjdhoble@gmail.com

Abstract: Here, we report the thermoluminescence (TL) behavior of cerium activated $Li_6Y(BO_3)_3$ phosphor, irradiated by carbon(C^{6+}) ion beam of 75MeV energy. The series of phosphor prepared by combustion synthesis at 500°C with cerium concentrations in the range of 0.5 to 5 mol % is characterized by scanning electron microscope (SEM) and TL. The TL glow curves of this phosphor obtained on exposure to carbon ion beam indicate simple nature, with a prominent peak at 132°C and a miniature at 264°C for the fluence of 5×10^{10} ions/cm². The phosphor was subjected to different fluences from 2×10^{10} to 1×10^{12} ions/cm². The fluence of 1×10^{11} ions/cm² produces maximum TL intensity in the phosphor. A variation of 1-4°C was witnessed in peak temperature with the change in fluence. The kinetic parameters - shape factor (μ), activation energy (E), and frequency factor (s) for the prominent glow peak of the prepared phosphor were evaluated using Chen's peak shape formula

Keywords: Sm(TTA)₃dpphen, β-diketonate, Photoluminescence, OLEDs, Solid State lighting.

Introduction

Carbon ion radiotherapy is gaining world-wide attention and acceptance in the field of radiation oncology. It possesses physical and biological advantages greater than that of protons, X-rays or photon therapy. Clinical experiences emphasize that carbon ions produce maximum biological effectiveness in regions of head, skull base, neck, lung, liver etc and various types of sarcomas due to the physical dose deposition in the target. Spread out Bragg peak (SOBP), linear energy transfer (LET) ensures irreparable damage to the DNA of cancerous cell without adverse effect on the surrounding tissue with reduced treatment time than photon irradiation [1,2].

Single crystals of cerium doped $Li_6Y(BO_3)_3$ have proved to be promising neutron scintillator as they possess large cross section for thermal neutrons. Also, lower Z effective imparts them insensitivity to gamma- rays which proves helpful in mixed field radiations. Singh *et. al. and* Fu *et. al.* have successfully studied these crystals for thermal neutron detection[3-5].

However, no study on carbon ion irradiation has been found. Here we present the thermoluminescence study of $Li_6Y(BO_3)_3$:Ce^{3+} phosphor on carbon (C^{6+})ion irradiation.

Experimental

Synthesis

$LiNO_3$, $Y(NO_3)_3$, H_3BO_3 and NH_2CONH_2 , pure reagents all of analytical grades were used as the starting materials to prepare $Li_6Y(BO_3)_3$: Ce^{3+} phosphor. H_3BO_3 served as the flux and urea NH_2CONH_2 as the fuel, needed for combustion. $CeNO_3$ was used for doping Ce^{3+} into the host lattice. A homogenous paste of these reagents taken in stoichiometric proportion was formed by mixing and crushing using mortar pestle. This paste was removed in china dish. Metal nitrates betrothed as oxidizer and urea employed as a reducer helped to realize the combustion synthesis of oxides. The quantity of the oxidizers and fuel to be consumed were decided using their total oxidizing and reducing valencies, to produce heat for combustion. The precursor was placed in a preheated vertical furnace maintained at 500°C . The mixture boiled and released combustible gases which generated a flame on ignition and could bring about froth formation of the desired product. The phosphor was ready in less than 10 minutes. Hence, combustion synthesis serves as a fast and easy synthesis method for phosphor generation. Being an exothermic reaction it helps to attain high temperatures easily which facilitates phosphor formation with the evolution of light and heat. The phosphor was

crushed using mortar pestle into fine powder and was then used for subsequent characterizations.

For carbon irradiation, pellets were prepared of the phosphor powder. 5 tons of pressure was imparted onto 150 mg of phosphor powder using hydraulic press with the help of die of 1cm diameter. A beam of C^{6+} ions beam of 75 MeV energy with current of 0.5 pnA was generated using a 16 MV tandem van de Graff type Electrostatic Accelerator (15 UD Pelletron) at the Inter-University Accelerator Center (IUAC), New Delhi, India. Kanjilal *et al.* have discussed the accelerator in detail [6]. The ion beam was magnetically scanned over an area of 10 mm × 10 mm of the sample surface. A batch of pellets with different concentrations of Ce ions, was exposed to a fluence of 5 x 10^{10} ions/cm². The concentration giving the maximum TL intensity (Ce 0.5mol%) was then exposed to different fluences between $2 \times 10^{10} - 1 \times 10^{12}$ ion cm².

Characterization

Phase purity of the phosphor sample was confirmed using PAN-alytical, X'Pert Pro, X-ray Diffractometer. Nickel filtered   Cu Kα radiation (λ=1.5406 A°) generated at 45 kV and 40 mA was used in the 2θ range of 10° to 100° with a scan step size of 0.01° and time per step of 20 sec respectively. The morphology of the phosphor was investigated by SEM-JEOL make, 6380A scanning electron microscope. TL emission spectra were recorded using a Harshaw TLD reader (Model 3500) at IUAC, New Delhi. The measurements were carried out in an open atmosphere at a linear heating rate of 5°C /s.

Results and Discussion

SEM Analysis
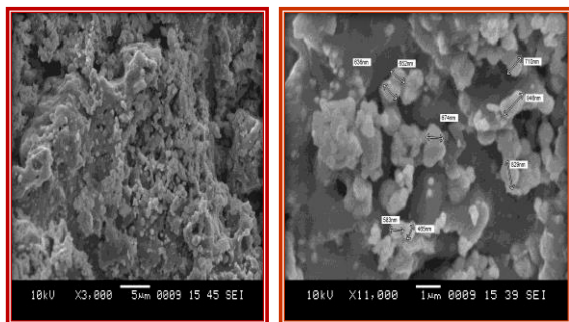
Figure 1: SEM graphs of $Li_6Y(BO_3)_3:Ce^{3+}$ phosphor viewed

at different magnifications.

The surface morphology of the phosphor was studied by JEOL-JSM6380A scanning electron microscope at different magnifications.. The SEM images of $Li_6Y(BO_3)_3:Ce^{3+}$ phosphor as seen in Figure 1 indicate the grains with partly distorted polyhedral structure. The high resolution images of the phosphor surface show grains with average diameter between 0.4 to 1μm and also clusters that may be formed due to synthesis conditions.

## Analysis of TL glow curve of carbon (C^{6+}) ion irradiated $Li_6Y(BO_3)_3:Ce^{3+}$ phosphor

The TL glow curves of C^{6+} ion beam irradiated $Li_6Y(BO_3)_3:Ce^{3+}$ phosphor studied for the fluence of 5 x 10^{10} ions/cm² are presented in Figure 2. The glow curve clearly indicates simple nature with a prominent peak at 132°C and a miniature at 264°C. The variation of TL glow peak intensity as a function of Ce concentration was also studied. Glow curve structure remains the same with change in TL intensity. The TL intensity saturates too early, is highest for lowest Ce^{3+} concentration of 0.5 mole % and decreases for all higher concentrations due to saturation of traps. This effect termed as concentration quenching of TL was first reported by Medlin in calcite [7].

The effect of activator seen in the form of difference in intensity of the TL peaks may be caused due to variation in the number of trapping or luminescent centers or defects generated by the activator.
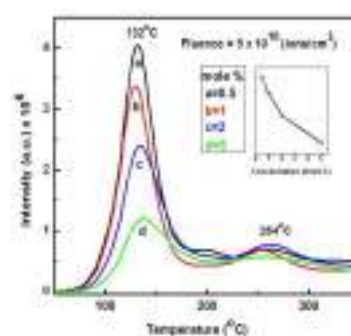
Figure 2: TL glow curves of C^{6+} irradiated $Li_6Y(BO_3)_3:Ce^{3+}$ phosphor for different Ce^{3+} concentration for fluence of 5 x 10^{10} ions/cm²

To further investigate the effect of fluence on the TL response, the phosphor was subjected to different fluence from 2 x 10^{10} to 1 x 10^{12} ions/cm². The result is presented in Figure 3. The shape of the TL glow curve remains the same even with change in fluence, however, an appreciable change is noted in the TL intensity. A variation in peak temperature of 1-4°C was witnessed with changing fluence which may be due to change in trapping and recombination process. The fluence of 1 x 10^{11} ions/cm² produced maximum TL intensity in the phosphor from the 75MeV carbon ion beam.
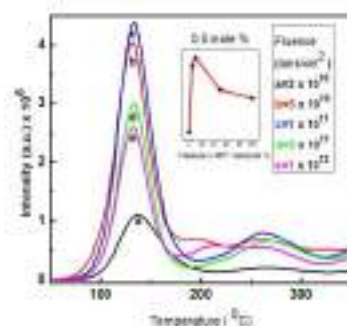
Figure 3: TL glow curves of $Li_6Y(BO_3)_3:Ce^{3+}$ phosphor for different fluence of C^{6+} beam

The TL glow curve for 0.5 mole % of Ce concentration with highest intensity was studied further using Chen's peak shape method. The low temperature peak at 132°C follows general order kinetic as predicted from the value of μ whereas the high temperature peak at 264 °C obeys the second order kinetics. Kinetic parameters for this glow curve are derived are given in Table 1.

Table 1: Kinetic parameters of $Li_6Y(BO_3)_3:Ce^{3+}$ phosphor

Peaks	Kinetic Parameters					
	T_M (^oC)	I_M	M	E (eV)	B	s (s^{-1})
Peak1	132	4.38×10^6	0.51	1.26	1.9	1.98×10^{15}
Peak2	264	8.08×10^5	0.52	1.41	2	5.12×10^{12}

Conclusion

The present, $Li_6Y(BO_3)_3:Ce^{3+}$ phosphor studied for heavy particle carbon beam irradiation withstand the high energy from 75MeV carbon beam for different fluences. Difference in intensity of the dominant peaks in two phosphors may be due to variation in the number of trapping or luminescent centers or defects generated by the activator. Low temperature peak at 132 °C dominate the TL response. The high temperature peak observed at 264 °C does not easily fade off and is thus needed for radiation dosimetry so that it can retain the absorbed signal for considerable time. Efforts need to be carried out to increase the intensity of this TL peak in the present phosphor to be useful for application in radiation and health dosimetry.

Acknowledgment

References

[1] A.D. Bhatt. Carbon Ions-A New Horizon in Radiation Oncology. *J Nucl Med Radiat Ther* , 2013,**4**,154..

[2] H. Tsuji, T. Kamada, M.i Baba, H.i Tsuji, H.i Kato,S. Kato, S. Yamada, S.Yasuda, T. Yanagi, H. Kato.Clinical advantages of carbon-ion radiotherapy, *New Journal of Physics*, 2008,**10**, 075009.

[3] A.K. Singh, M. Tyagi, S.G. Singh, D.G. Desai, B. Tiwari, S. Sen, S.C. Gadkari and S.K. Gupta.Development of Ce doped Li6Y(BO3)3 crystal based portable solid state detectors for thermal neutrons, *BARC Newsletter, Technology Development Article*, 2015;20-24.

[4] Z. Fu, S.Pan, F. Yang, S.Gu, X.Lei,Y. Heng,G. Ren, M. Qi. Neutron detection properties of Li6Y(BO3)3:Ce crystal. *Radiation Measurements* 2015,**72** ,39-43.

[5] A.K. Singh, M.Tyagi, S.G.Singh, B.Tiwari, D.G.Desai, S.Sen, S.S.Desai, S.S Ghodke, S.C.Gadkari. Performance characteristics of thermal neutron detectors based on Li6Y(BO3)3:Ce single crystals. *Nuclear Inst. and Methods in Physics Research, A*, 2015, 804, 189-193.

[6] D. Kanjilal,S. Chopra ,M.M. Narayanan,I.S. Iyer,V. Jha,R. Joshi,S.K. Datta.Testing and operation of the 15UD Pelleton at NSC*, Nucl. Instr. Methods Phys. A*, 1993 **328**;:97-100.

[7] R. Chen, J.L. Lawless and V. Pagonis.A model for explaining the concentration quenching of thermoluminescence, *Radiation Measurements* 2011, **46**,1380-1384,.

ARTICLE

A Comparative Analysis of L-Nicotine Content in Various Tobacco Samples

Amit Taksande[a] , Archana Moon [b] and Drishti Singh [c]

[a, b, c] University Department of Biochemistry, Rashtrasant Tukadoji Maharaj Nagpur University, Nagpur
[c]Corresponding Author: moon.archana@gmail.com)

Abstract: Nicotine was extracted from tobacco and areca nuts samples using different solvents. The estimation of nicotine was carried out by a colorimetric method. The method is based on the following principle: Nicotine reacts with bromine water to form dibromonicotine which then reacts with potassium iodide to liberate iodine. The liberated iodine oxidizes leuco crystal violet to form crystal violet dye. This crystal violet dye shows maximum absorbance at 592nm. This method was applied for the determination of nicotine in tobacco leaves, areca nuts and cigarettes

Keywords: Nicotine, Tobacco leaves, Areca nuts, cigarettes

Introduction:

Tobacco use is a major public health problem worldwide and the numbers of smoking-related deaths are second only to malaria [1]. Nearly one third of adults are smokers and majority started the habit as adolescents. Sadly the number of smokers continues to increase in developing nations, where availability and marketing of tobacco products (cigarettes, bidi, gums, processed leaves, etc.) has increased faster than the public health education. These statistics highlight the fact that tobacco is a strong motivator of a very unhealthy behavior [2]. Nicotine is a parasympathomimetic alkaloid found in the nightshade family of plants *Solanacae* and is a stimulant drug [3]. In its pure form it is a rapid acting, extremely toxic drug [5]. The action of nicotine is very complicated. It is a mild stimulant which has an effect upon the heart and brain. It stimulates the central nervous system causing irregular heartbeat and blood pressure. People who smoke or chew tobacco are known to have such problems and if taken for long time nicotine also leads to lung and mouth cancers [1]. Tobacco is primarily derived from the species *Nicotiana tabacum,* although it is produced from other species. Once tobacco has been grown, harvested, cured and processed, it is used to produce a number of different products like cigarette, spittoons, snus, cigars, gutka and bidis. Nicotine has also been detected in potatoes, eggplants and sweet peppers [4].

Nicotine, one of the highly toxic tobacco alkaloid present in tobacco leaves and cigarette smoke appear to be a promising tracer for environmental tobacco smoke (ETS) because of its specificity for tobacco. The threshold limit value reported for nicotine is 0.05mg/m^3 [8]. The most important symptoms of exposure to nicotine are bronchitis, emphysema, Cyanosis, and exenation of the central nervous system. Excessive smoking has been implicated in lung cancer, bladder cancer and cancer of larynx and oesophagus [9]. Cigarette contains 8-20 mg of nicotine (depending on the brand) but only approximately 1 mg actually absorbed in the human body [4].

Materials and Methods:

1. **Sample collection and processing:** Six different tobacco leaves, three types of areca nuts and five different brands of cigarettes were procured from local market. Also saliva sample of people who chew tobacco were collected. The leaves were shade dried. The completely dried leaves were macerated in a mechanical grinder to yield a fine powder. The powder (50g) was extracted in a Soxhlet apparatus using solvents of increasing polarity i.e. 300ml of each Petroleum ether, chloroform, acetone, methanol and water. For study of enzymatic and antibacterial activity 20g of the sample was extracted by cold maceration method using 100ml of methanol. The extract was completely dried and stored until further use.

2. **Phytochemical study:**

2.1 **Qualitative study:** Hot soxhlet and cold extract of tobacco and areca nuts samples were used for qualitative estimation of phytochemicals like alkaloids, tannins, phenols, proteins and sugars [10].

2.2 **Quantitative study:**

a. **Determination of phenols:** Total phenolic contents were determined by the Folin-Ciocalteu method. $1000\mu g$ extract + 1mL Folin-Ciocalteu reagent + shake + wait for 3 min + 3mL 2% Na2CO3 + keep for 2 hr. Read absorbance at 760 nm. Gallic acid was used as standard (1-10μg). The

total phenolic contents were expressed as mg of Gallic acid equivalents (GAE)/g of plant material [11].

b. Determination of alkaloids: 5g sample + 200 ml 10% acetic acid in ethanol + cover it and incubate for 4hr + filter. Take this extract + keep on boiling water bath to remain one fourth original volume + drop wise ammonium hydroxide until complete precipitation + allow the solution to settle + collect precipitate + wash with dilute NH4OH + filter. Take residue, dry it and weigh [12].

c. Determination of tannin: 50µL extract + make up to 7.5mL with water + 0.5mL Folin-Denis reagent + 1mL Na_2CO_3 + make up to 10mL with water. Read at 700nm [13].

3. Estimation of Nicotine: To 10µl of extract in a test tube 3ml if bromine water was added and the mixture was shaken gently for ~2mins. Excess of bromine was removed by adding formic acid drop wise after which 2ml of potassium iodide and 1ml Leuco crystal violet was added and the mixture was shaken for few minutes. 1ml of 2M NaOH was added slowly. After incubation at 37°C for 25 mins absorbance was measured at 580nm. A standard graph was obtained by carrying out the above procedure with pure Nicotine [8].

4. Thin Layer Chromatography: Slurry of Silica Gel G (2g) + POP (0.5g) was prepared in 5ml distilled water and poured over a glass plate to form a thin layer. These prepared plates were air dried and activated at 100-120°C for 20mins. The extract (10µl) was spotted over an activated plate 1cm above from the bottom. The spotted plates were kept in a chamber containing mobile phase (toluene: acetone: ethanol: ammonia) and allowed to run 3/4th of the height of the plate. Spraying reagent (Dragendorff's Reagent) was used to detect the spot on the plate [14].

Table 1: Mobile phase and spraying reagent for phytochemical:

Phytochemical	Mobile phase	Spraying agent	Color developed after spraying	Reference No.
Alkaloid (Nicotine)	Toluene : acetone : ethanol : ammonia (40:40:6:2)	Dragendorff's reagent	Orange	14

5. High Performance Liquid Chromatography: High performance liquid chromatography of nicotine was carried out by LC COLUMN: Reverse phase method by using methanol as a solvent.

6. Antibacterial activity of tobacco samples: Preparation of discs: The Whatmann filter 1 was cut into 6mm diameter circle. Plant extract (10mg,20mg, 40mg, 60mg and 100mg) obtained by cold extraction was put onto discs

and air dried. The completely dried discs were used for antibacterial assay by Bauer- Kirby method [15].

7. Antioxidant activity assay: Antioxidant activity was determined by reducing power assay: 100µl plant extract + 2ml distilled water + 2.5 ml sodium phosphate buffer + 2.5ml potassium ferricyanide. Incubate the mixture at 50°C for 30mins. Add 2.5ml 10% TCA and centrifuge at 3000 rpm for 10mins. To 2.5ml of supernatant add 1.5 ml distilled water + 0.5ml Ferric chloride. Read at 700nm.

8. Enzyme activity assay:

a) Peroxidase assay: The peroxidase activity was carried out by Pyragallol method [16].

b) Phenol oxidase assay: Phenol oxidase activity was determined by catechol oxidase method [17].

9. Nitrosamine estimation: In 250ml beaker 24ml 0.4N HCl + 2g Zinc acetate were added. To which 1ml of saliva sample was added and the solution was mixed on a shaker for 1 hour. After filtration through Whatmann filter 1, pH was adjusted to 2.0 using NaOH and the volume was made up to 100ml. the solution was heated and evaporated at 90-95°C until 3-5ml remained. The contents were cooled to room temperature and 5ml Ehrlich's reagent was added. After 10mins, the volume of reaction mixture was made up to 10ml with distilled water and the absorption was measured at 458nm [18].

Results and Discussion:

Qualitative study: The phytochemical screening of the tobacco and areca nut samples were carried out. The data in the table 2 shows that nicotine concentration was found to be highest in soxhlet extracts of the samples, which means that nicotine is not heat labile, and can be efficiently extracted by using Soxhlet apparatus. The highest concentration of nicotine was found in Fresh tobacco leaves; hence it can mean that processing of tobacco has an effect on nicotine concentration.

Table 2: Yield of Nicotine in mg/g of plant

Plants	Soxhlet extract	Cold extract
Fresh leaves	71.37	70.17
Dried leaves	40.64	38.17
A	49.21	38.17
B	32.37	26.75
C	24.21	17.89
D	27.42	23.51
Areca nuts I	70.17	67.51
Areca nuts II	53.35	38.87
Areca nuts III	47.8	35.25

The table 3 showed that estimation of nicotine in different cigarette brand, Marlboro has the highest nicotine concentration.

Table 3: Concentration of Nicotine in Cigarettes

| Brands	Conc. (mg/g)
Navy Cut	123.2
Gold Flake	119.1
Bristol	93.6
K-10's	106.4
Marlboro	140.4

Thin Layer Chromatography and High Performance Liquid Chromatography: Nicotine in the samples was also analyzed by TLC (Figure 1) and HPLC methods. The Rƒ value of nicotine by TLC was found to be 0.48 (Table 4) and its retention time by HPLC was found to be 3.01 (Figure 2) respectively.

Table 4: Thin layer Chromatography Rƒ value of nicotine

PHYTOCHEMICAL	Rƒ Value
Nicotine	**0.48**
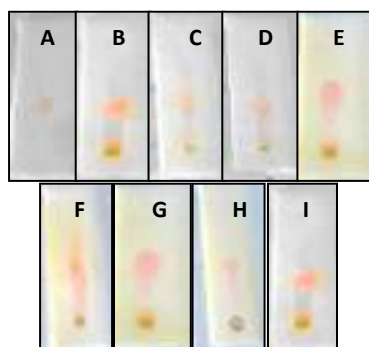
Figure1: TLC Chromatogram of Nicotine in different Sample (A-Nicotine Standard, B-Sample A, C-Sample B, D-Sample C, E-Sample D, F- Fresh Leaves, G-Area Nuts-I, H- Area Nuts-II and I- Area Nuts-III)
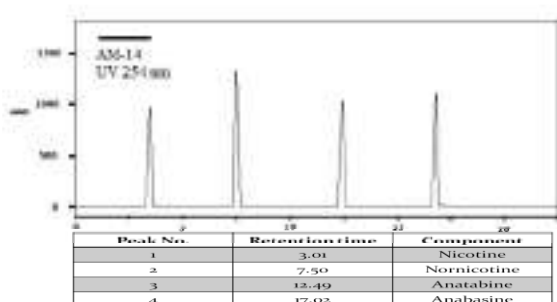
Figure 2: High Performance Liquid chromatography (HPLC) of nicotine and other alkaloids

Antibacterial activity of tobacco samples: The antibacterial activity of tobacco samples was also studied. Figure 3 Nicotine standard showed antibacterial activity against *E. coli.* Also Tobacco Sample B proved to have an effect on the bacteria.
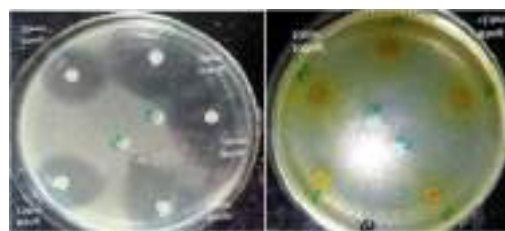
Figure 3: Antibacterial activity of nicotine standard and tobacco sample

Enzyme activity assay: The activity of phenol oxidase (Graph 1) and peroxidase (Graph 2) was found to be highest in fresh leaves of tobacco. This shows that enzyme activity is lost during processing and curing of tobacco products.
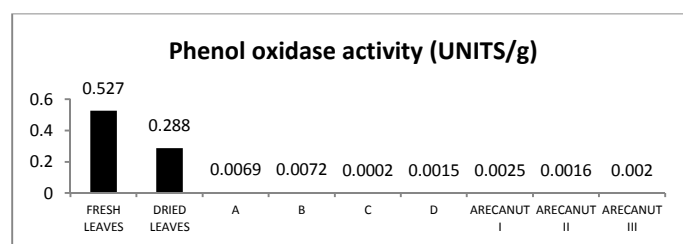
Graph 1: Phenol oxidase activity in cold extracts of tobacco and areca nuts
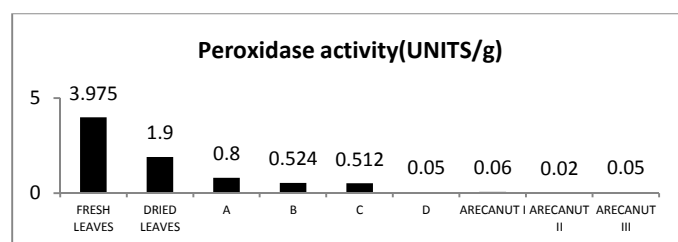
Graph 2: Peroxidase activity in cold extracts of tobacco and areca nuts

Nitrosamine estimation: Tobacco specific Nitrosamines are present in the saliva of those who chew tobacco (*Gutka*)(Table 5)*.* The nitrosamine concentration was estimated in 5 subjects. Saliva sample of a subject who doesn't consume any form of tobacco product was also collected as negative control. It was found that nitrosamine was present in all the 5 subjects, while the negative control had nil concentration of nitrosamine. Tobacco specific Nitrosamines are potent carcinogens responsible for lung, throat and oral cancer.

Table 5: Subjects and nitrosamine concentration (μg/ml of saliva)

Subjects	Age	Intake of tobacco/ day	Nitrosamine conc. (μg/ml of saliva)
Subject I	45 Years	2-3 times	0.02201
Subject II	45 Years	1-2 times	0.02199
Subject III	50 Years	5-6 times	0.02203
Subject IV	55 Years	2-3 times	0.02198
Subject V	45 Years	Once a week	0.02

Conclusion:

The concentration of nicotine in this work is reliable and may be used for further. The various method was successfully applied for determination of nicotine in five different brands of commercial cigarettes as well as from different tobacco leaves, three types of areca nuts. The finding in this work confirm that the fresh tobacco leaves content high amount of nicotine.

Copyright Statement

*Author is solely responsible for the plagiarism.

Acknowledgement:

The authors express appreciation to Dr. Archana Moon for her valuable input and advice in the preparation of this paper.

References

1. World Health Organization (WHO) Cancer 2006 Feb.

2. American Cancer Society; Cancer statistics 2008.

3. Bilkei-Gorzo A, Rácz I, Michel K, Darvas M, Rafael Maldonado López, Zimmer A. (2008). "A common genetic predisposition to stress sensitivity and stress-induced nicotine craving". Biol. Psychiatry 63 (2): 164–71.

4. Hany A. Omara and Salma MM Attaf ; 'Spectrophotometric determination of nicotine in cigarette, tobacco and biological samples'; World journal of Pharmacy and Pharmaceutical Sciences, vol 3, issue 8. 1327-1340, 2014.

5. Erickson DJ, Lenk K M, Foster J L-"Latent class of young adults based on use of multiple types of tobacco and products" Nicotine TobRes.2014, Aug16.

6. Wei Min Zhang Jing Wei WenXue Chin HaiDe Zhang "Chemical composition & phenolic Antioxidants of Arica seeds" - Advances in Biomedical Engineering vol 1-2, 2011.

7. R.Jayakrisnan, Aleyamma Mathew, Kamala Lekshmi, Paul Sebastian, PatricFinne and AnttiUutela. "Nicotine dependence among smokers in a selected rural population in Kerela". Asian Pacific Journal of Cancer Prevention Vol 3, 2012.

8. AnupamaAsthana, RachanaRastogi, G.Sunita and V.K.Gupta- "Spectrophotometric method for the determination of Nicotine." Journal of the Chinese Chemical Society, 2004, Vol-51, 949-953.

9. Newcomb P.A; Storer B.E; Marcus P.M; 'Cigarette smoking in relation to risk pf large bowel cancer'. Cancer Res, 1995, 55, 4906.

10. Evans, W.C. and rd E.G. Treasa, 1978. Pharmacognosy, 11 Edition, Ballier tindall, London, pp: 115-222.

11. Karen S and Venon S Total phenol analysis: automation and comparison with manual methods. American Journal of Enology and Viticulture 1977; 28(1): 49-55.

12. Sini K R et al. Antioxidant Potential of dried root powder of *Capparis grandiflora* wall ex Hook & Thompson. International Journal of Pharmaceutical Research & Development 2010; 2(9): 50-55.

13. Mukharjee S et al. Evaluation of Comparative free radical quenching potential of Brahmi (*Bacopa monnieri*) & Madookparni, AYU 2011:32(2): 258-264.

14. Sharma V & Palliwal R. Preliminary phytochemical investigation and thin layer chromatography profiling of sequential extracts of *Moringo oliefera* pods. International Journal of Green Pharmacy. 2013: 7(1): 41-45.

15. Bauer AW et al. Antibiotic susceptibility testing by a standardized single disc method. American Journal of Clinical Pathology. 1966; 45(4_: 493-496.

16. Martina Mackowa et al. 'Quantitative detection of plant peroxidase'. Chem Listy 2001; 95: 130-132.

17. Science and Plants for school, polyphenoloxidase assay: www.saps.org.uk

18. L.Ceh & F. Ender: A sensitive method for the colorimetric determination of volatile nitrosamines in food products and air, Fd. Cosmet Toximol, 1978, vol 16, pp. 117-121.

ARTICLE

Organic White Light Emission from mixture of Allamanda with Rhodamine B Extracts

Mohammad Mubeen[1], S. J. Dhoble[2] and Abhay D. Deshmukh[1 a)]
[1]Energy Materials and Devices Laboratory, Department of Physics, RTM Nagpur University, Nagpur. M.H
[2]Nanomaterials Research Laboratory, Department of Physics, RTM Nagpur University, Nagpur. M.H
Corresponding author: abhay.d07@gmail.com

Abstract: The Organic White light emitting materials have attracted remarkable attention in the recent years due to their wide application in Organic Solid State Lighting, so that the design of such materials are interesting and extremely challenging. Here in we have developed a simple and eco-friendly method for the synthesis of Organic White light emitting materials (OWLED) using Allamanda flower. Allamanda is a genus flowering plant commonly available everywhere. The Allamanda species have yielded several chemical compounds one of them is Allamandin, the elemental and the mass spectroscopy analysis established the molecular formula as $C_{15}H_{16}O_7$. Allamanda extracts shows bluish white three emission bands of 430 nm, 465 nm and 510 nm at 380 nm UV excitation in double distilled water with Commission Internationale d'Eclairage (CIE) chromaticity index (0.20, 0.29). The Rhodamine-B shows orange emission band at 615 nm at 380 nm UV excitation in double distilled water with CIE index of (0.62, 0.37). The mixture of Allamanda flower and Rhodamine-B extracts, almost produced white light emission (WLE) with CIE index of (0.32, 0.35) in double distilled water at 380 nm UV excitation. It is also possible to get the white light by using the polyvinyl alcohol (PVA) film with the same extract mixture of CIE index (0.25, 0.36) at 380 nm UV excitation. The extraction process of these dyes are extremely cheap, eco-friendly and very simple

1 Introduction

With the ever increasing global dependence on non-renewable energy sources such as coal, oil and natural gas, the development of alternative renewable energy supplies is given top priority. Energy became an essential commodity in our lives. Lighting plays an important role in our day-to day life and also to Commerce and Industry worldwide as it consumes large amount of the total energy produced. Nearly 90% of the global energy supply is generated from carbon based fuels which is creating a serious environmental problem worldwide. So the energy should be generated eco-friendly and used very efficiently. The energy can be efficiently utilized using white light emission devices [1-4].

Organic white light emitting material have been attracted a significant interest in recent years due to their broad applications in display devices, back lights, lasers, indicators, chemical sensors and LED's[5-10]. Till now there have been variety of materials used to generate the white light emission, including Forster resonance energy transfer (FRET)[11, 12], photophysical

phenomenon[13], Inter-and intra-molecular charge transfer[14], hydrogen bonding mediated J- aggregation[15], the mixing of monomer and excimer fluorescence[16], excited state intramolecular proton transfer (ESIPT)[17], etc.

So, in this paper we are going to generate white light emission using Allamanda flowers. Allamanda is a genus of flowering plants in the dogbane family, Apocynaceae. The elemental and the mass spectroscopy analysis established the molecular formula as $C_{15}H_{16}O_7$ [18]. Allamanda grows along river banks and other open, sunny areas with adequate rainfall and perpetually moist substrate. The genus name Allamanda honors the Swiss botanist and Physician Frederic-Louis Allamand (1783-1803). Allamanda is also known as golden trumpet[19]. Allamanda species have been used in Systems of traditional medicine for various purposes. The plant is used against jaundice, malaria[20], liver tumors[21], pathogenic fungi, HIV and enlarged speen. The Allamanda flower acts as a laxative and also shows antibiotic properties[22].

2 Materials and methods

2.1 Collection of materials

In this investigation, to prepare a plant material (Flowers), healthy, disease free plant of Allamanda flower was collected from RTM Nagpur University campus, Nagpur, Maharashtra, India in the month of January 2018. The Allamanda flower was washed thoroughly in running tap water to remove soil and dust particles and finally washed with double distilled water for 3 times.

Rhodamine B (RhB) $C_{28}H_{31}ClN_2O_3$ is purchased from SD Fine chemical India Ltd., Polyvinyl Alcohol (PVA) is purchased from Fisher Scientific India Ltd. All the chemicals are of AR grade and used as received.

2.2 Sample extraction and preparation

Allamanda flower (YF) extract was prepared in 10 mL of double distilled water. In brief, Allamanda flowers grinded in mortar and piston for 5 mints. This mixture is added in 10mL of double distilled water and kept for sonication for 30 mints. After sonication this extract was centrifuged at 3500 rpm for 10 mints. After that flower extract was collected and used for further characterization and it is labeled as YF.

Rhodamine B (RhB) extract was prepared in 10 mL of double distilled water. In brief 0.1mg of RhB was added to the double distilled water and kept for sonication about 30 mins, then centrifuge about 3500 rpm for 10 mints. After that RhB extract was collected and used for further characterizations.

2.3 Preparation of PVA film

The PVA dry film was prepared in 10 ml of double distilled water. In brief, 1 gm. of PVA was dissolved in 10ml of double distilled water at 50^0C for 2 hr. This solution was poured into the flat-bottomed dish in such a manner that a uniform thin layer of liquid covers the surface. This dish was kept at room temperature and the film was allowed to dry naturally. The dry PVA film was easily detached from the dish.

2.4 Characterization

The photoluminescence (PL) emission spectra were measured at room temperature using Shimadzu RF-5301PC spectrofluorophotometer with a 150 W xenon lamp as the excitation source. The Excitation and Emission monochromator band passes were kept at 5 nm and the quartz cell cuvette (1× 1 cm) was used. The Commission Internationale d'Eclairage (CIE) color coordinates were calculated by using freely online available Osram Sylvania software[23].

3. Result and Discussion

The UV-Vis absorption spectra and the Photoluminescence (PL) spectra carried out in the double distilled water as an extraction medium. Figure 1 shows the UV-Vis absorption spectra (black) and PL emission spectra (blue) of Allamanda flower (YF) at 380 nm UV excitation. The YF shows the strong absorption around at 350-500 nm with maximum at 440 nm. This absorption is due to the π-π* electronic transitions. The YF extract shows the bluish white emission with three emission bands at 430 nm, 465 nm and 510 nm respectively as shown in figure 1 and the corresponding CIE [23] color coordinates index are (0.20,0.29). For the same UV excitation RhB extracts shows the strong Orange emission at 615 nm as shown in figure 3 and the CIE color index are (0.62,0.37) as shown in figure 4. It is found that the point A and the point B are in opposite direction of the white light emitting region in the CIE Chromaticity diagram as shown in figure 8. This will suggest that by mixing the YF and the RhB extracts we can get the WLE.
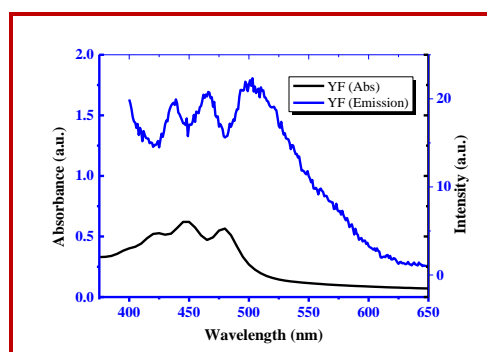

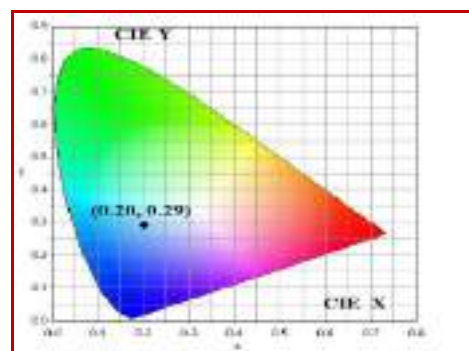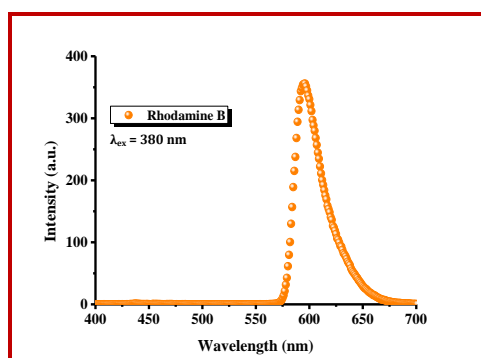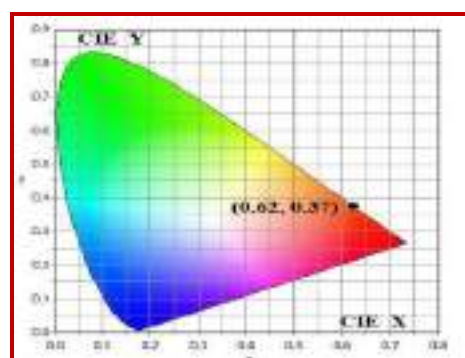**Figure 1.** Absorbance and PL spectra of YF extract at 380 nm UV excitation.

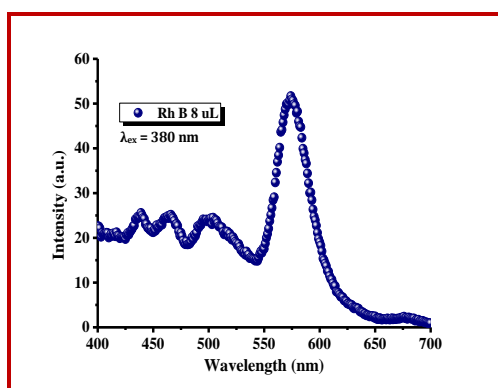**Figure 2. CIE-1931 diagram.** Chromaticity plot for color coordinates of YF.

Figure 3. PL emission spectra of RhB extract at 380 nm UV excitation.
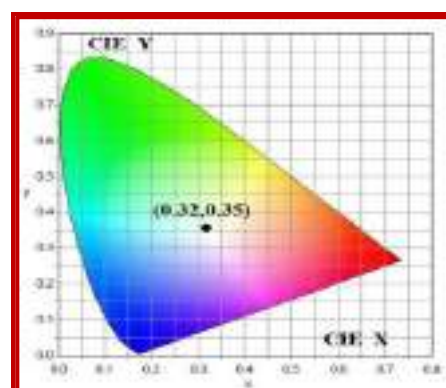

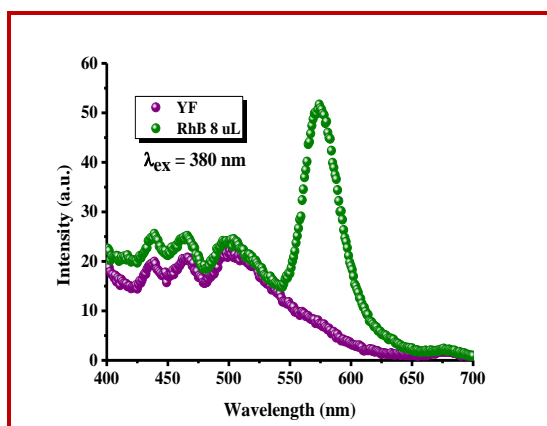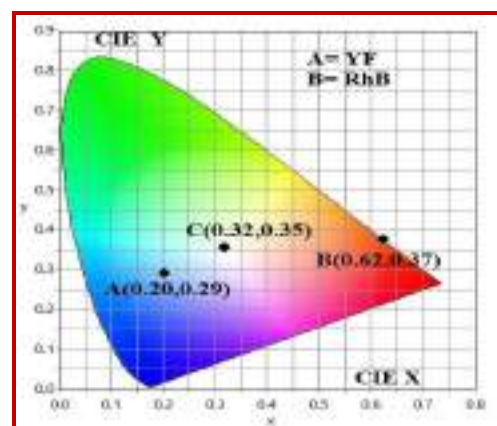**Figure 4. CIE-1931 diagram.** Chromaticity plot for color coordinates of RhB.

The excitation wavelength was fixed at 380 nm for PL spectra. The sequence of solution was prepared by varying the relative concentration of YF and RhB extracts. It can be seen that the point D (0.32, 0.35) corresponding to the 1:0.004 molar ratio of YF and RhB extracts respectively is very close to the WLE. It can be also observed that the tendency of color coordinates bends and passes very close to pure white light coordinates. The emission spectrum corresponding to point C which is shown in figure 8 is covering the entire visible spectrum (400-650nm). The excitation and emission spectrum clearly shows that for 380 nm UV excitation, the emission covers the entire visible spectrum up to 650 nm.

Figure 5. PL emission spectra of mixture of YF and RhB extract at 380 nm UV excitation.

Figure 6. CIE-1931 diagram. Chromaticity plot for color coordinates of WLE solution.
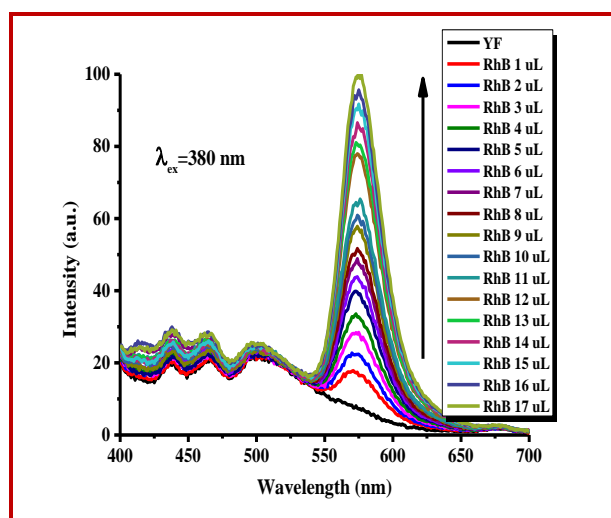

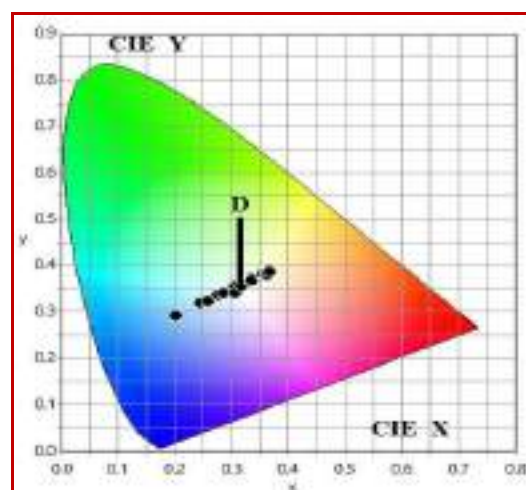**Figure 7.** PL emission spectra of mixture of YF and RhB extract at 380 nm UV excitation.

Figure 8. CIE-1931 diagram. Chromaticity plot for color coordinates of A) YF, B) RhB extracts and point C denoted the pure WLE coordinates.
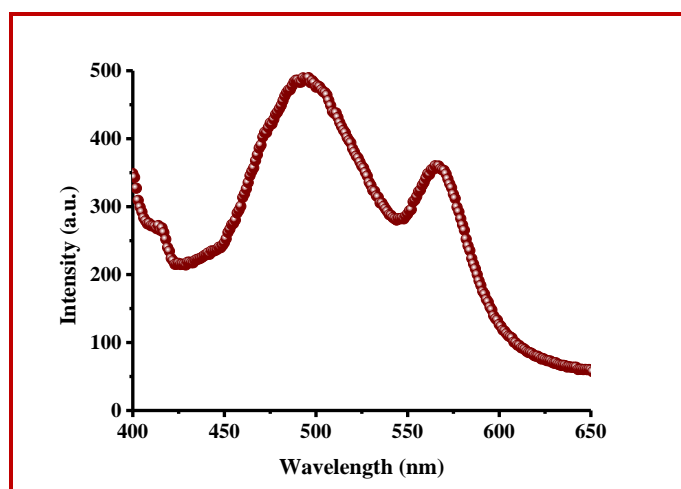
Figure 9. PL emission spectra of mixture of YF and RhB extract at 380 nm UV excitation.
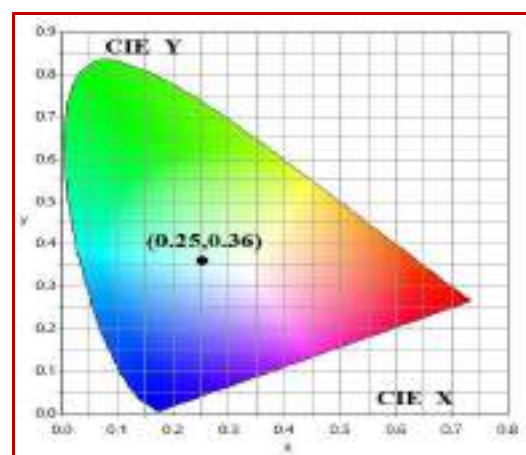

Figure 10. CIE-1931 diagram. Chromaticity plot for color coordinates after mixing YF and RhB in double distilled water.

As we can observe from the above experiment, in which as the RhB concentration is increased to fix amount of YF, the emission intensity of the YF also slightly increases. So that the results in extended emission spectrum covers the entire visible region i.e., 400-650nm

Figure 11. PL emission spectra of WLE incorporated PVA film at 380 nm UV excitation, inset shows white light emitting PVA film at 380 nm excitation.

Figure 12. CIE-1931 diagram. Chromaticity plot for color coordinates of WLE incorporated PVA film at 380 nm UV excitation,

3   Conclusions

In conclusion, we have successfully generated white light emission from natural and eco-friendly dyes in our laboratory at 380 nm UV excitation using green and simple method. The mixture of the YF and RhB almost we got the white light, with a CIE coordinate index (0.32, 0.35) in double distilled water and CIE coordinates index o (0.25, 0.36) in PVA film at 380 nm UV excitation. Thus the White light emission from low cost and ecofriendly resources would be very important for the lighting and display devices applications.

References

1. Forrest, S.R. and M.E. Thompson, Introduction: Organic Electronics and Optoelectronics. Chemical Reviews, 2007. 107(4): p. 923-925.

2. Xiao, L., et al., Recent Progresses on Materials for Electrophosphorescent Organic Light-Emitting Devices. Advanced Materials, 2011. 23(8): p. 926-952.

3. Xia, Z., et al., Recent developments in the new inorganic solid-state LED phosphors. Dalton Transactions, 2016. 45(28): p. 11214-11232.

4. Su, L., et al., Recent Progress in Quantum Dot Based White Light-Emitting Devices. Topics in Current Chemistry, 2016. 374(4): p. 42.

5. Fleetham, T., et al., Single-Doped White Organic Light-Emitting Device with an External Quantum Efficiency Over 20%. Advanced Materials, 2013. 25(18): p. 2573-2576.

6. Reineke, S., et al., White organic light-emitting diodes with fluorescent tube efficiency. Nature, 2009. 459: p. 234.

7. Jang, E., et al., White-Light-Emitting Diodes with Quantum Dot Color Converters for Display Backlights. Advanced Materials, 2010. 22(28): p. 3076-3080.

8. Gather, M.C., A. Köhnen, and K. Meerholz, White Organic Light-Emitting Diodes. Advanced Materials, 2011. 23(2): p. 233-248.

9. Wang, J., W. Lin, and W. Li, Three-channel fluorescent sensing via organic white light-emitting dyes for detection of hydrogen sulfide in living cells. Biomaterials, 2013. 34(30): p. 7429-7436.

10. Liu, J., et al., Selective Ag(I) Binding, H2S Sensing, and White-Light Emission from an Easy-to-Make Porous Conjugated Polymer. Journal of the American Chemical Society, 2014. 136(7): p. 2818-2824.

11. Sanju, K.S., P.P. Neelakandan, and D. Ramaiah, DNA-assisted white light emission through FRET. Chemical Communications, 2011. 47(4): p. 1288-1290.

12. Zhang, X., D. Gorl, and F. Wurthner, White-light emitting dye micelles in aqueous solution. Chemical Communications, 2013. 49(74): p. 8178-8180.

13. Mukherjee, S. and P. Thilagar, Organic white-light emitting materials. Dyes and Pigments, 2014. 110: p. 2-27.

14. Park, Y.I., et al., A new pH sensitive fluorescent and white light emissive material through controlled intermolecular charge transfer. Chemical Science, 2015. 6(1): p. 789-797.

15. Molla, M.R. and S. Ghosh, Hydrogen-Bonding-Mediated J-Aggregation and White-Light Emission from a Remarkably Simple, Single-Component, Naphthalenediimide Chromophore. Chemistry – A European Journal, 2012. 18(5): p. 1290-1294.

16. Liu, Y., et al., π-Conjugated Aromatic Enynes as a Single-Emitting Component for White Electroluminescence. Journal of the American Chemical Society, 2006. 128(17): p. 5592-5593.

17. Park, S., et al., A White-Light-Emitting Molecule: Frustrated Energy Transfer between Constituent Emitting Centers. Journal of the American Chemical Society, 2009. 131(39): p. 14043-14049.

18. Kupchan, S.M., et al., Isolation and structural elucidation of allamandin, and antileukemic iridoid lactone from allamanda cathartica. The Journal of Organic Chemistry, 1974. 39(17): p. 2477-2482.

19. Gangwar, R.K., et al., Catalytic activity of allamanda mediated phytosynthesized anisotropic gold nanoparticles. Advances in Natural Sciences: Nanoscience and Nanotechnology, 2013. 4(4): p. 045005.

20. Haron, F.F., et al., Bioassay-guided Isolation of Antifungal...n from Allamanda Species (Apocynaceae). Journal of Biological Sciences, 2013. 13(3): p. 158-162.

21. Schmidt, D.d.F.N., et al., Evaluation of the anti-proliferative effect the extracts of Allamanda blanchetti and A. schottii on the growth of leukemic and endothelial cells. J Pharm Pharmaceut Sci, 2006. 9(2): p. 200-2008.

22. Mani, S. and J.W. Lawson, In vitro modulation of inflammatory cytokine and IgG levels by extracts of Perna canaliculus. BMC Complementary and Alternative Medicine, 2006. 6(1): p. 1.

23. For CIE co-ordinates software, see Osram Sylvania, (2013), available at: https://www.sylvania.com/en-us/tools-and-resources/Pages/LED-ColorCalculator-Version History.aspx. 2017.

ARTICLE

A Comparative Study of Thermal and Chelation Properties of 2-Hydroxy/4-Hydroxy acetophenone-Guanidine-Formaldehyde Terpolymers

S.C. Srivastava,* Mahejabeen Azizul Haque, L.J. Paliwal

Post Graduate Teaching Departmet of Chemistry, Rashtrasant Tukadoji Maharaj Nagpur University, Nagpur – 440033, (MS) India (Corrresponding Author; vijaytn6@gmail.com)

Abstract: The two terpolymers 2-hydoxyacetophenone-guanidine-formaldehyde (2-HAGF) and 4-hydroxyacetophenone-guanidine-formaldehyde (4-HAGF) have been synthesized under identical programmed experimental conditions by microwave irradiation at 300 W at a preset time of 20 min. and temperature of 140 °C. The synthesized product has been characterized on the basis of elemental analysis, FTIR, and ^{1}H NMR spectral data. The thermal degradation studies of these terpolymers have been carried out by TG, DTG and DTA techniques to determine their decomposition behaviour and relative thermal stabilities. The decomposition kinetics have been evaluated by Freeman Carroll and Sharp Wentworth method and compared. The metal ion chelating ion-exchange properties for Cu^{2+}, Zn^{2+}, Pb^{2+} and Fe^{3+} have been studied with both the resins in order to compare their chelating ion-exchange behaviour in different electrolytes and at different pH.

Introduction

The versatile properties and application of polymers and terpolymers have attracted the attention of academicians and industries towards the synthesis of terpolymer resins for their various applications as the polymers can be designed as per the requirement. Polymers and terpolymers find their applications as semiconductors[1], adhesives, ion exchange resins[2-5], catalyst, thermally stable materials[6,7] and many more. Energy sources for the syntheses of the terpolymers reported so far were either on an oil bath, water bath or hot plates, which were time taking and not very much environment friendly. In recent years microwave irradiation technique has been used for the synthesis of organic compounds which is an environmental friendly and a green approach in the synthetic chemistry [8]. However, no work has been done on synthesis of terpolymers using microwave irradiation.

Jadhav et. al. [9,10] has reported the synthesis, characterization and thermal degradation properties of the terpolymers using 2,2'-biphenol monomer moiety. Patrik Michael [11] studied structural and thermal decomposition properties of a terpolymer derived from salicylic acid, guanidine and formaldehyde. Polymeric resins synthesized by condensation of hydroxybenzoic acid with formaldehyde and amines have been reported by W.B Gurnule et. al.[12,15]. Metal ion uptake capacity of terpolymer synthesized from substituted benzoic acid has been reported by M. Karunakaran et. al.[13]. Shah et. al.[14] has

reported the use of salicylic acid/ formaldehyde/ resorcinol resins for the removal and separation of heavy metal ions in a binary mixture. A green synthesis and characterization of thymol-guanidine-formaldehyde terpolymer has been studied by Kukade et. al.[16].

The present work describes the synthesis, characterization, thermal degradation, and ion exchange properties of 2-HAGF and 4-HAGF terpolymers synthesized by microwave irradiation method.

Experimental

Materials and methods

2-hydroxyacetophenone, 4-hydroxyacetophenone and guanidine of S.D.fine and formaldehyde from Qualigens fine chemicals are used without purification. The synthesis of the terpolymer has been has been carried out on CEM focused microwave synthesis system. The elemental analysis for C, H, and N is carried out on Elemental Vario EL III at SAIF Cochin. FTIR (KBr) spectrum is obtained on Spectrum RX-IFTIR in the scanning range of 4000 cm-1 to 450 cm-1 at SAIF, Chandigarh. 1H NMR at 400 MHz and 13C NMR at 100MHz in DMSOd6 have been recorded on Bruker Avance-II 400 NMR spectrometer at SAIF, Chandigarh. The TG/DTA/DTG data of the terpolymers

have been obtained on Perkin Elmer model Diamond at SITC, Cochin.

Synthesis of 2-HAGF and 4-HAGF Terpolymers

A mixture of 2-hydroxyacetophenone (0.05 mol), guanidine (0.05 mol) and formaldehyde (0.1mol) was taken in presence of 25 ml of 2 M hydrochloric acid as a catalyst and subjected to the microwave irradiation for 20 min. at 300 W maintained at a temperature of 140 °C. A yellow colour product of 2-hydroxyacetophenone-guanidine-formaldehyde (2-HAGF) terpolymer was obtained and purified by dissolving in 10 % NaOH solution and reprecipitating with 1:1 HCl/Water (v/v). The 4-hydroxyacetophenone-guanidine-formaldehyde (4-HAGF) has been synthesized in similar manner as mentioned above, by reaction of 4-hydroxyacetophenone with guanidine and formaldehyde in 1:1:2 molar ratios respectively at 300 watt at a prefixed temperature of 140°C for 20 min. The reaction schemes for synthesis of 2-HAGF and 4-HAGF terpolymers are given in Scheme 1 and 2.
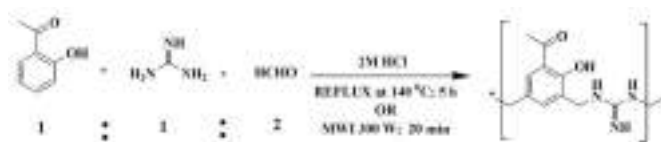
Scheme 1. Synthesis of 2-HAGF Terpolymer
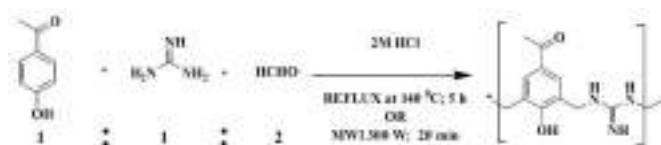
Scheme 2. Synthesis of 4-HAGF Terpolymer

Results and discussion

Characterization of 2-HAGF and 4-HAGF Terpolymers

Elemental analysis: The terpolymers 2-HAGF and 4-HAGF are analyzed for C, H, and N contents (Table 1) and the % values obtained are in agreement with the theoretical calculated values for the empirical formula of repeat unit as shown in Scheme 1 and 2.

Table 1 Elemental analyses of 2-HAGF and 4-HAGF terpolymers

Terpolymer	Colour	m.p. °C	% Yield	Empirical formula	Time (min.)	Elemental Analysis, Exp. (Calcd.) (%)		
						C	H	N
2-HAGF	Yellowish Orange	>280	65	$C_{11}H_{13}N_3O_2$	20	60.68 (60.00)	6.73 (6.36)	18.80 (19.09)
4-HAGF	Light Yellow	>280	64	$C_{11}H_{13}N_3O_2$	20	55.76 (60.00)	6.19 (6.36)	17.90 (19.09)

Spectral Studies

FTIR Spectra: The FTIR spectra of 2-HAGF and 4-HAGF terpolymers (Figure 1) depict phenolic –OH group at 3365 and 3336 cm^{-1} respectively and –NH stretching frequency at 3066 and 3135 cm^{-1} respectively. The stretching frequencies observed at 2871 and 2950 cm^{-1} indicate presence of -CH$_2$ group in 2-HAGF and 4-HAGF terpolymers respectively. The >C=O (acetyl) group shows its presence at 1683 and 1664 cm^{-1}. The C-O stretching has appeared at 1278 and 1281cm^{-1} respectively for 2-HAGF and 4-HAGF terpolymers. The para substitution in 4-HAGF terpolymer is seen at 893 cm^{-1}
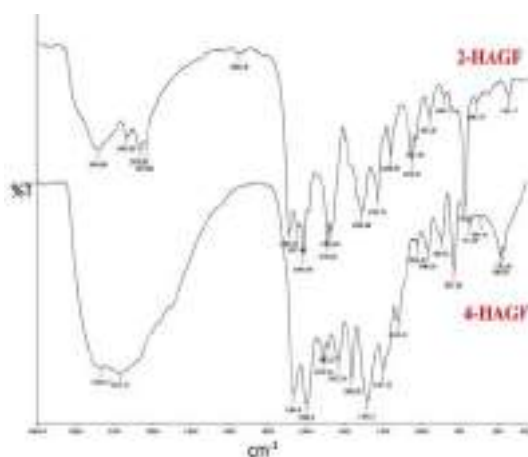
Figure 1: FTIR Spectra of 2-HAGF and 4-HAGF Terpolymers

NMR Spectra: The ^{1}H NMR spectrum of 2-HAGF terpolymer (Figure 2) depicts chemical shift δ 8.2 ppm for a proton of Ar-OH, a broad signal at δ 7.0 – 6.7 ppm may be due to the presence of two protons of Ar-H, a signal at δ 1.0 ppm may be due to –CH$_2$ proton. The signal at δ 2.00 ppm indicates presence of three

protons of -CH$_3$ and δ 8.2 – 8.7 ppm supports the presence of two protons of –NH. While, the ^{1}H NMR spectrum of 4-HAGF

terpolymer (Figure 3) shows the signal for Ar-OH proton at δ 10.5 ppm and the signal at δ 7.2-6.5 ppm represents the two protons of AR-H. The -CH$_2$ bridging proton is displayed at δ 2.8 ppm and the three protons of CH$_3$ are supported by the signal at δ 2.3 ppm. The signal displayed at δ 4.5-5.0 ppm confirms the presence of two protons of –NH group.
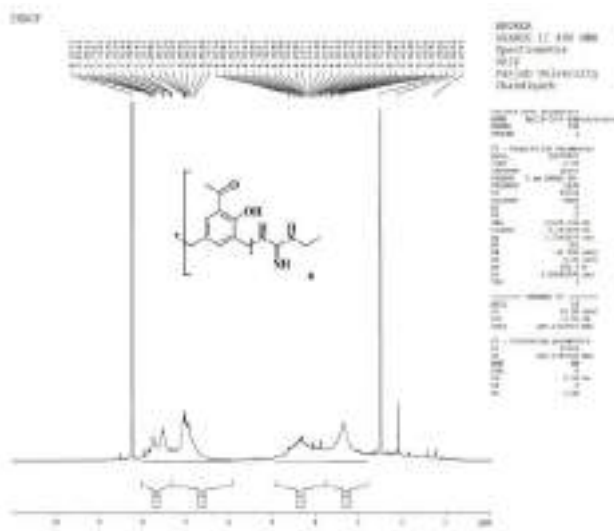

Figure 2: ^{1}H NMR Spectrum of 2-HAGF Terpolymer
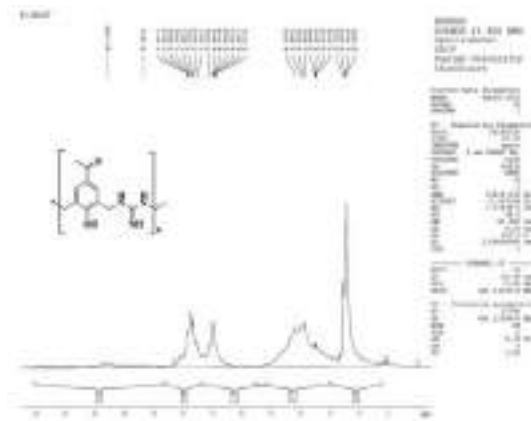
Figure 3: ^{1}H NMR Spectrum of 4-HAGF Terpolymer

Thermal Studies: The thermogram of 2-HAGF terpolymer (Figure 4,5) (Table 2) indicates decomposition in three consecutive stages of degradation. The first stage of decomposition observed in the temperature range of 38-250°C may be due to loss of moisture and lattice water. The second stage of decomposition reports the loss of –COCH$_3$, -CH$_2$ groups in the temperature range of 250-400°C and the third stage of decomposition takes place in the temperature of 400-735°C suggesting the loss of NH-C(NH)-NH groups. The theoretical and experimental values are found to be in good agreement with each other. The thermal degradation of 4-HAGF terpolymer (Figure 4,6) (Table 2) occurs in three consecutive stages. The first stage in the temperature range of 38-150°C indicates the loss of trapped moisture. The second stage of degradation obtained in the temperature range of 150-370°C is due to loss of –COCH$_3$ and the third stage of degradation confirms the loss of NH-C(NH)-NH group of terpolymer.

Table 2 Thermal behaviour of of 2-HAGF and 4-HAGF terpolymers

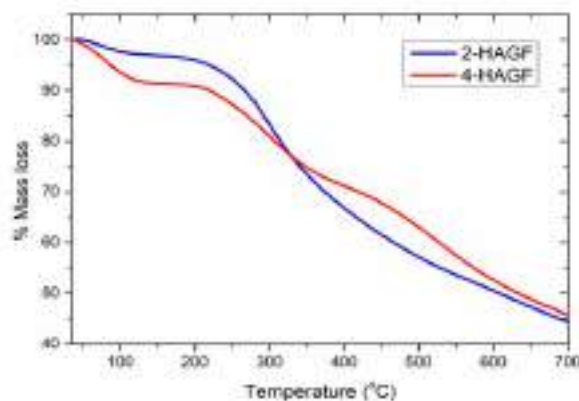| Terpolymer	Decomposition Stages	Temp. Range (°C)	% Wt. loss		Species degraded	Residue (%)
			Expt.	Calcd.		
2-HAGF	I	38-250	7.76	7.72	-OH	
	II	250-400	25.50	24.55	-COCH$_3$, -CH$_2$	42.42
	III	400-735	24.32	25.91	NH-C(NH)-NH	
4-HAGF	I	38-150	8.60	7.72	-OH	
	II	150-370	18.18	19.55	-COCH$_3$	46.70
	III	370-700	26.52	25.91	NH-C(NH)-NH	

Figure 4: Thermograms of 2-HAGF and 4-HAGF Terpolymers
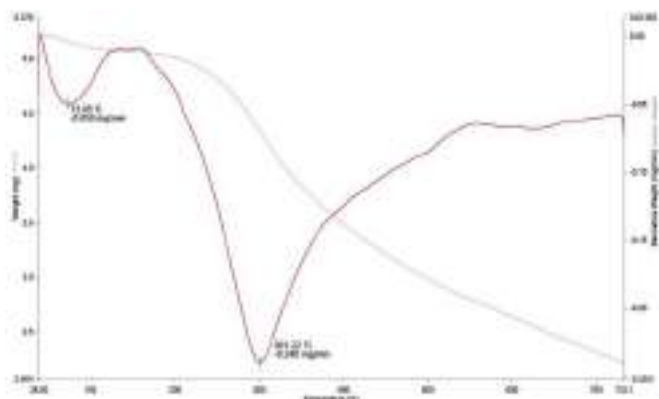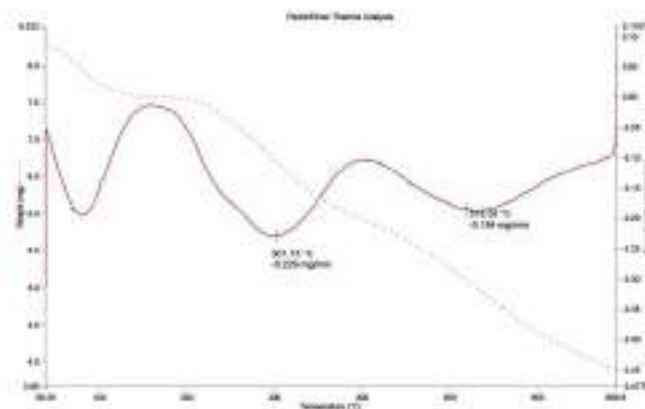
Figure 5: DTG of 2-HAGF Terpolymer

Figure 6: DTG of 4-HAGF Terpolymer

Ion-exchange Studies of 2-HAGF and 4-HAGF Terpolymers

In 2-HAGF terpolymer, Cu^{2+} adsorption value is found to be 73 % in 1 M K_2SO_4 electrolytic solution at pH 3. The Zn^{2+} adsorption value in 1 M solution of KCL at pH 4 is found to be 25 %. For Pb^{2+} metal ion, 89 % adsorption is found 0.1 M KCL electrolytic solution at pH 3. While the adsorption value of Fe^{3+} ion is found to be 90 % in all the three electrolytic solutions viz. KCL, KNO_3, and K_2SO_4 at 2.5 pH. The metal ion uptake values and distribution ratios of 2-HAGF terpolymer resin is given in Table 3 and 5.

In 4-HAGF terpolymer, Cu^{2+} adsorption is found to be 76 % in 0.1 M KCL electrolytic solution at pH 3 and Zn^{2+} adsorption of about 28.18 % in 1 M KCL electrolytic solution at pH 4. The Pb^{2+} metal shows 89.27 % adsorption in 0.1 M KCL solution at pH 3. Whereas, Fe^{3+} metal ion adsorption in 1 M KCL electrolytic solution is found to be 93.91 % at pH 2.5. The metal ion uptake values and distribution ratio of 4-HAGF terpolymer resin is tabulated in Table 4 and 6.

Consequent upon the comparison of chelating ion-exchange behaviour of the above mentioned terpolymers viz. 2-HAGF and 4-HAGF, it may be inferred that the terpolymer 4-HAGF has an edge over 2-HAGF with higher adsorption values for all the metals ions under study viz. Cu^{2+}, Zn^{2+}, Pb^{2+} and Fe^{3+} at their respective pH values of 3, 4, 3 and 2.5, respectively in KCl electrolytic solution of varying molarities as mentioned above.

Conclusion

The 2-HAGF and 4-HAGF terpolymers have been synthesized under similar experimental conditions and perusal upon the ion-exchange analytical data it is observed that 4-HAGF has an edge over 2-HAGF terpolymer. The reason may be attributed to the hydroxy group at the para-position of the phenol which is supposed to be more active for the hydrogen bonding as compared to the 2-HAGF terpolymer. Hence, 4-HAGF may be a suitable polymer for the removal or enrichment of Cu^{2+}, Pb^{2+} and Zn^{2+} values in the waste water effluents generated from the various mining and allied industries. It is economically viable and cheaper as well. The terpolymer 4-HAGF adsorbs Fe^{3+} ions to the tune of 93.91 % and the adsorbed Fe^{3+} may be used for the bracketing of the blue dust iron and may be used in the blast furnace of steel plants. Winning of copper values may also be possible and lead pollution can also be controlled by using with 4-HAGF terpolymer. The two terpolymers do not melt but char above 280°C and demonstrates its thermal stability.

Table 3 Metal ion uptake of 2-HAGF Terpolymer

Metal ion	pH	Electrolyte concentration (mL^{-1})	Metal ion uptake (%) in presence of different electrolytes		
			KCl	KNO$_3$	K$_2$SO$_4$
Cu^{2+}	2.00	0.1	63.00	18.00	35.00
		0.5	19.00	17.00	22.00
		1.0	-	-	70.00
	3.00	0.1	70.00	18.00	56.00
		0.5	19.00	19.00	58.00
		1.0	19.00	19.00	73.00
	4.00	0.1	60.00	22.00	56.00
		0.5	33.00	18.00	56.00
		1.0	22.00	18.00	70.00
	5.00	0.1	38.00	38.00	47.00
		0.5	35.00	30.00	30.00

Metal ion	pH	Electrolyte concentration (mL⁻¹)	KCl	KNO₃	K₂SO₄
		1.0	32.00	30.00	56.00
Zn²⁺	2.00	0.1	1.50	1.90	1.50
		0.5	2.00	2.00	2.50
		1.0	11.50	15.00	20.00
	3.00	0.1	4.50	3.00	2.30
		0.5	4.00	0.10	2.30
		1.0	15.00	0.10	18.00
	4.00	0.1	6.00	6.00	2.00
		0.5	16.00	5.80	2.80
		1.0	25.00	20.00	18.00
	5.00	0.1	5.90	5.50	1.50
		0.5	6.00	5.50	6.50
		1.0	20.00	20.50	21.00
Pb²⁺	2.00	0.1	88.00	1.50	-
		0.5	0.40	4.20	-
		1.0	0.25	4.00	-
	3.00	0.1	89.00	4.20	-
		0.5	4.00	8.00	-
		1.0	4.00	4.00	-
	4.00	0.1	18.00	5.90	-
		0.5	2.80	7.60	-
		1.0	7.60	0.40	-
	5.00	0.1	2.00	2.90	-
		0.5	0.50	9.00	-
		1.0	0.50	2.00	-
Fe³⁺	2.00	0.1	88.00	87.00	8.80
		0.5	88.00	87.00	8.80
		1.0	88.00	87.00	8.80
	2.5	0.1	88.50	88.50	88.00
		0.5	88.00	89.00	88.50
		1.0	90.00	90.00	90.00

Table 4 Metal ion uptake of 4-HAGF Terpolymer

Metal ion	pH	Electrolyte concentration (mL⁻¹)	Metal ion uptake (%) in presence of different electrolytes		
			KCl	KNO₃	K₂SO₄
Cu²⁺	2.00	0.1	70.00	20.00	40.00
		0.5	20.00	20.00	20.00
		1.0	0.00	0.00	75.00
	3.00	0.1	76.00	20.00	60.00
		0.5	20.00	0.00	60.00
		1.0	20.00	0.00	75.00
	4.00	0.1	50.00	20.00	60.00
		0.5	40.00	20.00	60.00
		1.0	25.00	20.00	75.00
	5.00	0.1	40.00	50.00	50.00
		0.5	40.00	10.00	30.00
		1.0	37.50	0.00	62.50
Zn²⁺	2.00	0.1	0.00	2.42	2.42
		0.5	0.00	0.00	3.00
		1.0	12.79	17.92	23.05
	3.00	0.1	5.10	2.42	2.42
		0.5	3.00	0.00	0.00
		1.0	17.92	0.00	20.49
	4.00	0.1	7.66	7.66	2.42
		0.5	18.00	7.46	3.00
		1.0	28.18	23.05	20.53
	5.00	0.1	7.66	7.66	2.42
		0.5	7.70	5.10	7.70
		1.0	20.50	20.50	23.05

Metal ion	pH				
Pb^{2+}	2.00	0.1	88.29	1.44	-
		0.5	0.46	7.29	-
		1.0	0.46	3.39	-
	3.00	0.1	89.27	4.37	-
		0.5	2.42	7.27	-
		1.0	2.42	4.37	-
	4.00	0.1	19.98	6.32	-
		0.5	3.37	10.22	-
		1.0	10.22	0.46	-
	5.00	0.1	2.50	3.39	-
		0.5	0.46	10.22	-
		1.0	2.42	2.42	-
Fe^{3+}	2.00	0.1	89.85	87.81	89.85
		0.5	89.85	89.85	89.85
		1.0	87.81	89.85	89.85
	2.5	0.1	89.85	89.85	89.85
		0.5	88.83	91.88	89.85
		1.0	93.91	91.88	91.88

Table 5 Distribution ratio of 2-HAGF Terpolymer

Metal ion	pH	Electrolyte concentration (mL^{-1})	Metal ion uptake (%) in presence of different electrolytes		
			KCl	KNO$_3$	K$_2$SO$_4$
Cu^{2+}	2.00	0.1	2520	720	1400
		0.5	760	680	880
		1.0	-	-	2800
	3.00	0.1	2800	720	2240
		0.5	760	760	2320
		1.0	760	760	2920
	4.00	0.1	2400	880	2240
		0.5	1320	720	2240
		1.0	880	720	2800
	5.00	0.1	1520	1520	1880
		0.5	1400	1200	1200
		1.0	1280	1200	2240
Zn^{2+}	2.00	0.1	60	76	60
		0.5	80	80	100
		1.0	460	600	800
	3.00	0.1	180	120	92
		0.5	160	4	92
		1.0	600	4	720
	4.00	0.1	240	240	80
		0.5	640	332	112
		1.0	1000	800	720
	5.00	0.1	236	220	60
		0.5	240	220	260
		1.0	800	820	840
Pb^{2+}	2.00	0.1	3520	60	-
		0.5	16	168	-
		1.0	10	160	-
	3.00	0.1	3560	168	-
		0.5	160	320	-
		1.0	160	160	-
	4.00	0.1	720	236	-
		0.5	112	304	-
		1.0	304	16	-
	5.00	0.1	80	116	-

Metal ion	pH		KCl	KNO$_3$	K$_2$SO$_4$
		0.5	20	360	-
		1.0	20	80	-
Fe^{3+}	2.00	0.1	3520	3480	3520
		0.5	3520	3520	3520
		1.0	3520	3520	3520
	2.5	0.1	3540	3540	3520
		0.5	3520	3560	3540
		1.0	3600	3600	3600

Table 6 Distribution ratio of 4-HAGF Terpolymer

Metal ion	pH	Electrolyte concentration (mL^{-2})	Metal ion uptake (%) in presence of different electrolytes		
			KCl	KNO$_3$	K$_2$SO$_4$
Cu^{2+}	2.00	0.1	2800	800	1600
		0.5	800	800	800
		1.0	0.00	0.00	3000
	3.00	0.1	3040	800	2400
		0.5	800	0.00	2400
		1.0	1000	0.00	1000
	4.00	0.1	2000	800	2400
		0.5	1600	800	1200
		1.0	1000	1000	3000
	5.00	0.1	1600	2000	2000
		0.5	1600	400	1200
		1.0	1500	0.00	2500
Zn^{2+}	2.00	0.1	0.00	97	97
		0.5	0.00	0.00	120
		1.0	511	716	922
	3.00	0.1	204	97	97
		0.5	120	0.00	0.00
		1.0	716	0.00	819
	4.00	0.1	306	306	97
		0.5	720	298	120
		1.0	1127	922	101
	5.00	0.1	306	306	97
		0.5	308	204	308
		1.0	820	820	922
Pb^{2+}	2.00	0.1	3532	58	-
		0.5	18.00	292	-
		1.0	18.00	136	-
	3.00	0.1	3570	175	-
		0.5	97	291	-
		1.0	97	175	-
	4.00	0.1	799	253	-
		0.5	136	408	-
		1.0	409	18	-
	5.00	0.1	100	136	-
		0.5	18	409	-
		1.0	97	97	-
Fe^{3+}	2.00	0.1	3594	3512	3512
		0.5	3594	3594	3512
		1.0	3512	3594	3512
	2.5	0.1	3594	3594	3594
		0.5	3553	3675	3594
		1.0	3756	3675	3675

Acknowledgements

References

[1]   A.D. Kushwaha, V.V. Hiwase, A.B. Kalambe; *Der Pharma Chemica*, 2012, **4(1)**, 460-467.

[2]   V.D. Mane, N.J. Wahane, W.B. Gurnule; *J. Appl. Polym Sci.*, 2009, **111(6)**, 3039-3049.

[3]   Tarase M.V., Zade A.B., Gurnule W.B.; J. Appl. Polym Sci., 108(2), (2008) 738-746.

[4]   D.K. Raval, B.N. Narola, A.J. Patel; *Iran Polym, J.*, 2005, **14(9)**, 775-784.

[5]   S.A. Patel, B,S. Shah, R.M. Patel, P.M. Patel; *Iran Polym J.,* 2004, **13(6)**, 445-453.

[6]   K.M. Khedekar, V.V. Hiwase, A.B. Kalambe, S.D. Deosarkar; *J. Chem.*, 2012, **9(4)**, 1911-1918.

[7]   R. Manavalan, M.M. Patel; *Der Makromolekular Chemie*, 2003, **108(4)**, 717-723.

[8]   R. Dua, S. Shrivastava, S.L. Shrivastava, S.N. Shriastava; *Middle East Journal of Scientific Reserch*, 2012, **(11)**, 846.

[9]   M.M. Jadhao, L.J. Paliwal, N.S. Bhave; *J.Appl. Polym and Sci.,* 2005, **101(1)**, 227-232.

[10]   .M. Jadhao, L.J. Paliwal, N.S. Bhave; *J.Appl. Polym and Sci.,* 2005, **96(5)**, 1606-1610.

[11]   E.P.P. Michael, P.S. Lingala, H.D. Juneja, L.J. Paliwal; *J. Appl. Polym. Sci.*, 2004, **92**, 2278-2283.

[12]   W.B. Gurnule, P.K. Rahandale, L.J. Paliwal, R.B. Kharat; *Synth. React. Inorg, Met-Org. Chem.*, 2003, **11**, 1187.

[13]   M. Karanakaram, A. Burkanudeen; *Orient. J. Chem.*, 2003, **19**, 225.

[14]   B.A. Shah, A.V. Shah, R.R. Bhatt; *Iran. Polym, J.*, 2007, **16**, 173.

[15]   W.B. Gurnule, J.V. Khobragade, M. Ahamad; *Der. Pharma. Chem.*, 2014, **6**, 334.

[16]   S.D. Kukade, R.R. Naik, S.V. Bawankar; *Rasayan J. Chem.*, 2015, **8**, 349-351.

ARTICLE

Preparation of strongly luminescent carbon dots from pomegranate for enhancing the c-Si solar cell efficiency

Sonal P. Ghawade[a*], S.J. Dhoble[b] and Abhay D. Deshmukh[a*]

[a*]Dept. of Physics, Energy Materials and Devices Laboratory, RTM Nagpur University, Nagpur, India

[b]Dept. of Physics, Nanomaterials Research Laboratory, RTM Nagpur University, Nagpur, India
Corresponding author- abhay.d07@gmail.com

Abstract: Herein, a simple, green, and low-cost way was developed in the synthesis of fluorescent carbon dots (CDs) using one-pot hydrothermal treatment of red pomegranates juice. By employing Pomegranates carbon dots (Pom-CDs), we have achieved a high efficiency of 9.09% in c-Si solar cells. The efficiency enhancement is based on the photon downshifting phenomenon Pom-CDs to make more photons absorbed in UV-visible region wavelength range (300nm-500nm) and re-emits them at a longer wavelength, whereas photovoltaic (PV) device exhibits significantly better response. . The short circuit current and the fill factor are increased from 26.91mA/cm2 to 31.9 mA/cm2 and 51.42% to 51.90% respectively. The work demonstrated here holds the promise for incorporating pom-CDs based materials in commercially available solar devices for developing ultrahigh efficiency photovoltaic cells in the future

Introduction

The advance of clean and renewable energy is fundamental to meet ever-increasing global energy demands arising from fast economic expansion and rising world population, while minimizing pollution, fossil-fuel depletion and global warming[1]. At present, new technologies for energy conversion (e.g., solar cells and fuel cells) and energy storage (e.g. Supercapacitors and batteries) are under demanding research. Because the performance of these devices depends strongly on the materials employed. The various promising nanomaterials with desired nanostructures and large surface areas have been developed for applications in energy–related devices.

Preparation of fluorescent carbon dots with diverse emitting colours from plant sources have been a current focus of research[2–5]. Carbon dots are obtained from carbonization of organic molecules. So, their optical properties (absorption and fluorescence) are different from their starting materials. Carbon dots have been used as alternatives for quantum dots and organic dyes due to their less toxicity, stable fluorescence, good biocompatibility and aqueous solubility[6–9]. In respect to photovoltaic, the spectral mismatch between the energy band gap (Eg) of the photoactive layer and the photon energy distribution of the incident solar spectrum degrades device performance, that is, the loss of excessive photon energy (E>Eg) via non radiative relaxation[10] and the transmittance loss of sub-band gap ligh

(E<Eg). This discrepancy can be enhanced by shifting high-energy photons into lower energy photons[11].

Here we are focused on the Luminescence down-shifting phenomenon. Luminescence down-shifting (LDS) was originally proposed by Hovel et al[12] in order to overcome the low spectral response in the blue region of the solar spectrum in c-Si solar cells. The LDS process involves the modification of the incoming spectrum by absorbing light in the short wavelength region and shifting it to longer wavelengths where the spectral response of the solar cell is more efficient. In this paper, we present a simple and eco-friendly synthesis of CDs from fresh red pomegranate juice. The strongly photoluminescent as-obtained CDs exhibited an excitation-dependent emission behaviour, with the PL intensities dependent on the excitation wavelength showing red shift. Typically, synthesized CDs show the maximum Photoluminescence intensity at 400nm excitation wavelength. Pomegranate derived CDs luminescence properties and spectral convertors study have not been investigated in the previously. There are no reports on the IV characteristics properties of Pom-CDs by hydrothermal method. Herein, Pom-CDs are proposed to be a promising UV-absorbing spectral converter for c-Si solar cells since it exhibits broadband absorption in the whole UV region of 350–500 nm and emits intense visible lights. In this work, we aim to enhance the absorption in blue region and red luminescence by introduction of Pom-CDs. The photoluminescence properties and IV study of solar cell were investigated in details.

2. Experimental

2.1 Material Preparation

Red pomegranate was purchased from local market of Nagpur, India. All the chemical agents in the research were analytically pure without further purification. The double distilled water was used throughout the experiments

2.2 Synthesis of pomegranates juice derived C-Dots:-

The C-dots were prepared by hydrothermal treatment of fresh pomegranates juice in water as shown in fig.1. The preparation of fluorescent CDs from pomegranates was carried out as follows. 10 mL of pomegranates juice was transferred into 80mL Teflon-Lined autoclave and heated at 160 °C for 6 h. After the reaction is over, the autoclave was cooled down naturally; resulted yellow aqueous solution was obtained. The large particles were removed from yellow aqueous solution by centrifugation at 5000 rpm for 30 min. A clear yellow solution of highly fluorescent pom-CDs was obtained. The as-prepared pom-CDs were finally diluted in water for further characterization and use. Highly concentrated C-dots in water shows yellow color (light) confirms the formation of c-dots. The prepared c-dots were showing greenish yellow color at 380nm excitation.

Fig.1. Schematic illustration for the hydrothermal synthesis of c-dots from Pomegranates juice having green photoluminescence.

2.3 Deposition of Luminescence Downshifting layer of Pom-CQDs:

Pom-CDs were deposited directly onto the surface of solar cell using spray coating technique. Before coating the c-Si solar cell surface were cleaned with acetone repeatedly and dried at room temperature. The coating solution was prepared with particular concentrations of Pom-CDs, the solution of c-dots used for spraying. The Particular concentrations of Pom-CDs were spray coated and kept for drying at room temperature.

Characterizations

All the spectroscopic studies were carried out using prepared solution of carbon dots loaded into quartz cuvettes. Photoluminescence, PLE spectra recorded using Shimandzu 5301PC spectroflurometer with 1.5nm slit width. I–V measurements were performed using a solar simulator with Xe arc lamp and an AM 1.5 global filter. Four-wire I–V measurements (Metrohm Potentiostat 128N) were conducted at 25°C under a simulated AM 1.5G spectrum at one-sun intensity.

Results and Discussion:

Red pomegranates juice was selected as the green and natural precursors for the fabrication of CDs. After hydrothermal treatment, some yellow or light brown solutions are achieved, implying the formation of CDs. To characterize the fluorescent properties of Pom-CDs, we carried out photoluminescence (PL) measurements. The excitation dependent photoluminescence mechanism of the carbon dots has not yet been utilized for improving the spectral response of solar cell. Therefore, in depth and systematic investigation is required to verify the competence of c-dots as luminescent downshifting layer from previous literature. This confirmed that the bright fluorescence originated from the synthesized carbon dots (Fig. 2). Yellow solution of pom-CDs strongly absorbs at 350-500 nm with maximum at 460nm fig.2 (a) and it shows wide absorption band range because of different size distribution pom-CDs in water suspension. As shown in Fig. 2b, with an increase in the excitation wavelength from 360 nm to 500 nm by an increment of 20nm, the emission from Pom-CDs gradually shifted to higher wavelengths accompanied by a decrease in fluorescence intensity. The emission spectra of the carbon dots was broad, ranging from 490 (violet) to 553 nm (green), with a dependence on the excitation wavelengths. A most intense broad emission peak at 505 nm is observed when the sample is excited by 400nm as shown in fig 2(b). The CDs also show excitation-dependent PL emissions ranging from 490 to 553 nm, in which the PL emission peaks shift to longer wavelengths as the excitation wavelength increases, along with a decrease in their PL intensities. It is noted that the excitation dependent emission may be associated with the anti-Stokes photoluminescence of CDs[13]
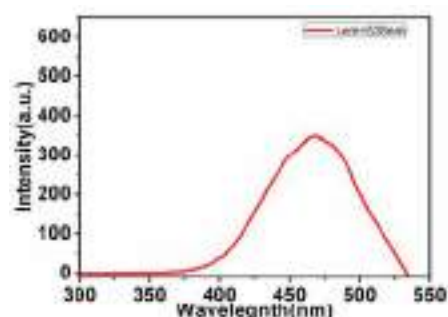
Fig. 2(a) Excitation spectra of Pom-CDs dots monitored at emission wavelength 538nm.
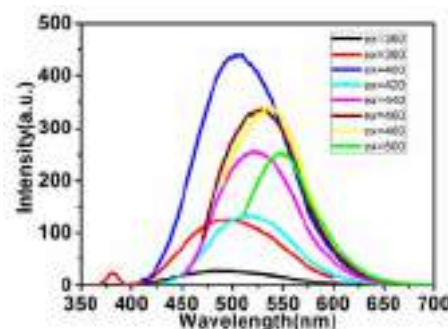
Fig.2 (b) Photoluminescence emission spectra of carbon dots at different excitation wavelengths from 360 to 500 nm for 6hrs.

The spectra display a typical excitation wavelength dependent characteristic, and the emissive wavelength is red shifted under excitation with longer wavelengths[14,15]. The PL spectral shift with excitation wavelength is a fundamental feature of radiative recombination caused by the quantum confinement effect because the size distribution induces a corresponding distribution of the energy gaps. Significantly, the as-obtained CQDs can freely disperse in water with transparent appearance without further ultrasonic dispersion, and exhibit good photostability, that is, luminescence properties and appearance remains unchanged after storing for one year in air at room temperature.
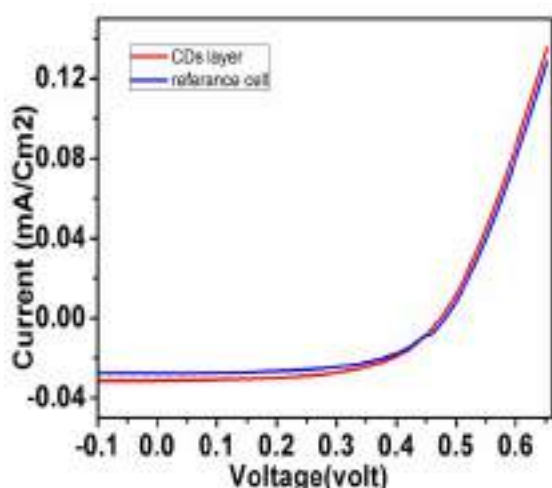
Fig.3 Current versus voltage (I–V) characteristics of c-Si solar ells with and without Pom-CDs layer measured under 1 sun, AM 1.5 G simulated solar illumination.

In the present study, the introduction of Pom-CDs layer applying to front surface on the C-si solar cells leads to the increase of short-circuit current (Isc) from 26.91mA/cm² to 31.9mA/cm² and fill factor (FF) from 51.42% to 51.90% due to the photon downshifting effect of Pom-CDs by absorbng UV light and convert UV photons into visible photons. The optical improvement due to the downshifting effect of Pom-CDs gives rise to a high efficiency of 9.09 %. The detailed photovoltaic parameter for Pom-CDs is presented in table. The realization of high efficiency Pom-CDs based c-Si solar cells demonstrated here makes Pom-CDs attractive for large area, high efficiency, and commercially available cell production in future. Therefore, the enhancement in cell efficiency can indeed be attributed to the increase in photocurrent and light absorption.

Table 1:- Performance Details of the solar cells studied in this work with and without layer of Pom-CDS

Sample	Isc(mA/cm²)	Voc(volt)	FF (%)	η
Reference cell	26.91	0.6533	51.42	7.26
CDS layer	31.9	0.6549	51.90	9.09

Conclusions

In this work, a simple, low-cost and one-step hydrothermal treatment of Pomegranates juice has been demonstrated for the synthesis of water-soluble carbon dots (C-dots). The strongly photoluminescent C-dots exhibited an excitation-dependent emission behavior, interesting downshifting photoluminescent property. The CDs layers absorbed UV light and emit visible light by energy-down-shifting. The rapid fabrication of CDs combined with c-Si solar cell bearing wavelength dependent photoluminescence behavior significantly enhances the photo-response of solar cell achieving an efficiency of 9.09 %compare to 7.26% in bare cell. The combination of spray coated Pom-CDs layer on top of c-Si solar cell considerably enhanced the short circuit current and power conversion efficiency of c-Si solar cell. The pomegranates juice derived carbon dots could be directly applied to front surface of photovoltaic cell in future. It is expected that the Pom-CDs LDS layer demonstrated in this work will have important applications in future high efficiency, low-cost solar cells.

Acknowledgements

References

1   T. Q. Duong, Annu. Prog. Rep. Energy Storage Res. Dev., 2002, 8111.

2   S. Sahu, B. Behera, T. K. Maiti and S. Mohapatra, Chem. Commun., 2012, 48, 8835.

3   H. Huang, J.-J. Lv, D.-L. Zhou, N. Bao, Y. Xu, A.-J. Wang and J.-J. Feng, RSC Adv., 2013, 3, 21691.

4   J. Wang, Y. H. Ng, Y.-F. Lim and G. W. Ho, RSC Adv., 2014, 4, 44117–44123.

5   B. S. B. Kasibabu, S. L. D'souza, S. Jha, R. K. Singhal, H. Basu and S. K. Kailasa, Anal. Methods, 2015, 7, 2373–2378.

6   S. N. Baker and G. A. Baker, Angew. Chemie Int. Ed., 2010, 49, 6726–6744.

7   H. Li, Z. Kang, Y. Liu and S.-T. Lee, J. Mater. Chem., 2012, 22, 24230.

8   P. G. Luo, S. Sahu, S.-T. Yang, S. K. Sonkar, J. Wang, H. Wang, G. E. LeCroy, L. Cao and Y.-P. Sun, J. Mater. Chem. B, 2013, 1, 2116.

9   V. Singh and A. K. Mishra, Sensors and Actuators B-Chemical, 2016, 227, 467–474.

10   A. Marti and G. L. Araujo, Sol. Energy Mater. Sol. Cells, 1996, 43, 203.

11   B. M. van der Ende, L. Aarts and A. Meijerink, Phys. Chem. Chem. Phys., 2009, 11, 11081–95.

12   H. A. Ahmed, J. Walshe, M. Kennedy, T. Confrey, J. Doran and S. J. McCormack, Adv. Energy Res., 2013, 1, 117–126.

13   J. Shen, Y. Zhu, C. Chen, X. Yang and C. Li, Chem. Commun., 2011, 47, 2580–2582.

14   L. Wang and H. S. Zhou, Anal. Chem., 2014, 86, 8902–8905.

15   Y.-Q. Zhang, D.-K. Ma, Y. Zhuang, X. Zhang, W. Chen, L.-L. Hong, Q.-X. Yan, K. Yu and S.-M. Huang, J. Mater. Chem., 2012, 22, 16714.

ARTICLE

Kaluza Klein Type FRW Cosmological Model with Extended Chaplygin Gas

S. Khadekar,*[a] N. A. Ramtekkar [b]

Abstract: In this paper we have proposed the extended Chaplygin gas equation of state of the form $p = \sum_n A_n \, \rho^n - B(H)/\rho^\propto$, where $B(H) = B_0 H^{-m}$, A, m $\propto$ are positive constants as a model of dark energy for which it recovers barotropic fluids with quadratic equation of state. We have obtained scale factor dependence energy density for particular values of n, m, $\propto$ and observed that Hubble expansion parameter and dark energy density are decreasing with increasing n. Similarly for arbitrary values of n, m and $\propto$ we have also obtained evolution of scale factor, Hubble expansion parameter, time dependent dark energy density and deceleration parameter in the frame work of Kaluza Klein type FRW cosmological model
Keywords: Kaluza Klein cosmology, Extended Chaplygine gas

INTRODUCTION

An interesting model to describe dark energy is Chaplygin gas [7, 8]. Pure Chaplygin gas (CG) obeys equation of state [9] of the form,

$$p = -\frac{B}{\rho}, \tag{1}$$

where p and ρ are pressure and energy density respectively and B is positive constant.Which is not consistent with observational data [10]. Therefore, an extension of Chaplygin gas model is praposed [11-13], which is called generalized Chaplygin gas (GCG).

The equation of state (EoS) for GCG is given by

$$p = -\frac{B}{\rho^\alpha}, \tag{2}$$

where B is positive constants and $0 \le \alpha \le 1$. At high energy GCG behaves almost like a pressure less dust where as at low energy regime it behaves like a dark energy (DE), its pressure being negative and almost constant. Thus GCG smoothly interpolates between a nonrelativistic matter dominated phase in the early universe with a DE dominated phase in the late universe. This interesting property of GCG has motivated cosmologist to consider it as a candidate for dark matter and DE models. It is also possible to study viscosity in GCG [14-19]. However, observational data ruled out such a proposal. Then GCG was extended to the modified Chaplygin gas (MCG)

[20]. The MCG equation of state has two parts : the first term gives an ordinary fluid obeying a linear barotropic EoS, and the second term relates pressure to some power of the

inverse of energy density. So here we are essentially dealing with a two-fluid model.

Modified Chaplygin gas obeys EoS of the form,

$$p = A\rho - \frac{B}{\rho^\alpha}, \tag{3}$$

where $0 < A < 1/3 , 0 \le \alpha \le 1$ and B are positive constants. However, it is possible to considerbarotropic fluid with quadratic EoS or even with higher order EoS [29,30]. Therefore, it is interesting to extend MCG EoS which recovers at least barotropic fluid with quadratic EoS.

Here we have proposed an extended model of Chaplygin gas as a model for dark energy which recovers barotropic fluid with quadratic equation of state. We also discussed the resulting equation of state parameter and investigated numerically the behaviour of some cosmological parameter such as scale factor, Hubble expansion parameter, energy density and deceleration parameter.

In this paper we introduced the extended Chaplygin gas equation of state proposed by [Pourhassan and Kahya (2014)] as defined in Eq. (4) and study the behaviour of different cosmological parameters by choosing B as a function of Hubble paramtere in the frame work of Kaluza Klein theory of gravitation.

$$p = \sum_n A_n \rho^n - \frac{B}{\rho^\alpha}. \tag{4}$$

This paper is organized as follows: In section 2 we have obtained Einstein field equations for five-dimensional space time. In section 3 we consider extended Chaplygin gas model with $B(H) = B_0 H^{-m}$, and discussed behaviour of different cosmological parameters. Here we have obtain solution for the arbitrary value of n and m with $\propto = 1/2$ and discussed its graphical representation in subsections. In section 4 we have obtain deceleration parameter and compare results with the observational data. In section 5 we have discussed results obtained for different cases and give conclusion.

Field equations and their solutions:

The Kaluza Klein type Friedmann–Robertson-Walker (FRW) universe is described by following metric,

$$ds^2 = dt^2 - a^2(t)[dr^2 + r^2(d\theta^2 + \sin^2\theta \, d\phi^2) + d\psi^2] \tag{5}$$

where a(t) is the scale factor.

The Einstein's field equations are given by:

$$R_\upsilon^\mu - \frac{1}{2} R g_\upsilon^\mu = T_\upsilon^\mu, \tag{6}$$

where T_υ^μ is energy momentum tensor. It is assumed that our universe is filled with the extended Chaplygin gas which plays role of dark energy with equation of state (4). In this case energy momentum tensor can be written as follows:

$$T_\upsilon^\mu = (p + \rho)\delta_0^\mu \delta_\upsilon^0 - p\delta_\upsilon^\mu, \tag{7}$$

where $\rho(t)$ is the energy density and $p(t)$ is the isotropic pressure. Also, $u^0 = 1$ and $u^i = 0 \, (i = 1, 2, 3)$ with $g^{\mu\upsilon} u_\mu u_\upsilon = 1$.

Einstein field equation for the metric (5) and energy momentum tensor (7) in higher dimensional space time are given by

$$H^2 = \frac{\dot{a}^2}{a^2} = \frac{\rho}{6}, \tag{8}$$

$$\frac{\ddot{a}}{a} + \frac{\dot{a}^2}{a^2} = \frac{-p}{3}. \tag{9}$$

We assume law of conservation of energy $(T_{:j}^{ij} = 0)$ which gives,

$$\dot{\rho} + 4H(\rho + p) = 0. \tag{10}$$

Extended Chaplygin gas equation of state:

For the study of behaviour of different cosmological model here we have consider extended Chaplygin gas equation of state (4) with B as function of Hubble expansion parameter of the form:

$$B(H) = B_0 H^{-m}. \tag{11}$$

In this case equation of state (4) extended to the following form,

$$p = \sum_n A_n \rho^n - \frac{B_0 H^{-m}}{\rho^\alpha}. \tag{12}$$

By using Eq. (8) in Eq. (12) we get,

$$p = \sum_n A_n \rho^n - \frac{B_0 \sqrt{6}^m}{\rho^{\alpha + \frac{m}{2}}}. \tag{13}$$

To get the special solution for the following particular cases we have consider only last term of expansion in Eq. (13).

3.1 n = 1:

For this case if we assume $A_1 = A$, the equation of state for extended Chaplygin gas defined in Eq. (13) reduces to,

$$p = A\rho - \frac{B_0 \sqrt{6}^m}{\rho^{\alpha + \frac{m}{2}}}. \tag{14}$$

By using Eq. (14) in Eq. (10), we get following energy density,

$$\rho = \left[\frac{B_0 \sqrt{6}^m}{1 + A} + \frac{C}{a^{4(1 + \alpha + m/2)(1+A)}} \right]^{\frac{1}{1 + \alpha + m/2}} \tag{15}$$

where C is constant of integration.

By using Eq. (15) in Eq. (8) Hubble parameter is defined as:

$$H = \frac{\dot{a}}{a} = \frac{1}{\sqrt{6}} \left[\frac{B_0 \sqrt{6}^m}{1 + A} + \frac{C}{a^{4(1 + \alpha + m/2)(1+A)}} \right]^{\frac{1}{2(1 + \alpha + m/2)}} \tag{16}$$

By using numerical method we have solved the Friedmann equation and obtain the time dependent of scale factor in plots of Fig.1 (a) and (b) for different parameters.

Here we have fix A, B, m and observed the behaviour of scale factor for different values of α. Fig. 1(a) shows that scale

factor increases with increasing α in early universe and Fig. 1(b) shows that it decreases with increasing n in late universe.

In Fig. (2) we have fix A, m, and α and for varying B it is find that in the early universe value of B is not important and it is reasonable because density is high at the initial stage and second term of equation of state become negligible. In Fig. (3) we take A = (1- α)/(1+ α), B = 3, m = 2 and represent behaviour of scale factor for different values of α. Fig. (3) shows that scale factor increases with increasing α.

3.2 Arbitrary n, m and α =1/2:

In the above subsections we have discussed cases for arbitrary n and particular values of m and α. By generalizing results obtained for different values of n and m we obtain expression of energy density for following two cases:

3.2.1 Arbitrary n, m is odd and α =1/2:

$$\rho = \left[\frac{\gamma a^{6+2m} + Ca^{-4a\left[\frac{3+m}{2} + \sum_n \left(n+\frac{m+1}{2}\right)\gamma^{n-1}\right]}}{a^{6+2m}} \right]^2 \qquad (17)$$

where γ is root of the equation,

$$(A+1)\gamma^{\frac{m+3}{2}} + A\sum_n \gamma^{n+\frac{m+1}{2}} - B_0\sqrt{6^m} = 0. \qquad (18)$$
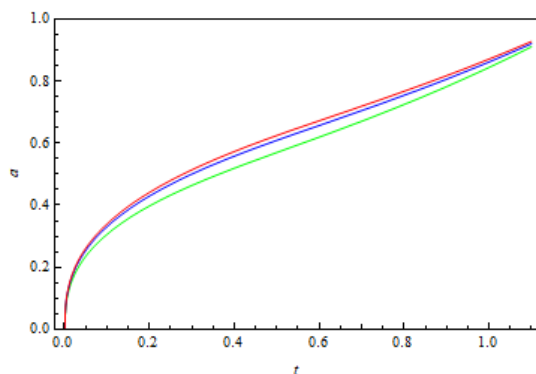
(a)
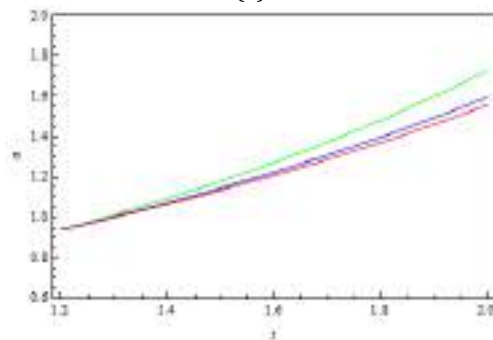
(b)

Fig.1: Scale factor versus time for B=3, A=1/3, m=2,

α = 0.1 (green line), α =0.7 (blue line), α = 1(red line)
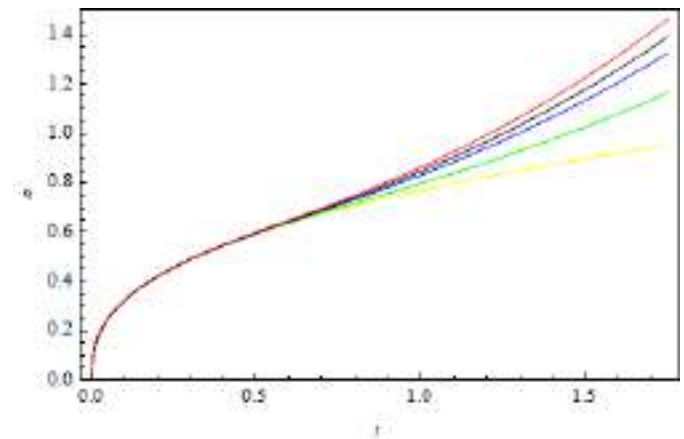
Fig.2: Scale factor versus time for A=1/3, m=2, α = 0.5, B = 0 (yellow line), B =0.6 (green line), B=1.8 (blue line), B=2.5 (black line), B= 3.4 (red line)
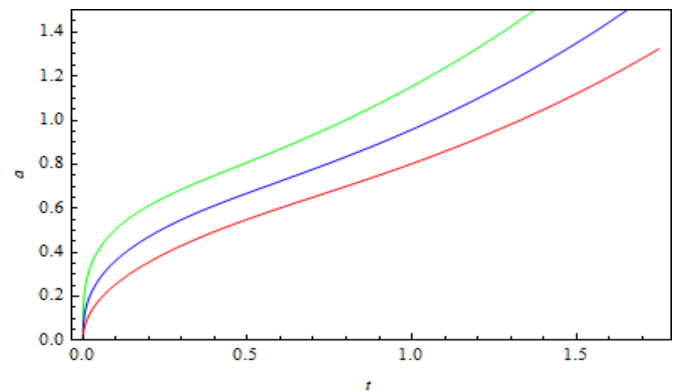
Fig.3: Scale factor versus time for B=3, A=1- α /1+ α, m=2 α =0.1 (green line), α =0.5 (blue line), α =0.9 (red line)

(a)

(b)
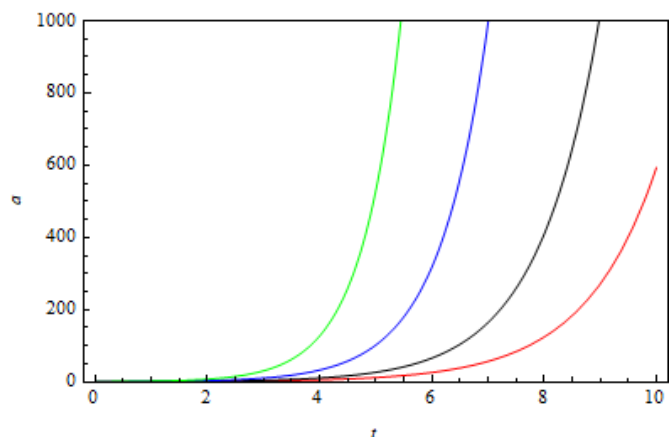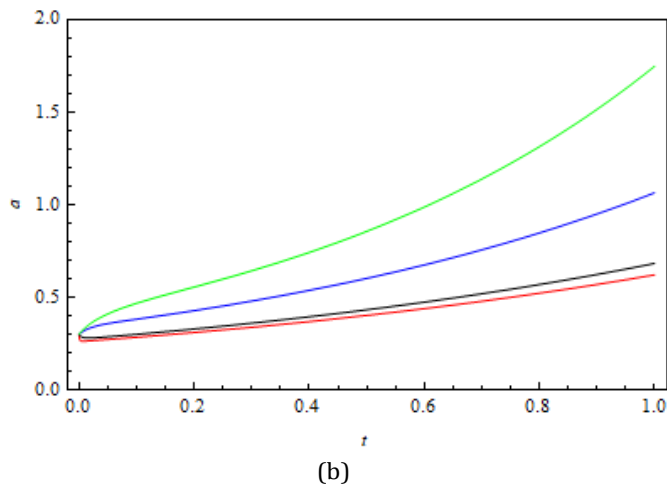
Fig.4: Scale factor versus time for B=3, A=1/3, m = 1, α = 0.9, n = 1 (green line), n = 2 (blue line), n = 3(black line), n = 4 (red line)**.**
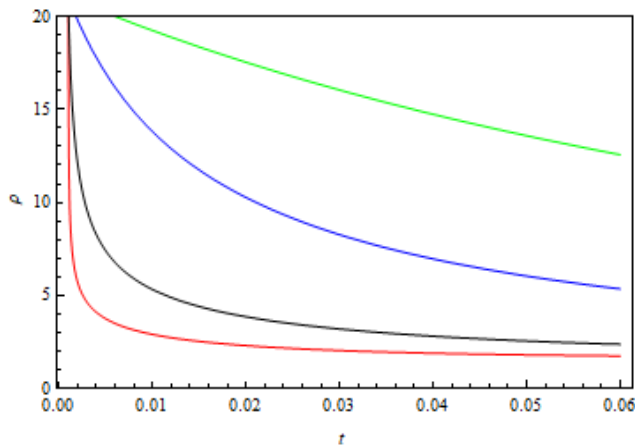
3.2.2 Arbitrary n, m is even and α =1/2:

$$\rho = \left[\frac{\xi a^{6+2m} + Ca^{-2a\left[3+m+\sum_{n}(2n+m+1)\xi^{2(n-1)}\right]}}{a^{6+2m}} \right]^2 \quad (19)$$

where ξ is root of the equation,

$$(A+1)\xi^{m+3} + A\sum_{n}\xi^{2n+m+1} - B_0\sqrt{6^m} = 0. \quad (20)$$

3.3 Arbitrary n, m and α:

For arbitrary values n, m and α we define differential equations for different cosmological parameters.

Using Eq. (8) and (13) in (9) and by assuming $A_n = A$ we get the following second order differential equation in terms of scale factor:

$$2\frac{\ddot{a}}{a} + \frac{\dot{a}^2}{a^2} + \frac{1}{3}\sum_{n}6^n A\left(\frac{\dot{a}}{a}\right) - B_0 6^{\frac{m}{2}+1}\left(\frac{\dot{a}}{a}\right)^{-2\left(\alpha+\frac{m}{2}\right)} = 0,$$

(21)

We can solve Eq. (21) numerically to obtain behaviour of scale factor versus time. Fig. (5) shows that increasing n decreases value of scale factor and Fig. (6) shows variation of scale factor against varying n at the early universe.
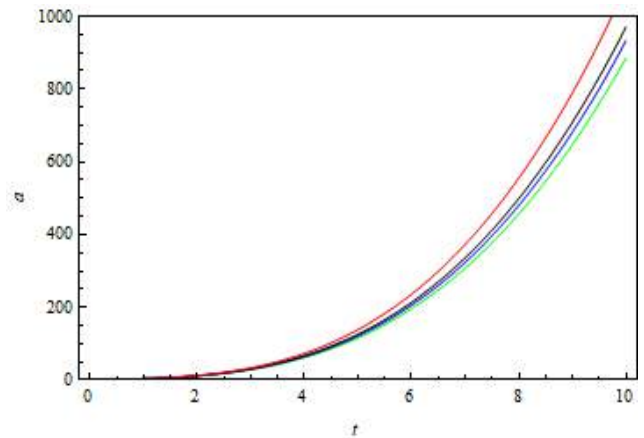
Fig.5: Scale factor versus time for B=3, A=1/3, m = 2, α = 0.11 (green line), α =0.9 (blue line), α =0.5 (red line)**.**

$$\dot{\rho} + \frac{4}{\sqrt{6}}\left[\rho^{\frac{3}{2}} + A\left(\sum_{n}\rho^{n+\frac{1}{2}}\right) - B\sqrt{6^m}\rho^{-\left(\alpha+\frac{m-1}{2}\right)}\right] = 0$$

(22)

To study nature of dark energy density solved Eq. (31) numerically. Results of numerical analysis are represented by Fig. (8) to Fig. (10). From the figures, it is clear that energy density is decreasing function of time. In the Fig (8) and (9) we can see that energy density decreases with increasing n and decreasing m. Fig. (10) shows that value of α doesn't affect energy density.

By using Eq. (8) we can rewrite Eq. (9) as follows:

Fig.6 Energy density versus time for B=3, A=1/3, m = 2, α =0.9, n = 1 (green line), n = 2 (blue line), n = 3 (black line), n = 4 (red line)**.**
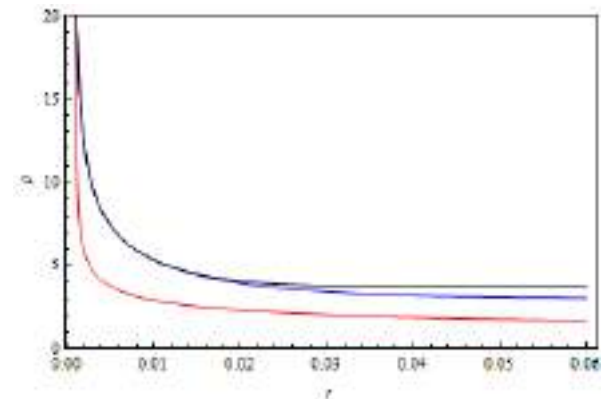
Fig.7: Energy density versus time for B=3, A=1/3, n = 4, α = 0.3, m = 1 (red line), m = 6 (blue line), m = 11 (black line).
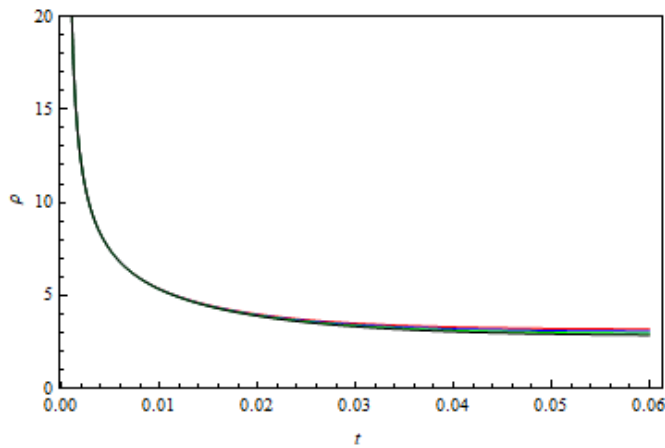
Fig.8: Scale factor versus time for B=3, A=1/3, n = 3, m = 6, α = 0.1 (red line), α =0.3(blue line), α =0.5 (green line), α =0.7 (black line).
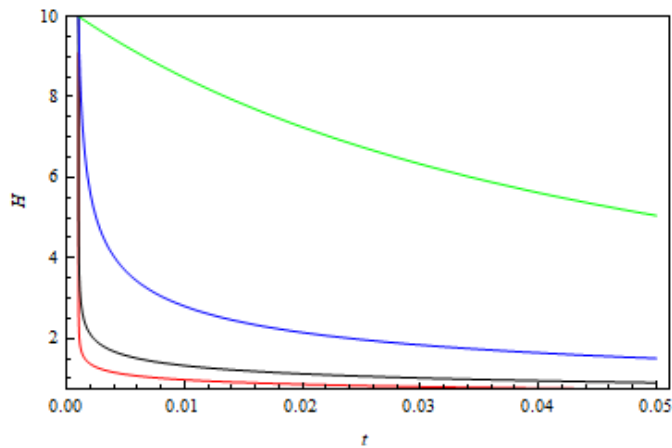
$$\dot{H} + 2H^2 = \frac{-p}{3}. \text{(23)}$$

Using Eq. (8) and Eq. (13) in Eq. (32), we get following differential equation for Hubble expansion parameter

$$\dot{H} + 2H^2 + \frac{1}{3}\left[A6^n H^{2n} - B6^{-\alpha} H^{-2(\alpha+m/2)} \right] = 0. \text{(24)}$$

Numerical solution of above equation is represented by Fig. (9) and shows that similar to energy density Hubble expansion parameter is decreases with increasing n.

4. Deceleration parameter

In section 3.3 we have discussed behaviour of scale factor, energy density and Hubble expansion parameter by using numerical solutions. Since we cannot study analytical behaviour of these parameters from Eq. (30), (31) and (33) we would like to find one more parameter to get detailed information about the dynamics.

The deceleration parameter is an important parameter in cosmology which describes cosmic dynamics for the late time

acceleration. A positive deceleration parameter represents a decelerating universe, negative value describes accelerating universe and q=0 shows expansion of universe with constant rate. The deceleration parameter is given by

$$q = -\left(\frac{\dot{a}}{a} \right)^{-2} \frac{\ddot{a}}{a} = -1 - \frac{\dot{H}}{H^2} \qquad (25)$$

Using Eq. (8) and (13) in Eq. (34) we get

$$q = 1 + 2\left[\sum_n A\rho^{n-1} - \frac{B\sqrt{6^m}}{\rho^{\frac{m}{2}+\alpha+1}} \right]$$

(26)

At the early universe with high density the deceleration parameter may be reduced to the following expression:

$$q = 1 + 2\left[\sum_n A\rho^{n-1} \right] \qquad (27)$$

In the case of n = 1 and A = -1 we recover results of Λ CDM where q = -1.

On the other hand late time behaviour (low density limit) of deceleration parameter may be described by

$$q = 1 - 2B\rho^{-(\alpha+1)} \qquad (28)$$

Again, special case of α = -1 and B =1 gives q=-1.

5 Conclusion

In this paper we present FRW cosmological models of dark energy with extended Chaplygin gas of the form

$$p = \sum_n A_n \rho^n - \frac{B_0 H^{-m}}{\rho^\alpha},$$

where A, B_0, m and α are positive constants. From which we get barotropic fluids with quadratic equation of state. We

Fig.9: Hubble parameter versus time for B =3, A =1/3. M =2, α = 0.9, n = 1 (green line), n = 2 (blue line), n = 3 (black line), n = 4(red line).
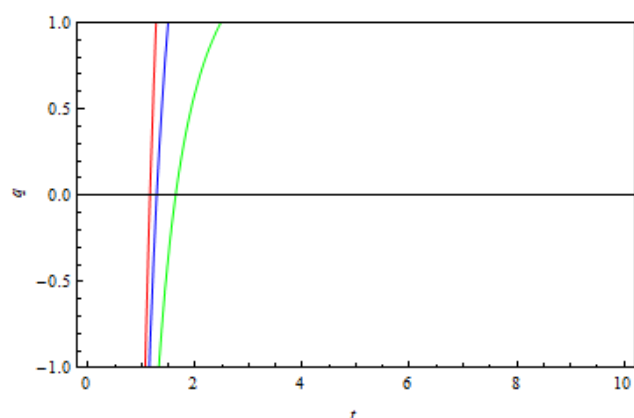
Fig.10: Deceleration parameter versus time for B =3, A =1/3. M =2, α = 0.7, n = 1 (green line), n = 2 (blue line), n = 3(red line).

have obtained scale factor dependence energy density for particular values of n, m and α , and observed that Hubble expansion parameter and dark energy density are decreasing with increasing n. Similarly, for arbitrary values of n m, α we have also obtained evolution of scale factor, Hubble expansion parameter, time dependent dark energy density and deceleration parameter.

By using numerical method, we have solved the Friedmann equation and obtain the time dependent of scale factor in plots of Fig. (1)-a and (1)-b for different parameters.

Here we have fix A, B, and m, and observed the behaviour of scale factor for different values of α . Fig. (1)-a shows that scale factor increases with increasing α in early universe and Fig. (1)-b shows that it decreases with increasing n in late universe.

In Fig.2 we have fix A and α and for varying B it is find that in the early universe value of B is not important and it is reasonable because density is high at the initial stage and second term of equation of state become negligible.

Behaviour of cosmological parameters such as energy density, Hubble expansion parameter, deceleration parameter discussed by using numerical methods. It is found that energy density is decreasing function of time and it decreases with increasing n and decreasing m. Similar to energy density Hubble expansion parameter is decreases with increasing n.

Then we investigated nature of deceleration parameter in early time and late time universe.

5 References

[1]   A. Kamenshchik, U. Moschella, and V. Pasquier, "An alternative to quintessence," *Physics Letters, Section B*, vol. 511, no. 2–4, pp. 265–268, 2001.

[2]   M. C. Bento, O. Bertolami, and A. A. Sen, "Generalized Chaplygin gas, accelerated expansion, and dark-energy-matter unification," *Physical Review D*, vol. 66, Article ID043507, 2002.

[3]   V. Gorini, A. Kamenshchik, U.Moschella, and V. Pasquier, "The Chaplygin gas as a model for dark energy," in *Proceedings of the 10th Marcel Grossmann Meeting*, pp. 840–859, Rio de Janeiro, Brazil, 2003.

[4]   N. Bilic, G. B. Tupper, and R. D. Viollier, "Unification of dark matter and dark energy: the inhomogeneous Chaplygin gas," *Physics Letters B*, vol. 535, pp. 17–21, 2002. Advances in High Energy Physics 11

[5]   D. Bazeia, "Galileo invariant systemand themotion of relativistic *d*-branes," *Physical ReviewD*, vol. 59, no. 8, Article ID085007, 1999.

[6]   L. Xu, J. Lu, and Y. Wang, "Revisiting generalized chaplygin gas as a unified dark matter and dark energy model," *European Physical Journal C*, vol. 72, no. 2, pp. 1–6, 2012.

[7]   H. Saadat and B. Pourhassan, "Effect of varying bulk viscosity on generalized chaplygin gas," *International Journal of Theoretical Physics*, vol. 53, no. 4, pp. 1168–1173, 2014.

[8]   X.-H. Zhai, Y.-D. Xu, X.-Z. Li et al., "Viscous generalized chaplygin gas," *International Journal of Modern Physics D*, vol. 15, p. 1151, 2006.

[9]   Y.D. Xu, Z. G. Huang, and X.H. Zhai, "Generalized Chaplygin gas model with or without viscosity in the w-w plane," *Astrophysics and Space Science*, vol. 337, no. 1, pp. 493–498, 2012.

[10]   H. Saadat and B. Pourhassan, "FRW bulk viscous cosmology with modified Chaplygin gas in flat space," *Astrophysics and Space Science*, vol. 343, no. 2, pp. 783–786, 2013.

[11]   H. Saadat and H. Farahani, "Viscous Chaplygin gas in non-flat universe," *International Journal ofTheoretical Physics*, vol. 52,no. 4, pp. 1160–1164, 2013.

[12]   A. R. Amani and B. Pourhassan, "Viscous generalized Chaplygin gas with arbitrary α," *International Journal of Theoretical Physics*, vol. 52, no. 4, pp. 1309–1313, 2013.

[13]   U. Debnath, A. Banerjee, and S. Chakraborty, "Role ofmodified Chaplygin gas in accelerated universe," *Classical and Quantum Gravity*, vol. 21, no. 23, pp. 5609–5617, 2004.

[14]   E. V. Linder and R. J. Scherrer, "Aetherizing Lambda: barotropic fluids as dark energy," Physical Review D, vol. 80, no. 2, Article ID 023008, 2009.

[15]   F. Rahaman, M. Jamil, and K. Chakraborty, "Revisiting the classical electron model in general relativity," Astrophysics and Space Science, vol. 331, no. 1, pp. 191–197, 2011.

[16]   B. Pourhassan and E. O. Kahya, "FRW Cosmology with the Extended Chaplygin Gas", Hindawi Publishing Corporation Advances in High Energy Physics, Volume 2014, Article ID 231452.

ARTICLE

The effect of acid on compressive strength of fly ash composite

Swati Joshi,*a S.K.Ubalea and S.J. Dhobleb
aDepartment of Physics, M.P.Deo Dharampeth Science College, Nagpur -440033, India
bDepartment of Physics, RTM Nagpur University, Nagpur -440033, India
Corresponding Author: sjdhoble@rediffmail.com

Abstract: The present paper deals with an investigation into durability of fly ash composite when exposed to solutions of hydrochloric acid and sulphuric acid of different concentrations. The fly ash composite is manufactured by using a class F fly ash and alkaline activators. The fly ash is the solid waste that is obtained as a by-product after burning of pulverised coal in thermal power station. Due to huge production, the fly ash disposal is a major concern to world that is responsible for enviroment degradation. This fly ash could be reused, recycled and can be compounded with suitable inorganic chemicals to get some value added products. The composites were prepared by compounding fly ash, lime and sodium hydroxide.The fly ash composite test samples prepared were immersed in sulphuric acid and hydrochloric acid solutin for 28 days. The main parameters studied were the physical properties, evolution of weight, compressive strength. The change in weight implies absorption property and sustainability in compressive strength indicates the durability. Compressive strength is a very important parameter for the design of structures. Result shows that the composites, which were subjected to acid test, have a direct relationship between the ability of composite to resist sulphuric acid and hydrochloric acid. In case of acidic environment, compressive strength of composited shows a varied result hence these samples can be converted into value added commercial product, which can be termed as the effective utilisation of fly ash as a waste management

Keywords : Fly ash composite, environment degradation, compressive strength.

Introduction

In India, major problems faced by coal based thermal power plants are the handling and disposal of fly ash. Fly ash is generally captured by electrostatic precipitators or in filter fabric collectors in dry mode, which is further, dumped in ash yard or ash pond. Technological improvements in thermal power plant operations and fly ash collection systems, electrostatic precipitator, have improved the collection of fly ash. Ash handling is a big task in power station. A fly ash at ESP is collected on dry basis in the big bags and directly loaded on the transport vehicle or in ash storage silo. Fly ash is having a huge production hence it should be utilised quantitatively so that it will be used up to full extent. The fly ash is disposed off as a waste material into several hectors of valuable land as ash pond through ash pipes. This land degradation can be reduced by increased utilization of fly ash and efforts are needed to use fly ash in environmental friendly way also. Thus, land requirement for disposal of fly ash can be controlled and minimised by effective utilisation of fly ash. At present fly ash is used in various sectors such as cement, filler, road embankments, brick manufacturing and tile manufacturing etc. The fly ash used for the making of composite was collected from the coal fired

thermal power plant of Khaperkheda, Nagpur, India. A cenospheres, a part of bottom ash, is a lightweight, inert, hollow sphere made largely of silica and alumina and filled with air or inert gas, typically produced as a by-product of coal combustion at thermal power plants. The cenospheres are used in a wide variety of materials i.e. paints and finishes to plastics and sealing. Although they have been used in concrete for some time, their use is not widely known. The fly ash particles are typically spherical. These are finer than portland cement and lime particles. The particle size of F type fly ash ranges in diameter from 1 micron to 150 micron [1]. The composite is made up from the alkali activated fly ash have good compressive strength hence can be used for flooring tiles, pavements or blocks. Compressive strength development is a primary measure of the utility of materials used in different applications of the construction industry [2]. For investigating the durability of these tiles over acid attack of different concentrations and its effect on their strength is studied. Our aim is to protect the composite from acid rain attack. *Acid rain* is caused by emissions of sulphur dioxide (SOX) and nitrogen oxide (NOX) from industries, which react with the water molecules in the atmosphere to produce *acids*. It can also be used for making sewage pipes and should be able to with stand in the acidic environment. Hence, it is decided that

composite should face the acid test with commonly found acids and should withstand in hot water. The concentration of acid used is 0.1 M or 1% concentrated likewise 2%, 3% and 4% acid were used.

2. Experimental

Specimens Preparation - For analysing the composition, the fly ash was subjected to chemical analysis. The principal constituents of fly ash were investigated and examined at Anacon laboratory, Nagpur. From the chemical analysis result, table no.1, it was found that the fly ash contained SiO_2(55.81%), Al_2O_3(25.41%), FeO_3(9.35%).

Table 1 Composition of fly ash

Sn	Compositions	% amount
1	Silica	55.81
2	Aluminium Oxide	25.41
3	Iron Oxide	9.35
4	Titanium Oxide	0.28
5	Manganese oxide	0.21
6	Calcium Oxide	1.28
7	Others	5.22

The composite was prepared by compounding sodium hydroxide and lime with fly ash in definite proportions. After proper mixing with the help of these mixture circular discs of fixed diameter (d) were prepared from the above composition by applying certain pressure in pressing machine. These discs were allowed to dry for 2 days and then kept in water for curing for 14 days and treated at 200 degree Centigrade to get experimental sample.

Test Procedure - Sulphuric acid is a strong mineral acid, which is soluble in all proportions of water. Attack by sulphuric acid which occurs in different forms can be considered as the most common cause of acid corrosion of composite [3]. The sample composites was immersed in the solutions of hydrochloric acid and sulphuric acid for 28 days. The aim is to analyse its corrosiveness and durability property at regular intervals.To study hot water effect, the fly ash composite sample was kept in hot water for 24, 48 and 72 hours at constant temperature 75 degree Centigrade.

3. Results and Discussion

Alkali-activation means a reaction between a strong alkalis and amorphous aluminosilicate material such as the coal fly ash results formation of aluminosilicate gel. The composite so formed is alumina-silicate polymer in alkaline environment. This alkali silicate is responsible for dissolution of raw materials and give rise to favorable strength [4].

3.1 Visual observations - Acid-exposed surface of the specimen shows the composite were remained structurally intact, no noticeable change in colour, firstly it was observed that it changed to slight yellowish in colour, no significant expansion or change in size; no visually observable cracks were found [5].

3.2 Hot water treatment – Hot water when treated with the specimen, firstly its compressive Strength increased and the get stabilised. The result of the different samples cured for different time shows the compressive strength (CS) goes on increasing as in table 2. The alkali activation due to temperature rises the remaining polymerization reaction that continues further to increase in CS and get stabilised with increased CS.

Figures 1 and 2 show the structural changes in fly ash pallets after HCl and H_2SO_4 treated sample.

Table 2. Effect of hot water

Sn	Hours of fly ash composite in hot water	Compressive strength in N/mm2
1	24	54.44
2	48	38.82
3	72	46.49

3.3 Acid (HCl & H_2SO_4) treatment on specimen –

The treatment of a composite with a strong acid may result in a direct attack on the aluminosilicate framework. This attack will cause breakage of the Si–O –Al bonds [2], increased number of Si–OH and Al–OH groups in the fly ash composite which directly affects the compressive strength. The chemical process of strengthening the composites under goes three steps; those are dissolution, orientation and hardening. Now due to breakage in the bonding of the composites depolymerisation takes place that affect the bonds for reduction in CS.

Table 3. Change in mass of composites in HCl Acid (all weights in gm).

Sn	No of days	HCl 1% weight	HCl 2% weight	HCl 3% weight	HCl 4% weight
1	0	52.93	53.13	53.81	53.21
2	7	67.31	66.51	67.67	67.43
3	14	67.9	66.9	68.94	68.59
4	21	68.46	67.25	69.23	69
5	28	68.88	67.29	69.44	69.41
6	32	57.15	57.52	59	59.44

The gain in mass shows in table 3 due to absorption of acid which later on evaporates from the pecimen but gain is very less. Figure 3 shows effect on compressive strength variation of fly ash with variations of acids treatment.

Fig 1. HCl treated specimen.

Fig 2. H_2SO_4 treated sample

Table 4. Compressive strength HCl treatment

Sn	HCl concentration% on composite	Compressive strength N/mm2
1	1	38.27
2	2	31.35
3	3	30.75
4	4	18.82

Table 5. Compressive strength H_2SO_4 treatment

Sn	H_2SO_4 concentration% on composite	Compressive strength N/mm2
1	1	35.29
2	2	29.6
3	3	27.01
4	4	23.83

Change in CS(%) = (CS4%-CS1%)/(CS1%)

The compressive strength which comes to be 23% less in case of sulphuric acid and 55% less in case of hydrochloric acid that indicates that CS is lowered similar trend was also reported by R.Kumar [8]
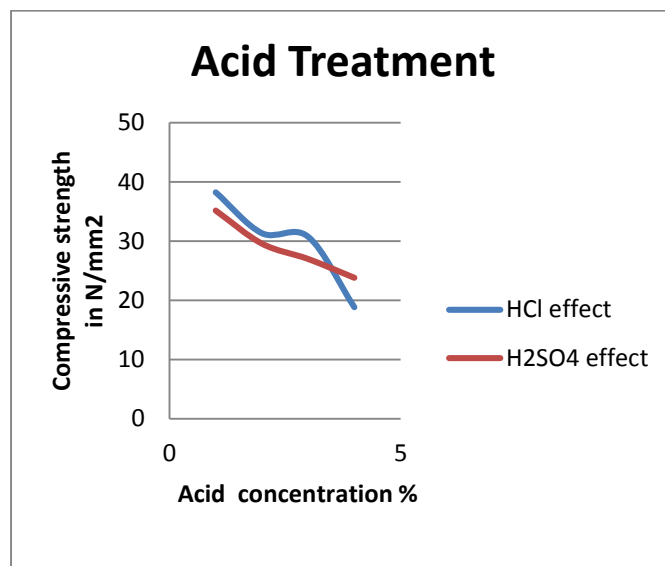
Fig 3. Effect on compressive strength of fly ash with variations of acids i.e. HCl and H_2SO_4 treatment in different concentrations.

The composite undergo depolymerisation of aluminosilicate polymers and liberation of silicic acid, replacement of Na and K cations by hydrogen ion and de-alumination of the crystlline structure which tends weakening of the Al-O-Si bond structure [4]. It is also connected to condensation of siliceous polymer, in the process of sulphuric acid attack deposition of specimen crystals inside pores, air voids or cenospheres, and probably shrinkage micro-cracks resulting from the leaching of sodium and calcium tends to cause internal stresses that ultimately lead to expansion of the fly ash composites layer.

4. Conclusion

Although there is decrease in the compressive strength of fly ash composites for all samples, significant decrease in compressive strength is observed when the concentration of HCl is equal to 4% while in case of H_2SO_4 the decreasing slope of compressive strength is not so stiff. It can be concluded that the prepared fly ash composite is durable sample that now can be used in acidic environment and can withstand hot atmosphere. Result shows that the composites which were subjected to acid test have a direct relationship between the ability of composite to resist sulphuric acid and hydrochloric acid. For long run, these composites can be converted into durable tiles or other usable products, which can definitely enhance the utilisation of fly ash.

5. Acknowledgement

6. References

1. Fly ash geopolymer concrete as future concrete by R.Ghosh, Anil Kumar, Sanjay Kumar, *International Journal of Advanced Scientific and Technical Research*, 2013, **3(6),** 260-271.

2. Effect of alkali-activator and rice husk ash content on strength development of fly ash and residual rice husk ash-based geopolymers , Chao-Lung Hwang, *Constructionand Building Materials*, 2015, **101**, 1–9.

3. Sulphuric acid attack on hardened paste of geopolymer cement , Ali Allahverdi, Frantisek Škvara ,*College of Chemical Engineering,* 2005,**05**, 221-229.

4. Mechanism and Chemical Reaction of Fly Ash Geopolymer Cement- A Review , A.M. Mustafa Al Bakri , H. Kamarudin , M.M.A. Abdullah, K. Hussin , *International Journal of Pure and Applied Sciences and Technology*, 2011,**01**, 1-10.

5. Resistance of the fly ash based geopolymer mortars in Sulfuric acid ,Suresh Thokchom , Partha Ghosh, Somnath Ghosh , *ARPN Journal of Engineering and Applied Sciences*, 2009, 4(1), 65-70.

6. Fly ash geopolymer pastes in sulphuric acid , Suresh Thokchom in *International Journal of Engineering Innovation & Research*, 2014, **6 (3),** 943-947.

7. Effect of geopolymer cement on microstructure, compressive strength and sulphuric acid resistance of concrete, E. Hewayde, M. Nehdi, *Magazine of Concrete Research,* 2006, **05**, 321–331.

8. Effect of acidic environment on self compacting concrete, P.K.Gupta, R.Kumar, *International Journal of Civil Engineering and Technology*y, 2017, **8 (2),** 595-606 .

<div style="background:green">

ARTICLE

</div>

Fate of Organochloro and other Pesticide Residues in Soil and Aquatic Environment and their Neuro-toxic Effects

B. Madhava Rao^; K. Gajanan[1*]; Manoj A. Pande[2]

^ Late Professor Emeritus, Dept. of Applied Chemistry, KITS Ramtek .
[1]Asst. Professor, Dept. of Applied Chemistry ,KITS Ramtek-441 106 ,Nagpur, M.S.
[2]Asst.Professor & Head, Dept. of Chemistry, T.G. Mahavidyalaya, Ramtek-441 106, Nagpur, M.S.

Abstract: The use of pesticides made possible to a greater extent the prevention of animal and plant diseases and also helped in increased food production. However, pesticides are no found distributed throughout the environment particularly in soil and aquatic environment and cause a number of neurotixic effects as a result of their existence. A general appraisal of the types of pesticides, their pathways into environment as well as the causes for the persistence of pesticides in soil and in aquatic environment as well as the causes for the persistence of pesticides in soil and in aquatic environment are of paramount importance. In developing countries, the environmental impact of these pesticide residues, particularly organochlorines has only slowly become apparent and in many cases the findings caused great concern. Organochloro pesticides normally called as persistent pesticides can get into the body system after bioamplification and further tamper with the mechanism of nerve impulse transmission. In this regard, a thorough understanding of the mechanism of bioamplification mode of physiological action and toxicity and lethal dosage(LD_{50} oral) of pesticide residues is a necessity for an environmentalist in exploring alternatives

Introduction:

Types of Pesticides

At present over 10,000 different pesticide formulations. These compounds are frequently classified according to their intended target, as shown by the following categories (1,2,3)

(i) Insecticides, (ii) Herbicides, (iii) Fungicides, (iv) Other specific pesticides, (v) Fumigants, (vi) Antibiotic fungicides, (vii) Repellants and (viii) Chemosterilants.

Pesticide Pathways into Environment (4,5,6)

(a)   The compounds may be absorbed by soils.
(b)   They may move downward through the soil in liquid or solution form and be lost by leaching.

They may vaporize and be lost to atmosphere without any chemical change.

(c)   They may undergo biodegradation within or on the surface of the soil.
(d)   They may be broken down by soil micro-organisms.
(e)   They may resist to the various degradation processes.

The last pathway is of particular importance in determining the effects of a given pesticide on the environment. This property is related to persistence, which is defined as the time required for a pesticide to lose at least 95% of its activity under normal environmental conditions and rates of application. Activity loss is completed when the pesticide has been totally decomposed (degraded) or otherwise inactivated by chemical or biological processes. Nonpersistent pesticides remain in the environment for 1-12 weeks, moderately persistent ones remain 1-18 months and persistent pesticides endure 2 years or longer. Obviously, if degradation is rapid there is little potential for accumulation of the toxic species with in the environment.

The pesticides, chlorinated hydrocarbons fall into persistent category. The degration times for these pesticides are measured in terms of years (**Fig.1**).   Some pesticides, such as organophosphates and carbamates decompose rapidly in soil and a result of hydrolysis and their persistence is measured in weeks.
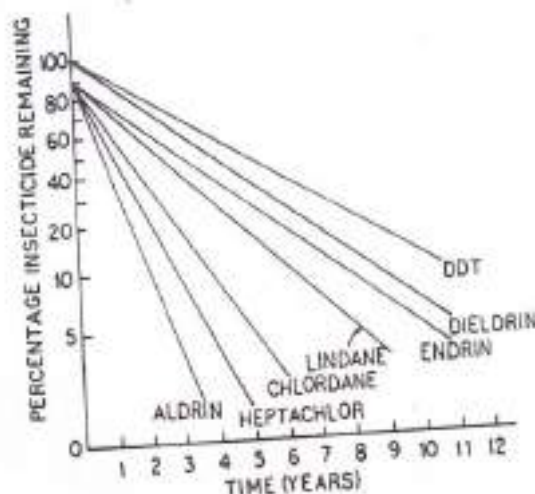
Fig.1 Degradation time for chlorinated hydrocarbons in soil

There is a significant variation in the time required for pesticides degradation, as determined by field studies, for a single compound. Although structure is the major factor involved in degradation rates, environmental conditions also play an important role. For pesticide residues in soils, factors such as soil type, amount of organic matter, bacteria and extent of cultivation are of importance. In aquatic environments sorption properties are extremely important, since sorption into sediment allows pesticides to settle to the bottom of the water body where microbial activity can take place (6,7,8).

The complete chemistry involved in the degradation of pesticides in not very clear, some generalizations can be made, for example organophosphorous and carbamate compounds usually degrade rapidly as a result of hydrolytic reactions. Chlorinated hydrocarbons on the other hand, do not hydrolyse but are broken down by slow microbial actions. It is believed that on an average, 25% of the production of DDT (Dichloro Diphenyl Trichloro ethane) is likely to have been transferred to the oceans (7).

Materials & Method:

Persistence of Pesticides in Aquatic Environment (7,8,9,10)

Despite a large influx of persistent pesticides, particularly DDT, into the marine environment, the concentration of pesticide residues in natural waters are quite low as a result of dilution. Pesticide concentrations are in the ppb range for fresh water and in ppt range for ocean water. However, even these low concentrations are matters of concern because of the ability of many plants and animals to concentrate the pesticide molecule within their tissues. Chlorinated hydrocarbons, although relatively insoluble in water (1.2 ppb for DDT) are quite soluble in fats and oils, which are found in all living organisms.

The chief known hazard of persistent pesticides in the marine environment is the concentration process mentioned above. This process, often called biological amplification, produces striking results in some cases. DDT and other chlorinated hydrocarbons, for example, maybe taken up selectively (due to their fat and oil solubility) by plankton and small fish. These in turn are eaten by larger organisms. When the process is repeated though several levels in a food chain, ex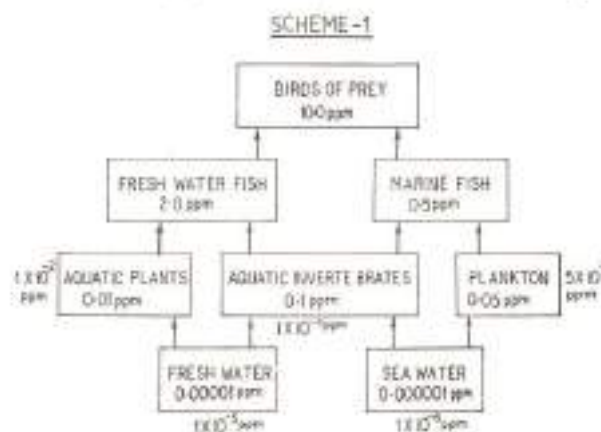tremely high pesticide concentrations results in species at the top of the chain. The solubility of chlorinated hydrocarbons in fats and oils an the typical values for a DDT food chain concentration pattern are given in the following scheme-1.

The most important aspect of lipids in relation to environmental pollution is their non-polar, hydrophobic nature. Pesticides of low polarity such as DDT, chloromethyl mercury (II), and other organic or organometallic substances tend to concentrate in the lipid portions of humans and other organisms, initiating the process of bioamplification (10,11,12). Furthermore, hydrophobic compounds may be much more likely to be absorbed by an organism because of the nature of the lipids in the membranes through which they must pass.

Bilogical membranes may consist of several layers of cell and cell walls usually consist of a mixture of about 60% protein and 40% lipid together with a small amount of carbohydrates. The lipids are mainly amphipathic and are arranged in bi-layer with their hydrophilic heads extending into the aqueous media on either side of the membrane and their hydrophobic tails mingling in the interior. Protein molecules may be located on the membrane surface or may penetrate partially or fully through the lipid bilayer.

In order to enter into the human body, any foreign substance must pass through several membrane barriers. Absorption from the external environment can occur through membrane in the mouth, the gastrointestinal tract, the lungs and the skin. Insuide the body additional impediments such as the blood-brain barriers, cell membranes or in the case of a pregnant women, the placental barrier may be encountered. In each case mental ions or highly polar substances will be turned back unless they can be converted in some way to non-polar forms.

Persistence is important because the amount of pesticide residue in the environment depends on the rate at which the chemical compounds involved decompose to less harmful substances. This problem in applied chemical kinetics is complicated by the lack of control over the conditions (temperature, moisture, catalysts etc.) under which the decomposition must proceed(7).

Even though a pesticide any decompose to another compound there is not guarantee that the newly formed product molecule will have less toxic properties that in the parent. For instance, one of the principal decomposition products of DDT is dichloro diphenyl ethane (DDE), which has been implicated in egg shell thinning in birds, and when aldrin decomposes it produces dieldrin, a slightly more toxic compound. The non-polar lipid "tails" form the interior of the membrane while polar "heads" extend into the aqueous medium and take up the toxic substances. Globular protein molecules are embedded in the lipid bilaryer. The reaction pathways by which pesticides decompose are also different under different conditions. It is essential in evaluating the environmental impact of any pesticide that the toxic effect of all possible decomposition products be taken into account in addition to the effects of the compound itself.

The pathways for decomposition of DDT, aldrin and parathion (6,7) are indicated in Scheme 2. Residues of relatively persistent pesticides such as DDT and dieldrin in soil, air and water are usually in ppb or ppt range, low enough to make accurate analysis difficult and too low to account for the quantities found in human diets (9). The phenomenon of bioamplification as explained earlier, is quite efficient for these compounds, since they are quite lipid soluble **(6).**

Results & Discussion:

Mode of Action and Toxicity of Pesticides (9,11,13,14)

In many cases the precise mechanisms by which pesticides kill plants or animals are not known. On a molecular scale the action of dieldrins apparently results from a complex series of reactions initiated by depression of the gene regulating synthesis of the enzyme R Nase, This permits excessive synthesis of RNA and protein which migrate to the stem of the plant, where cell division and proliferation occur on a massive scale. The plant's circulatory system is disrupted and the roots die of starvation.

The effects of insecticides on nerve transmission may be divided into two classes, depending on the point at which they occur (12,14).

Two substances, acetyl choline and norepinephrine are known to be involved in the synaptic transmission in a neuron

and trigger an appropriate response in the adjacent cell. Organophosphates and carbamates interfere (13,14,15) with synaptic transmission by inhibiting acetylcholinesterase which nicotinoids interfere with synaptic transmission between nerve and muscle cells. On the other hand, DDT and its analogs apparently affect axonic transmission, producing prolonged volleys of impulses which result in tremors and finally paralysis as shown in scheme-2,
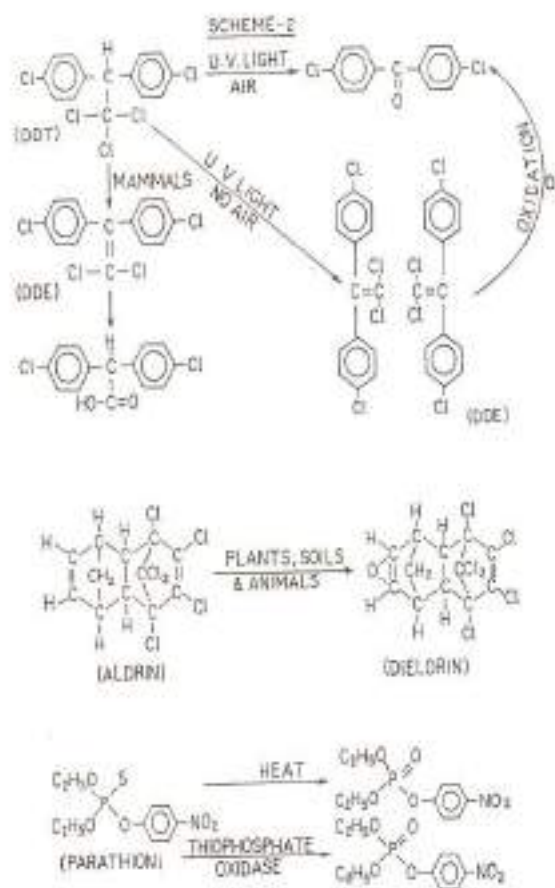
Pathways for decomposition of DDT, ALDRIN and PARATHION

Neurotoxic Effects of Pesticides :

In animals, organophosphates, charbamates cause inhibition of acetylcholine stearase which nicotinoids cause inhibition of neuromuscular junctions. Pyrethroids and organochlorines cause neurotoxication resulting into paralysis. However, triazines, carbamates and substituted ureas cause inhibition of photosynthesis and chlorophyll synthesis in plants. Carbamtes cause inhibition of oxidative phosphorylation (energy transfer) and organo-chlorines cause inhibition of pantothenate (Vitamin B) synthesis and hormone functions (14,15,16).

Table 1 summarizes the data obtained for lethal dosage of pesticides on rats (17,18,19)

Table 1

S.No.	Pesticides	LD_{50} oral (mg/Kg)
01.	Aldrin	54-56
02.	Arochlor(PCB)	250
03.	Carbaryl	540
04.	DDT	420-800 (60-75 dog)
05	Dieldrin	50-55
06	Endrin	5-43
07	Heptachlor	90
08	Lindane	125-200
09	Malathion	480-1500
10	Methoxy chlor	5000-6000
11	Mirex	300-600
12	Parathion	4-30
13	Nicotine	50-60
14	Pyrethrins	820-870
Herbicides		
01	2,4D	666
02	Dioxin (2,4,5,-T contaminated)	0.03
03	2,4,5 –T	300(100 dog)
04	Pentachlorophenol	27-80
05	Mercurials	100

Note : The larger the LD the less toxic is the substance. Data from D.Pimental "Ecological Effects of Pesticides on Non-target Species "Executive Office, U.S.Govt. (1971) and other references (18,19).

Conclusion:

*The environmental impact of these pesticide residues, particularly organochlorines has only slowly become apparent and in many cases the findings caused great concern. A thorough understanding of the mechanism of bioamplification mode of physiological action and toxicity and lethal dosage(LD_{50} oral) of pesticide residues is a necessity for an environmentalist in exploring alternatives.*In conclusion we have also discussed about the fate of Organochloro and other Pesticide residues in Soil and Aquatic Environment and their Neuro-toxic Effects.

Acknowlegement:

References

1. Donald, E.H.F. Chemistry of Pesticides: D.Von Nostrand Co. Inc. USA, 1957.

2. Pesticides in the Aquatic Environment: USEPA Publications,Washington, D.C., 1972.

3. Stijve, T. Pesticide Chemistry: CRC Press, 1982; N.York, Vol.IV,pp.95-100.

4. Edwards, C.A., Environmental Pollution by Pesticides: Plenum Press, 1973, New York, 1973.

5. Shrom, M.S., W.Miles J.R., .Harries C.R & McEwen F.L, Water Res. 1980, 14,1089.

6. Faust, S.D., Fate of Organic Pesticides in Aquatic Environment: Advances in Chemistry Series. Vol.III, Amer. Chem.Soc. 1972.

7. Petane & Zike, Nature,1987, 325,316.

8. Khan, H.M. & W.Khan, M.A.,Arch, Environ.Contam.Txicol, 1974, 2,289.

9. Murty, A.S, Taxicity of Pesticides to Fish Chapter I, PP.1936, Vol. I,CRC Press ().

10. Lichtenstein E.P,.Fuhremann T.W. , Schulz K.R. & Agric J..Food Chem. 1971, 19,718.

11. Idem, Taxicity of Pesticides to Fish: Chapters I&III,Vol.II,CRC Press. 1986.

12. Matsumura F,Bovsch G.M & Misato,Environmental T.Taxicology of Pesticides, Chapter III: Academic Press, New York,1972.

13. Kohn G.K., Mechanism of Pesticide Action :Amer. Chem. Soc. Symposium Series-II,1974.

14. Cutkemp, L.C, Koch, R.B & .Desaiah D,Insecticide Mode of Action: Academic Press, New York, 1982.

15. Johnson, W.W & Finley M.T, Handbook of Acute Toxicity of Chemicals to Fish and Aquatic Invertebrates: Resource Publication, "137, fish & Wild Life Service, U.S.Department of the Interior, Washington, D.C. 1980.

16. Epstein, S.S. & Legator M.S., The Mutagenicity of Pesticides: P.52 MIT Press, Cambridege, Massachusettes, 1971.

17. Pimentel, D. Ecological Effects of Pesticides on Non-target Species: Executive Office,U.S.Govt. Printing office,1971.

18. Kudesia V.P., Water Pollution: Pragati Prakashan Publication,1980, 198-200.

Manual of Analytical Methods for the Analysis of Pesticides in Human and Environmental Samples: USEPA Publication, Washington, D.C.,1980.

ARTICLE

Mining Geological Studies of Palaspani Manganese Ore Mine, Chhindwara District, Madhya Pradesh, India

Akash P. Raut[1], Hemant V. Hajare[2], Ashish R. Jagtap[3]

[1] Assistant Professor, ITM College of Engineering, Kamptee, INDIA
[2] Principal, ITM College of Engineering, Kamptee, INDIA
[3] MSc. Geology, Department of Geology, Nagpur, INDIA

Abstract: India is the third largest producer of manganese ore in the world. The countries most important ore deposits are Syngenetic, epigenetic and lateritic. Supergene enrichments associated with the first two groups. On the basis of mode of occurrence and association with different kinds of country rocks, the Indian manganese ore deposits have been classified as Gondites, Kodurites and Laterite. Indian manganese ore deposits occur mainly as metamorphosed bedded sedimentary deposits associated with Gondite Series (Proterozoic) of Madhya Pradesh, Maharashtra, Gujarat, Odisha and with Kodurite Series (Archaean) of Odisha and Andhra Pradesh and Proterozoic sedimentary manganese deposits of Penganga Group Adilabad district of Telangana. The subject area is a part of the Proterozoic terrain of Sausar Group of rocks consisting ofmarble, Calc-granulites, schist's,quartzites, gondite etc. The general strike of the ore body is NNW-SSE with dip of 75° towards south.The environmental aspects are being monitored regularly and seasonally by an environmental laboratory as approved by DGM- MP (Bhopal). As such the portability of air is fresh and unpolluted in this area

Keywords: Manganese;Gondite; Syngenetic and Supergene Enrichments; Environmental aspects

Introduction

Manganese makes up about 1000 ppm (0.1%) of the Earth's crust, making it the 12th most abundant element [1]. Geochemically, Mn behaves like Mg, Fe, Ni and Co and tends to partition into minerals that form in the early stages of magmatic crystallization. Significant quantities of Mn persist, however, in melts and can be plentiful in late-stage deposits such as pegmatites. Mn is readily depleted from igneous and metamorphic rocks by interactions with surface water and groundwater and is highly mobile, as Mn (II), in acidic aqueous systems. Near the Earth's surface, Mn is easily oxidized, giving rise to more than 30 known Mn oxide/hydroxide minerals. These oxides are the major players in the story of the mineralogy and geochemistry of Mn in the upper crust and the major sources of industrial Mn.

Indian manganese ores are preferred by many as they are generally hard, lumpy and amenable to easy reduction.In the Indian continent, the deposition of manganese must have taken place in varying environmental settings and by different geological processes but the sedimentary mode of formation far outweighed other methods such as supergene enrichment etc. [2]. These manganese ores have been selectively exploited either for direct use or for sweetening the otherwise available phosphor-rich ores. Favorable geological and geomorphological settings, existing well connected rail and road links, easy amenability of ores to beneficiation and liberal Govt. policies make the exploitation of Indian manganese deposits practically a no risk proposition.

The 96% of global production of manganese today is from barely 8 countries viz. China (17%), RSA (15%), Australia & Brazil (12% each), Gabon, India and Kazakhstan (9% each) and Ukraine (8%) in decreasing order of tonnages raised annually.

The global resource base is close to 52 billion tones including Indian reserve of about 378 million tones [3] [4].

Manganese is a vital component of steel and over 90% of manganese produced world over is used for metallurgical purpose. Ore utilization mode and smelting practice vary from Operator to operator but the general world-wide approval is to produce high-carbon ferromanganese. Mn ore deposits are not evenly distributed in geologic time. Instead they cluster in three groups, one in the Palaeo-Proterozoic, the second in the Neo-Proterozoic and the third in the Cenozoic. There is also a striking disappearance of sediment-hosted deposits from 1800 Ma to 1100 Ma. The Palaeo-Proterozoic peak is by far the largest and corresponds in time to the major episode of Banded Iron Formation deposition. Iron formation is also a common companion for the Neo-ProterozoicMn deposits, but the Cenozoic peak, largely confined to the Oligocene, has no associated Fe mineralization [4].

In recent years world manganese production has increasingly come from large sedimentary deposits of shallow marine origin. Stratigraphic units containing valuable manganese concretions consist of carbonates of fine clastic and represent deposition during high sea level stands, particularly on the margins of stratified basins [4].

Geology

India is the third largest producer of manganese ore in the world. the countries most important ore deposits occur in the form of sedimentary stratified metamorphic deposits in the Dharwar system, the manganese deposits are generally either Syngenetic (sedimentary) as in Madhya Pradesh and Maharashtra, epigenetic 82%-87% manganese (residual enrichment and oxidation) as in Jharkhand, Orissa, Goa and Karnataka or lateritic and supergene enrichments associated with the first two groups. On the basis of mode of occurrence and association with different kinds of country rocks, the Indian manganese ore deposits have been classified as:

A) Gondites ores which are associated with metamorphosed manganiferous sediments.

B) Kodurites ores which are produced due to reactions the country rocks and an invading magma or composition.

C) Lateriod ores which are produced to metasomatism replacement and residual concentration. Georgia has huge deposits of manganese ore India is the third largest producer of manganese ore in the World. The country's most important ore deposits occurring (in the form of sedimentary stratified metamorphic deposits) in the Dharwar system.

In India, extensive and rich manganese deposits occur in Madhya Pradesh, Orissa, Jharkhand, Andhra Pradesh, Maharashtra and Karnataka [2]. Indian manganese deposits display some distinct geological formations which are:

A) Deposits associated with the Khondalite rocks (garnet, sillimanite, gneisses) found in the Srikakulam District of Andhra Pradesh and in the kalahandi and Koraput districts in Orissa.

B) Deposits associated with in the iron bearing rocks (schist's) found in Karnataka states in the Sandur Hills [5].

C) Deposited associated with limestone and dolomite which occur in the Sausars-manganese –marble and Adilabad manganese ore associated with the limestone province of Madhya Pradesh, Jharkhand and Gangapur, Ratnagiri in Maharashtra and Adilabad districts in Andhra Pradesh.

Indian manganese ore deposits occur mainly as metamorphosed bedded sedimentary deposits associated with Gondites Series (Archaean) of Madhya Pradesh (Balaghat, Chhindwara & Jhabua districts), Maharashtra (Bhandara & Nagpur districts), Gujarat (Panchmahal District), Odisha (SundergarhDistrict) and with Kodurites Series (Archaean) of Odisha (Ganjam & Koraput districts) and Andhra Pradesh (Srikakulam & Visakhapatnam districts) and Proterozoic sedimentary manganese deposits of Penganga group Adilabad District Andhra Pradesh [4].

General Geology

The rock unit exposed in this region of the subject area belongs to Gondite suite of Rocks of Proterozoic system.

Local Geology:

The Mining lease area is a part of small basin and distantly surrounded by high hillocks. It is gently undulating with low gradient into the adjacent small rain fed tanks. The surface plan with elevation contours shows the elevation to be ranging from a maximum of 506m. Palaspani manganese mine is located at the western end of MP-Maharashtra belt, roughly 200 km long and 2 km wide. The erosion of Deccan Traps and Lametas in Kanhan valley, trending NNW-SSE roughly in direction, have exposed older (Tirodi) Gneiss and overlying sausar Group of rocks consisting of marble, calc-granulite, schist's quartzites, gondites etc. which house manganese ore bodies. The Ore in the pits is generally Pyrolusite- brownish black to black in colour and it is hard in nature. The general strike of the ore body is NNW-SSE with dip of 75° towards South

Figure 1: Location Map of the Study Area
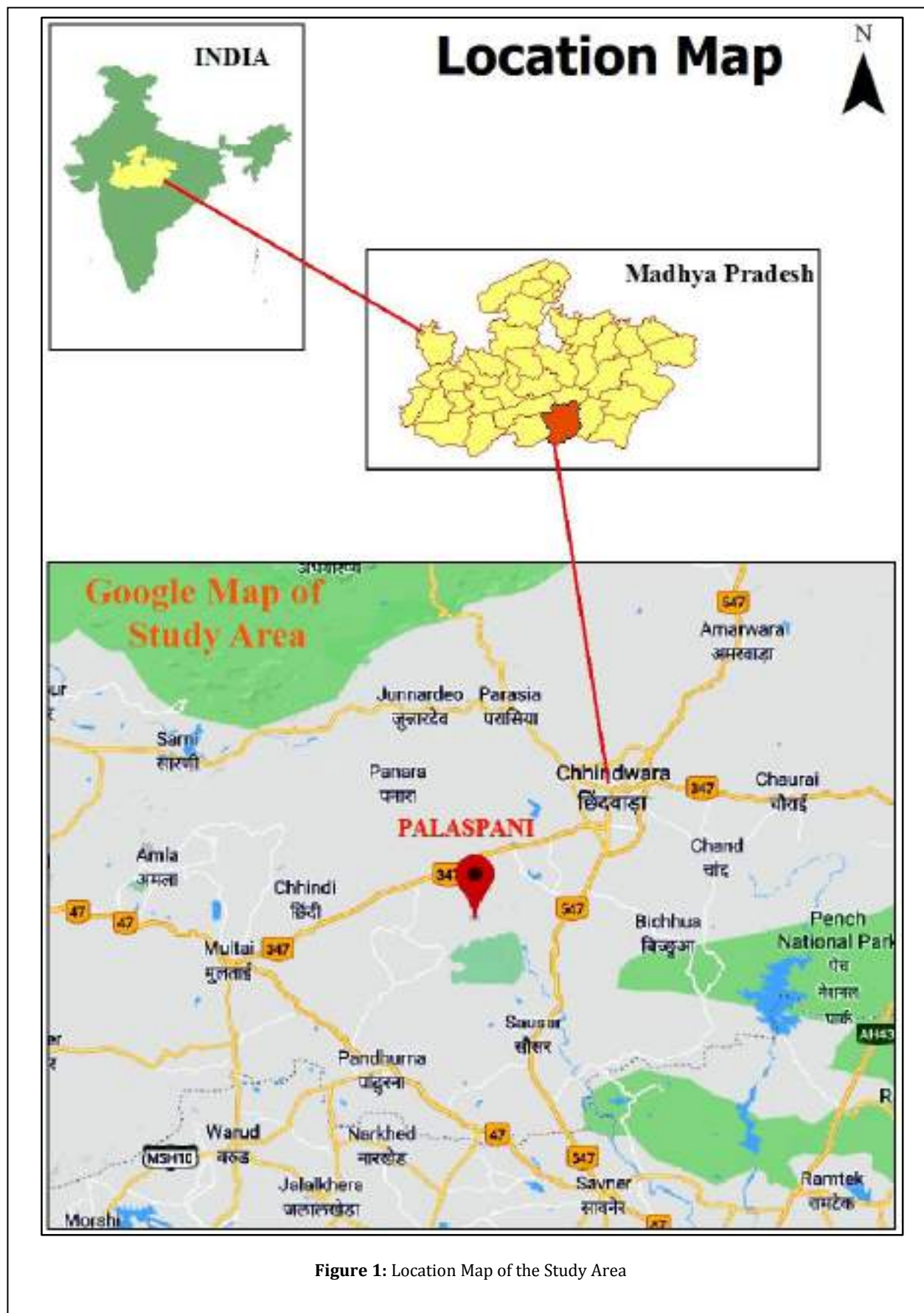
Table 1: showing Geological succession, as observed in the mine area and surrounding, is as follows [6]:-

Pegmatites and quartz veins (intrusive)
Mica schists with quartzite bands
H.W.Manganese Ore
Gondite /quartzite
F.W. Manganese Ore
Quartz Gondite
Sausar Group
Dolomite
------------------Unconformity--------------------
Tirodi Gneiss

Geology of the area is discussed above in general. But pit wise geological behavior of the ore-deposits and country rocks are found to have undergone changes which are highlighted belowin brief:

(i) The cumulative strike length of the ore-deposits is around 1300min the E-W direction in general but local folds between pits have changed the strike directionThus, strike behaves in S shape more or less. From one extremity of pit no. 1 to pit no. 6, it is almost E-W.

(ii) It is also found that ore-deposits pinch from pit no.6 towards pit no.1.

(iii) In Pit no. 1, 2 and3, there are two bands of ore-deposits. One is Primary ore deposits of varying thickness of 3m to 5m and secondary ore-deposits of 5m to 8m thickness and they are separated by an intrusion of varying width from 4m to 8m. The Intrusion consisting of mainly Quartzite intruded with Gondite and Pegmatites are very hard and dips very steeply at + 80°.

(iv) The Primary ores in Pit nos. 1, 2, 3 and 4 are hard and lumpy while it is friable in Pit nos. 5 and 6.

(v) The width of Primary ore-deposits in Pit nos.4 & 5 has been found as increasevarying from 5m to 7.5m. The primary ore in Pit nos.5 & 6 is friable and formation of fines is more than those in Pit no. 1 to Pit no.4.

(vi) The primary ore grade in general is high above 45% while secondary ore grades are found to vary from 25% to 35% in general.

(vii) In Pit no.5 while working from almost surface level i.e., around 405 MRLto 420 MRL downwards, it was found that in eastern part of Pit no.5, the strike was almost E-W while in the western part the strike direction was found to have almost N40°E to N40°W indicating that, there was intense folding or fault without noticeable throw.

(viii) area between Pit no.4 and Pit no.5 from the surface level up to 320MRL, i.e., nearly 75m-80m below surface. At 320MRL, Ore-body is taking turn towards NE at eastern end with more than 5m width in Pit no.5

which it appears, is extending towards pit no.4 and may join Pit no.4. Similarly, there is a barren area between Pit no.5 and Pit no.6 from surface up to around 375 MRL.

Methodology

During this study core samples from 42 drill holes were collected at 1 meter interval below ground level. These samples were chemically analyzed at site laboratory to calculate major oxide percentage in each sample.

Result And Discussion

The following graph represents the change in Silica %, Phosphorous % and Iron % of core samples collected at 1 meter interval below ground level.
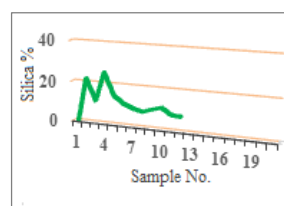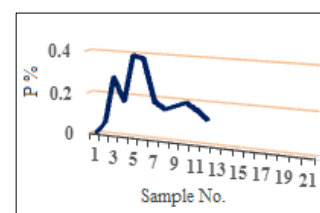
Figure 2 (a)   Figure 2 (b)

Figure 2 (c)

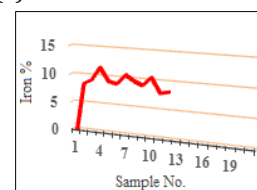In borehole no. 3B (Figure 2 a ,b ,c) it is observed that Values of silica, Phosphorous and Iron gets increased first then get decreased continuously indicating increase grade of the manganese
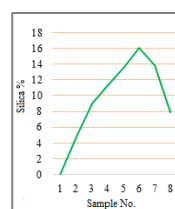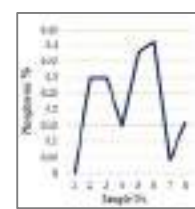

Figure 3 (a)   Figure 3 (b)

Figure3 (c)

In Borehole no. 6 (Figure 3 a, b, c) the observation seen is similar as borehole no. 3B. These all indicates increasing grade of manganese with the increasing depth.

Economic Axis

1) The Manganese mineralization in the subject mine is strata bound and is confined to Gondite formation and a detailed exploration by means of Core bore holes (42) had been carried out. Thus the detailed exploration parameter has been fulfilled.

2) The mine is in operation continuously since 1909. All the pits (6) are in operation except 1 and 6 no. Even in lean period, the lessee continued the mining operation. Thus the mining of the Manganese ore is viable.

3) So far whatsoever Manganese ore produced from the mine was marketed. The Manganese ore of the mine has very good mineral composition both in respect of elements of Mn and othersi.e. Fe and P and put together is 50%. It is best suitable for blending of Manganese ore of the other mines of the lessee which are low in Fe and high P content. The ore is hard and lumpy in nature and sold to Steel plants with the end use specifications as given below [7].

Table 2: Comparison of Marketable Mn Grade

Element	Symbol	Ferro-manganese Industries	Silico-manganese Industries
Manganese	Mn	+38%	+20%
Iron	Fe	9%max	10%max
Silica	SiO_2	20%max	40%max
Alumina	Al_2O_3	3%max	3%max
Phosphorous	P	0.18%max	0.22%max
Size		75mm to 10mm	80%
		10mm to 3mm	20%

Thus the grade of the ore produced from the mine is marketable, since it is meeting end use specifications of the industry.

Environmental Management Plan

Baseline Information

i) Existing land use Pattern: The subject area is a private patta land; it is being used for mining. The details of exiting land use pattern as on date is given below:

Table 3: Details of Existing Land use Pattern

a)	Area covered by excavation	28.05 Ha
b)	Area covered by dumps (old & new)	3.40 Ha
c)	Mineral storage including sub-grade and Reject	3.00 Ha
d)	Area covered by site services	1.00 Ha
e)	Area covered by roads	1.20 Ha
f)	Area covered by plantation	3.40 Ha
	Total	**40.05 Ha**

ii) Water Regime: Palaspani Mine is an open cast mine at present and the same is going to turn to underground workings shortly. Generally the ground water table in this locality is below 37m from the ground level. The pit has gained a depth of 30-40m. The rainwater on surface flows through the slopes and drains out the lease area. The water accumulates due to seepage in the pit is being bailed out by deploying a 50hp pump. Kanhan river is situated nearly a km away in the north that is the source of major drainage of the entire area [7].

iv) Quality of Air, Water and Ambient Noise Level: The subject area is away from industries. There is no scope of air, water & sound pollution by industries. The environmental aspects are being monitored regularly and seasonally by an environmental laboratoryas approved by DGM- MP (Bhopal). As such the portability of water (i.e. flow of groundwater & water table level)& air are fresh and unpolluted in this area. The environmental monitoring stations are shown in the Environmental Management Plan [7].

v) Climatic Conditions: The area has a sub-tropical climate. The peak summer will be in the month of May. Highest temperature of 40°C is recorded in this area during the month of May and the lowest temperature of 10°C is recorded in the month of January. The rainfall in this area is about 1100mm. The dominant wind direction is from NE [7].

vi) Human Settlement: The following villages are located within 10km radius of the mining lease area. The population and occupation of the villages with respect to applied area are given in the following table 4 [7].

Table 4: Human settlement with main occupation

Name of village	Population	Main Occupation of people
Bargabadi	439	Agriculture
Haranberdi	10	Agriculture
Kuddam	889	Agriculture
KorparwadiKhud	874	Agriculture
Piplakhanan	1214	Agriculture
RanpethDawami	171	Agriculture
Rohana	1020	Agriculture
Sitapar	280	Agriculture

vii) Public Building, Places of Worship and Monuments: There are no Public Building, places of workshop and Monuments within or near by the area.

Conclusion

The ores are associated with manganese silicate rocks (Gondite bearing rock) which from lenticular bands intercalated along the strike of a complex series of metamorphic rocks traversed by granites and pegmatite.

From the point of economic axis, the ore produced from mine consists of graded ore (80%), sub-grade minerals (15%) and wastes (5%). The graded ore is divided into two types. One is hard & lumps (20 mm to 80mm) which is 60% whereas fines (-20mm) which is 40%.Thus the grade of the ore produced from the mine is marketable especially for Ferro-manganese industries.

Acknowledgement

Reference

[1] Emsley, John:"Manganese" Nature's Building Blocks: An A-Z Guide to the Elements. Oxford, UK: oxford university press.2001, pp. 249–253. ISBN 0-19-850340-7.

[2] Jawed, Tallit;Siddiquie;F. N. Mineragraphic study of manganese Ore Deposits of Kandri, Mansar, Beldongri and Satak Mines, Nagpur District (Maharashtra) Central India, Internatoinal Journal of Geosciences (5)2010,pp. 710-727.

[3] Indian Mineral Year Book - Manganese Ore, Indian Bureau of Mines, Nagpur, January, 2009,pp. 34(19-47).

[4] Anjaneyulu, M.; Nagaraju, K.; Vorsu, Ravi, Mining Geological Studies of Avagudem Manganese Vizianagaram District, Andhra Pradesh, India. International Journal of Scientific and Research Publication, 2015: Volume 5, Issue 7.

[5] Structural and stratigraphy of manganese ores of kumis, shimoga schist belt, Karnataka, India.

[6] Geology and Mineral Resources of Madhya Pradesh, Geological Survey of India, 2013: Miscellaneous Publication No. 30 (XI), Revised Edition, pp.14.

[7] Executive Summary of Palaspani Manganese Ore Mine (ML-54.129 ha), approved by 5th meeting of the reconstituted committee for Environmental appraisal of Mining Project (Non-coal), Ministry of Environmental & Forest, India, 2013: pp. 1-7.

ARTICLE

Studies on Insect diversity in anthropogenic habitats of Gondia city of Vidarbha region.

S **Juneja (Banerjee) Sheetal B.**

Department of Zoology
Dhote Bandhu Science College, Gondia..
Email: sb107banerjee@gmail.com

Abstract: To assess the insect biodiversity in various natural and anthropogenic habitats of Gondia district of Vidarbha region of Maharashtra state a year-long survey was conducted. In present study, 462 insects were collected in vicinity of Gondia city. Identified specimens belonging to eight selected orders (Coleoptera, Hymenoptera, Diptera, Hemiptera, Odonata, and Lepidoptera) represented 33 families, 84 genera, and 64 species. The order Lepidoptera represented highest diversity in terms of 38 genera and 33 species among the eight orders investigated. This was followed by order Coleoptera which had 14 genera and 06 species. Studied six orders can be arranged in a descending diversity order as: Lepidoptera, Coleoptera, Odonata, Diptera, Orthoptera, , Dictyoptera , Hemiptera and Hymenoptera

Introduction

Biodiversity is one of the important cornerstones of sustainable development and represents the biological wealth of a given nation. Insects are the major component of the world's biodiversity. They are one among the most efficient pollinators of flowers, which in turn help in the production of fruits, seeds and food crops, so essential for the survival of all animals including man. Being sensitive organisms, they react to the slightest changes in the environment and hence are very good ecological indicators.

Insects and plants are becoming extinct because of habitat loss, over exploitation, pollution, over population and the threat of global climate changes. (Current Science, 2006). Their decline is a warning signal to all of us. In order to asses and monitor the impact of disruption and modification of natural profile through our utilization and management of natural resources, surveys to study the biodiversity are done. This research paper attempts to study insect diversity in and around anthropogenic habitats of Gondia city of Vidarbha region.

THE STUDY SITE

Gondia District

Methods Adopted For The Study

Collection

Collections of various insects groups were made from all the Villages and area in vicinity of Gondia city. The insects collections particularly butterfly and beetles were carried out in the early hours of the day because butterflies are usually active at early sun rise, therefore, it was easy to observe and collect them.   Broadly following methods were adopted for the collection.

(a) **Hand picking**: Small Coleopteran like Coccinellidae, Chrysomelidae, Curculionidae, etc. were collected by hand with the help of a fine forcep. The forcep was used carefully to avoid damage to the insect. Insects like leaf-miner (Diptera), bark inhabiting beetles, insects living under stones and leafleters (Coleoptera) were collected by hand picking.

(b) **Aerial netting**: Aerial net was used to collect free living flying insects like Odonata, Lepidoptera, Diptera etc. Soft bodied insects like Lepidoptera were gently removed from the bottom of the bag, after it becomes enclosed in the bag by a rapid twist of the handle; often the fold of the net enclosing the insect was removed after killing by vapour of the killing agent.

Preservation for taxonomic study

 Insects with hard body were pinned directly by piercing pin through the body and care was taken to choose the correct size and number of pin (each insect pin has a specific number) to avoid damage to the internal part. The point at which the pin was inserted also varies order wise. The pinned insects are spread with the help of spreading board which consists of two flat parallel pieces of soft wood with an inner groove lined by cork. Two narrow paper strips were used to hold and spread the wings, and after adjustment of the wings at a desirable position the collected specimen was pinned using a fine pin.

Result and Discussion

In the present study, 462 insects were identified. The identified specimens belonging to eight orders (Coleoptera, Hymenoptera, Diptera, Hemiptera, Odonata, and Lepidoptera) represented 33 families, 84 genera, and 64 species. The order Lepidoptera represented highest diversity in terms of 28 genera among the six orders investigated. This was followed by order Coleoptera which had 21 genera. Studied six orders can be

arranged in a descending diversity order as: Lepidoptera, Coleoptera, Diptera, Orthoptera and Dictyoptera, Hemiptera, Odonata and Hymenoptera. Kulkarni *et al.* (2012) have reported 101 species of odonates from the entire Maharashtra state.

Ashish T. and Pankaj K. (2015) carried out Odonata surveys in Maharashtra during 2006–2014. Compilation of all these studies along with other authenticated records resulted in a checklist of 134 species of Odonata belonging to 70 genera representing 11 families.

The probable cause of decline in number of insects of this area may be the increase in anthropogenic movements due to expanding urbanization. Since the last decade, the city has expanded which have resulted in loss of natural habitats. Urban development is expected to have a deleterious impact on insect populations with reduction in the area of natural and semi-natural habitats.

Order	Family	Genus	Species	Common name	Number
LEPIDOPTERA	Pieridae	*Colotis*	*daneous*	Crimson tip	6
	Papilionidae	*Graphium*	*nomius* (Esper)	Spot Swordtail	7
		Graphium	*agamemnon*	Tailed Jay	1
		Papilio	*polymnestor*	Blue Mormon	4
		Pachliopta	*aristolochiae*	Common rose	5
		Pachliopta	*hector*	Crimson Rose	4
		Papilio	*polytes*	Common mormon	2
		Papilio	*demoleus*	Citrus fly	19
	Nymphalidae	*Danaus*	*chrysippus*	Plan tiger	10
		Danaus	*genutia* (Cramer)	Striped Tiger	2
		Danaus	*plexipus*	Monarch	3
		Euploe	*core core*	Common Indian Crow	13
		Hypolimnas	*misippus*(Linnaeus)	Danaid egg fly	04
		Hypolimnas	*bolina* (Linnaeus)	Great Eggfly	2
		Neptis	*hylas* (Linnaeus)	Common Sailer	1
		Junonia	*atlites* (Linnaeus)	Graypancy	1
		Junonia	*almana*	Peocockpancy	3
		Junonia	*hierta* (Fabricius)	Yellow Pansy	4
		Junonia	*iphita* (Cramer)	Chocolate Pansy	3
		Junonia	*lemonias* (Linnaeus)	Lemon Pansy	4
		Junonia	*orithya* (Linnaeus)	Blue Pansy	2
		Phalanta	*Phalantha* (Drury)	Common Leopard	3
		Ariadne	*merione* (Cramer)	Common Castor	5
	Sphingidae	*Acherontia*	*styx*	Death,s Hawk Moth	8
		Agrius			11
		Macroglossum	*stellatarum*	Humming bird Moth	9
	Lycaenidae	*Chilades*	*prrhasius*	Small cupid	02
		Catochrysops	*strabo*	Forget me not	06
		Tarucus	*extricatus*	Rounded pierrot	04
Coleoptera	Buprestidae	*Sternocera*		Metalic blue green jewel beetle	8
	Hydrophilidae	*Hydrophilous*	*olivaceous Fabricius*	Aquatic beetle	10
	Carabidae	*Anthia*	*sexguttata*	Tiger beetle	4
		Megalodache		Tiger beetle	5
		Orthophagus	*sagglturus*	Dung beetle	5
		Carabus		Ground beetle	9
	Meloidae	*Mylabris*	*phalerantae*	Blister beetle	3
	Gyrinidae	*Dineutes*	*indicus Aube*	Beetle	1
		Hispa		Pumpkin	1
	Dytiseidae	*Dytiscus*	*marginalis*	Great Diving bbeetle	2
		Cybister	*tripunctatusasiaticusSharp*	Common water beetle	5
	Scarabaeidae	*Helicopris*	*bucephalus*	Scarab beetle	5
	Cicindellidae	*Cicinidela*	*sexpunctata Fabricius*		8
	Curculionidae	*Cyrtotrathelus*	*longimanus Fabricius*	Bamboo beetle	5
	Coccinellidae	*Coccinella*	*septempunctata Linnaeus*	Seven spot lady bird beetle	12
	Cerambycidae	*Stromatium*	*barbatumFabricius*		3
		Aeolesthes	*holosericea Fabricius*		3
Dictyoptera	Blattidae	*Periplaneta*	*americana*	Cockroach	17
	Mantidae	*Acrita*	*territis*	Mantid	5
		Mantis	*religiosa*		6
Odonata	Cardulegasteridae	*Cardulegaster*		Dragonfly	17
		Orthetrum	*farinosum*	Dragonfly	12
		Aeshna	*cyanea*		11
Hemiptera	Pyrrhocoridae	*Dysdercus*	*cingulatus*	Red cotton bug	13
		Bagrada	*hilaris*	Painted bug	5
	Pentatomidae	*Halyomarpha*		brown marmorated stink bug	7
		Chlorachrau		Sting bug	3
	Belostomatidae	*Belostoma*	*indica*	Giant water bug	5
Hymenoptera	Apidae	*Apis*	*dorsata*	Honey bee	12
Orthoptera	Acrididae	*Hieroglyphus*	*banian*	Ricegrass hoppers	9
		Hieroglyphus	*nigrorepletus*		7
		Acrida	*turritaLinnaeus*		6
		Neoconocephalus	*neocoptera*	Cone head	7
	Psychidae	*Clania*	*crameri*		6
	Gryllidae	*Metrioptera*	*Bush cricket*		4
		Gryllodes	*sigillatusWalker*		3
		Gryllus	*bimaculatus*		05
		Callogryllus	*Orientalis Boliver*		05
Diptera	Asillidae	*Hyperechia*		robberfly	3
	Oestridae	*Hypoderma*	*bovis*	Cattle warbelfly	2
	Culicidae	*Aedes*		Mosquito	13
		Anopheles		Mosquito	12
		Culex		Mosquito	12
	Tabanidae	*Tabanus*		Horsefly	8
	Trypetidae	*Dacus*	*cucurbitacae*	Cucurbit fruit fly	2
	Muscidae	*Musca*	*nebulo*	House fly	7
		Stomoxys		Stable fly	5

Sr. No.	Name of order	Total No. Of genus	% of genus	Total No. of individuals	% of individuals
1.	Lepidoptera	29	38.15	141	30.51
2.	Coleoptera	17	22.36	92	19.91
3.	Dictyoptera	03	3.94	28	6.06
4.	Odonata	03	3.94	40	8.65
5.	Hemiptera	05	6.57	33	7.14
6.	Hymenoptera	01	1.31	12	2.59
7.	Orthoptera	09	11.84	52	11.25
8.	Diptera	09	11.84	64	13.85
	Total	76		462	

Conclusion

Preventing the global decline in biodiversity is a major task for conservation biologists. Although habitat loss has been identified as a key factor driving extinction processes, our knowledge on the habitat requirements of many endangered species, particularly invertebrates, is still sparse. Present is the first ever study on the insect fauna in the anthropogenic habitat of Gondia city of Vidarbha region. This study may be used as indicator of biodiversity and can be used to determine the status and distribution of these indicators species which will serve as baseline information for further comparisons.

References:

1. Ashish D. Tiple and Pankaj Koparde . Odonata of Maharashtra, India with Notes on Species Distribution. *Journal of Insect Science,* 2015; vol 15(1): 1-10http://dx.doi.org/10.1093/jisesa/iev028

2. Current Science . News, Meeting Report. Biodiversity of Insects*. Current science,*2006; Vol.91, No.12, P. No. 1602-1603.

3. Kulkarni P. P., Babu R., Talmale S., Sinha C., Mondal S. B. . Insecta: Odonata. *In* Director, Zoological Survey of India (ed.), *Fauna of Maharashtra: state fauna* Series. Zoological Survey of India, Kolkata, WB; 2012, pp. 397–428.

ARTICLE

Simulation of utility tied Micro inverter for Solar Photovoltaic system

Ashutosh Sudhirrao Werulkar[1], P.S.Kulkarni[2]
[1]Department of Electronics and Telecommunication Engg.,St.Vincent Pallotti College of Engg. and Technology,Gavsi Manapur, wardha Road, Nagpur awerulkar@stvincentngp.edu.in
[2]Department of Electrical Engineering, Visweswarayya National Institute of Technology, Nagpur,

Abstract: In this work, the simulation of utility connected PV systems with Solar Micro inverter has been highlighted. The topology is simple, symmetrical and easy to control. PSpice 9.1 software is used for simulation. Focus is to simulate every component of the system. Sun, Solar module and utility inverter are the different components used in simulation. For simulation purpose, two irradiance profiles have been assumed. In profile one solar radiation data for 5 days have been considered and waveforms are generated for utility Connected Solar PV system. In others radiation profile, continuous increasing values of solar radiation have been considered for simulation purpose. The various waveforms satisfy the interface of the utility connected inverter. In both trends of radiation patterns, change in the inverter current and power is seen. Other desirable features of this system include good efficiency due to optimal number of switching devices and reduced switching losses. The soft switching technique is to be implemented for the utility connected PV system

Key words:- Micro-inverter; Maximum power point; PSpice; Photovoltaic; Solar modules; Utility

Introduction

India is a developing country and energy is a vital input for any economy especially for a developing country like India whose population is 17% of world. But, it only possesses 0.4% of world's oil, 0.4% of natural gas and 6% of coal reserves. This fact of availability of energy resources can be taken as a gross deficiency because India is the fourth largest consumer of energy in the world after USA, China and Russia. Recently Govt. of India has announced to provide 24x7 power to all by 2022. It is an imminent imperative that India evaluates the trade-off that it would have to make to reach a goal which is a balanced one of energy security, energy access and sustainability

In order to move towards above objectives, it is very much essential to evaluate the components of Indian energy ecosystem, its supply and demand as well as the interlinking networks. The interlinking of these components also needs to be judged. Fortunately, India has the vast potential of renewable energy. Increasing the domestic supply and exploiting India's vast potential of renewable energy can be an action which may play a major role in decreasing India's dependence on the imported energy resources. It can also address its growing concerns about climate change. It is also important that demand sectors play an important role in reducing the amount of energy required to deliver the same amount of services. Energy efficiency and electrification of demand are two important interventions to be considered and looked at under the same lens as supply

interventions. Transmission and Distribution networks need to be strengthened and Smart Grids and storage solutions need to be deployed and these can be the interventions that would underpin the move towards a more secure energy scenario for India

Photovoltaic is one of the fastest growing solar energy technologies. Solar energy is a good renewable energy. Because solar energy is clean and find it everywhere. Photovoltaic devices commonly called solar cells or modules, use semiconductor material to directly convert sunlight into electricity. Solar cells have no moving parts. Power is produced when sunlight strikes the semiconductor material and creates an electric current. With the cost of solar cell decreasing, the conversion of the solar energy to electric energy is increasingly becoming economically viable. Solar panel Generates the power at 12V DC but there are some loads which requires higher/lower voltages to operate so for supplying such loads we can use DC-DC converters and by using this converters we can improve the efficiency of the solar Photovoltaic system.

According to the announcement of the National Action Plan on climate change in June 2008, which identified development of solar energy technologies in the country as a National mission, the Government of India has launched Jawaharlal Nehru National Solar Mission (JNNSM) which aims at development and deployment of solar energy technologies in the country to achieve parity with grid power tariff by 2022. The objective of the national solar mission is to establish India as a global leader in solar

energy, by creating the policy conditions for its diffusion across the country as quickly as possible. Solar Photovoltaic (PV) is the only technology that directly converts sunlight to DC electricity. Attractive advantages of PV technology include a free and abundant fuel supply; little or no pollution or operation/maintenance costs (once installed), and unlimited system life.

Grid connected PV system with net metering is being implemented in India and so also in Maharashtra state as a step towards achieving the goals of National Solar Mission of India.

[1] to [4] cover basic concept of Solar PV system with power Electronics applications. Magazine (2009) in [5] covers the theme of solar charge controller. Castaner (2002) in [6] discussed modeling of photovoltaic systems using PSpice. Lee et al (2008) in [7] covers the resistive control of battery charging using microcontroller. Masoum et al [8] (2004) explains Microprocessor controlled optimal battery chargers. Boico and Lehman (2007) in [9] explain about Solar Battery Chargers for NiMH batteries. Moharil (2009) in [10] presented a case study of solar PV system for Sagardeep Iceland. Barca et al (2008) in [11] presented a novel MPPT charge regulator for a photovoltaic stand-alone telecommunication system. The Techno Economic Optimum Sizing of a standalone Solar Photovoltaic System is suggested by Kolhe [12]. Jain and Agarwal [13] proposed single stage inverter topology for grid connected PV systems. Werulkar and Kulkarni[15] performed Analysis of Microcontroller based Solar Charge controller for solar Home Lighting System. A residential PV system along with utility power supply is an amicable solution for the purpose of using renewable energy in an intelligent manner to save energy of the nation. The residential PV system can be a choice based system for an individual family to contribute for increased use of renewable energy technology in solar energy category and thereby controlling the effect of greenhouse gases[16] Microchip is the company to provide different applications of solar PV systems [17].

The aims and objectives of this paper is to simulate grid connected Solar PV system using PSpice software. Initially, the Simulation of the Solar spectrum, Silicon Solar cell, Solar cell modules of 37Wp and 74 Wp connecting in parallel to form a solar array is done. Finally Simulation of grid connected Solar micro inverter has been done. For Simulation purpose the solar panels of 37Wp and 74Wp are connected in parallel. While simulating, two simulation profiles have been assumed, a radiation profile of 5 days and a continuous increasing radiation profile. The various results are generated in the graphical form. For Simulation purpose a radiation pattern of Nagpur city has been considered using digital solar radiation pyranometer available in EE department of VNIT.

EQUIPMENTS IN ELECTRICAL ENGINEERING DEPT. OF VNIT, NAGPUR-INDIA

The Department of Electrical Engineering VNIT, Nagpur purchased the Solar Home lighting system. It consists of 37 Wp solar panel, solar charge controller, battery 45Ah, 14W,12V DC fan , 9w 12V CFL lamps 2Nos.

Fig. 1 shows photograph of Solar Home lighting system and Fig.2 shows photograph Digital Solar Radiation Pyranometer available in Electrical Engg. Department of VNIT campus.

Fig 1: Solar Home Lighting System in EE dept.

DIGITAL PYRANOMETER AT ELECTRICAL DEPARTMENT, VNIT

Fig.2: Digital Solar Radiation Pyranometer in EE dept. of VNIT Campus.

The Digital Solar Radiation Pyranometer in EE dept. of VNIT Campus can measure the solar beam and global radiation on the horizontal surface after every minute. The Data is being stored in the form of Excel work sheet. From September 13,2010 onwards, the solar radiation data for Nagpur city is available for every minute till date.

The Components of the Digital Radiation Pyranometer are as follows,

1. Solar Radiation Sensor

- Temperature range : -40 to +80∘ c

- Range 0 to 2000 W/m²

Sensitivity 15 μv/W.m²

2. Solar Panel Output voltage: 12v DC, Wattage: 10Wp

3. Data Shuttle The Data Shuttle is pocket-sized device that can be used to download and transport the data from logger to a computer

4. USB

The spectrum of the radiated energy by a black body can be obtained by the Planck's black body radiation model, which is given as

$$P_\lambda(d\lambda) = \frac{2\pi hc^2 \lambda^{-5}}{e^{\frac{hc}{\lambda kT}} - 1} \qquad (1)$$

where $P_\lambda (d\lambda)$ is the energy radiated per unit time per unit area in the wavelength range between λ and λ+ dλ in W/m², T-Temperature of the black body,h is planck's constant, c is the speed of light and k is the boltzmann's constant. Considering the Sun's temperature as 5760 K, a spectrum of the black body radiation can be plotted. This is known as extra terrestrial radiation, the solar radiation just outside the earth's atmosphere Fig.3 shows PSpice simulated output of standard spectrum of Sun.
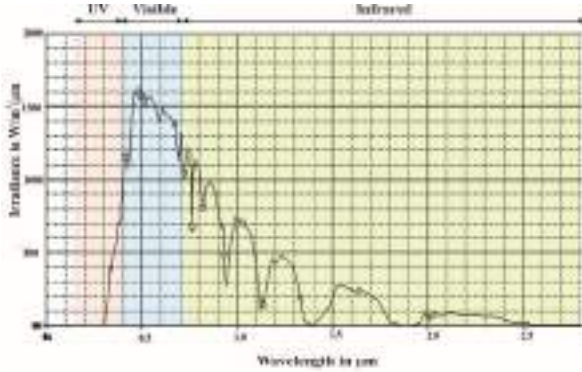
Fig.3: PSpice simulated output of standard spectrum of Sun.

The monthly averaged daily global radiation on a horizontal surface H_{ga} is given by the following equation,

$$\frac{H_{ga}}{H_{oa}} = a + b\left(\frac{S_a}{S_{\max a}}\right) \qquad (2)$$

here H_{oa} is a monthly averaged extra terrestrial Solar radiation at horizontal surface (at top of the atmosphere, S_a and $S_{\max a}$ are the monthly averaged daily sunshine hours and maximum possible daily sunshine hours(the day length) at a given location. Here a and b are constants and its values for Nagpur are a=0.27 and b=0.50 [2]

Monthly average of the extraterrestrial radiation on horizontal surface is given by

$$H_0 = \frac{24}{\pi} S(1 + 0.033\cos\frac{360n}{365})(\omega_s.\sin\phi.\sin\delta + \cos\phi.\cos\delta.\sin\omega_s)$$
$$(3)$$

Tilt factor for beam radiation,

$$r_b = \frac{\cos\theta}{\cos\theta_z} = \frac{\omega_{st}.\sin\delta.\sin(\phi - \beta) + \cos\delta.\cos(\phi - \beta).\sin\omega_{st}}{\omega_s.\sin\delta.\sin\phi + \cos\delta.\cos\phi.\sin\omega_s}$$
$$(4)$$

Tilt factor for diffuse radiation:

$$r_d = \frac{1 + \cos\beta}{2} \qquad (5)$$

Tilt factor for reflected radiation:

$$r_r = \rho\frac{1 - \cos\beta}{2} \qquad (6)$$

Hence monthly averaged daily total radiation on tilted surface is given by,

$$\frac{H_T}{H_g} = (1 - \frac{H_d}{H_g}).r_b + \frac{H_d}{H_g}.r_d + r_r \qquad (7)$$

Using above information, Solar global radiation on tilted surface is calculated for Nagpur using digital solar radiation pyranometer for May 16,2011

Fig.4 shows Solar Global Radiation on Horizontal and Tilted Surface at Latitude and at Latitude±15°on May 16,2011 in EE department of VNIT, Campus Nagpur city. The radiation data generated through digital solar radiation pyranometer is used for graphical results.
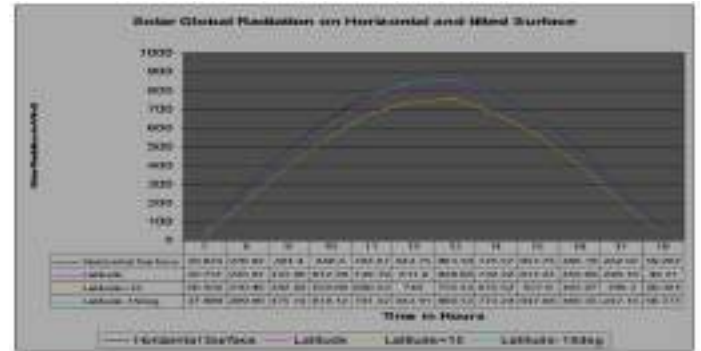
Fig.4:-Solar Global Radiation on Horizontal and Tilted Surface at Latitude and at Latitude±15°on May 16,2011 in EE department of VNIT, Campus Nagpur city

ELECTRICAL CHARACTERISTICS OF SILICON PV Solar Panels:-
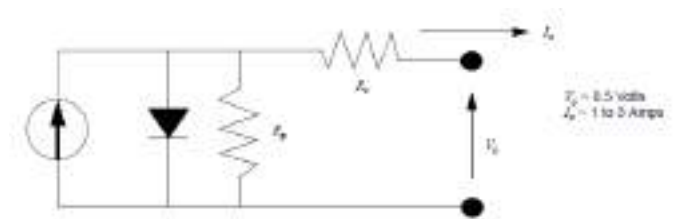
Fig. 5: Equivalent circuit of a Solar Cell.

Fig. 5 shows the equivalent circuit of Solar cell. A Solar Cell is a kind of P-N junction semiconductor device. It converts light energy into electrical energy. The equivalent circuit of the Solar cell is composed of the internal series resistance(R_s),and the shunt resistance (R_p)of the diode. The output characteristics of the solar cell depend on the irradiance and the operating temperature of the cell. The Solar cell output characteristics of the Solar cell as[14] is given by,

$$I_S = I_{ph} - I_{sat}[\exp(\frac{q(V_s + I_s R_s)}{AKT}) - 1] - \frac{V_s + I_s R_s}{R_p} \quad (8)$$

In (8), it is assumed that R_s equals zero and R_p equals infinity, thus the equation can be simplified as

$$I_S = I_{ph} - I_{sat}[\exp(\frac{qV_s}{AKT}) - 1] \qquad (9)$$

The I-V equation of the Solar cell can be given by

$$I_{total} = I_0(e^{qV/kT} - 1) - I_L \qquad (10)$$

where $I_L = qAG(L_n + L_p + W)$, the light generated current, which indicates that the carriers generated within the volume of cross-sectional area A and length $(L_n + L_p + L_w)$ contributes to the I_L.

The open circuit voltage of the solar cell is given by the equation,

$$V_{oc} = \frac{kT}{q} \ln(\frac{I_L}{I_0} + 1) \qquad (11)$$

Figures 6 and 7 show I-V and P-V characteristics of 37 Wp solar panel for the solar home lighting system.
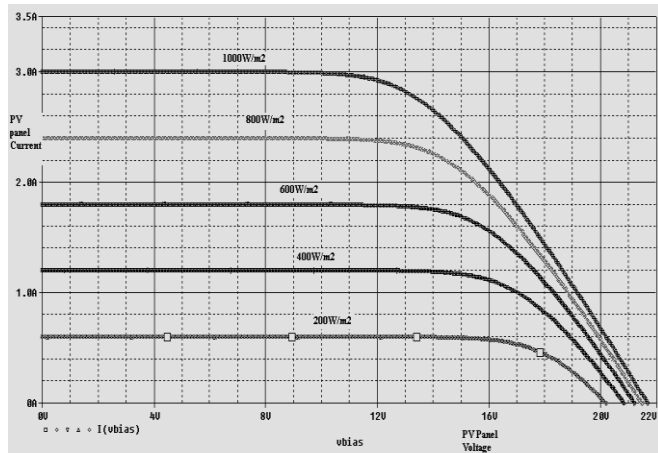
Fig.6: Simulated I-V characteristics of 37Wp solar panel for different solar radiations
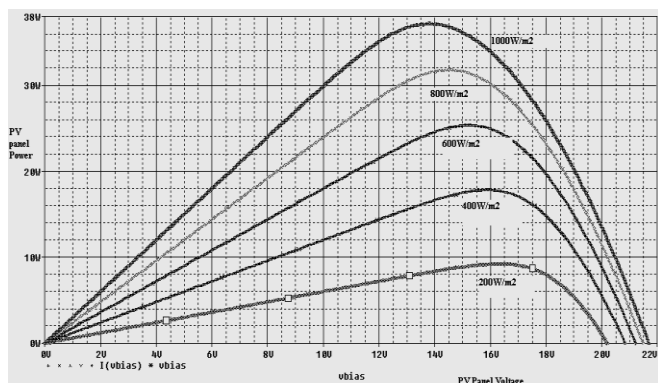
Fig.7: Simulated PV characteristics of 37Wp solar panel for different solar radiations

An additional solar panel of 74Wp is added in parallel to the existing 37Wp panel.

This has increased the power generation capacity of Solar panel to 111Wp.The modified

I-V and P-V characteristics of combined 37Wp Solar panel and 74Wp Solar panel is shown in figures 8 and 9
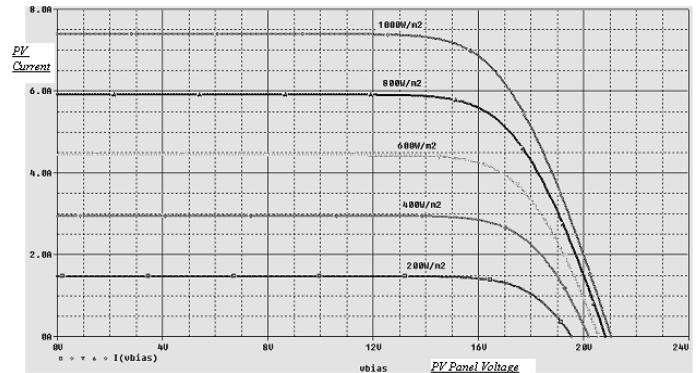
Fig.8 Simulated I-V characteristics of 111(37+74)Wp solar panels for different solar radiations
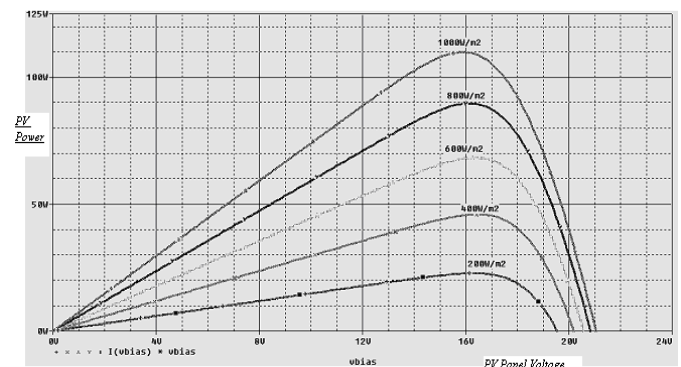
Fig.9:-Simulated P-V characteristics of 111(37+74)Wp solar panels for different solar radiations

The effort is being made to design a 100W single phase sine wave inverter which will be connected to utility. Initially results are generated using PSpice Simulation software.Fig.10 shows the general block diagram of a utility tied inverter
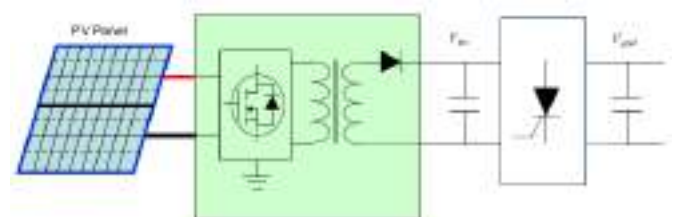
Fig.10: General block diagram of a utility tied inverter [16]

Simulation of utility tied inverter and PV system using PSpice 9.1

The PV generator consists of a 111Wp (37Wp+74Wp) panels having following parameters.

SPECIFICATION OF 37WP SOLAR PANEL:

Solar Panel Specifications of Home Lighting System Nominal electrical output @ 25⁰ C and STC condition Pmax=37
Watts;Vmp=16.4Volts;V_{oc}=21.0V;Imp=2.2Amps;I_{sc}=2.6Amp

SPECIFICATION OF 74WP SOLAR PANEL:-

A Solar Panel of 74Wp is added in parallel with the 37W$_p$ panel. The newly added 74W$_p$ panel has following specifications. At

STC(1000 W/m², AM 1.5 spectrum cell, temp=25°C.All values are nominal unless designated as tested. Rated power(P_{max}=75W_p), Open Circuit voltage, V_{oc}=21V,Short Circuit current(I_{sc})=4.8A, Voltage at maximum power(V_{mp})=17V,Current at maximum power(I_{mp})=4.41A

Fig.11 shows the photograph of 37Wp Solar panel.

Fig.11: 37Wp Solar panel

SPECIFICATION OF SOLAR UTILITY TIED MICRO- INVERTER (MICROCHIP MAKE) [18]

220 Watt, single PV cell module (36V) micro inverter

 Maximum Power Point Tracking = 99.5%

Maximum Power Point Tracking voltage – 25 VDC – 45 VDC

 DC short circuit current: – 10A

AC output voltage range: – 180 VAC – 264 VAC

45 Hz – 55 Hz

 90 VAC – 140 VAC

 55 Hz – 65 Hz

 Output Current THD – <5%

Fig.12 shows the Pspice diagram used for simulation of a grid connected Solar PV system for 111W Solar panel.
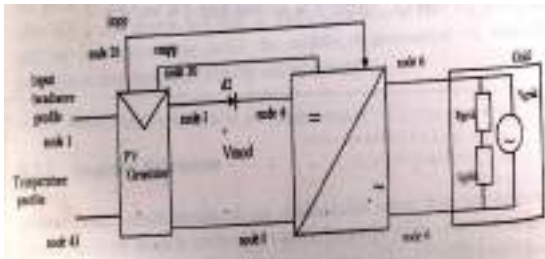
Fig 12:- PSpice utility tied inverter diagram used for simulation purpose [5]

SIMULATION RESULTS: The system is   simulated using PSpice Software by using Fig, 12. The time units of the irradiance profile have been scaled down from real measured data, by a factor 1e^{-6}

RADIATION PROFILE FOR 5 DAYS:- In this profile, x axis ends at 400ms corresponding to approximately 115 hours (5 days) of real time. The efficiency of the inverter is considered to be unity, nf=1.Fig. 13 shows the radiation profile waveform for 115 Hours. The y-axis shows the radiation in W/m²

.Scale for Y-axis is 1V= 1W/m²
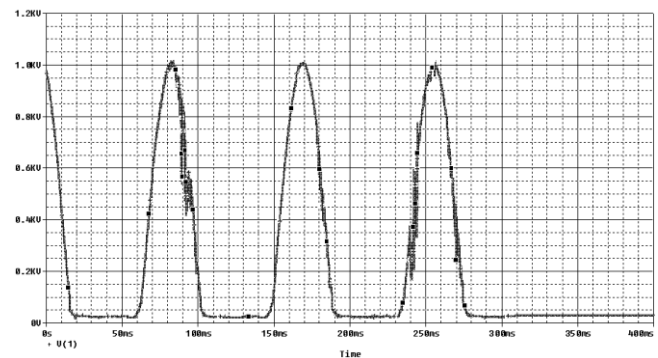
Fig. 13:-Radiation profile assumed for simulation of utility tied inverter

The grid can be modeled as an ideal sine wave voltage source, having a RMS voltage value of 220V and a frequency of 50Hz, connected to parallel load formed by the series connection of a resistor and inductor, L_{grid}=0.5mH,R_{grid}=14.4Ω.Fig.14 shows simulated inverter output power.
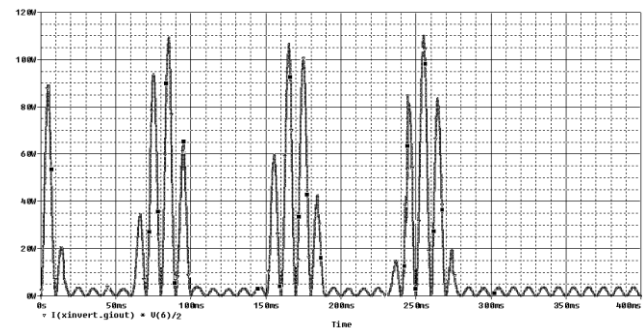
Fig.14-Simulated inverter output power

Fig.15 shows Inverter input current and fig.16 shows PV generator output current at its MPP.
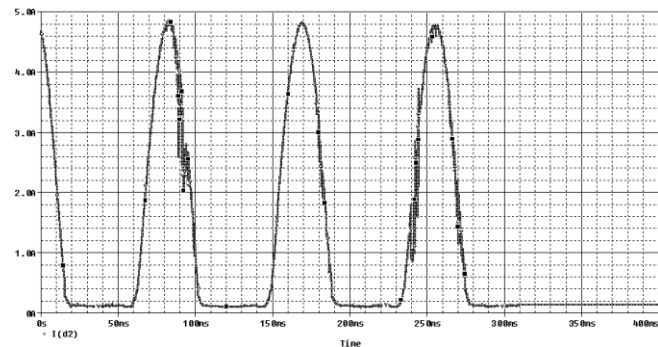
Fig.15: Inverter input current
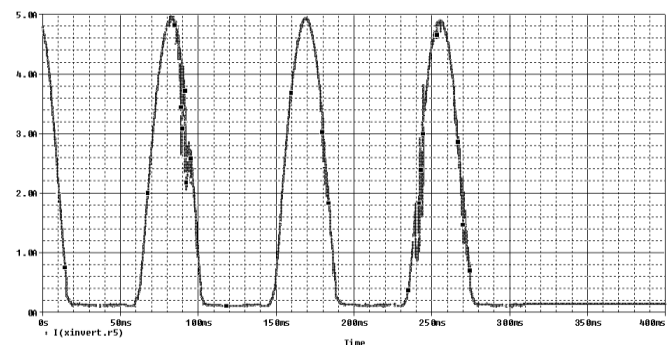
Fig.16:- PV generator output current at its MPP.

Fig.17 shows the voltage evolution at the inverter connection to the grid point, inverter output
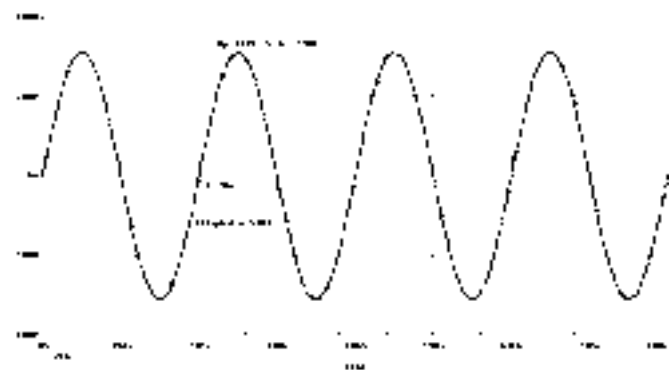
Fig.17:-The voltage evolution at the inverter connection to the grid point, inverter output

Fig 18 shows MPPT confirmation of voltage point of work at the inverter input.
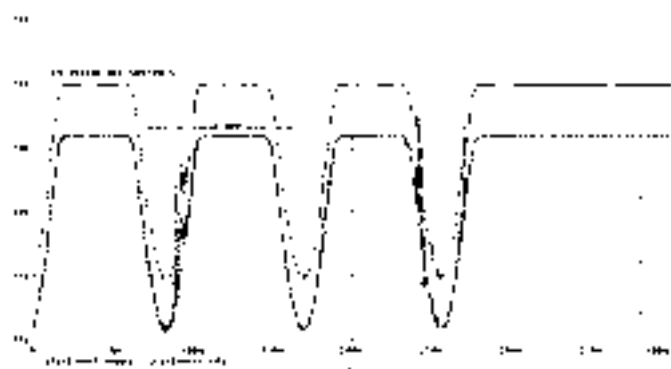
Fig 18:- MPPT confirmation of voltage point of work at the inverter input.

RADIATION PROFILE FOR CONTINUOUS INCREMENT

Fig.19 shows a continuous increase in the radiation profile for simulation purpose

Scale for Y-axis is 1V= 1W/m²
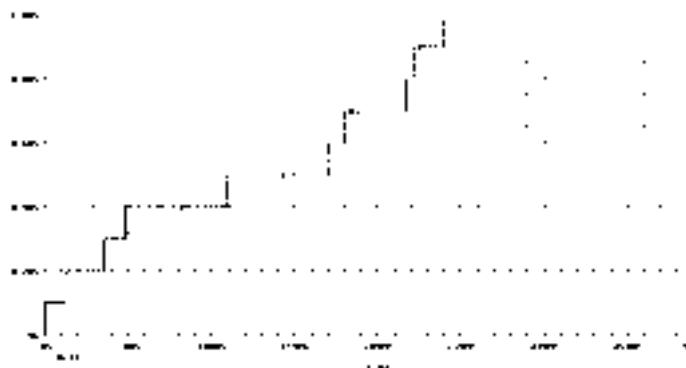
Fig.19 A continuous increase in the radiation profile for simulation purpose

Fig.20 shows the current evolution at the inverter connection to the utility point and
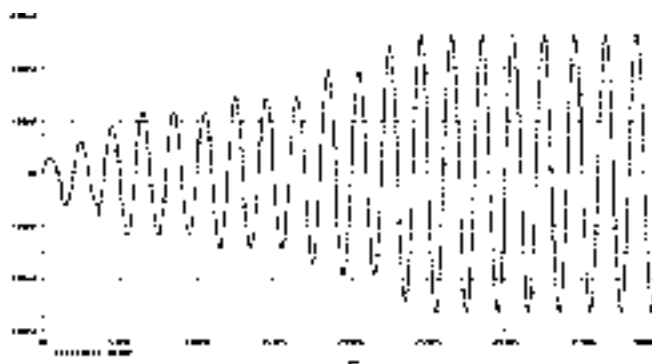
Fig.20:-The current evolution at the inverter connection to the utility point and Fig.21 shows the inverter output power.
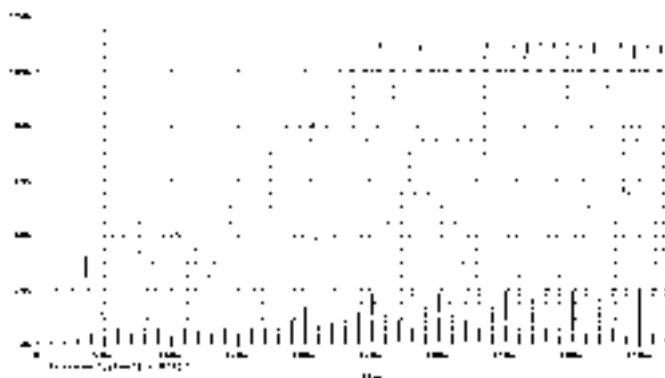
Fig.21:- Inverter output power

DESIGN OF NON ELECTROLYTIC CAPACITOR [18]

With a known value of ripple voltage, the capacitance value can be designed using the following formula,

$$C = \frac{P_m}{2\pi . f_r . V_m . V_r} \tag{12}$$

Where C- Capacitor, P_m – Maximum power point power of Solar Panels

f_r - Ripple frequency, V_m – Maximum Power point voltage and V_r – Ripple Voltage

Conclusion:-

Moving from centralized inverters to distributed inverters optimizes the energy harvest.

• Incorporating converters into the solar panel modules reduces installation costs.

• Improves system reliability from 5 to 20 years by reducing converter temperatures and removing fans.

• Replacing hard-switching techniques with soft switching improves efficiency and reduces heat dissipation.

• Standardized designs (hardware and software) improve reliability and reduce costs – from cottage industry to mass production.

• Eliminates electrolytic capacitors (due to high failure rate) – designs require higher voltages to reduce current, which allows use of lower capacitance non-electrolytic capacitors.

- Converters that are tied to the utility eliminate the need for batteries in many applications. Batteries are very expensive, require maintenance, and are short-lived.

- Microinverters tend to be lower powered (only a few hundred watts), which tends to lower internal temperatures and improve reliability.

- Micro inverter solar systems require many inverters to handle a specific power level – driving up production quantities, which reduces cost.

Acknowledgements

References:

[1] Sukhatme S.and Nayak J. Solar Energy, Third Edition,Tata Mc-Graw Hill Education Pvt. Ltd. New Delhi, 2010

[2] Solanki C.S. Solar Photovoltaics Fundamentals, Technologies and Applications, PHI Learning Private Limited, New Delhi, India,2009.

[3] Rasid M.H.: Power Electronics for Renewable Energy Sources, Power Electronics Handbook, Academic Press, 2001,

[4] Masters G.M. Stanford University" Renewable and Efficient Electric power System". John Wiley and Sons Ltd., 3rd Edition, 2004.

[5] Castaner L. and Silvestre S., "Modeling of Photovoltaic Systems using PSpice".J. Willey & Sons, Ltd., 2002.

[6] Mukerjee A.K. and Thakur Nivedita "Photovoltaic Systems-Analysis and Design"PHI Learning Private Limited,2011

[7] Lee J. H., Bae H. S.and Cho B. H. "Resistive Control for a Photovoltaic Battery Charging System using a Microcontroller;" IEEE Transactions on Industrial Electronics, 2008, 55, 7, 2767

[8] Masoum M.A. S. Badejani S. and Fuchs E.F. "Microprocessor Controlled new class of optimal battery chargers for photovoltaic applications". IEEE Transactions on Energy Conversion, 2004,19,3, 599.

[9] Boico F. Lehman B. and Shujaee Khalil "Solar Battery Chargers for NiMH Batteries" IEEE transactions on Power Electronics, 2007,22,5, 1600.

[10] Moharil R. M. and Kulkarni P. S. "A case study of Solar Photovoltaic Power System at Sagardeep Island, India", International Journal Renewable and Sustainable Energy Reviews, 2009, 13, 673.

[11] Barca G., Moschetto A., Sapuppo C., Tina G.M., Giusto R. and Grasso A.D. "A novel MPPT charge regulator for a photovoltaic stand-alone telecommunication system" , SPEEDAM 2008, International Symposium on Power Electronics, Electrical Drives, Automation and Motionary ,235.

[12] Kolhe Mohan "Techno-Economic Optimum sizing of a stand-alone solar photovoltaic system"; IEEE transactions on energy conversion, 2009,4,2, 511.

[13] Jain Sachin and Agarwal Vivek, "A single stage Grid Connected Inverter Topology for Solar PV Systems with Maximum Power Point Tracking" IEEE transactions on Power Electronics, 2007,22,5,1928.

[14] Park Sang, Cha Gil-Ro , Jung Yong-Chae and Won Chung-Yuen, "Design and Application for PV Generation System Using a Soft-Switching Boost Converter with SARC", IEEE Transaction On Industrial Electronics,2010,57,2, 515

[15] A.S.Werulkar, P.S..Kulkarni "Analysis of Microcontrollers based Solar Charge Controller for Solar Home Lighting System" selected for publication in 3rd International Conference on "Advances in Energy Research" (ICAER 2011) to be conducted on December 9-11,2011 in Department of Energy Science and Engg.at IIT, Bombay.

[16] Werulkar Ashutosh Sudhirrao, Kulkarni Prakash S."A Case Study of Residential Solar Photovoltaic System with Utility Backup in Nagpur, India" Renewable and Sustainable Energy Reviews, 2015, 52, 1809

[17] www.microchip.com

[18]http://ww1.microchip.com/downloads/en/AppNotes/0144 4A.pdf

ARTICLE

Modeling, Simulation and Analysis of Permanent Magnet Synchronous Motor

Jyoti Agrawal[1*], Sanjay Bodkhe[2]

[1*]Department of Electrical Engineering, G. H. Raisoni College of Engineering, Nagpur, India
[2]Department of Electrical Engineering, Shri Ramdeobaba College of Engineering & Management, Nagpur, India
E-mail: jyotigovindagrawal@gmail.com[1*], bodkhesb@rknec.edu[2]

Abstract: This paper deals with the modeling, simulation and analysis of three-phase permanent magnet synchronous motor (PMSM). Suitable reference frame transformations are introduced so as to obtain a d-q model of PMSM from the well-known model of synchronous machine, removing the equations of field current dynamics and damper windings. A detailed mathematical model of permanent magnet synchronous motor is required to analyze the instantaneous effects of changing voltages, currents, frequencies and torque on the motor. The effectiveness of speed sensorless drive is based upon development of correct plant model. Therefore, correct model of motor is the key requirement to control any motor properly. The detailed modeling of permanent magnet synchronous motor and derivation for electromagnetic torque is carried out in this paper. The mathematical model thus obtained is convenient for MATLAB simulations. Simulation results confirm the validity of theoretical analysis

Keywords—PMSM; reference frame transformation; electromagnetic torque; MATLAB/Simulink

NOMENCLATURE

B	damping constant, (N/rad/s)
i_{as}, i_{bs}, i_{cs}	instantaneous stator phase currents, (A)
$i_{\alpha s}, i_{\beta s}$	d- and q-axes stator currents in stator reference frame, (A)
i^r_{ds}, i^r_{qs}	d and q-axes stator currents in rotor reference frame, (A)
i^*_s	stator current reference, (A)
J	total moment of inertia, (kg-m^2)
L_d, L_q	stator d- and q-axes self-inductances in rotor reference frame, (H)
L_{dd}, L_{qq}	stator d and q-axes self-inductances in stator reference frame, (H)
L_{dq}, L_{qd}	mutual inductances between d- and q- axes windings, (H)
L_{ls}	leakage inductance
P	Number of poles

R_s	stator resistance per phase, (Ω)
T_e	electromagnetic torque, (N-m)
T_l	load torque, (N-m)
P	differential operator, d/dt
v_{as}, v_{bs}, v_{cs}	input phase voltages, (V)
$v_{\alpha s}, v_{\beta s}$	d- and q-axes stator voltages in stator reference frame, (V)
v^r_{ds}, v^r_{qs}	d- and q-axes stator voltages in rotor reference frame, (V)
$\lambda_{\alpha s}, \lambda_{\beta s}$	d- and q-axes stator flux linkages, (Wb)
λ_{af}	armature flux linkages, (Wb)
θ_r	rotor position, (radians)
ω_r	electrical rotor speed, (rad/s)
ω_m	mechanical rotor speed, (rad/s)
δ	torque angle, (rad)

Introduction

In recent years, PMSMs appear a good choice not only for industrial and robotics applications, but also for Hybrid Electrical Vehicles (HEV), because of their advantages like simplicity, torque density, high efficiency and high power factor when compared with other conventional motors [1], [2].

PMSM has also overcome the limitations of synchronous motor by using the high energy permanent magnets instead of electromagnets to provide field excitation, this result in low maintenance and less rotor loss. Different magnetic materials are available out of which most of the PM motors use Neodymium Iron boron (NdFeB) rare earth magnets as they provide highest energy and residual flux density thereby enhancing the performance of PMSM drives [3]. Modeling is the foremost step which helps in a better understanding of the motor. Moreover it introduces the basics for understanding and examining the various advanced control schemes like vector control, direct torque control and sensorless control [4]. The back EMF voltage waveform for PMSM is sinusoidal in shape and requires sinusoidal current to produce constant torque. Reference frame transformations are introduced to obtain a *d-q* model of PMSM, since it is easily adapted to study the performance of PMSM [5]. With these transformations the three ac quantities are reduced to dc quantities in steady state [6].

A three-phase PMSM consists of three-phase windings spaced 120 electrical degrees from one another on the stator and rotor with PMs. The dynamic model of three phase motor is described by a set of stator differential equations with time-varying coefficients. As the inductance varies with rotor position such a dynamic model makes the calculation of machine parameters very complex, cumbersome and inconvenient [7]. Therefore, a conceptual simplicity is obtained by transforming the variables from three-phase '*a-b-c*' into two-phase '*d-q*' thus eliminating the dependency on rotor position. The direct '*d*' axis lags quadrature '*q*' axis by 90 electrical degrees. Hence, it is convenient to represent the motor model in a *dq* frame rotating with the speed of rotor. The most well-known transformation methods available are Clarke and Park transformation. The mathematical model of three-phase PMSM may be represented with a two-pole, 2-ϕ configuration along *dq*-axes which offers ease of only single set of windings on stator.

The *d-q* model of PMSM is used to examine the transient behavior of a vector controlled PMSM speed drive. The main objective of this paper is to show that the *d-q* model is sufficient in order to study the PMSM in detail.

This paper is structured as follows: Section I begin with providing a general introduction and reviewing briefly about a study of PMSM, focusing on the modeling of PMSM. Section II presents the detailed mathematical modeling of PMSM. Section III uses the PMSM model to present some key simulation results to analyze the performance and use of PMSM model. Finally, the paper is concluded in section IV.

MATHEMATICAL MODEL OF PMSM

To reduce the complexity, some assumptions are made while deriving the dynamic model of PMSM as follows [8], [9]:

- Saturation effect and parameter changes are ignored.
- Inductance versus rotor position is sinusoidal.
- Balanced stator windings with sinusoidally distributed mmf.
- Back electromotive force (EMF) waveform is sinusoidal.
- Friction and windage losses are small.

Under these assumptions the stator (*abc*) voltage equation in stationary reference frame are described by the below differential equation

$$v_{abcs} = R_s i_{abcs} + p\lambda_{abcs} \tag{1}$$

where,

$$\left(v_{abcs}\right) = \begin{bmatrix} v_{as} \\ v_{bs} \\ v_{cs} \end{bmatrix}; \left(i_{abcs}\right) = \begin{bmatrix} i_{as} \\ i_{bs} \\ i_{cs} \end{bmatrix}; \left(\lambda_{abcs}\right) = \begin{bmatrix} \lambda_{as} \\ \lambda_{bs} \\ \lambda_{cs} \end{bmatrix} \tag{2}$$

In the (1) winding resistance of all phases are equal i.e. $R_s = R_a = R_b = R_c$ and therefore represented as a constant, not in matrix. Rotor equations do not exist for PMSM as rotor consists of PM.

The flux linkages of the stator winding λabcs can be written as

$$\lambda_{abcs} = \lambda_{abcs(s)} + \lambda_{abcs(r)} \tag{3}$$

where,

$$\lambda_{abcs(s)} = \begin{bmatrix} L_{aas} & L_{abs} & L_{acs} \\ L_{bas} & L_{bbs} & L_{bcs} \\ L_{cas} & L_{cbs} & L_{ccs} \end{bmatrix} \begin{bmatrix} i_{as} \\ i_{bs} \\ i_{cs} \end{bmatrix}$$

and

$$\lambda_{abcs(r)} = \lambda_m \begin{bmatrix} \sin\left(\theta_r\right) \\ \sin\left(\theta_r - \dfrac{2\pi}{3}\right) \\ \sin\left(\theta_r + \dfrac{2\pi}{3}\right) \end{bmatrix} \tag{4}$$

Assuming, Stator inductance matrix =

$$L_s = \begin{bmatrix} L_{aas} & L_{abs} & L_{acs} \\ L_{bas} & L_{bbs} & L_{bcs} \\ L_{cas} & L_{cbs} & L_{ccs} \end{bmatrix}$$

The self-inductances in (4) are the functions of rotor position and they are described below.

$$L_{aas} = L_{1s} + L_A - L_B \cos 2\theta_r \qquad (5)$$

$$L_{bbs} = L_{1s} + L_A - L_B \cos\left(2\theta_r + \frac{2\pi}{3}\right) \qquad (6)$$

$$L_{ccs} = L_{1s} + L_A - L_B \cos\left(2\theta_r - \frac{2\pi}{3}\right) \qquad (7)$$

The mutual inductances in are given by

$$L_{abs} = L_{bas} = -\frac{1}{2}L_A - L_B \cos\left(2\theta_r - \frac{2\pi}{3}\right) \qquad (8)$$

$$L_{acs} = L_{cas} = -\frac{1}{2}L_A - L_B \cos\left(2\theta_r + \frac{2\pi}{3}\right) \qquad (9)$$

$$L_{bcs} = L_{cbs} = -\frac{1}{2}L_A - L_B \cos 2\theta_r \qquad (10)$$

It can be noted from (5) - (10) that all the elements of L_s are rotor position dependent due to which its solution becomes bulky. Therefore, it is necessary to eliminate the dependency on rotor position by transformation.

Equations (3) and (4) can be represented compactly as

$$\begin{bmatrix} \lambda_{as} \\ \lambda_{bs} \\ \lambda_{cs} \end{bmatrix} = L_s \begin{bmatrix} i_{as} \\ i_{bs} \\ i_{cs} \end{bmatrix} + \lambda_m \begin{bmatrix} \sin(\theta_r) \\ \sin\left(\theta_r - \frac{2\pi}{3}\right) \\ \sin\left(\theta_r + \frac{2\pi}{3}\right) \end{bmatrix} \qquad (11)$$

A. Reference frame transformation

The term reference frame transformation implies transforming the variables from 3-ϕ (*abc*) system to stationary (*αβ*), or rotating (*dq*) two phase system [6]. These transformations are essential to decrease the complexity of several derivations. So to eliminate the dependency of inductances on rotor position, the 3-ϕ variables are transformed into rotating (*dq*) two phase variables [10]. This transformation from *abc* reference frame to *dq* rotating reference frame may be performed in a one step or two different steps. For this purpose the well-known Clarke, Park, Inverse Clarke and Inverse Park transformations are modeled and implemented.

The 3-ϕ quantities (*abc*) are transformed into 2-ϕ quantities (*αβ*) in stationary reference frame by Clarke transformation as follows

$$i_\alpha = i_a, \; i_\beta = \frac{1}{\sqrt{3}}i_a + \frac{2}{\sqrt{3}}i_b \; \text{ and } i_0 = \frac{2}{3}\left(i_a + i_b + i_c\right) \quad (12)$$

The 2-ϕ variable in stationary (*αβ*) reference frame are transformed to 2-ϕ variables in rotating (*dq*) reference frame by Park transformation as follows

$$i_d^r = i_\alpha \cos\theta + i_\beta \sin\theta \; \text{ and}$$

$$i_q^r = -i_\alpha \sin\theta + i_\beta \cos\theta \qquad (13)$$

B. Voltage equations in rotor (dq) reference frame

The *dq* voltages in rotor reference frames are obtained from *abc* voltages through Park transformation as follows [11], [12]

$$v_{dqs}^r = \left[T^r\right] v_{abcs} \qquad (14)$$

where, $\left[T^r\right] = \frac{2}{3} \begin{bmatrix} \cos\theta_r & \cos\left(\theta_r - 120°\right) & \cos\left(\theta_r + 120°\right) \\ \sin\theta_r & \sin\left(\theta_r - 120°\right) & \sin\left(\theta_r + 120°\right) \\ \frac{1}{2} & \frac{1}{2} & \frac{1}{2} \end{bmatrix}$

The voltage equations describing the PMSM operation in rotor reference frame are

$$\begin{bmatrix} v_{ds}^r \\ v_{qs}^r \end{bmatrix} = R_s \begin{bmatrix} i_{ds}^r \\ i_{qs}^r \end{bmatrix} + p \begin{bmatrix} \lambda_{ds}^r \\ \lambda_{qs}^r \end{bmatrix} + \omega_r \begin{bmatrix} -\lambda_{qs}^r \\ \lambda_{ds}^r \end{bmatrix} \qquad (15)$$

where, $\lambda_{ds}^r = L_d i_{ds}^r + \lambda_{af}$

and $\lambda_{qs}^r = L_q i_{qs}^r \qquad (16)$

Substituting the value of flux linkages from (16) into (15), the voltage equations v_{ds}^r and v_{qs}^r are written as

$$\begin{bmatrix} v_{ds}^r \\ v_{qs}^r \end{bmatrix} = R_s \begin{bmatrix} i_{ds}^r \\ i_{qs}^r \end{bmatrix} + p \begin{bmatrix} L_d i_{ds}^r + \lambda_{af} \\ L_q i_{qs}^r \end{bmatrix} + \omega_r \begin{bmatrix} -L_q i_{qs}^r \\ \left(L_d i_{ds}^r + \lambda_{af}\right) \end{bmatrix} \qquad (17)$$

Above equation is rewritten as below

$$\begin{bmatrix} v_{qs}^r \\ v_{ds}^r \end{bmatrix} = \begin{bmatrix} R_s + L_q p & \omega_r L_d \\ -\omega_r L_q & R_s + L_d p \end{bmatrix} \begin{bmatrix} i_{qs}^r \\ i_{ds}^r \end{bmatrix} + \omega_r \lambda_{af} \begin{bmatrix} 1 \\ 0 \end{bmatrix} \quad (18)$$

It should be noted from (18) that the impedance matrix is no longer dependent on rotor position and has constant value of inductances.

The dynamic equations of PMSM are assembled finally and written as [13], [14]

$$p i_{ds}^r = \left(-\frac{L_q}{L_d} \omega_r i_{qs}^r - \frac{R_s}{L_d} i_{ds}^r + \frac{1}{L_d} v_{ds}^r \right) \quad (19)$$

$$p i_{qs}^r = \left(-\frac{R_s}{L_q} i_{qs}^r - \frac{L_d}{L_q} \omega_r i_{ds}^r - \frac{\lambda_{af}}{L_q} \omega_r + \frac{1}{L_q} v_{qs}^r \right) \quad (20)$$

$$p \omega_r = \frac{1}{J} \left(T_e - B \omega_r - T_l \right) \quad (21)$$

$$p \theta_r = \omega_r = \omega_{rn} \omega_b \quad (22)$$

These equations (19) - (22) describe the entire behaviour of PMSM and are modeled using MATLAB software [8].

C. Equivalent circuit of PMSM

The equivalent circuit of PMSM in rotor (dq) reference frame can be obtained based on the dynamic equations (18) and is shown in Fig. 1 [15].

(a)

(b)
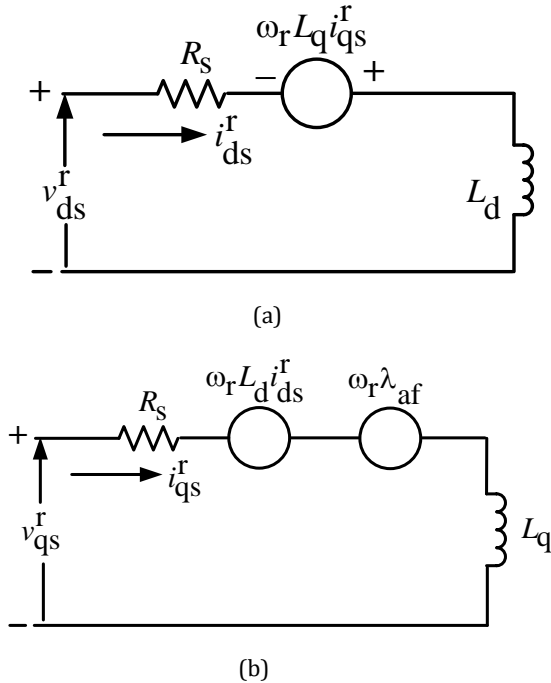
Fig. 1. Dynamic electric equivalent circuits of PMSM in rotor reference frame. (a) d-axis (b) q-axis

The i_{ds}^r and i_{qs}^r currents are constant quantities during steady-state operation. Hence the dynamic electric equivalent circuit of

PMSM can be reduced to the steady-state equivalent circuit shown in Fig. 2.

D. Instantaneous power and electromagnetic torque

The instantaneous input power to the PMSM can be represented as

$$P_i = \left[v_{as} i_{as} + v_{bs} i_{bs} + v_{cs} i_{cs} \right] \quad (23)$$

(a)

(b)
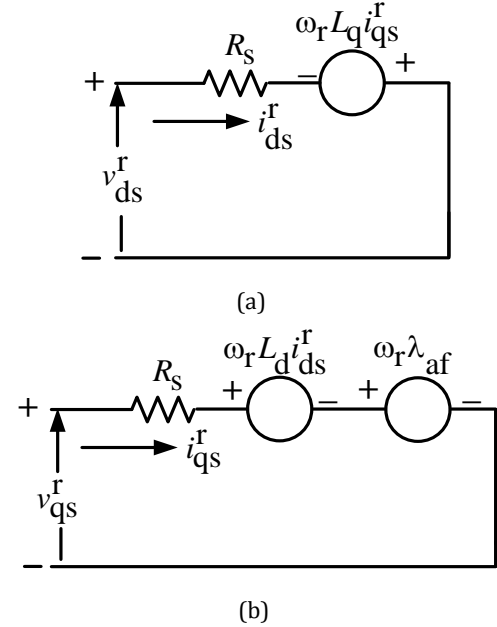
Fig. 1. Steady-state electric equivalent circuits of PMSM in rotor reference frame. (a) d-axis (b) q-axis

The stationary three phase quantities of the stator are transformed into two-axis rotating dq- frame by using Park's transformation as

$$P_i = \frac{3}{2} \left[v_{ds}^r i_{ds}^r + v_{qs}^r i_{qs}^r + 2 v_0 i_0 \right] \quad (24)$$

Under the assumption of balanced three-phase machine, $v_0 = i_0 = 0$, (24) becomes:

$$P_i = \frac{3}{2} \left[v_{qs}^r i_{qs}^r + v_{ds}^r i_{ds}^r \right] \quad (25)$$

The mechanical output power (P_o) can be calculated by replacing the terms on the right hand side of (25) i.e. v_{qs}^r and v_{ds}^r with the associated speed voltages as

$$P_o = \frac{3}{2} \left[-\omega_r \lambda_{qs}^r i_{ds}^r + \omega_r \lambda_{ds}^r i_{qs}^r \right] \quad (26)$$

The output power is the product of electromagnetic torque and mechanical rotor speed

$$P_o = T_e \omega_m \quad (27)$$

where, ω_m is the mechanical rotor speed (rad/s) which is given by $\omega_m = \dfrac{2}{P}\omega_r$

Therefore, electromagnetic torque from (26) and (27) is obtained as

$$T_e = \frac{P_O}{\omega_m} = \frac{\frac{3}{2}\left[-\omega_r \lambda_{qs}^r i_{ds}^r + \omega_r \lambda_{ds}^r i_{qs}^r\right]}{\omega_m} \qquad (28)$$

The expression of torque in terms of inductances can be given by

$$T_e = \frac{3}{2}\frac{P}{2}\left[\lambda_{af} + \left(L_d - L_q\right)i_{ds}^r\right]i_{qs}^r \qquad (29)$$

The dq-axes currents in the rotating frame of reference are obtained as [16]

$$\begin{bmatrix} i_{ds}^r \\ i_{qs}^r \end{bmatrix} = i_s \begin{bmatrix} \cos\delta \\ \sin\delta \end{bmatrix} \qquad (30)$$

where, i_s is the peak of phase current.

The d-axis winding which is rotating at ω_r is aligned with the rotor flux and its linkages. The stator current phasor i_s is the resultant of d- and q- axes component and is leading the rotor flux linkage phasor by δ radian known as torque angle. The d- axis component along rotor flux axis is responsible for producing flux only, hence it is known as flux producing component represented by 'i_f' whereas the q- axis component in quadrature with rotor flux axis is responsible for producing torque only, hence it is known as torque producing component represented by 'i_T'.

Substitution of (30) into the torque expression gives

$$T_e = \frac{3}{2}\frac{P}{2}\left[\lambda_{af} + \left(L_d - L_q\right)i_s\cos\delta\right]i_s\sin\delta \qquad (31)$$

Finally, the torque expression can be obtained as

$$T_e = \frac{3}{2}\frac{P}{2}\lambda_{af}i_s\sin\delta + \frac{3}{2}\frac{P}{2}\left[\frac{1}{2}\left(L_d - L_q\right)i_s^2\sin\left(2\delta\right)\right] \qquad (32)$$

It is apparent from the torque expression that it has two terms. The first term on the R.H.S. of (32) resembles to "synchronous torque (T_{es})" due to the interaction of rotor flux and stator q-axis current in rotating frame of reference. The 2nd term on the R.H.S. of (32) resembles to "reluctance torque (T_{er})" due to the inductance variation (saliency).

Simulation Results and Discussion

The dynamic equations of PMSM have been simulated in MATLAB environment to analyze the performance of PMSM. The PMSM was modeled using (19)-(22) and the parameters used for calculations are given in Table I.

The stability of PMSM is determined by using root locus technique. Fig. 3 illustrates the sketch of root locus using its dynamic model. From the plot it is observed that PMSM is a stable system as all the poles lie in left half of s-plane [8].

TABLE 1

Parameters of PMSM and Control System

Symbol	Parameter	Value and units
B	Damping constant	0.0005 Nm/rad/s
I_b	Base current	4 (A)
J	Moment of inertia	0.0002 kgm²
L_d	Stator d-axis inductance	12 (mH)
L_q	Stator q-axis inductance	5.7 (mH)
P	Stator Pole pairs	4
R_s	Stator Phase resistance	1.2 (Ω)
λ_{pm}	PM flux-linkage	0.123 (Wb)
T_L	Load torque	0 (N-m)
T_b	Base torque	2.43 (N-m)
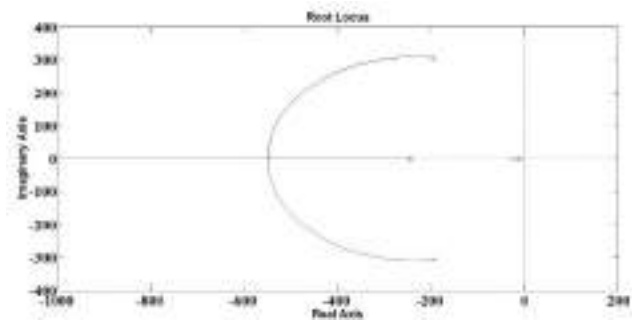
Fig. 2. Sketch of root locus.

The electromagnetic, synchronous and reluctance torque as a function of torque angle (δ) represented by (32) are depicted in Fig. 4. From the loci it can be noted that the peak occurs at an angle greater than 90º. So the chosen torque angle region is 90º < δ < 180º [12]. Angle at which maximum torque takes place for different magnitudes of stator current (i_s) is shown in Fig. 5. It is significant in optimum torque per ampere control (OTPAC) strategy for PMSM.

Fig. 6 shows the simulation results for transforming the stator three phase voltages to two phase voltages in rotating (dq) reference frame and from there recovering stator currents and electromagnetic torque under constant rotor speed of 376.99 rad/s. It is seen from Fig. 6 (b) and Fig. 6 (d) that the stator voltages in rotor (dq) frame of reference are constants and the recovered current in abc frame is sinusoidal [17]. It is noted from the response of electromagnetic torque shown in Fig. 6 (e) that the torque is negative demonstrating that motor is generating and delivering power to source [18].
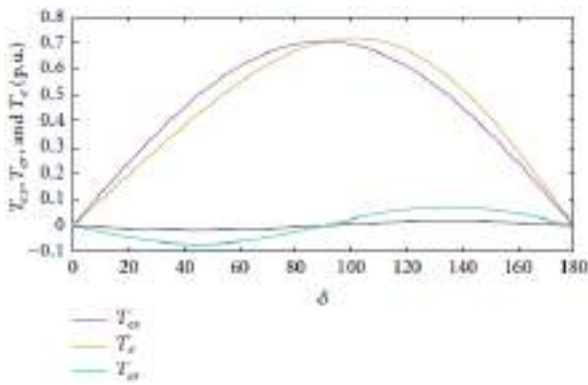
Fig. 3. Synchronous, reluctance and air gap torques versus δ
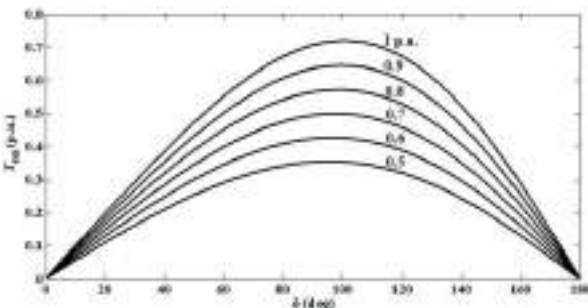
Fig. 4. Air gap torque versus δ for various stator currents

(a)

(b)

(c)

(d)

(e)
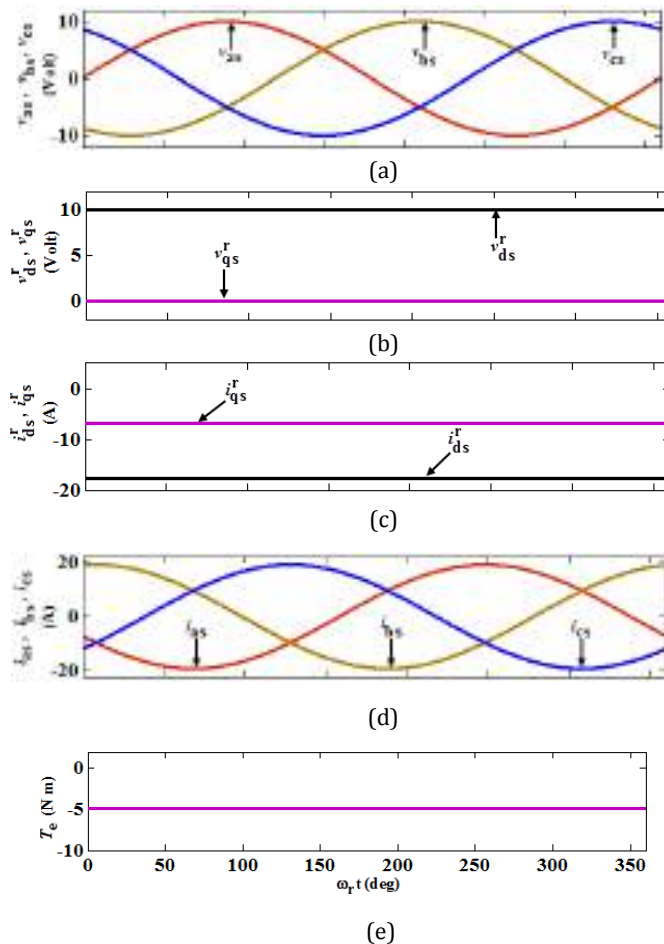
Fig. 5. The rotating, abc frames stator voltages, currents and torque under constant speed.

Using the machine parameters given in Table I, the simulation results shown in Fig. 7 are plotted in normalized unit under no load condition. Fig. 7 illustrates the loci of *dq*-axes voltages in rotor frame, obtained from Park's transformation. The stator current response appears to attain high magnitude with oscillations in normalized torque, which results in rotor oscillations. It can be noted from Fig. 7 (e) that the rotor speed itself is oscillatory and so the rotor position obtained from rotor speed is also oscillatory. Hence, *dq*-axes voltages are not constant as transformation matrix is the function of θᵣ. Such kind of operation is not desirable but it occurs as no control is imposed on PMSM [19].

(a)

(b)

(c)

(d)

(e)
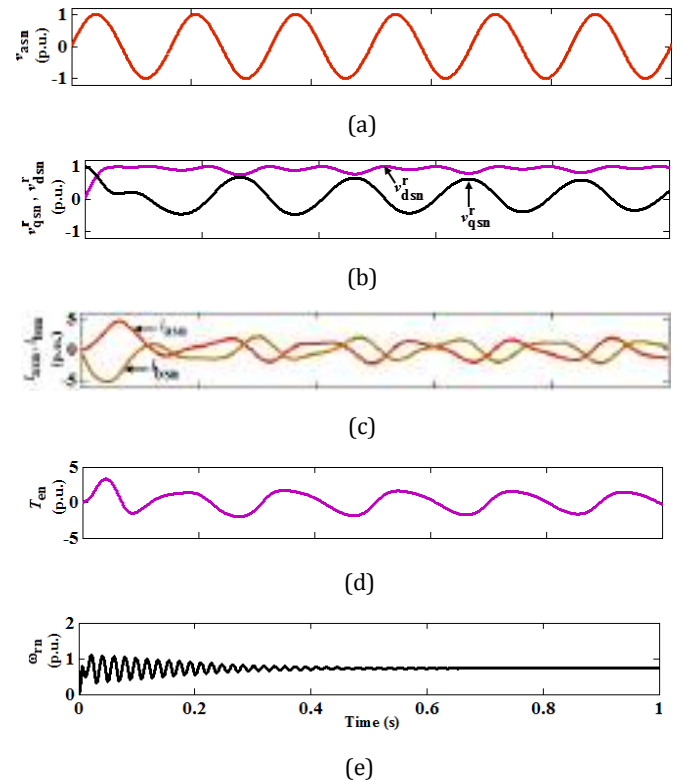
Fig. 6. Dynamic simulation of PMSM using p. u. model.

Conclusion

This paper has discussed the dynamic modeling of a three-phase PMSM. The equations that describe the performance of PMSM can be expressed in stationary (*αβ*) and rotating (*dq*) reference frames, but the most commonly used orientation is rotating frame of reference as it reduces the complexity. Observing the entire system from rotor reference frame, results in the disappearance of position dependent inductances thus leading to the simplification of differential equations. The detailed mathematical modeling of PMSM is carried out and equivalent two-phase model is derived. Using this model both steady state and transient behavior of PMSM can be studied. The theoretical background of PMSM was supported by the simulation results using MATLAB/Simulink software.

References

[1] M. Zafarani, T. Goktas, B. Akin and S. E. Fedigan, "Modeling and Dynamic Behavior Analysis of Magnet Defect Signatures in Permanent Magnet Synchronous Motors", *IEEE Trans. Ind. Appl.*, vol. 52, no. 5, pp. 3753-3762, September/October 2016.

[2] W. Xu, Y. Jiang and C. Mu, "Novel Composite Sliding Mode Control for PMSM Drive System Based on Disturbance Observer", *IEEE Trans. Applied Superconductivity*, vol. 26, no. 7, pp. 3753-3762, October 2016.

[3] J. Hong, D. Hyun, S. Lee, J. Yoo and K. Lee, "Automated Monitoring of Magnet Quality for Permanent-Magnet Synchronous Motors at standstill", *IEEE Trans. Ind. Appl.*, vol. 46, no. 4, pp. 1397-1405, July/August 2010.

[4] S. K. Sul. *Control of Electric Machine Drive Systems*, IEEE Press, 2011.

[5] P. Vas. *Sensorless Vector and Direct Torque Control*, Oxford University Press, 1998.

[6] Paul C. Krause, Oleg Wasynczuk and Scott D. Sudhoff, *Analysis of electric machinery*, IEEE Press, 1995. Elect., vol. 35, no. 4, pp. 537-541, November 1988.

[7] R. Krishnan. *Permanent Magnet Synchronous and Brushless DC Motor Drives*, CRC Press, 2010.

[8] P. Pillay and R. Krishnan, "Modeling of Permanent Magnet Motor Drives", *IEEE Trans.Ind. Elect.*, vol. 35, no. 4, pp. 537-541, November 1988.

[9] T. Sebastian, G. R. Slemon and M. A. Rahman, "Modelling of Permanent Magnet Motors", *IEEE Trans.Magn.*, vol. 22, no. 5, pp. 1069-1071, September 1986.

[10] N. Mohan., *Advanced Electric Drives Analysis, Control and Modeling using Simulink*, MNPERE, Minneapolis, 2001.

[11] B. K. Bose, *Power Electronics and Motor Drives: Advances and Trends*, Academic Press, Elsevier, 2006.

[12] P. Wood, *Theory of Switching Power Converter*, Van Nostrand-Reinhold, New York 1981.

[13] P. Pillay and R. Krishnan, "Modeling, simulation, and analysis of permanent-magnet motor drives, Part I: The permanent-magnet synchronous motor drive", *IEEE Trans. Ind. Appl.*, vol. 25, no. 2, pp. 265-273, March/April 1989.

[14] R. Krishnan. *Electric Motor Drives: Modeling, Analysis, and Control*, Prentice-Hall, Upper Saddle River, NJ, 2001.

[15] J. Chiasson, *Modeling and High Performance Control of Electric Machines*, Chichester, John Wiley & Sons, 2005.

[16] H. A. Rub, A. Iqbal and J. Guzinski, *High Performance Control of AC Drives with MATLAB/SIMULINK*, Wiley, 2012.

[17] Bimal K. Bose, *Modern Power Electronics and AC Drives*, Prentice Hall PTR, 2002.

[18] I. Boldea and S. A. Nasar, *Electric Drives*, CRC Press, 2006.

[19] J. W. Finch and Giaouris, D, "Controlled AC Electrical Drives," *IEEE Trans. Ind. Elect.*, vol. 55, no.2, pp. 481-491, February 2008

ARTICLE

Studies of Macrobenthos in Simbhora Lake of Ta. Morshi , District- Amravati(M.S)

Sarita S.Nimgare[1]and Ujwala W.Fule[1]

Hutatma Rashtriya Arts and Science College, Ashti.
E mail Id- patankar.kargi@gmail.com

Abstract: Pollution is a major cause of environmental deterioration. The use of macrobenthos as bio-indicator in the assessment of water quality realized better understanding in the field of limnology as compared to biotopes characteristics.Insect and molluscs are the tolerant species in the changing condition of water ecosystem The present study is carried out to study macrobenthos in Simbhoralake in the year 2013-2014. In the present investigation, total 23 species from four major groups were observed viz. Gastropoda, Nematoda, Oligocheta and Insecta. In Gastropoda 09 species were recorded, in Nematode 03 species, in Oligocheta 02 species and in Insecta 9 species

Keywords: Macrobenthos, Simbhoralake, Water, Quality

Introduction

Benthic organisms which inhabit on the bottom of water body. This group of organism recognized as very important group in detecting the water quality and these organisms move away from pollution site. They have shown sensitivity to pollution. They can be relatively easily collected handles and identified. They are linked with food web of fishes and also play an important role in mud water exchange of biological nutrients. Better understanding in recent years about benthos and its environment results of their exploitation from water bodies. Water bodies leading to enrichment of the nutrient level beyond proper line. The present study is carried out to study macrobenthos in Simbhoralake during year 2013-14.

Material and method :

During the period of investigation, Benthos-macro invertebrates collected through netting and hand picking from three sites of Simbhoralake during year 2013-14. Separate samples were collected brought immediately in laboratory and preserved in 4% formalin. Identification was done with the help of standard text.

Observation and Results:

Benthic macroinvertebrates:I.

In the present investigation, total 23 species from four major groups were observed viz. Gastropoda, Nematoda, Oligochetaand Insecta. In Gastropoda 09 species were recorded, in Nematode 03 species, in Oligocheta 02 species and in Insecta 9 species. Gastropoda consist of 9 species, which are *Bellamyabengalensis* (Lamark), *Gyraulusconvexiusculus* (Hutton), *Indoplanorbisexustus* (Deshayes), *Lymnaeaaccuminata* (Lamark), *Pilaglobosa, Thiarascabra, Thiaratuberculata* (Muller), Tendipstentips, Cyclotopsis*. Among which *Bellamyabengalensis* (Lemark) and *Indoplanorbisexustus* (Deshayes) and *Thiarascabra*were dominantly observed. However, *Thiaratuberculata* (Muller) were least in appearance. The benthic macroinvertebrates represented in the Table 1 and photo plate I

Table 1: Macroinvertebrates in Simbhora lake during year 2013-14

Sr. No.	Name of Macroinvertebrates
A)	**Gastropoda**
1	*Bellamyabengalensis (Lamark)*
2	*Gyraulusconvexiusculus (Hutton)*
3	*Indoplanorbisexustus (Deshayes)*
4	*Lymnaeaaccuminata (Lamark)*
5	*Pila sp.*
6	*Thiarascabra*
7	*Thiaratuberculata (Muller)*
8	*Tendipestentipes*
9	*Cyclotopsis*
B)	**Nematode**
1	*Diplogasterfactor*
2	*Planeria sp.*
3	*Rhabdolimus minor.*
C)	**Oligocheta**
1	*Limnodrilushoffmeisteri*
2	*Tubifextubifex (Muller)*
D)	**Insecta**
1	*Ophiogomphus sp.*
2	*Aniseps sp.*
3	*Anopheles larva*
4	*Chironomus sp.*
5	*Corixa sp.*
6	*Culex larva*
7	*Dineutus sp.*
8	*Eristalis sp.*
9	*Notonecta sp.*

Plate 1: Macro-benthos in Simbhoralake.

Discussion:

Benthos plays an important role in the secondary productivity of fresh water lakes through exchanging of allochthonous and autochthonous materials in a lake ecosystem. Benthic organisms are of great ecological significance because they constitute the food of fish and their productivity plays an important role in sustaining food chain and food web.

In the present investigation, total 23 species from four major groups were observed viz. Gastropoda, Nematoda, Oligocheta and Insecta. In Gastropoda 09 species were recorded, in Nematode 03 species, in Oligocheta 02 species and in Insecta 9 species. Similarly, Gorai*et al.,* (2005) reported 4 groups of Benthic organisms consisting Gastropoda (3species), Insects larvae (one species), Oligochaetae (8 species). Zade and Sitre (2012) recorded Nematoda 01 species, Oligocheta 09 species, Insecta 01 species and Gastropoda 02 species at Urban lake. Shrrinivas (2004) recorded total 13 species of macrobenthicinvertebrates belonging to three major groups. Annelids, Anthropods and Mollusca have been encounted in the ilttoralzone of Banjara lake. Tijare (2012) recorded 11 species of Gastropods in some lentic water bodies of Gadchiroli District.

Benthos plays an important role in the secondary productivity of fresh water lakes through exchanging of allochthonous and autochthonous materials in a lake ecosystem. Benthic organisms are of great ecological significance because they constitute the food of fish and their productivity plays an important role in sustaining food chain and food web.

Acknowledgement:

References-:

1. Chandrashekhar, S.V.A.(1994). Macrozoobenthic fauna as indicator of pollution in HussainSagar , Hydrabad. Oikoassay, 11(1and 2) pp. 13-15.

2. Gorai, A.C., Rekha, Gupta, P. Chattarj and T. Chatterjee (2005): Studies on the macro-zoobenthos of two fresh water ponds, Dhanbad, Jharkhand, India. *J. of Aqua. Biol. 20* (2): *Pp.* 58 - 62.

3. Mylinski, E.andGinsburg, W. (1977). Macroinvertabrate as indicators of pollution. J. AWWA.69 pp. 530-534.

4. Sarkar,S.K.(1989). Seasonal abundance of benthos macrofauna in a fresh water pond .Envi. And Ecol.pp.113-116.

5. Tijare, R.V. (2012): Biodiversity of Mollusca present in some lentic water bodies of Gadchiroli District, M.S. India.*J. Bionano Frontiers Spe.Issu. Vol. 5(2-1) Pp.55-56*

6. *Vasisht, H.S.and Bandal, R.S.(1979). Seasonal variation of benthic fauna in some North Indian lake and ponds. India. J.Envi. 6(2) pp. 33-37.*

7. Zade, S.B. and Sitre S.R. (2012): Biodiversity of benthic macroinvertebrates in a polluted Urban lake of Nagpur M.S. India .*J. Bionano Frontiers Spe.Issu. Eco Reso. Pp.67-69*

ARTICLE

Seasonal Changes In Physico-Chemical Characteristics Of Simbhora Lake, District-Amravati (M.S.)

Ujwala W. Fule[1] and Sarita S. Nimgare[2]
HutatmaRashtriya Arts And Science College, Ashti.
E mail Id- patankar.kargi@gmail.com

Abstract: Physico-chemical characteristics study of Simbhoralake district Amravati was carried out from year 2013-14. The water is used for irrigation of the field. The parameters studied includes ambient temperature, water temperature, pH, conductivity, transparency, Free CO_2, total alkalinity, total dissolved solid, total hardness, calcium hardness,magnesium hardness, biochemical oxygen demand, chemical oxygen demand, dissolved oxygen.The seasonal analysis over the period of one year suggest that the lake water is suitable for drinking purpos

Keywards:Physico-chemical,Parameters,Simbhora lake, Water, Quality

Introduction

Water of good quality is required for living organisms. The quality of water is described by its physical, chemical and microbial characteristics. But, if some correlations were possible among these parameters, then significant ones would be fairly useful to indicate the resources as usually described according to its physical, chemical and biological or bacteriological characteristics.

Carbon di-oxide is added to aquatic ecosystem by directly being mixed from atmosphere, In addition to this, the other sources are rain water, in flowing ground water and the respiration of aquatic flora and fauna. Biochemical oxygen Demand (BOD) is the amount of oxygen utilized by micro organism is stabilizing the organic matter in aerobic condition DO measurement forms the basis of BOD analysis. It gives an indication of load of biodegradable organic materials present in the water body.

Organic matter in a sample also can be reacted directly with oxygen at a high temperature to produce carbon dioxide. Too much organic matter addition to the lentic and Iotic system increases the levels of COD and changes the composition of oxygen requiring organisms variation in the organic matter inturn, changes COD levels show diversity in the autotrophic and heterotropic populations and decreases the productivity status. The energy budgets of the aquatic bodies also directly related to the levels of chemical oxidation in prescribed periods. (Dakshin

and Soni,1979). The present investigation deals with physico-chemical charecterstics of Simbhora lake during 2013-2014.

Material And Methods:

Physical Parameters:

1) Ambient and Water temperature: For measurement of temperature of water of Simbhora reservoir, Thermometer of portable digital water analysis kit was used.

2) pH: For the measurement of pH, portable digital water analysis kit was used.

3) Conductivity: For the measurement of conductivity, portable digital water analysis kit was used.

4) Transparency: The transparency of water was measured by Secchi disc.

Chemical Parameters:

1) Dissolved Oxygen: Dissolved oxygen from water samples was determined by Wrinkler's iodide azide method.

2) Free Carbon Dioxide: Free carbon dioxide from water samples was determined by titrimetric method.

3) Alkalinity: Alkalinity of water was estimated by titrimetric method.

4) Total Hardness: Total hardness of water samples was estimated by titrimetric method.

5) Calcium Hardness: Calcium hardness of water samples was estimated by titrimetric method.

6) Magnesium Hardness: Magnesium hardness of water samples was estimated by titrimetric method.

7) Total Solids, Total Dissolved Solids: Total Solids, Total Dissolved Solids and Total Suspended Solids were estimated by Gravimetric method.

8) Biochemical Oxygen Demand (BOD): For the determination of biochemical oxygen demand, titrimetric method was used.

9) Chemical Oxygen Demand (COD): For determination of chemical oxygen demand, titrimetric method was used.

Results and Discussion:

Physico-chemical parameters:
Seasonal variation and annual average of the physico-chemical parameters analysed are represented in Table-1.

Ambient Temperature:

In the present investigation, ambient temperature ranged from 27.00°C to 44.00°C. Seasonally, Maximum ambient temperature (atmospheric temperature) was recorded in summer, moderate in monsoon and minimum in winter season, similarly Ganesan and Sultana (2009) stated that Atmospheric Temperature 30 ^{0}C to 39 ^{0}C in Chropet lake. Aher*et al.,* (2007) observed Atmospheric temperature was higher in summer while lower in winter at Kagdipura swamp.

Water Temperature

In the present investigation, water temperature ranged from 22.10°C to 37.20°C. Seasonally, Maximum water temperature was recorded in summer, moderate in monsoon and minimum in winter season Thakare*et al.,* (2002) recorded water temperature between 32.0°C to 37.0 °C in Dhamaswadilake, Latur.Dhere and Gaikwad (2006) recorded the range of water temperature between 25.20 °C to 34.0°C in Karpara reservoir, Parabhani (M.S.)

pH

In the present investigation, pH value ranged from 7.08 to 8.16, seasonally, the maximum pH was recorded during monsoon season and minimum in winter.Kulkarni and Zade (2012) stated that the water was alkaline throughout the year with no definite seasonal variation.Salve and Hiware (2006) reported the maximum pH in summer and minimum in winter with slight increase in monsoon.

Conductivity

During the present study, Conductivity fluctuated between 0.190 megohm/cm to 0.450 megohm/cm. seasonally; the maximum conductivity was recorded in monsoon and summer season and minimum during winter. Similarly, these values are quite similar with Narayana*et al.,* (2008).

In the present investigation, the maximum conductivity found in summer may be due to high evaporation rate and discharge of domestic effluents and organic matter. The seasonal variation n in conductivity may be due to increase in concentration of salts entering into the lake with sewage.

Transparency

In the present investigation, Transparency value ranged from 28.00 cm to 64.00 cm, seasonally, minimum transparency was recorded during monsoon season and maximum during winter season, similarly, Pulle (2000) observed the transparency values in the range of 28.4 cm to 87.8 cm in Isapur dam and further reported that the transparency was maximum in month of May and minimum in August. Kadam*et al.,* (2007) recorded the range of transparency between 41.5 to 95.0 cm and 35.0 to 10.5 cm at two stations respectively, from Masoli reservoir, District Parabhani, Maharashtra.

Dissolved Oxygen (DO)

In the present investigation, dissolved oxygen value ranged from 4.80mg /ltr to 09.30 mg/ltr, seasonally, minimum dissolved oxygen was recorded during monsoon season and maximum during winter season. Jadhav*et al.,* (2012) stated that amount of DO in water is important source of oxygen for respiration of aquatic organisms and observed values of DO range from 5.2 to 8.2 mg / L at Bori reservoir. Thakor*et al.,* (2011) observed average DO 5.9 mg/ L during rainy season 5.4 mg/L during winter and 4.9 mg/L during summer season.

Free Carbon dioxide (Free CO_2)[

In the present investigation, Free CO_2 value ranged from 2.80 mg/ltr to 4.60 mg/ltr, seasonally, maximum free CO_2 was recorded in monsoon and summer and minimum in winter. Similarly, Rama Devi (2007) recorded the range between 1.7 mg/ltr to 2.8 mg/ltr from Ali Sagar dam. Chouhan and Sharma (2007) reported a minimum CO_2, 4.40 mg/ltr in month of June and maximum 44.0 mg/ltr in month of August from a religious lake Budha Pushkar near Ajmer, Rajasthan

Total Alkalinity

In the present investigation, Alkalinity values ranged from 195.00 mg/ ltr to 340.00 mg/ltr, seasonally, maximum alkalinity was recorded in monsoon and summer and minimum in winter. Similarly, Warhate and Chauhan (2012) observed range of alkalinity values 230.8 mg/ L to 370 mg/ L in an around MIDC area Chikhalathant near Naregaon. Kumar *et al.,* (2007) studied urban pond Telibandha, Raipur and reported alkalinity between 64.5 mg/ltr to 317 mg/ltr. and further stated that the condition is considered favourable for fresh water fish culture

Total Hardness

In the present investigation, Total Hardness values ranged from 70 mg/ltr to150 mg/ltr, seasonally, maximum Total Hardness was recorded in monsoon and minimum in winter season. Similarly, Thomas *et al., (*2011) observed the range of total hardness 230 mg/L to 457 mg /L with no significant variation. Kulkarni*et.al,* (1995) reported the range of hardness between 76.3 ppm to 172 ppm in Sadatpur reservoir at Ahemadnagar

Calcium hardness

In the present investigation, Ca- Hardness values ranged from 58.00 mg/ltr to 100.00 mg/ltr, seasonally, maximum Ca- Hardness was recorded in monsoon and minimum in winter season. Solanki (2006) reported Calcium content fluctuation between 21.66 pp to 66.44 ppm, average 39.86 ppm in Bellallake, Bodhan. Khobragade (2003) reported the calcium and magnesium hardness values in range of 56.11 to 160 mg/ltr and 36 mg/ltr to 104.2 mg/ltr at Lonarlake.

Magnesium Hardness

In the present investigation, Mg- Hardness values ranged from 14 mg/ltr to 76 mg/ltr, seasonally, maximum Mg- Hardness was recorded in the maximum hardness was recorded in monsoon and minimum in winter season. Solanki (2006) reported the Mg- hardness content varied between 32.74 to 99.46 ppm in Bellallake. Mohanta and Patra (2000) observed maximum values of Magnesium during summer and minimum during winter in the river Sanamachakandana at Keonjhargarh.

Total Solids (TS)

In the present investigation, Total Solids values ranged from 540.00 mg/ltr to 923.00 mg/ltr, seasonally, Total Solids values were maximum during monsoon and minimum during winter. Trivedi*et al.,* (2007) reported that total solid between 85 to 410 mg /ltr at closed Beel of Kalyani industrial area of West Bengal. Khanna and Bhutiani (2003) recorded the average value of total solids as 558.89 mg/ltr from Sitapur pond at Haridwar.

Total Dissolved Solids (TDS)

In the present investigation, the value of total dissolved solids ranged between 408 mg/ltr to 624.00mg/ltr. The maximum seasonal value observed in monsoon season and minimum value in winter season. Marganwar*et al.,* (2012) observed TDS of Ambazari lake ranges from 252-260 mg/L with an average 258.6 mg/L and Futalalake 322-357 mg/L with an average 336.3 mg/L.

Biochemical Oxygen Demand

In the present investigation, the minimum value of B.O.D. was recorded 4.52 mg /ltr and maximum 13.59 mg/ltr. Seasonally, the maximum B.O.D was recorded in summer season and minimum during winter season. Kumar *et al.,* (2007) recorded B.O.D. values from 55.92 to 61.22 mg/ltr in Telibandha pond, Raipur. Anita *et al.,* (2002) recorded the range of B.O.D. from 0.4 to 26 mg/ltr in Mir Alam Lake, Hyderabad.

Chemical Oxygen Demand

In the present investigation, the minimum value of C.O.D. 15.45 mg /ltr was recorded and maximum 39.50 mg/ltr. Seasonally, C.O.D values were minimum during winter season while maximum in summer, similarly, Ingole*et al.,* (2009) observed values of COD between 1.9 to 8.15 mg/L and stated that COD is a measure of oxygen equivalent to the requirement of oxidizing matter content by strong organic oxidizing agent. Mohan *et al.,* (2007) worked on NayaTalab, Jodhpur and recorded the values of C.O.D. between 535.00 mg/l ltr to 88. 00 mg/ ltr.

		Summer 2013			Monsoon 2013			Winter 2014			Total		
S. N.	**Parameters**												
1	Ambient Temp. (ºC)	38.78	±	5.20	37.48	±	2.24	31.25	±	2.92	35.83	±	3.45
2	Water Temp (ºC)	30.95	±	3.78	29.99	±	1.57	25.78	±	2.37	28.90	±	2.58
3	pH	7.66	±	0.31	8.08	±	0.08	7.30	±	0.20	7.68	±	0.20
4	Conductivity megohm/cm.	0.234	±	0.039	0.398	±	####	0.238	±	0.017	0.290	±	0.033
5	Transparency (cm)	54.63	±	5.13	29.13	±	1.29	48.00	±	9.87	43.92	±	5.43
6	D.O. (mg/lit)	6.39	±	1.47	5.80	±	0.47	9.31	±	1.73	7.16	±	1.23
7	Free CO_2 (mg/lit)	4.18	±	0.23	3.50	±	0.45	3.13	±	0.48	3.60	±	0.39
8	Total Alkalinity. (mg/lit)	250.00	±	59.51	298.25	±	####	276.25	±	47.39	274.83	±	50.05
9	Total Hardness. (mg/lit)	110.75	±	29.02	131.50	±	9.71	96.25	±	9.68	112.83	±	16.14
10	Ca-Hardness .(mg/lit)	69.50	±	7.92	90.00	±	8.28	68.75	±	6.94	76.08	±	7.71
11	Mg-Hardness. (mg/lit)	41.25	±	23.07	41.50	±	6.84	27.50	±	6.10	36.75	±	12.00
12	Total Solids. (mg/lit)	642.25	±	50.08	861.75	±	####	713.75	±	101.2	739.25	±	68.82
13	T.D.S. (mg/lit)	479.75	±	33.52	578.00	±	####	492.50	±	81.76	516.75	±	49.87
14	BOD .(mg/lit)	11.22	±	1.96	7.08	±	0.76	5.24	±	0.72	7.84	±	1.15
15	COD. (mg/lit)	34.18	±	2.83	18.48	±	1.56	31.51	±	4.54	28.06	±	2.98

Table : 1

Seasonal variations of physico-chemical parametersinSimbhora lake during year 2013-2014

Acknowledgement:

References:

1. Aher, S.K., Mane U.H. and Pawar B.A. (2007): A study on physico- chemical parameters of Kagdipura Swamp in relation to pisciculture, near Aurangabad, (M.S). India *J.Aquaboil., Vol. 22 (1) Pp. 93-96*

2. Anitha, G. (2002): Hydrography in relation to benthic macro-invertebrates in Mir-Alam lake Hyderabad, Andhra Pradesh, India. Ph.D. Thesis submitted to Osmnaia University, Hyderabad. A. P. India.

3. Ganesan, S. and Mazher Sultana (2009) A base line study of physico- chemical parameters and some trace metals in water Chrompet lake, Channai, India. *J. Aqua. Biol. Vol.24 (2) Pp. 131-141*

4. Ingole, S.B., Pawale R.G. and Wavde P.N. (2009): water quality studies on Majalgaon Dam, District Beed M.S. *J.Aquaboil., Vol. 24(1) Pp. 71-76*

5. Kadam, M.S., Pampatwar D.V. and Mali R.P. (2007): Seasonal variations in different physico-chemical characteristics in Masoli reservoir of Parbhani District. Maharashtra.*J.Aqua. Biol., Vol. 22 (2): Pp.110 - 112.*

6. Kukarni, R. and Zade S.B. (2012): Assessment of some physico –chemical characteristic of recreational water body, Ramalalake in Chandrapur India, with special reference to eutrophication. *Bionano Fronters, Spe. Issu. Pp. 63-66. .*

7. Kumar, N., Vardia H.K. and Saxena R.R. (2007): Seasonal variation in physico-chemicalcharacteristics of Urban Pond, Telibandha, Raipur. *NSL: Pp.189 - 192.*

8. Marganwar, R., Durvey V., KodateJ.andDhawas S. (2012): Physico- chemical charectristricts and quality of lake water of Nagpur city, M.S. India .*J. Bionano Frontiers Spe.Issu vol. 5 (2-1),Pp. 159-164*

9. Mohanta, B. K. and Patra A. K. (2000): Studies on the water quality index of river Sanamachhakandana at KeonjharGarh, Orissa., India. *Poll. Res. 19 (3): Pp.377-385.*

10. Narayana, J., Puttaiah E.T., and Basavaraja D. (2008): Water quality characteristic of Anjanpura reservoir near Shikaripura, Shimoga, Karnataka. *J.Aqua. Biol. 23 (1), Pp.59-63*

11. Paka, S. and Rao A.N. (1997): Interrelationship of physico-chemical factors of a pond. J*. Env. Bio. (18): Pp. 67 - 72.*

12. Pulle, J.S. (2000): Biomonitoring of Isapur Dam water. Ph.D. Thesis, Swami Ramanand Teerth Marathwada University, Nanded.

13. Rama, Devi, T. (2007) Study of some aspects of Hydrobiology of Alisagar Dam water, Ph.D. Thesis submitted, Swami Ramanand Teerth, Marathwada University, Nanded.

14. Solanki, V.R. (2006): Ecological studies on Bellal and Pandu Lakes of Bodhan, A.P. India. Ph.D. Thesis submitted, Osmania University, Hyderabad.

15. Thakor, F.J., Bhoi D.K., Dabhi H.R., Pandya S.N. and Chauhan N.B. (2011): Water quality index of Pariyellake District Kheda Gujarat. *J. Cur. Wol.Env, Vol 6(2): Pp. 225-231*

16. Thomas, D.R. Sunil B. and Latha C. (2011): Physico – chemical analysis of well water at Eloor industrial area Seasonal study. *J. Cur. Wol.Env, Vol 6(2): Pp. 259-264*

17. Trivedi, R.K., Suman K. Das, S.K. Raut and Das B.K. (2007): Assessment of physico-chemical status of a closed Beel of Kalyani Industrial Area of West Bengal. *NSL: Pp.404 - 406.*

18. Warhate S.R. and Gahokar A.R. (2012): Application of Water quality index for assessment of lakes in Wani region, processing Innervate 2012 Jankidevi Bajaj College Wardha *(M.S.). Pp. 58-60.*

ARTICLE

Nanocream: A review nanotechnological aspect

Harsha Virsingh Sonaye, Chandrashekhar A. Doifode, Lalit Ghansham Pund

Shri Sachhidanand Shikshan Santh's College of Pharmacy Koradi Nagpur

Abstract: Nanoparticles are defined as particles with size in the range of 1 to 100 nm at least in one of the three dimensions . Because of this very small size scale , they possess an immense surface area per unit volume , a high proportion of atom in the surface and near surface layers , and the ability to exhibit quantum effect.Nanotechnology represents one of the most capable technologies of the 21st century. Solid lipid nanoparticles introduced in 1991 represent an alternative carrier system to traditional colloidal carriers such as emulsion, liposomes and polymeric micro and nanoparticles Nanotechnology is widely used in various cosmetic and dermatological products like lipsticks, soap, antiwrinkle cream , perfumes, toothpaste etc. Nanoparticles serve as the fundamental building block for various nanotechnology applications..Nanotechnology is one of the most capable techniques which are safe and effective for targeted dug delivery system. Nanoparticulate delivery system have been developed for good therapeutic effect with low toxicity Nanotechnology is concerned with development and utilization of structures and devices with development and utilization of structures and devices with organizational features at the intermediate scale between individual molecules and about 100 nm where nanoparticles occur as compared to bulk materials. The overall objective is to disseminate knowledge of the physical, chemical and biological phenomenon and processes in structures that have at least one length scale ranging from molecular to approximately 100nm (or submicron in some situations) and exhibit novel properties because of size. Use of carrier system in nanotechnology has added advantage of improved skin penetration , depot effect with sustained release drug action .As compared to conventional drug delivery system is more prominent and exhaustive . Nanotechnology has completely novel characteristic and application over others. Nanotechnology is a key technology leading to product innovation . Nanotechnologies use materials on an incredibly small scale so that they take on new properties compared to their larger form . The technology has the potential to transform many of the everyday consumer products that we use and wide range of product are already on the market The focus of the article is on the specific properties , phenomenon and processes that are realized because of the nano size . Experimental and theoretical tool of investigation at nanoscale as well as synthesis , processing and utilization of particles and related nanostructure are integral part of this publication.

Creams

Creams are viscous semisolid emulsion system with opaque appearance in contrasted to translucent ointments. Consistency and rheological character depends on whether the creamis w/o or o/w.

- Properly designed O/W creams are elegant drug delivery system, pleasing in both appearance and feel post application.
- O/W creams are non greasy and are rinsable.
- They are good for most topical purpose and are considered particularly suited for application to oozing wounds.

Factors affecting skin penetration

The factors that influence skin penetration are essentially the same as those for gastrointestinal absorption, with the rate of diffusion depending primarily on the physicochemical property of drug and only secondarily on the vehicle, pH, and concentration (Anonymous,2008).The principle physicochemical factor in skin penetration is the hydration state of stratumcorneum, which affects the rate of passage of all substances that penetrate the skin. The clinical importance of hydration can be found in the use of occlusive plastic film in steroidtherapy. Here, the prevention of water loss from the stratum corneum and the subsequent increased water concentration in this skin layer apparently enhances the penetration of the steroid. The temperature of skin and the concentration of the drug play significant roles, but they are secondary to that of hydration. The solubility of a drug determines the concentration presented to the absorption site, the water or lipid partition coefficient influences the rate of transport. An inverse relationship appears to exist between the absorption rate and the molecular weight. Small molecules penetrate more rapidly than large molecules, but within a narrow range of molecular size, there is little correlation between the size and the penetration rate. The transdermal delivery depend on

1. Release of the medicament from the vehicle.

2. Penetration through the skin barrier.

3. Activation of the pharmacological response .[1]

Nanotechnology is the fastest growing area for the maintenance of skin health as well as for the diagnosis and management of cutaneous disease. It encircles the study of particles smaller than 100 nm in size [2]

Solid lipid nanoparticles (SLNs) are introduced as a carrier system for poorly water soluble drug and cosmetic active drug [3]. The prefix 'Nano' from nanotechnology it is a Greek word, in which 'Nano' means Small or little [4]. It has come to focus in recent year that there is an increase in need to study on nanomaterial at systemic and in cellular level not only for its therapeutic application but also to minimize the side-effect. In the beginning of 1990s there were only the research group of Muller, Gasco andWestern working on nanoparticles, but now in world there are more than 20 research groups working on lipid nanoparticles. In India Institute of Chemical Technology, Mumbai whichis one of the most leading institute of India is vigorously working on lipid nanoparticle.[5] Nanocream or semisolid emulsion is one of the pharmaceutical topical formulations that are applied externally[6]. The nanocream can be prepared by using high energy methods such as high shear stirring, high pressure homogenizers or ultrasound generators[7]. Generally, a nanocream is very useful in personal care and cosmetics because the small size of the droplets which are in the nano range of 100–600 nm [8] allow them to deposit uniformly onto the skin and enhances the efficient delivery of active ingredients through the skin[9,10]. Basically, the cream contains various drugs for different remedial properties in an appropriate semi solid base either hydrophobic or hydrophilic in character [11].

Advantages Of Nanoparticles

1 Large scale production is possible.

2 Long-term stability[3]

3 Controlled and sustained release of active drug can be achieved.

4 Organic solvents can be avoided

5 It can be lyophilized [12]

6 It can be freeze dried to form powder formulation.

7 Autoclaving and gamma radiation Sterilization is possible.

8 It improves skin protection with organic compound [13]

Disadvantages Of Nanoparticles

1 Poor drug loading capacity.

2 High water content of dispersion.

3 The low capacity to load hydrophilic drugs[12]

Method of Preparation Of Nanoparticle

1. High pressure homogenization

1.1 Hot homogenization

1.2 Cold Homogenization

2. Microemulsion technique

3. Ultrasonication or high speed homogenization

4. Double emulsion method

5. Spray drying method

1. High pressure homogenization

In high pressure homogenization liquid is pushed at high pressure (100-2000 bar) through an arrow gap. The fluid accelerates at very high velocity (1000 km/h). In this typical lipid contents in the range of 5-10% which represents no problem to the homogenizer. Higher lipid concentrations up to 40% have been also homogenized to lipid nanodispersions[14]It iswidely used than any other method due to following advantages-

1 Easy scale up

2 Powerful technique

3 Short production time

4 Feasibility is more

Hot homogenization

This method is similar to homogenization of an emulsion, because this is also carried out at temperature above the melting point of lipid. In this active compound is dissolved in solid lipid which is melted for Solid lipid Nanoparticle. Due to lowered viscosity of liquid phase smaller particle size is obtained at high temperature[15] in which lipid melt containing active compound is disperse in hot surfactant solution at the temperature 5-10°C by continuous high stirring to get pre-emulsion which is then passed through high pressure homogenizer and maintain same temperature (5-10°C) as above and three cycle at 500 bar or2 cycles at 800bar [16.]Because of high kinetic energy of particles, particle size is increased due to particle coalescence [3].

Cold homogenization

This technique is developed to overcome the problems which are associated with hot homogenization like temperature induced drug degradation and drug distribution into the aqueous phase during homogenization [15]in this active compound is dissolved or dispersed in melted solid lipid then cool down it. After solidification of mass, crush it and ground to obtain lipid micro particle. Dispersing the powder in a cold aqueous surfactant solution yields a cold presuspension of micronized lipid microparticles[17]This suspension is passed through a high pressure homogenizer at room temperature or below it, applying typically 5-10 cycles at 1500 bar[16]. as compared to hot

homogenization, broader particle size distribution and larger particle sizes are typical of cold homogenizedsample[18].

Microemulsion Techniques

This method is based on the dilution of microemulsions. Micro-emulsions are two-phasesystems composed of an inner and outer phase. Microemulsions are clear, thermodynamically stable system composed of a lipophilic phase, water, surfactant and co-surfactant[19].Microemulsions are produced at a temperature above the melting point of the lipids, so the lipid should have melting point above room temperature. At first lipids are melt at the temperature 65-70°C [15] the lipid (fatty acids and/or glycerides) are melted, a mixture of water, co-surfactant(s) and the surfactant is heated to the same temperature as the lipid and added under mild stirring to the lipid melt. A transparent, thermodynamically stable system is formed when the compounds are mixed in the correct ratio for micro emulsion formation. This microemulsion is then dispersed in a cold aqueous medium (38±2°C) under mild mechanical mixing, which ensure the small particle size due to precipitation. The ratio of microemulsionto cold water ranges from 1:10 to 1:50 using a specially developed thermostated syringe with gentle stirring the composition of microemulsiondetermines the dilution process[20] ·Surfactants and co-surfactants include lecithin, biliar salts, but also alcohols such as butanol. Excipients such as butanol are less favourable with respect to regulatory aspects. The SLN preparations are washed three times with distilled water and filtered using a membrane, the excess water removed either by ultra-filtration or by lyophilisation in order to increase the particle concentration**.** The microemulsion is prepared in a large, temperature-controlled tank and then pumped from this tank into a cold water tank for the precipitation step. Important process parameters during the scaling up are the temperatures of the

microemulsion and the water, but also temperature flows in the water medium and the hydrodynamics of mixing which should change as little as possible during scaling up to maintain the same product characteristics[21]

Ultrasonication or high speed homogenization

SLN were also developed by high speed stirring or sonication. The most advantage of this method is that, the equipments that are used here are very common in every lab[22]First step of this process is the addition of drug to previously melt solid lipid. Then in second step, the heated aqueous phase is added to the melted lipid and emulsified by using high speedstirrer or aqueous phase added to lipid phase drop by drop followed by magnetic stirring. The obtained pre-emulsion is ultrasonicated by using probe sonicator with water bath (at 0ºC).In order to prevent recrystalization during the process, the production temperature is kept at least 5 ºC above the lipid melting point. The obtained nanoemulsion (o/w) is filteredthrough a 0.45 μm membrane in order to remove impurities which are carrying out during ultrasonication. The obtained SLN is stored at 4 ºC. To increase the stability of the formulation, it is lyophilized by a lyophilizer to obtain freeze-dried powder and sometime mannitol (5%) was added into SLNs as cryoprotector[16]The

problem of this method is broader particle size distribution ranging into micrometer range. It also produces physicalinstability like growth of particle upon storage, and also causes potential metal contamination[23]

Double emulsion method

For the preparation of hydrophilic loaded SLNs, a novel method based on solvent emulsification-evaporation is used [4]In double emulsion technique hydrophilic drugs is dissolved in aqueous solution, and then emulsified in melted lipid[17]In this method the drug is encapsulated with a stabilizer to prevent drug partitioning to external water phase during solvent evaporation in the external water phase of w/o/w double emulsion[13]Stabilized primary emulsion is dispersed in aqueous phase which contains hydrophilic emulsifier. After that the double emulsion is stirred and is isolated by filtration[18]

Spray drying method

It is an alternative procedure to lyophilization in order to transform an aqueous SLNdispersion into a drug product. This method is cheaper than lyophillization[17]This method cause particle aggregation due to high temperature, shear forces and partial melting of the particle. In this method short drying time and consequently fast stabilization of feed material at moderate temperatures make spray drying method suitable for producing nanoparticles of drugs that are thermolabile[24].The best result is obtained with SLN concentration of 1% in a solution of trehalose in water or 20% trehalose in ethanol-water mixtures (10/90 v/v)[4].Due to high temperature and shear force it may cause aggregation of particle.

References:

1) Fakhry KR, Mohammed Hassan KA. Formulation and evaluation of diphenhydramine HCL release from different semi-solid bases (cream, gel and ointment). World J Pharm Res 2013;2:1306-24.

2) Kreilgaard, M; Pedersen, EJ and Jaroszewski, JW (2000), "NMR characterization and transdermal drug delivery potential of microemulsion systems", J Control Release, Vol. 69: 421-433.

3) Kamble VA, Jagdale DM and Kadam VJ: Solid Lipid Nanoparticles as Drug Delivery System. International Journal of Pharma and Bio Sciences 2010; 1(3):1-9.

4) Bangale MS, Mitkare SS, Gattani SG and Sakarkar DM: Recent NanotechnologicalAspects in Cosmetics and Dermatological Preparations. International Journal of Pharmacy and Pharmaceutical Sciences 2012; 4(2): 88-97.

5) Puri D, Bhandari A, Sharma P. and Choudhary D: Lipid Nanoparticles (SLN, NLC): ANovel Approach for Cosmetic and Dermal Pharmaceutical. Journal of Global Pharma Technology 2010; 2(5):1-15.

6) Sonje A, Thube R, Parmar V, Kumari G, Deshpande P. A review on penetration enhancer for semisolids. Asian J Pharm;1:94- Res Dev 2013107.

7) Farahpour MR, Habibi M. Evaluation of the wound healing activity of an ethanolic extract of Ceylon cinnamon in mice. Vet Med 2012;1:53-7.

8) Sharma N, Bansal M, Visht S, Sharma P, Kulkarni G. Nanoemulsion: A new concept of delivery system. Chron Young Sci 2011;1:2-6.

9) Bouchemal K, Briançon S, Perrier E, Fessi H. Nano-emulsion formulation using spontaneous emulsification: Solvent, oil and surfactant optimisation. Int J Pharm 2004;280:241-51.

10) Rajalakshmi R, Mahesh K, Kumar CK. A critical review on nanoemulsions. Int J Innov Drug Discov 2011;1:1-8.

11) Aulton ME. Aulton's Pharmaceutics: The Design and Manufacture of Medicines. 3rd ed. London: Churchill Livingstone; 2007.

12) Khan S: Solid Lipid Nanoparticle: A Review. World Journal of Pharmacy and Pharmaceutical Sciences 2012; 1(1): 96-115.

13) Patel A, Prajapati P and Boghra R: Overview on Application of Nanoparticles in Cosmetics. Asian Journal of Pharmaceutical Sciences and clinical Research 2011;1(2):40-55

14) Ekambaram P, Sathali AH and Priyanka K: Solid lipid nanoparticles: A Review.Scientific reviews and chemical communications 2012; 2(1): 80-102.

15) Waghmare AS, Grampurohit ND, Gadhave MV, Gaikwad DD, Jadhav SL: Solid Lipid Nanoparticle: A Promoising Drug Delivery System. International Research Journal of Pharmacy 2012; 3(4): 100-107.

16) Ramteke KH, Joshi S.A and Dhole S.N: Solid Lipid Nanoparticle: A Review. IOSR Journal of Pharmacy 2012; 2(6): 34-44.

17) Kamble MS, Vaidya KK, Bhosale AV and Chaudhari PD: Solid Lipid Nanoparticles and Nanostructured Lipid Carriers - An Overview. International Journal of Pharmaceuticlal, chemical and Biological Sciences 2012; 2(4): 681-691.

18) Garud A, Singh D and Garud N: Solid Lipid Nanoparticles (SLN): Method, Characterization and Applications. International Current Pharmaceutical Journal 2012; 1(11):384-393.

19) Sinha VR, Srivastava S, Goel H. and Jindal V: Solid Lipid Nanoparticles (SLN'S) -Trends and Implications in Drug Targeting. International Journal of Advances in Pharmaceutical Sciences 2010; 1(3): 65-89.

20) Parhi R, Padilama S: Production of Solid Lipid Nanoparticles-Drug Loading and Release Mechanism. Journal of Chemical and Pharmaceutical Research 2010; 2(1): 211-227.16.

21) Puri D, Bhandari A, Sharma P. and Choudhary D: Lipid Nanoparticles (SLN, NLC): A Novel Approach for Cosmetic and Dermal Pharmaceutical. Journal of Global Pharma Technology 2010; 2(5):1-15

22) Khan S: Solid Lipid Nanoparticle: A Review. World Journal of Pharmacy and Pharmaceutical Sciences 2012; 1(1): 96-115.

23) A Sharma VK, Diwan, Sardana S and Dhall V: Solid Lipid Nanoparticle: An Overview, International Journal of Research in Pharmaceutical Sciences 2011; 2(3): 450-461.